COMPUTATIONAL ANALYSIS OF SUPERCRITICAL CO_2 OXY-METHANE COMBUSTION

A Dissertation

by

ROHIT MISHRA

Submitted to the Graduate and Professional School of
Texas A&M University
in partial fulfillment of the requirements for the degree of

DOCTOR OF PHILOSOPHY

Chair of Committee,	Dorrin Jarrahbashi
Committee Members,	Adonios Karpetis
	Waruna Kulatilaka
	Jacob McFarland
Head of Department,	Guillermo Aguilar

August 2023

Major Subject: Mechanical Engineering

ABSTRACT

The major challenge in designing oxy-fuel combustors in supercritical power generation cycles is the lack of fundamental understanding of the combustion process at high pressures exceeding the critical point of the fuel and oxygen (~200 bar). This combustion process becomes unique as it uses supercritical CO_2 (sCO_2) streams with high dilution rates to achieve lower combustor exit temperature (~1150ºC). In the absence of reliable combustion diagnostics at such high pressure and temperatures, a high-fidelity yet numerically efficient modeling framework is needed to enable the design of sCO_2 oxy-combustors. Reactive turbulent combustion simulations are computationally very expensive which can be prohibitive when the combustion regime of interest is supercritical due to the challenges in implementing real-gas equation of state and considering multi-step species and reactions in combustion modeling. To overcome these challenges, two different computational frameworks have been developed in this study: (1) A Direct Numerical Simulation (DNS) integrated with a one-step chemistry mechanism and multispecies real-fluid properties to gain a fundamental understanding of supercritical mixing and combustion in the sCO_2 oxy-combustor designed by Southwest Research Institute (SWRI). (2) A high-fidelity turbulent reacting flow simulation Large Eddy Simulation (LES) real gas solver at supercritical combustion using a detailed chemistry mechanism comprised of several species and reactions for methane combustion is developed. To enable computational feasibility a new high accuracy fast chemistry reduction tool using machine-learning based tools is developed and validated *a-priori* and *a-posteriori*. The developed tool is integrated with an open-source real-gas combustion solver and 3D Large Eddy Simulations (LES) are conducted for SWRI combustor.

The results indicate noticeable distinctions between mixing and combustion behaviors predicted by ideal- and the real-gas Equation of State (EoS), particularly in the near-inlet region. The reacting flow predicted by the real-gas EoS showed a wider density gradient barrier which tends to impede mixing, a longer wavelength at the flame edge, and a smaller flame edge thickness. Differences were also noted between the consumption/production rates of key species between real and ideal cases where the ideal-gas case predicted higher rates due to higher heat release rate caused by differences in density and specific heat. Combustion behavior at different %CO_2 dilution showed that dilution has a major impact on key combustion metrics such as heat release rate, temperature, and flame edge thickness. Zero-D and DNS results showed a peak in heat release rate for a given air-fuel ratio and the lowest CO production for 75%-80% CO_2 dilution with a maximum flame temperature of 2000 K. The results will provide crucial insight for designing sCO2 oxy-combustors. A new reduction tool called the Supervised Learning Global Pathway Selection (SL-GPS) is developed and validated with a standard deflagration flame (Sandia Flame D) experiment. The new tool is integrated with the real gas effects for ILES of the SWRI combustor. The SL-GPS is able to capture the flame characteristics within satisfactory error margin as compared to the detailed case. The ILES of SWRI combustor shows unique ignition and flame kernel expansion behavior. The ignition occurs in the radially outward region of the injection at a high turbulence zone. The ignition kernel is composed mainly of the CO mass fraction among the minor species which indicates incomplete combustion. This CO mass fraction reduces as the flame propagates and secondary oxidation takes over converting CO to CO_2. The flame expands radially and axially and interacts with the wall where major swirl motion takes over and the flame collapses onto itself leading to formation of a thin stable flame centered on the axis. This stable flame is closer to the injection point as compared to the original ignition location.

DEDICATION

To my mother, for her unconditional love, constant support, patience, guidance, and encouragement!

ACKNOWLEDGEMENTS

First, I would like to extend my deepest gratitude to my committee chair Dr. Jarrahbashi for her constant mentoring, guidance, and support through the course of this research. Furthermore, I would like to thank Dr. Karpetis, Dr. Kulatilaka and Dr. McFarland for agreeing to be on my committee. Their continued support and time are greatly appreciated. This work would not be possible without the collaboration with my lab colleagues Sarvesh Mayilvahanan, Aaron Nelson, Prajesh Jangale, Daniel Jiwani and Abhishek Pachankar. I also want to thank the staff at High Performance Computing at Texas A&M University for computing support. Moreover, I express my sincere gratitude to Cummins Inc. for their generous support, which has been instrumental in the successful completion of my study. Additionally, I would like to extend my appreciation to Pioneer Natural Resources for awarding me the fellowships for the academic years 2021-2022 and 2022-2023, which have provided invaluable financial assistance in pursuing my academic goals.

I would like to extend my gratitude to the Department of Mechanical Engineering at Texas A&M University for supporting my doctoral studies through various Fellowships and Scholarships and resources that one can only find in a top U.S. institution. I appreciate the help of staff members in the High-Performance Research Computing at Texas A&M University.

Finally, this work would not be possible without the constant support and encouragement from my friends and family.

CONTRIBUTORS AND FUNDING SOURCES

This work was supervised by a dissertation committee consisting of Professors Jarrahbashi [advisor], Kulatilaka, and McFarland at the Mechanical Engineering Department, and Professor Karpetis at the Department of Aerospace Engineering. All the work conducted for this dissertation is completed by the student independently.

Graduate study was also supported by several fellowships and scholarships from Texas A&M University.

TABLE OF CONTENTS

Page

LIST OF FIGURES

Page

LIST OF TABLES

Page

1. INTRODUCTION

1.1 Background and motivation

The current energy crisis and rising atmospheric CO_2 levels warrants a need for new technological solutions.[1-3] Renewable energy technologies such as solar, wind, hydro-electric and biomass have been an active area of research and while there has been a lot of improvements they still face cost and reliability challenges.[4] Nuclear power on the other hand poses safety concerns for nuclear waste disposal. Using biofuels reduces the dependency on fossil fuels; however, it still contributes to CO_2 emission. To overcome these challenges, carbon capture technologies have been developed to reverse the emission from conventional power generation systems. These technologies increase the capital costs and energy requirements.[5] Major advancements in moving toward carbon-neutral technologies from hydrocarbon combustion standpoint include: (1) the Integrated Gastification Combined Cycle (IGCC) system where coal is partially oxidized with pure oxygen at high pressures forming CO_2 and H_2 which is burned in a gas turbine combined cycle power unit; (2) Flue gas scrubbing using amine solvent; and (3) Oxy-fuel combustion where a hydrocarbon fuel is burned in pure oxygen to eliminate NOx emission produced when air is used rather than oxygen. Oxy-fuel combustion uses greater than 95% pure oxygen which results in flue gas to be composed mainly of CO_2 and H_2O from which CO_2 can be sequestrated by condensing H_2O [6]. The main investment in oxy-combustion is the need for air separation unit (ASU). According to the exergy analyses [7, 8] the efficiency penalty for this method is 10.2% points where ASU contributes to 6.6% points. Research efforts have been directed towards reducing the irreversibility caused by the cryogenic distillation process used in air separation technologies. [9] These strategies contribute to higher electricity cost as compared to the hydrocarbon combustion without carbon neutral technologies.

Oxy-combustion with gaseous fuels has been used in Graz cycle [10], clean energy system (CES) [11] using water as the temperature moderator, semi-closed oxy-combustion combined cycle (SCOC-CC) [12], MATIANT cycle, [13] and Allam cycle. [14] The Allam cycle, a forerunner for direct-fired sCO_2 power cycle is an emerging technology that operates as a recuperated, high-pressure, closed-loop Brayton cycle employing supercritical CO_2 (sCO_2) as working fluid and employs an oxy-fuel combustion process using sCO_2 recirculation in the combustion chamber as a diluent. [6] This cycle, exploits the special thermodynamic properties of sCO_2 by eliminating the energy losses that exists in steam-based Rankin cycles such as heat of vaporization. Apart from reaching high efficiencies, it does not require any additional equipment/cost for compressing CO_2 which is a major by-product. The major challenge in commercializing the direct-fired sCO_2 oxy-combustion cycle is the design of oxy-combustors for direct-fired sCO_2 cycles. There is a lack of fundamental understanding of the supercritical oxy-combustion process that involves high pressures (~200 bar) and considerable fuel-air mixture dilution due to incorporating a substantial fraction of CO_2 recycled from the exhaust and injected back into the combustor to control the temperature rise and lower the turbine inlet temperature (~1150 ^{o}C). Unique thermophysical properties of supercritical fluids, lower flame temperatures, and high dilution rates pose major challenges in understanding the ignition behavior and flame propagation in oxy-fuel combustors. In the absence of reliable experimental diagnostics at such high-pressure and temperatures, researchers have resorted to computational study of the oxy-combustion process. [15, 16] Computational studies involve significant challenges such as numerical pressure oscillations, implementation of real-gas effects, lack of appropriate chemistry mechanisms at such high pressures and high diluent concentration, resolving turbulence-chemistry interactions, and high computational costs, particularly using realistic complex combustor

geometry. These major shortcomings motivate the present study. The computational tools and understanding gained from this study can contribute to the design of the next-generation of low-carbon technologies and future design of high-pressure gas turbines that work with other fuels, e.g., hydrogen, ammonia, and biofuel blends.

1.1.1 Allam Cycle

Allam cycle was first introduced by Allam et al. [14] as a high-pressure, oxy-fuel, sCO_2 closed-loop cycle to generate power at a lower cost with near-zero emission which utilizes sCO_2 as the working fluid. The theoretical efficiency for a natural gas Allam cycle is 59% based on Lower Heating Value (LHV), i.e., the amount of heat released by combustion without the latent heat of vaporization of water. The traditional power systems, i.e., natural gas combined cycle (NGC), supercritical coal cycles integrated with gasification combined cycles (IGCC) have reached near the theoretical efficiency limits and involve prohibitive carbon capturing costs. [17] CO_2 sequestration systems can increase the cost of electricity by 50 to 70% for capturing 90% of the CO_2 generated. [18] The above challenges and considering the fact that fossil fuels will remain the dominant source for power generation and aviation makes the Allam cycle an alternative option to reduce the emission and enhance the cycle efficiency. The Allam cycle combines the benefits of oxy-combustion processes and sCO_2 power cycles and overcomes limitations posed by earlier approaches. [19, 20] In addition, compactness of the power plant and smaller equipment footprint by operation at supercritical conditions has increased the interest in sCO_2 power generation cycles. [14, 21, 22] A schematic of the Allam cycle is shown in Figure 1. High-temperature CO_2 from the combustor exhaust is cooled and water is separated. High pressure CO_2 is then recirculated back into the combustion chamber along with the oxidizer and fuel. Ideally, the higher the sCO_2 percentage dilution, the lower the consumption of fuel and oxidizer since the composition of fuel-

oxidizer-diluent is constant. For a sCO_2 combustor, this percentage can be as high as 95%. The use of oxygen gas as an oxidizer instead of air demands an extra Air Separation Unit (ASU) to separate the pure oxygen from air. However, recuperating CO_2 recycle stream into the combustion chamber reduces the amount of fuel and oxygen required during combustion. Since CO_2 is at a high pressure it can be removed from the system at a high purity level and above the pipeline pressures which facilitates carbon capture without the need for further pressurization. These advantages reduce the cost of carbon capturing and offer low-cost energy production compared to the current natural gas combined cycle plants.

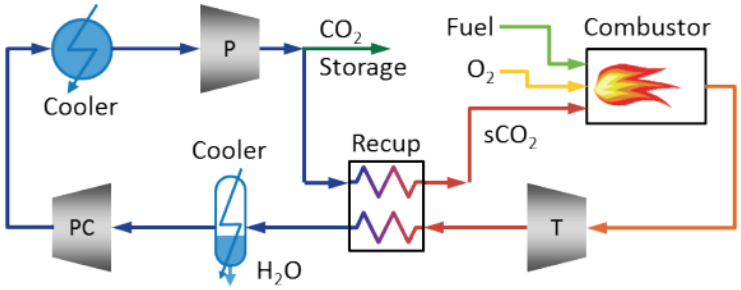

Figure 1. A schematic of the Allam cycle. Reprinted from [23]

Many studies have suggested improvements to the original Allam cycle. [24, 25] Chan et al. [26] performed an exergy analysis of their proposed improvement which showed 2.2 times the net power output than the original Allam cycle but the overall efficiency was only 49.32% which is higher than other oxy-combustion cycles, but 5% points lower than the original Allam cycle. The key result from this study is that the major portion of the exergy is lost in the combustors (~ 26%). This indicates the importance of designing sCO_2 combustors.

In addition, a mixture of oxygen, methane, and CO_2 at approximately 200-300 bar results in achieving an adiabatic flame temperature of ~2500 K. However, the use of recycled CO_2 as the diluent can reduce the exit temperature of the combustor to ~1423 K. Although this low temperature regime allows a more homogeneous combustion process and lower turbine inlet

temperature, the lower flame speeds raise concerns about flame extinction and stability. Major challenges in designing high pressure sCO_2 oxy-methane combustors is maintaining the flame stability at high pressure. [27] The challenge of running a turbine for thousands of hours of continuous operation while maintaining combustion efficiency requires a better understanding of the combustion process, material science, and life cycle analysis. Challenges in designing oxy-combustors for direct-fired sCO_2 cycles is the multitude of performance metrics that need to be accounted for. Some key design parameters include: injector design for mixing and flame stability, percentage split of recycled CO_2 diluent between injectors and cooling areas, target flame temperature which controls non-condensable products, and strategies to inject the diluent CO_2 for film cooling and thermal control. [28] High-fidelity combustion modeling integrated with appropriate chemical kinetics for the range of pressure and temperature relevant to sCO_2 cycles, and high-pressure thermodynamics can pave the way toward innovative and efficient combustor design.

Government (National Renewable Energy Laboratory (NREL), National Energy Technology Laboratory (NETL)), private (Southwest Research Institute (SwRI), Net Power, Cascade Technology, Combustion Research & Flow Tech.) and academic institutions (Georgia Tech and University of Central Florida [29] (UCF) among others) are working on developing a new combustor technology required for this sCO_2 cycle. The collective effort is planning for a full-scale 10 MWe Pilot facility for an indirectly heated closed-loop recompression Brayton cycle. Net Power has successfully tested an Allam cycle based power plant and delivered power to Electric Reliability Council of Texas (ERCOT) grid using a novel commercial scale 50 MW sCO_2 oxy-combustor designed by Toshiba at the La Porte facility in Texas, U.S.

1.1.2 Supercritical Phase

The fluid behavior above its thermodynamic critical point (supercritical, Figure 2) is characterized by a gas-like viscosity and diffusivity, but liquid-like density and solvating properties. Low viscosity and high diffusivity can lead to interesting transport behavior not seen in subcritical liquid and gas phases. The surface tension of fluids in supercritical regime is diminished, and the pure fluid becomes single-phase above its nominal critical point. Due to such highly varying properties, efforts were made to express the behavior of supercritical fluids as liquid-like and gas-like. Experimental studies [30-36] have shown an extension of the co-existence curve of gas and liquid to the supercritical region, namely the Fisher-Widom line, [37] Nishikawa's ridge, [30] the Frenkel line, [38] and the Widom line. [39] Banuti et al. [40] proposed a new and strongly defined cross-over across the Widom line that distinguishes between the liquid-like and gas-like regions in a homogeneous supercritical state space. A new interpretation of the Widom line, shown in Figure 3, is proposed based on the curvature of the Gibbs free energy where the supercritical cross-over is evaluated as a projection of the subcritical phase transition from a liquid to an ideal gas state to supercritical conditions.

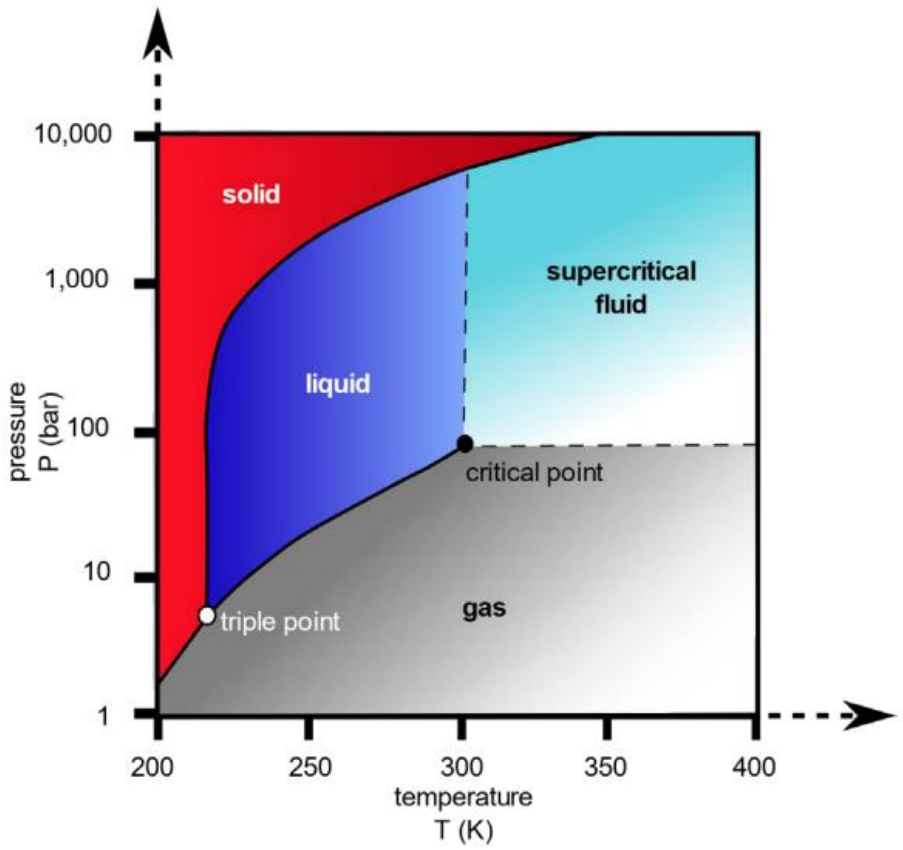

Figure 2. Pressure-temperature phase diagram for carbon dioxide [Finney, B. & Jacobs, M. (2010). Retrieved from https://commons.wikimedia.org/wiki/File:Carbon_dioxide_pressure-temperature_phase_diagram.svg.]

This revised phase space distinguishes the liquid-like and gas-like regions by crossing the Widom line. The jump from Widom to Frenkel line occurs at high pressures (~10 times the nominal critical point). The identification of the liquid-like and gas-like supercritical fluids becomes important for transcritical flows where the fluid transitions from a liquid-like density in the dense fluid region to a gas-like density in supercritical regime. The transcritical flows are bound to pressure oscillations and many studies are focused on alleviating this problem. [41-43] Transcritical flows are beyond the scope of this study as the temperature and pressure range for

Allam cycle is 1800K-3000K and 100bar-200bar respectively, which is well within the supercritical regime with respect to carbon dioxide.

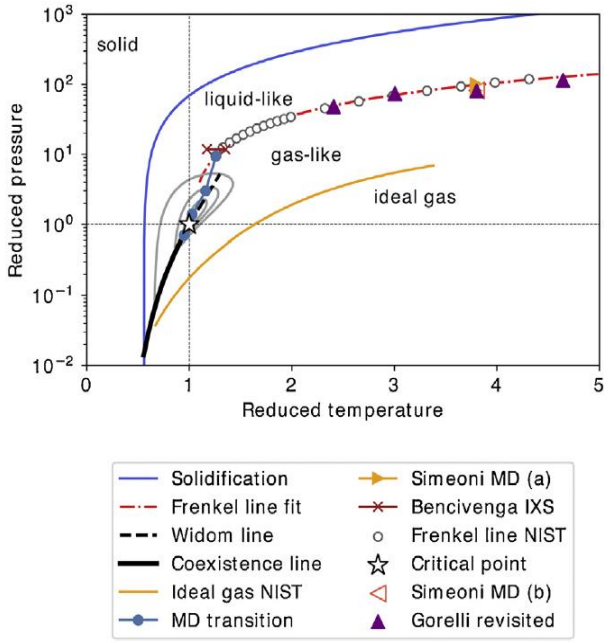

Figure 3. Revised pressure-temperature phase state for Argon shows the difference between the Widom and Frenkel lines separating liquid-like and gas-like regions Banuti et al. Reprinted from [40].

1.1.3 Supercritical Liquid Injection and Mixing

Accurate prediction of non-reacting supercritical mixing is imperative for modeling supercritical combustion. Supercritical fluid mixing with subcritical or other supercritical fluids leads to a binary/mixed state with a critical point deviating from the critical point of each of the constituents. [44] This condition commonly occurs in high-pressure liquid-fuel injection, e.g. liquid rockets, internal combustion engines, and power/propulsive gas turbines where a liquid fuel is injected into a supercritical environment. [45-47] The dynamics of subcritical injection includes primary atomization, secondary droplet breakup, and dilute spray dynamics. A cascade of droplet

breakup followed by vaporization eventually leads to mass, momentum and energy transfer leading to combustion. A phase diagram for various combustors [45, 48-50] shown in Figure 4 classifies different regimes, namely classical spray regime, transitional regime, and supercritical fluid regime. This figure indicates that supercritical behavior is expected in high-pressure diesel engines and gas turbines.

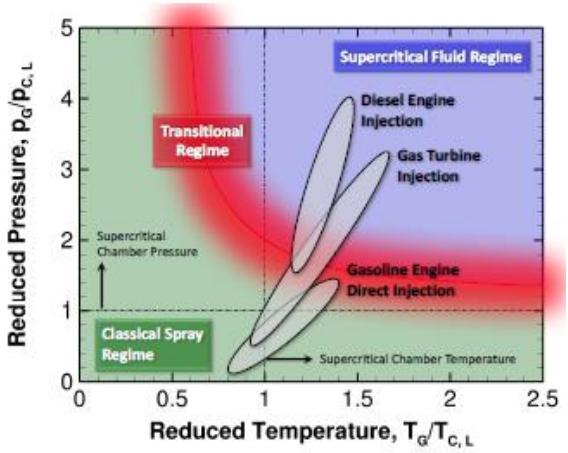

Figure 4: Combustion chamber behavior in practical combustors. Reprinted from [51].

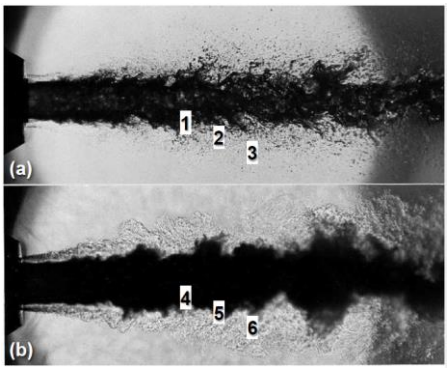

Figure 5. Experimental images highlighting differences between subcritical (top) and super-critical (bottom) injection. Reprinted from [44].

Figure 5 shows experimental images of subcritical and supercritical liquid injection. One major difference between subcritical and supercritical injection is the vanishment of surface

tension at supercritical conditions. [46, 52] In contrast to subcritical sprays, the dynamics of supercritical jet disintegration is dominated by diffusion rather than liquid atomization and spray formation. [51] Supercritical jets are subject to thermodynamic non-idealities and transport anomalies.

To understand the mixing and combustion phenomenon at supercritical conditions, several experimental studies have reported the mean longitudinal profiles of a scalar (temperature, density or mass fraction) along the jet axis, [44] radial profiles, [53] dense core length [54] and jet angle. [53, 55] Mayer et al. [56] carried out a series of experiments for supercritical N_2 injection in subcritical N_2 environment. One of the first attempts at understanding multi-species supercritical mixing is the injection of liquid nitrogen (LN_2) into gaseous hydrogen (GH_2) carried out by Oschwald et al. [57] and showed the difference between subcritical and supercritical mixing. Mixing of liquid oxygen and gaseous hydrogen (LOX-GH_2) by Ruiz et al. [58] has been widely used to validate models and gain a deeper understanding of the supercritical mixing. A common problem with experimental results is the limited resolution [58] which hinders the quantification of intermediate and small-scale turbulent structures. In addition, supercritical mixing does not follow the adiabatic mixing model and may lead to local heat absorption or heat release. [59] This may locally increase or decrease the temperature of the mixing layer. This behavior is not observed in subcritical fluid mixing where the mixed states are usually weighted average of thermal properties.

At supercritical conditions, the intermolecular forces are non-negligible, and thus density and specific heat capacity deviate from their ideal gas counterparts and capturing this behavior invokes the use of real-gas Equation of State (EoS) and appropriate supercritical mixing rules. Wang et al. [61] performed a linear stability analysis comparing supercritical nitrogen using ideal

and real-gas approach which showed that strong density stratification was observed for the real-gas case which tends to stabilize the mixing layer.

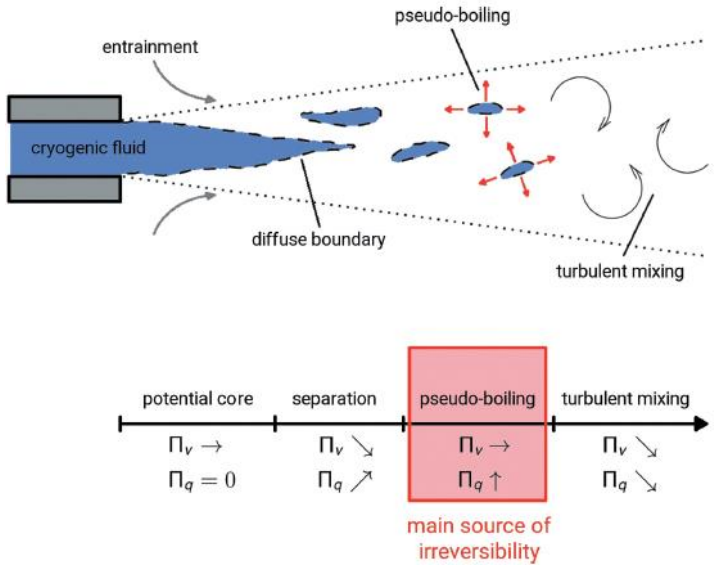

Figure 6. Physical model of the supercritical fuel disintegration process.$\boldsymbol{\Pi_v}$ is entropy generation due to viscous dissipation and.$\boldsymbol{\Pi_q}$ entropy generation due to heat transport. Reprinted from [60].

Another study [60] provides an insight into supercritical N_2 injection using an entropy generation analysis by identifying regions of mean entropy generation through viscous dissipation and heat transport. While the initial mixing phase was dominated by viscous dissipation, later stages of mixing were dominated by thermal transport. Based on this analysis, a physical model was proposed for supercritical fuel disintegration process shown in

Figure 6 as follows: potential core stage, separation stage, pseudo-boiling, and turbulent mixing. The peak in thermal expansion causes sudden density drop and a peak in isobaric specific heat capacity acting as an energy sink similar to the latent heat of vaporization. [62] The knowledge gaps from the literature search are highlighted in Table 1.

Table 1. Knowledge gaps identified from literature review

1. Experimental Challenges	2. Chemical Kinetics Data
• Difficult to get data from an actual sCO2 oxy-combustor due to high pressure and high temperature conditions. • Transient data for mixing and combustion required to understand the unique combustion strategy.	• Experimental data for mechanism limited. • Relevant mechanism for the highly varying combustor conditions required. • High CO2 dilution and high pressure makes this combustion strategy chemically unique.
3. Supercritical Thermodynamics	4. Computational modeling of real gas comb.
• Highly varying thermal properties have to be modeled. • Thermal effects of sCO2 dilution on mixing and flame not well understood. • Low temperature flame can have varying thermal behavior depending on the proximity to ignition location.	• For LREs: Combustion layer mostly ideal. • May not be true for sCO2 oxy-combustor. • Sub-critical combustion assumption will not hold true. • Computational cost for modeling of sCO2 oxy-combustion for practical combustors expensive because of chemistry mechanism and real gas thermal properties.

1.1.4 DNS vs LES

The major benefits and drawbacks of each method is discussed in Table 2.

Table 2. DNS vs LES

#	DNS	LES
1	Computationally expensive	Less expensive
2	Good for understanding underlying physics for canonical problems	Good for solving practical design and engineering problems
3	Resolved down to the Kolmogorov scale	Resolved enough to capture large eddies, smaller eddies are modeled
4	Reactive simulations with only one-step mechanism possible for real gas DNS of complex systems	Reactive simulations with multi-step mechanism possible but with appropriate reduction for LES
5	Provides good insights for steady state	Provides insights for transient effects as well since it captures multi-step reactions
6	Provides insights on mixing region and flame edge thickness	Provides insights on lift-off length and ignition delay
7	Quenching-re-ignition phenomenon cannot be captured due to one-step global mechanism	Quenching-re-ignition can be captured and details on achieving stable combustion can be extracted

1.2 Research Objectives

The main objective of this research is to understand the effect of percentage dilution on the highly varying thermo-chemical behavior of supercritical oxy-combustion process. Due to the lack of experimental data at such high pressure and temperature, the main research objective is achieved by developing a high fidelity yet low-cost computational framework to enable three-dimensional Computational Fluid Dynamic (3D CFD) integrated with finite-rate chemistry and real-gas effects relevant to supercritical carbon dioxide (sCO_2) oxy-methane combustion. The major challenges in modeling sCO_2 oxy-methane combustion involve (1) implementation of real-fluid behavior at high pressure (200 bars) with large sCO_2 dilution that affect the ignition, combustion process, and flame stability; (2) incorporating the multi-step and multi-species detailed chemical kinetics mechanisms relevant to high pressures and high diluent concentration in 3D simulations; (3) resolving turbulent-chemistry interactions at high pressures and high dilution rates. To overcome these challenges, this study is divided into the following four chapters:

Chapter 2: Direct Numerical Simulation of one-step supercritical oxy-combustion with real-gas effects.

Chapter 3: Developing reduced chemistry mechanisms for high-pressure oxy-combustion.

Chapter 4: Implementing Large Eddy Simulation of supercritical oxy-combustion using multi-step and multi-species reduced detailed mechanisms and identifying the flame morphology and flame stability by characterizing the DNS and LES results.

The successful completion of these phases has contributed towards a better understanding of high-pressure high-dilution supercritical combustion processes to enable designing future supercritical oxy-combustors. These combustors are key to improving the next generation of supercritical CO_2 cycles.

2. sCO_2 OXY-COMBUSTION USING SINGLE STEP COMBUSTION

2.1 Introduction

2.1.1 Supercritical CO_2 Mixing

The first step towards understanding sCO_2 oxy-combustion is resolving the mixing of sCO_2 and oxygen before combustion. Sengupta et al. [61] employed a DNS approach using a low-Mach number and fully-compressible solver of sCO_2 flow between a hot and cold plate. The key findings from this study are: (1) the density fluctuations near the wall that can alter the turbulence are more significant using a real-gas EoS compared to ideal-gas EoS and (2) the compressible effects were considerable even considering low Mach numbers. Ovais et al. [62] considered the mixing of CH_4/CO_2, CH_4/O_2, CO_2/O_2 streams at a supercritical pressure of 300 bar using a DNS approach and Peng-Robinson Equation of State(PR-EOS) is used to model the real-gas behavior while mass and heat flux vectors were derived from non-equilibrium thermodynamics and fluctuation theory. High density gradients were observed for all three mixing layers with increased presence of heavier fluid species within the mixing region. This study claimed that no significant departure from perfect gas was observed in all three cases. Purushottam et al. [63] assessed the effects of fluid compressibility and thermodynamic nonlinearities on the dynamics of sCO_2 mixing using an LES approach and showed that density gradients with respect to pressure and temperature are important modulators of the temperature and pressure field evolution.

2.1.2 Computational Modeling of Supercritical Combustion

Studies focused on supercritical combustion are historically relevant to liquid rocket applications involving liquid oxygen and gaseous hydrogen (LOX-GH_2). The interest in supercritical methane-oxygen combustion is growing as methane is accepted as an alternative fuel for rocket propulsion. Recent studies have focused on understanding the mixing and combustion

behavior of methane as a fuel for rocket propellant, [64-67] Moderate or Intense Low oxygen Dilution (MILD) combustion, [68-70] and power generation. [71-73] Among which, MILD combustion and oxy-fuel combustion at low pressure and subcritical regime are not relevant to this study. SCO_2 oxy-combustion significantly differs from this paradigm as the flow speed is significantly lower. In this section, the common practices in computational modeling of reacting flows are first discussed followed by recent findings on computational modeling of supercritical combustion.

Common approaches employed in computational modeling of reacting flows include Direct numerical Simulation (DNS), Large Eddy Simulation (LES), and Reynolds Averaged Navier Stokes (RANS). DNS becomes computationally expensive and is not feasible for flows relevant for engineering problems. In LES approach, spatial filtering is performed, and large eddies are solved while those that do not pass the filter are modeled. With the advancement in computational capabilities, LES has emerged as the prominent turbulence model [74]. The reacting flow simulations are based on finite rate chemistry and flamelet modeling. In finite rate chemistry, the species concentrations are solved as transported scalars with the chemical source terms solved using a stiff ordinary differential equation (ODE) solver. The reaction timescale of different species can vary during the simulations. Therefore, special ODE solvers, e.g., DVODE, [75] CVODE [76], Seulex, [77] Rosenbrock [78] is used to solve the system of stiff ODEs (i.e., the Jacobian matrix). Chemistry mechanism reduction methods reduce the number of species and reactions in finite rate chemistry modeling to enable computationally feasible simulations. In flamelet modeling however, the chemistry calculations are made *a priori* and tabulated based on key flow parameters, i.e., mixture fraction, and scalar dissipation rate to reduce the computational time without a need for solving the stiff ODE system during simulations. Another aspect of

reacting flow simulation is turbulence-chemistry interaction (TCI). Flamelet tables represent the connection between the mixture fraction and scalar dissipation rate which accounts for TCI. In finite rate chemistry models, TCI is implemented through the use of eddy dissipation models, e.g., Eddy Dissipation Concept (EDC) [79] for multi-step reaction and Eddy Dissipation Model (EDM) [80] for one-step reaction.

2.1.3 Combustion of Liquid Oxygen-Gaseous Hydrogen (LOX-GH_2)

One major challenge in modeling supercritical combustion is controlling the spurious pressure oscillations using the nonlinear real-gas EoS. Matheis and Hickel [81] studied multi-component vapor-liquid equilibrium (VLE) in modeling high-pressure fuel injection using cubic EOS and VLE calculations that represents the coexistence of supercritical states and subcritical two-phase states using a homogeneous mixture approach. This study also highlights the use of the fully conservative (FC) formulation in comparison to the quasi-conservative (QC) formulation. In the QC formulation, the traditional approach of total energy conservation is replaced by a pressure-evolution equation, which accounts for the variation of pressure with density, and provides an efficient and accurate means of modeling compressibility effects in high-speed flows. A benefit of using a QC formulation is a reduction in spurious oscillations when compared to a fully FC formulation at coarse grid levels. However, the use of QC formulation comes with the disadvantage of a loss of energy conservation, which can lead to incorrect temperature predictions. As the grid levels are refined, the QC energy losses and FC spurious oscillations reduce. Lacaze et al. [82] compared three methods to model supercritical mixing based on internal energy, pressure, and enthalpy and showed that the enthalpy-based formulation is the most accurate with least pressure oscillations.

The DNS benchmark configuration by Ruiz et al. [58] has been extensively used in the literature to understand supercritical mixing and combustion. Ma et al. [83] validated their proposed entropy-stable hybrid scheme to avoid spurious oscillations. Banuti et al. [84] ran LES simulations for the same configuration and showed that real-gas mixing is observed for the inert case. For the reactive case, the real mixing layer is thinner and is separated from the stoichiometric line as shown in Figure 7. Another computational study [85] that developed a combined approach for calculating the flamelet tables at sub and supercritical pressures conducted for a wider range of pressures for hydrogen and methane combustion also reported limited effects of real-gas behavior on the supercritical combustion layer.

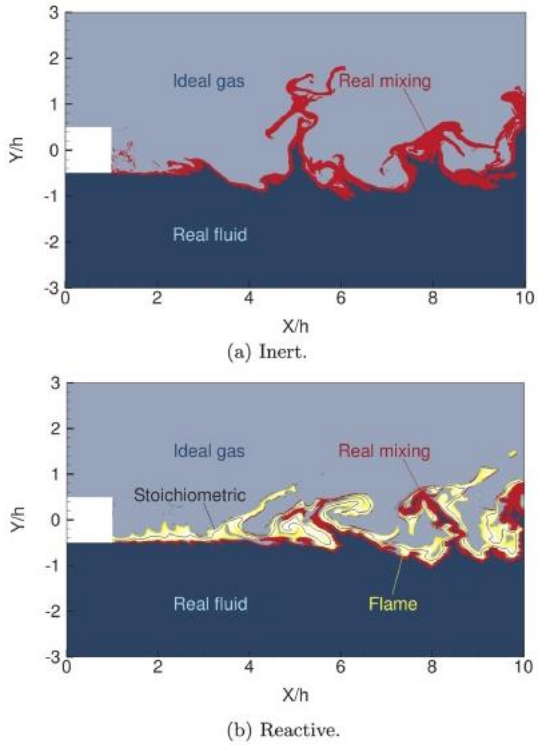

Figure 7. Domains of inert and reactive LOX (bottom stream) GH_2 (top stream) shear layers at a nominally supercritical pressure. Light and dark blue denote ideal-gas and real-fluid behavior, respectively. Real mixing is marked red and the flame is yellow. The black line corresponds to the stoichiometric mixture fraction. Reprinted from [84].

Oefelein et al. [86] employed DNS to understand the mixing and combustion of cryogenic oxygen-hydrogen shear-coaxial jet flame. The study reported that diffusion-dominated combustion occurs in the presence of large thermophysical property gradients, where transport processes play a dominant role in determining the combustion behavior. Particularly, the OH production rate profiles showed a significant drop, possibly due to fluctuations in heat release that might act as a triggering mechanism for combustion instabilities. Mardani and Barani [87] considered the effects of turbulence models, real EOS, chemical mechanisms, and chamber pressure. Comparing the results from the experimental results for OH emission, [88] the study showed that Soave-Redlich-Kwong EOS and k-ω turbulence model predicted the OH concentration with higher accuracy. Other studies [89, 90] employed the real-gas combustion model and showed that the flamelet model is able to better capture the temperature profile than the EDM model. However, it should be noted that the flamelet model used in this study was based on Peter's implementation [91, 92], which does not take into account real-gas effects. As the density and specific heat exhibit significant deviation from ideal values at supercritical conditions, these effects become increasingly relevant and should be considered in models. Although the real-gas EoS is used to predict density and Chung's transport[93] laws for predicting viscosity and thermal conductivity, the real-gas effects are not integrated with the governing equations. These shortcomings will be addressed in this study.

2.1.4 Combustion of Methane and Oxygen (CH_4-O_2)

Due to higher flame thickness, combustion of supercritical methane (CH_4-O_2) is subject to flame instability compared to LOX-GH_2 flames [94] which hinders anchoring of the CH_4-O_2 flames. Other experimental flame stability studies [95-97] showed the impact of the injector geometry and effect of combustor pressure on the flame. However, another study [95] showed that

the flame anchoring in methane combustion is similar for LOX-GH_2 flames, possibly due to the differences in injector geometry. The investigation revealed that, in addition to flame anchoring, the radial expansion of the flame greatly increases during the combustion of supercritical oxygen and methane, as compared to the combustion of transcritical oxygen and gaseous oxygen, and subcritical oxygen and gaseous oxygen. [98] This phenomenon is clearly depicted in Figure 8.

2.1.5 Computational Modeling of Supercritical CO_2 Oxy-Combustion

Unlike propulsion applications that involve high flow speeds and significant compressible effects, sCO_2 oxy-combustion occurs at lower speeds; thus, a variable density, low-Mach number approach is widely recognized as the most reliable and computationally feasible method for modeling sCO2 oxy-combustion. [99-101] The low-Mach number approach is based on the assumption that the velocity scales are much smaller than the speed of sound, thereby eliminating the need to model the effects of acoustic waves. The low-Mach number approach either employs a density-based compressible approach [51, 102-105] or an extension of the pressure-based incompressible solvers.

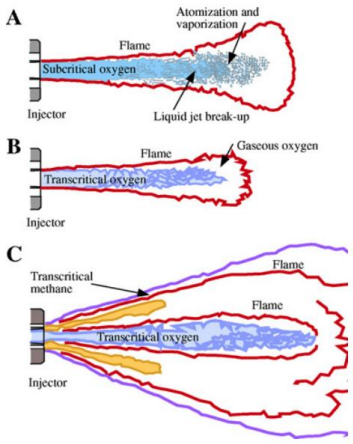

Figure 8. Schematic representation of cryogenic flames: (A) Subcritical oxygen-gaseous methane. (B) Transcritical oxygen- gaseous oxygen. (C) Transcritical oxygen-transcritical methane. Reprinted from [98].

Due to their highly expandable gas-like behavior and liquid-like density, momentum balance equations in supercritical fluids have a weak coupling between velocity and pressure. However, the accurate modeling of supercritical fluids, especially near the critical point, requires consideration of the equation of state (EoS) due to the significant density variation with temperature. To this end, numerical difficulties arise in calculating the heat propagation by thermoacoustic coupling in supercritical fluids. For low-Mach number flows however, this problem can be avoided by decoupling the density from the dynamic pressure that depends on both space and time. [106-109]

Computational studies of sCO_2 oxy-combustion so far are mainly focused on using an LES approach. There is only one recent study which applied a 2D-DNS [110] approach and two skeletal chemical mechanisms relevant to the oxy-combustion conditions, namely, (University of Central Florida) UCF-Mech [111] and (Georgia Tech) GT-Mech. [112] While the study provides valuable insight into the ignition process, it is important to note that a 2D mixing layer configuration was employed, which deviates from the typical configuration of a jet in practical combustors. In addition, the real-gas effects were not considered in modeling the reacting source terms in transport equations that become necessary in modeling supercritical combustion. These shortcomings indicate the need for DNS studies for practical combustors as will be discussed in this study.

Computational modeling of sCO_2 oxy-combustion using an LES approach has been discussed in recent studies. Strakey [15] provided important insights into the modeling of a canonical, single injector direct-fired sCO_2 combustor. A comparison of various Turbulence Chemistry Interaction (TCI) modeling approaches, i.e., laminar, flamelet, and Filtered Density Function (FDF) on CO production and flame characteristics have been compared to the equilibrium values calculated using the GasEQ code. [113] The laminar model overpredicted CO

concentration compared to the FDF due to the latter having a robust treatment of turbulent reaction rates. Flamelet models have been found to perform better at higher O_2 concentrations, while they tend to perform poorly for lower O_2 concentrations. This is because the flamelet assumption, which assumes a steady-state balance between the chemical reaction and turbulence, is invalid at the lowest O_2 concentration where chemical kinetics are slow as compared to turbulent mixing. At low O_2 concentrations, the combustion becomes more sensitive to the detailed reaction mechanism, and a more detailed kinetic model or a fully resolved LES approach may be required. Although the results shown by FDF models were most physical, the model is 10 times more computational expensive than the flamelet model.

Several studies [114-116] have developed a three-feed flamelet model which is of importance to sCO_2 oxy-combustion in which fuel, oxidizer, and diluent (CO_2) are considered as the three feeds. Doran et al. [115] created a flamelet formulation for a two-fuel stream and a single-oxidizer stream. Yu et al. [116] performed LES simulations with different formulations of a three-feed combustion system (fuel, oxidizer and CO_2 diluent) incluidng non-adiabatic quasi-two-dimensional flamelet (Q2DF). The authors concluded that the scalar dissipation rate associated with the diluent stream plays a critical role in cases where the diluent mixture fraction is high. Furthermore, they highlighted the necessity of considering the mixing of the diluent stream with other streams in order to obtain accurate predictions. The model agreed with the experimental measurements of thermo-chemical scalars at one bar which is not relevant to supercritical combustion. Kasuya et al. [114] employed an LES/flamelet approach for a three-feed sCO_2 oxy-methane combustor at 300 bar. The results showed that the flamelet scheme can better capture the temperature at the combustor outlet. Zambon et al. [28] extended the flamelet progress variable approach (FPV) for a three-stream configuration at 300 bar including another CO_2 stream for film

cooling. However, the implementation of the real-gas EOS with FPV tables and treatment of reacting source terms in transport equations to account for real-gas behavior were not addressed. Keum et al. [117] employed a combination of detailed finite-rate chemistry and large eddy simulation (LES) to gain insights into swirl stabilized combustion. Their results indicates that the flame brush and turbulent intensity are directly proportional and decrease as the background pressure increases. Kumar et al [118] investigated the effects of CO addition on a direct-fired oxy-fuel combustor using a numerical simulation approach. The study found that the addition of CO to the oxidizer stream resulted in an increase in the flame temperature and a decrease in the flame length. Furthermore, the study showed that the CO present in the exhaust gas, which is recirculated with the CO_2 stream, does not form a feedback loop, indicating that CO_2 capture and storage is not compromised in the presence of CO. The first attempt at designing and successfully testing a sCO_2 turbine and combustor system with varying percentage of O_2 in the inlet stream was made by Iwai et al. [16] The oxygen percentages significantly affected the maximum combustor temperature and the length of the recirculation zone. The combustor was successfully tested by ramping up the combustor pressure by gradually increasing the fuel, oxidizer and sCO_2 mass flow rate. The equivalence ratio at 300 bar pressure is reported to be between 0.82-0.92. However, the equivalence ratio varied between 0.3-0.9 during the ramping up phase. The maximum combustion exit temperature achieved is reported to be 1673 K.

While the above studies provide a preliminary understanding of the sCO_2 oxy-combustion, there are key questions that are yet to be answered. Several assumptions made in current studies need to be revisited to reflect the nature of supercritical combustion with sCO_2 dilution. Supercritical combustion relevant to liquid rocket engines occurs at conditions where fluids are cryogenic. Thus, combustion occurs after liquid jet atomization and transitions from subcritical to

supercritical conditions. For sCO_2 combustion however, the ambient CO_2 and the mixing layer are in a supercritical phase and two-phase effects do not likely occur unless a major drop in pressure occurs. Therefore, implementing the real-gas effects in reacting flow simulations becomes imperative. This study proposes incorporating the real-gas effects while calculating the chemical source terms and delineating the turbulence and thermal mixing effects using finite-rate chemistry in 3D modeling using practical combustor designs.

2.2 Computational Methods

A DNS-based solver integrated with real-gas effects has been developed for this study to capture the supercritical effects. The presented simulations are considered "DNS-like" [119] as the mesh size is slightly larger than the Kolmogorov scale as detailed in Appendix. To this end, the NGA [120] code is employed which is a high-order, fully conservative, low Mach number, and variable density solver that has been extensively validated for both non-reactive [121, 122] and reactive flow simulations.[123, 124] The governing equations for one-step combustion are as follows:

Mass conservation

$$\frac{\partial \rho}{\partial t} + \nabla \cdot (\rho \mathbf{u}) = 0 \tag{1}$$

Momentum conservation

$$\frac{\partial \rho \mathbf{u}}{\partial t} + \nabla \cdot (\rho \mathbf{u} \otimes \mathbf{u}) = -\nabla p + \nabla \cdot \boldsymbol{\tau} \tag{2a}$$

$$\tau = \mu(\nabla \boldsymbol{u}^t + \nabla \boldsymbol{u}) - \tfrac{2}{3}\mu \nabla \cdot \boldsymbol{u}\boldsymbol{I} \tag{2b}$$

Species conservation

$$\frac{\partial \rho Y_i}{\partial t} + \nabla \cdot (\rho \mathbf{u} Y_i) = \rho \dot{\omega}_i + \nabla \cdot (\rho D_i \nabla Y_i) \tag{3}$$

Energy conservation $$\frac{\partial \rho T}{\partial t} + \nabla \cdot (\rho \mathbf{u} T) = \rho \dot{\omega}_T + \nabla \cdot (\rho D_T \nabla T), \quad (4)$$

where, ρ is the fluid density, $\mathbf{u}$ is the velocity vector, p is the pressure, $\boldsymbol{\tau}$ is the shear stress tensor, Y_i is the mass fraction of the i^{th} species, T is the temperature. D_i and D_T represent the mass diffusivity of the i^{th} species and thermal diffusivity, respectively. $\dot{\omega}_i$ and $\dot{\omega}_T$ are combustion source terms calculated based on the one-step combustion model [125] discussed in Appendix.

Properties such as density, specific heat, viscosity, and diffusivity can significantly vary between real-gas and ideal-gas conditions. Therefore, unlike the original solver that uses an ideal EoS, Peng-Robinson [126] EoS is implemented in this study to calculate the real-gas density. As multiple species in the real-gas regime are mixed, the properties of the mixture are calculated using the mixing rules developed by Chung et al. [93] To find the real-gas specific heat, an adjustment is made to the ideal gas specific heat by implementing a departure function. Chung's transport rule [93] is used to obtain viscosity and diffusivity. The averaged mass diffusion coefficient, i.e. D_i is calculated using the Fickian law.[127] The binary diffusion coefficient $D_{i,j}$ is calculated using Fuller's model [128] and Takahashi's correction.[129] The thermal, transport and mixing rules implemented in the code are detailed in Appendix.

2.3 Results and Discussion

2.3.1 Non-Reacting Supercritical Mixing

In this section, we demonstrate the differences in predicting supercritical mixing behavior using ideal-gas and real-gas EoS for two supercritical mixing cases: (1) single-species (N_2 injected into N_2) and (2) multi-species (H_2 injected into N_2) which have been commonly used in validating computational models at supercritical conditions. Understanding the differences observed in the mixing behavior between ideal- and real-gas predictions in this section will shed light on the combustion behavior at supercritical conditions.

2.3.2 Single-Species Supercritical Injection

The injection of supercritical N_2 into subcritical N_2 based on Mayer et al. [56] experiment which is widely used for validating numerical models is used to validate our developed DNS-based solver with real-gas thermal and transport rules as described in Appendix. The basic configuration of the experiment is the injection of N_2 at 140 K into N_2 at 40 bar pressure and 298 K temperature. Validation of the thermal and transport properties is performed against the NIST database discussed in Appendix. In addition, more details of the experimental conditions for the validating case and computational setup are provided in Appendix.

The results from the real-gas mixing for N_2-N_2 injection are shown in Figure 9. The contour plots of density and temperature in Figure 9a-d show that the density gradient between the two streams is initially significant for the real-gas case due to the higher temperature difference between the injected and ambient N_2. This leads to a highly dense supercritical N_2 core mixing with a lower-density N_2 environment. The core disintegration occurs further downstream of the inlet as compared to the ideal-gas case and the flow starts moving radially outward once the core completely disintegrates and supercritical mixing prevails. This behavior is reflected in Figure 9e-f which shows the density gradient contours. For the ideal-gas case, more enhanced mixing is noticed near the injection region with the incoming stream. For the real-gas case, the density gradient drastically decreases after mixing is improved due to thermal diffusion. This drop in density reduces the density gradient allowing for the shear layer to develop and form small eddies around the less dense core region which contributes to the disintegration of the core and motivates mixing and radial expansion of the jet Figure 9g-h shows the vorticity contours ($\boldsymbol{\omega} = |\nabla \times \boldsymbol{v}|$) superimposed with the iso-line of density gradient set as 2×10^5 kg/m.^{4} As the initial sharp density gradient vanishes, vortical structures penetrate into the core region.

Quantitative analysis of the density gradient for the real-gas case is shown in Figure 10. As mentioned earlier, the density gradient is significantly larger near the injector and the core disintegrates between x = 10 to 15 mm where the density gradient drops (Figure 9e-f). Post x =15 mm, the flow becomes more homogeneous as supercritical turbulent mixing takes over. Larger density gradients create a barrier that delays the core disintegration and the subsequent turbulent mixing. Subcritical injection is characterized by a breakup process involving the development of ligaments and break up into liquid droplets that evaporate and mix with the ambient fluid. In supercritical injection, however, instead of the formation of ligaments and droplets, the core starts to heat up from the periphery leading to a decrease in density gradient. The peripheral region then becomes susceptible to the shear layer of the hot and low-density ambient nitrogen which leads to turbulent mixing in the absence of phase change and surface tension effects that tend to delay the mixing at subcritical conditions. Current simulations with the real-gas EoS capture the experimental data for density reasonably well for the simulation data averaged over 50 ms as shown in Figure 11. An average error of 12% is noticed at x/D =30. The mismatch near the nozzle has been attributed to wall heating effects and the lack of accurate measurements in that region as highlighted in previous studies.[132, 133] In addition, the coarsening of the mesh due to scaling can lead to a loss of accuracy in the axial direction.

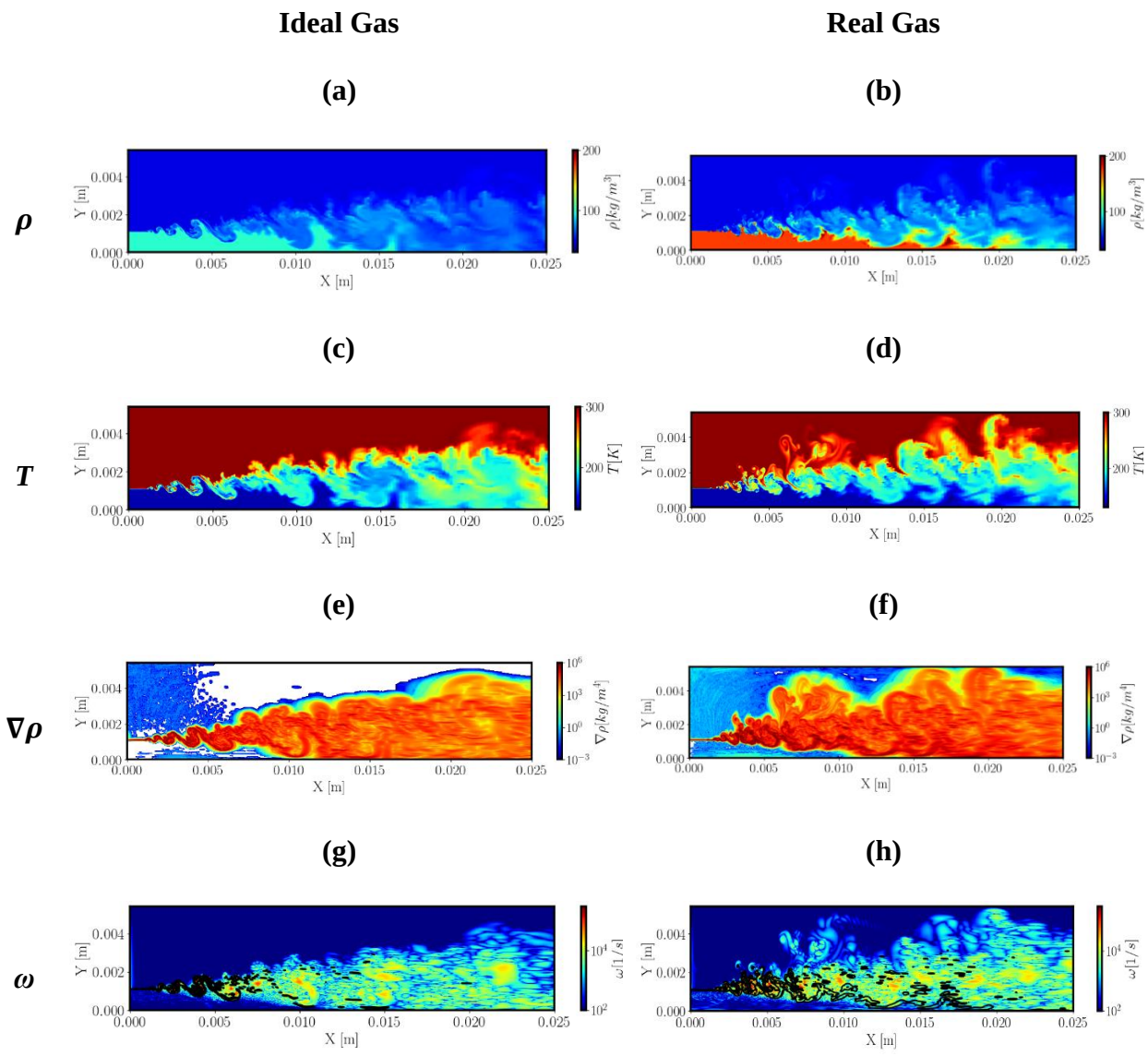

Figure 9. Contour plots for N_2 at 140 K injected into N_2 at 40 bar pressure and 298 K temperature at t = 0.64 s and comparison between ideal-gas and real-gas EoS predictions: (a-b) density; (c-d) temperature; (e-f) density gradient and (g-h) vorticity overlapped on iso-line for density gradient at 2×10^5 kg/m^4.

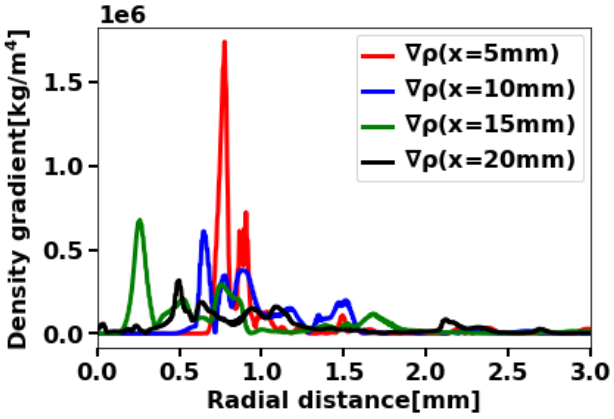

Figure 10. Comparison of radial distribution of the density gradient at t = 0.64 s for N_2 injection (real gas EOS).

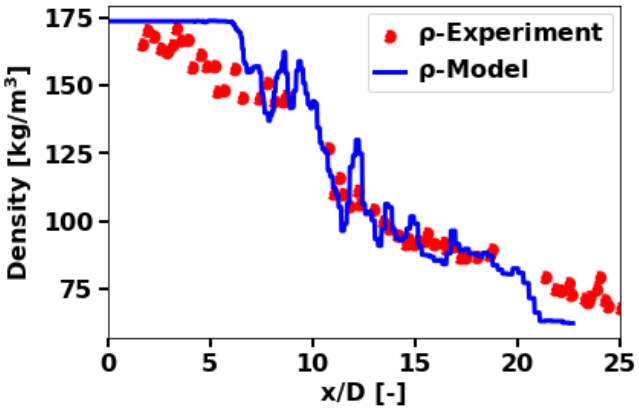

Figure 11. Centerline density compared with Mayer et al. experiments [56] averaged for t = 0.59-0.64 s (real gas EOS).

2.3.3 Multi-Species Supercritical Injection

To test the mixing rules implemented in the DNS solver (described in Appendix), the injection of H_2 into N_2 is considered and the results are validated against the experiments of Oschwald et al. [57] The basic configuration of this experiment is the injection of a nitrogen jet at 140 K with a hydrogen co-flow at 270 K into a nitrogen environment at 298 K temperature and 40 bar pressure. The details of the experimental and computational setup are described in Appendix and a brief discussion of the properties calculated using the mixing rules is presented in Appendix.

Figure 12 shows the comparison of the N_2-H_2 injection using the ideal-gas EoS versus the PR-EoS. Major differences are observed in the flow structures including a shorter core length (Figure 12a-d) and lower density gradient (Figure 12g-h) between the injected and ambient nitrogen predicted by the ideal-gas EoS. The real-gas case exhibits a longer core length due to higher density gradients that delay the core disintegration similar to the N_2-N_2 injection.

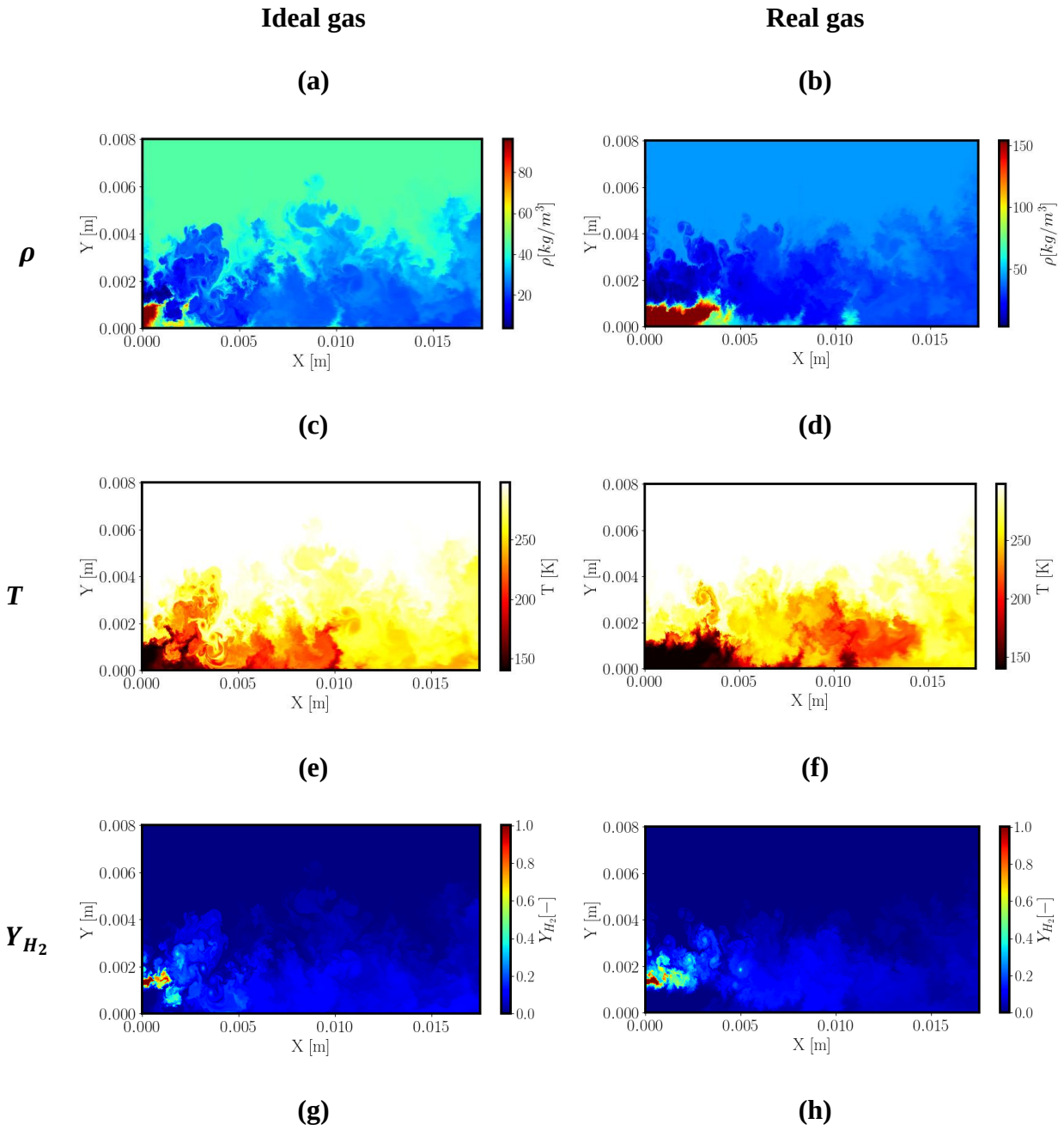

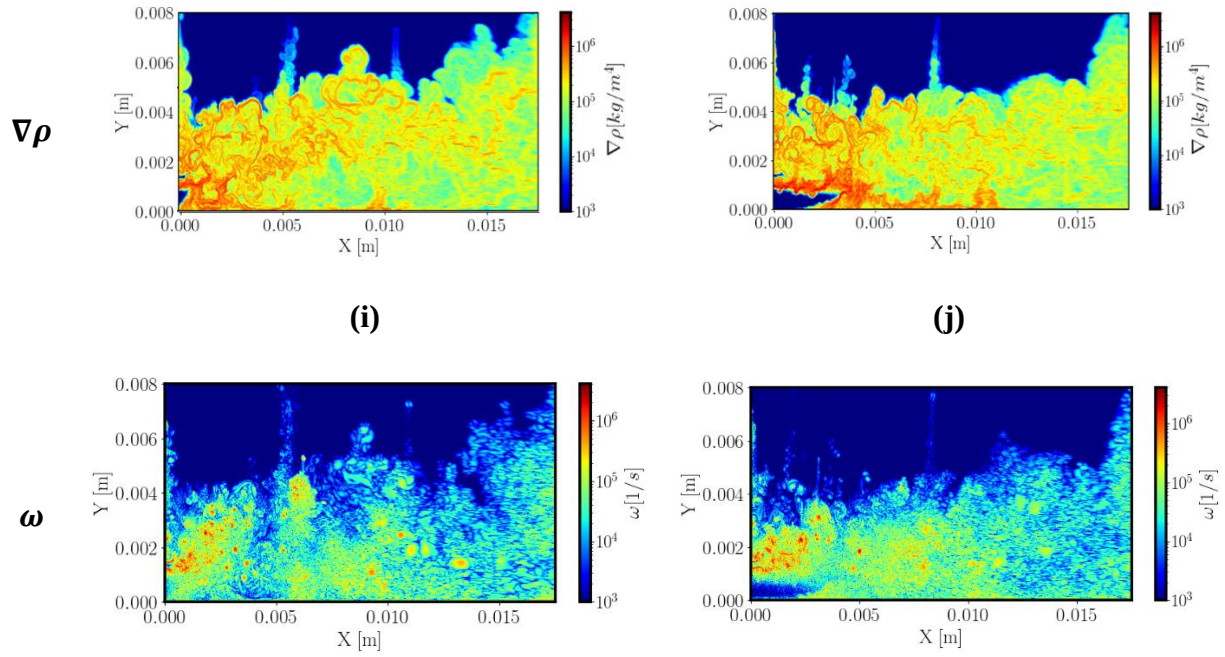

Figure 12. Contour plots for N_2-H_2 mixing compared between ideal-gas and real-gas EoS: (a-b) density, (c-d) temperature, (e-f) H_2 mass fraction, (g-h) density gradient, and (i-j) vorticity.

The ideal-gas EoS predicts a lower density than the real-gas at supercritical conditions evident from the lower density gradients for the ideal-gas case in Figure 12(g-h). Such lower density gradient promotes vorticity generation due to the fast-moving H_2 stream and quick disintegration of the core which further enhances mixing. For the real-gas case however, the high-density gradient creates a barrier between the two fluids which impedes the penetration of vortical structures into the core region and delays the core disintegration (Figure 12b, d, f, and h). The ideal-gas case shows a more enhanced mixing behavior and larger eddies very close to the inlet where the core disintegrates which are less pronounced in the real-gas case as seen in Figure 12i-j. This behavior is highlighted in Figure 13 which focuses on the mixing behavior in the near-injector region by showing the vorticity contours overlapped with the iso-line of constant density gradient set at 3×10^5 kg/m^4. For the ideal-gas case, the core disintegration is seen upon jet introduction to the ambient, and a higher vorticity is observed near the jet axis when the density

gradient vanishes (Figure 13a). For the real-gas case, the density barrier between H_2 and N_2 streams is evident by the integrated density gradient iso-line (red solid box) which is broken in the ideal-gas case. As N_2 is heated by the ambient fluid, the density gradient decreases due to heat transfter and creates vortical structures that further promote jet core disintegration (red dashed box). Figure 13 also shows that thermal diffusion promotes the generation of turbulent vortical structures downstream of the inlet (red dash-dot box). As thermal diffusion heats the core region, the vortices disintegrate the core which results in an improved mixing. These results highlight the significance of implementing the real-gas effects at supercritical conditions for accurate prediction of the mixing behavior prior to combustion.

Finally, a quantitative comparison of the radial distribution of density at different axial locations downstream of the inlet in Figure 14 indicates that the real-gas model agrees with the experiments. The mismatch seen near the injection point is observed in previous studies [130, 131] and has been attributed to the nozzle wall heating due to the incoming nitrogen stream.

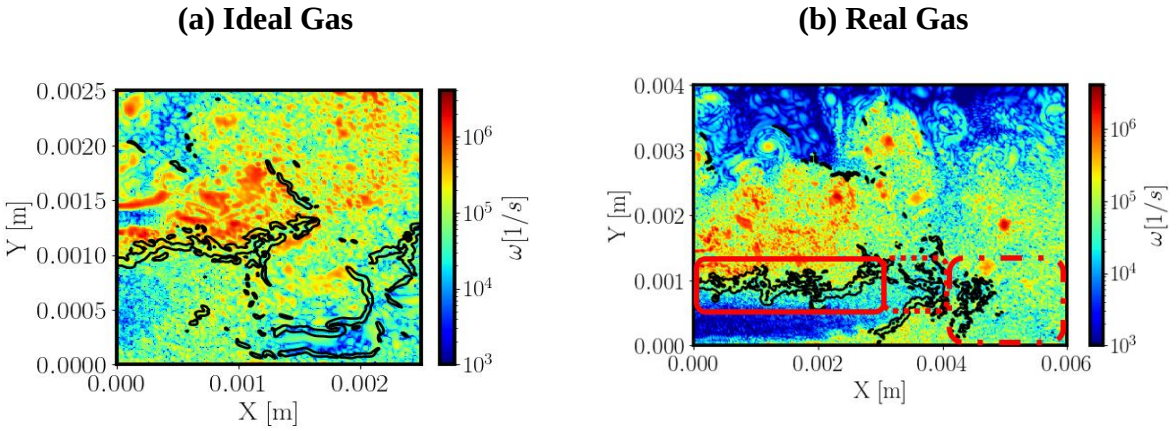

Figure 13. Comparison of the vorticity contours overlapped with the iso-line of density gradient (3×10^5 kg/m^4) for (a) ideal and (b) real-gas mixing behavior for N_2-H_2 mixing. The solid red box in the real-gas case (b) shows that the density gradient creates a barrier that impedes the penetration of vortical structures in the coflow. The dashed red box shows the drop in density

gradient caused by thermal diffusion, and the red dash-dot box shows the enhanced mixing region. (Size of domain is different, with real gas case zoomed out to show mixing behavior)

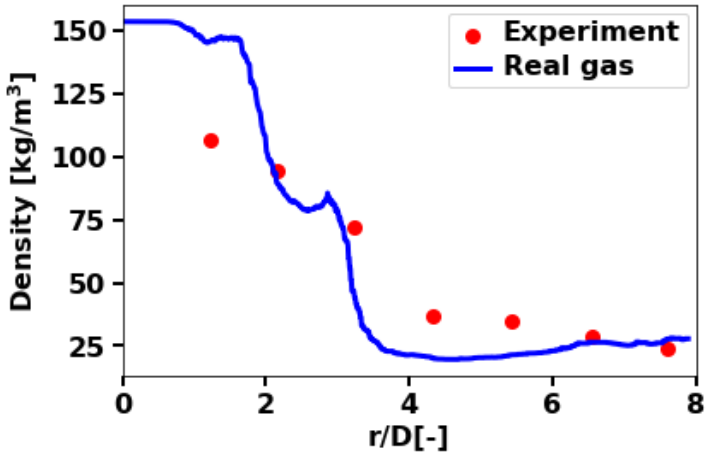

Figure 14. Comparison of the axial density profile for N_2 following Oschwald et al. experiments. [57]

2.3.4 Supercritical CO_2 Oxy-Methane Combustion using SWRI Combustor Configuration

Computational Model

The combustor design proposed by SWRI [132] with 86% sCO_2 dilution is adopted for modeling the mixing and combustion behavior of sCO_2 oxy-combustion using 2D-DNS and a single-step chemistry mechanism for methane combustion. The swirl angle has been neglected and fuel, oxidizer and CO_2 streams are assumed to be completely mixed at the inlet as detailed in Appendix along with the reduced computational domain. A schematic of the computational domain, initial conditions for fuel and oxidizer, and boundary conditions are shown in Figure 15. Methane, oxygen, and sCO_2 with 86% dilution as a premixed stream at 913 K enter the combustion chamber filled with pure CO_2 at 988 K and 200 bar. Simulations have been repeated for both real-gas and ideal-gas EoS and the results are compared for non-reacting and reacting flow conditions. The properties for fuel, oxidizer and sCO_2, case setup, total grid points, numerical schemes, and the one-step chemistry mechanism are given in Appendix.

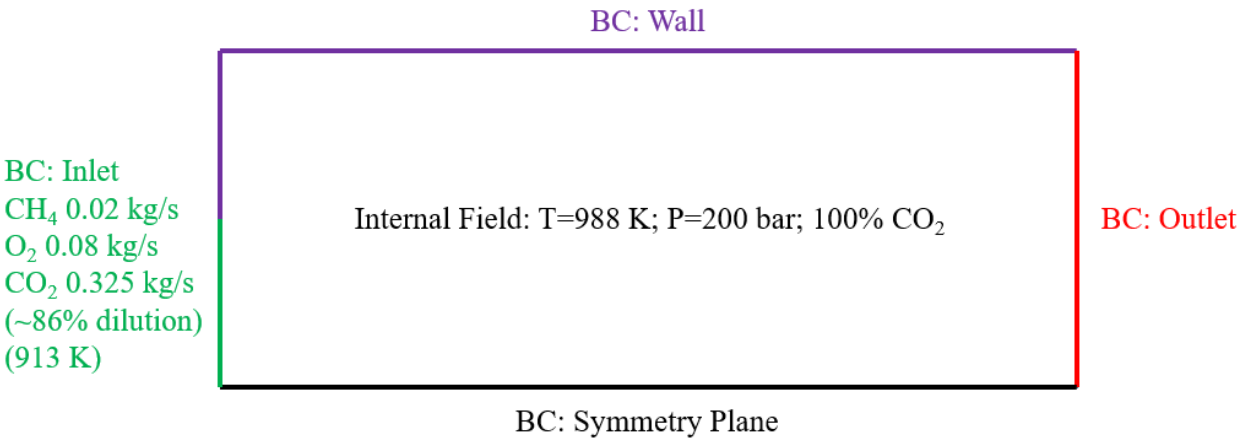

Figure 15. A schematic of the SWRI case setup and the initial and boundary conditions (i.e., BC).

Mixing Behavior and Flame Propagation using Ideal- and Real-Gas EoS

The non-reacting flow simulation results for the SWRI configuration depicted in Figure 16 show the behavior of supercritical mixing of oxygen and methane mixture with sCO_2 by portraying the contour plots for density, temperature, density gradient, and the iso-line of density gradient (3×10^5 kg/m^4) overlapped with vorticity contours. The density gradient iso-line is extended further downstream (x = 0.2 m) for the real-gas case while it ends at a shorter distance downstream of the inlet (x = 0.015 m) for the ideal-gas case. This behavior is similar to the supercritical two-species mixing cases before where the onset of core disintegration was closer to the inlet for the ideal-gas case. As a result, mixing is enhanced for the ideal-gas case in the absence of the large density gradient barrier which occurs in the real-gas case. The density gradient iso-line shown in the vorticity contours of Figure 16 further highlights the density gradient barrier for the real-gas case and higher vorticity for the ideal-gas case.

The effects of such discrepancy in predicting the mixing behavior on the combustion behavior are shown in the contour plots of density, temperature, and density gradient for the reacting case in Figure 17. Difference in density contours is noticed downstream where more entrainment is seen for the real gas case owing to the higher flame edge wavelength which will be discussed later.Although the overall flame propagation behavior visible in temperature and density contours appears to be similar between ideal- and real-gas cases, noticeable differences are observed in the density gradient which is substantially higher for the real-gas case, particularly near the inlet.

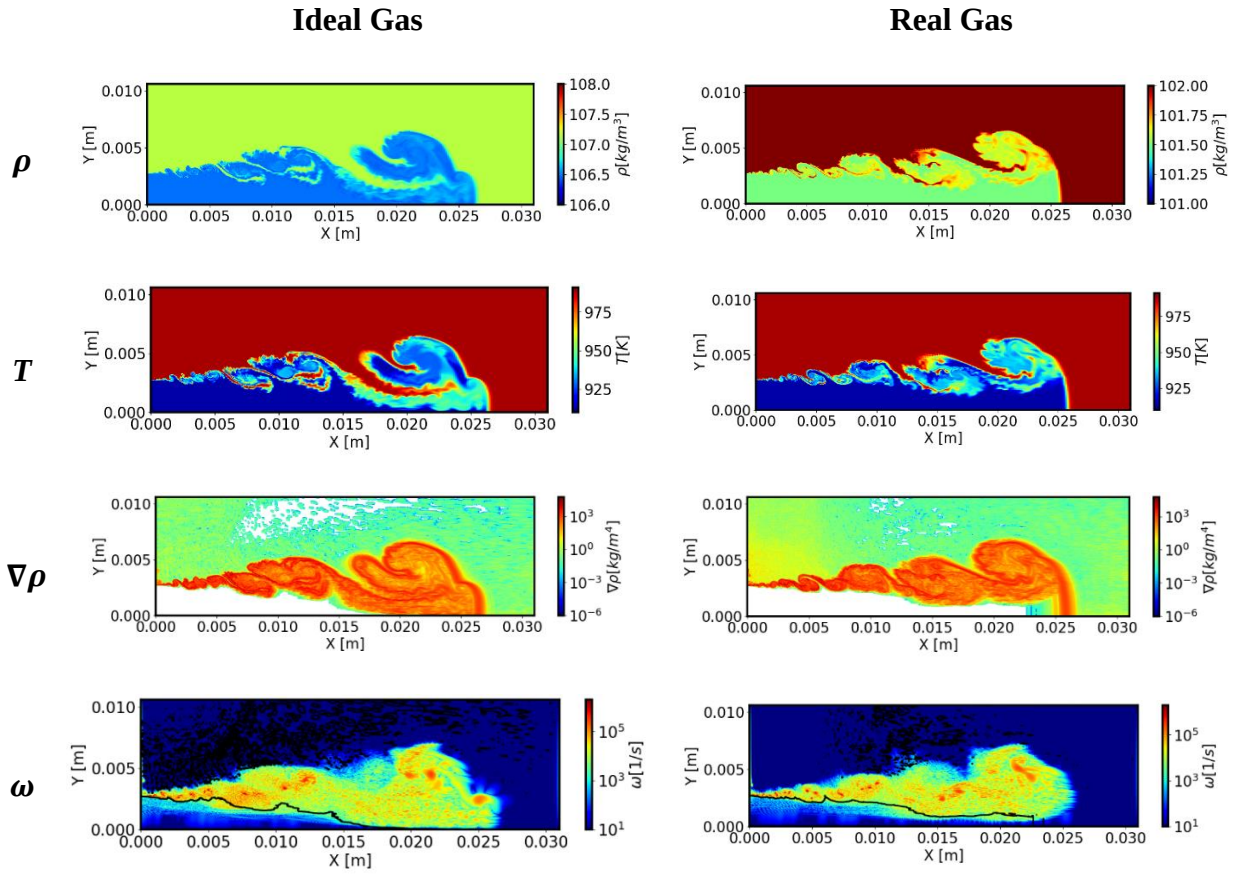

Figure 16. Contour plots for density, temperature, density gradient, and the iso-line of density gradient (3×10^5 kg/m^4) overlapped with vorticity contours for the non-reacting SWRI case.

Figure 11 shows that the heat release rate (HRR) for the ideal- and real-gas cases appear the same despite the discrepancies observed particularly along the axial direction. Quantitative comparison of HHR along the radial direction at two different axial locations (i.e., $x = 5$ mm and 10 mm) denoted by red arrows in Figure 18a-b are shown in Figure 18c-d, respectively. Figure 18c shows that the HRR peak occurs at a further radial distance for the ideal-gas case which indicates that the flame has a wider radial span at $x = 5$ mm. At $x = 10$ mm (Figure 18d), this trend is reversed. The peak in HRR in the real-gas case is extended more radially compared to the idea-gas case. The higher HRR for the ideal-gas case closer to the inlet is due to more enhanced mixing in that region consistent with the non-reacting flow behavior shown in Figure 16. For the real-gas case, the mixing is improved further downstream of the inlet which is consistent with the HRR radial profile where the HRR peak lags the ideal-gas case in the near-inlet region and catches up further downstream. To further reflect on the effects of mixing behavior on combustion behavior, Figure 19 shows the radial distribution of density gradients at three different axial locations, i.e., x = 1, 5, 10, and 15 mm from the inlet.

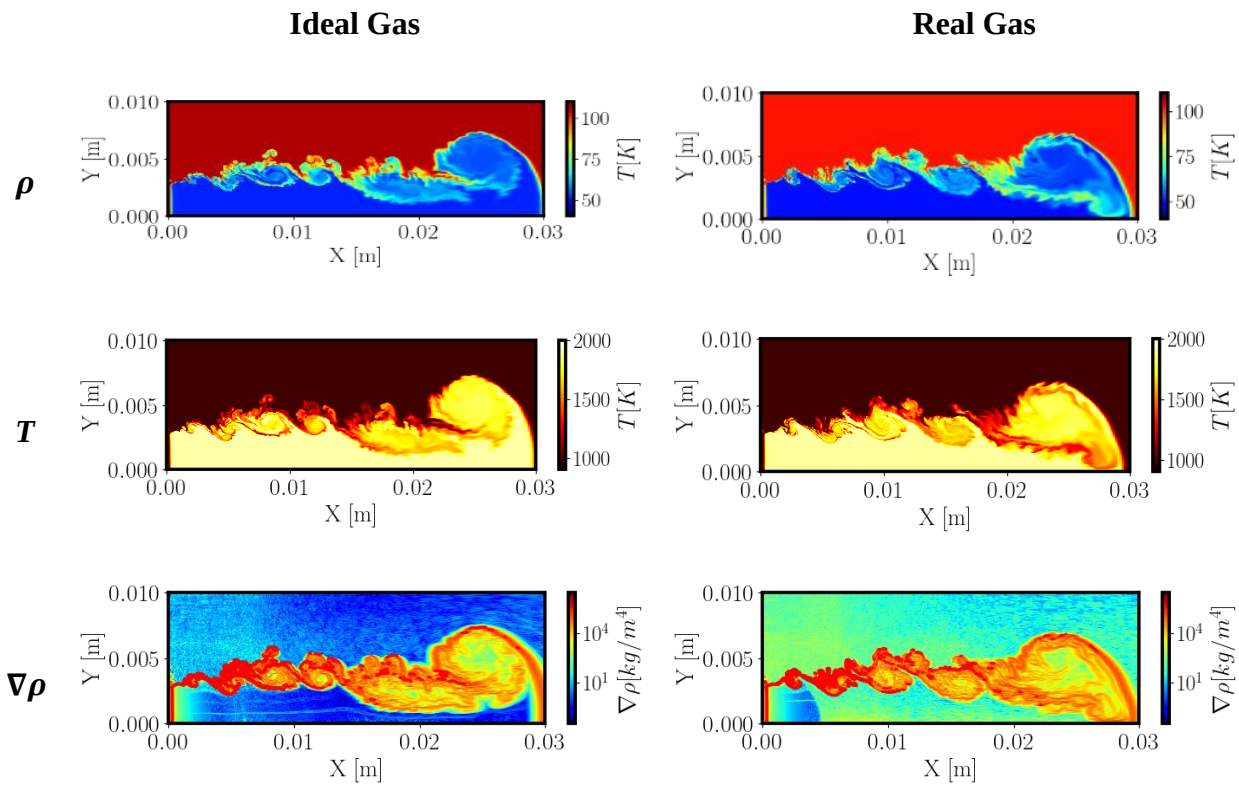

Figure 17. Contour plots for density, temperature, and density gradient for the reacting SWRI case.

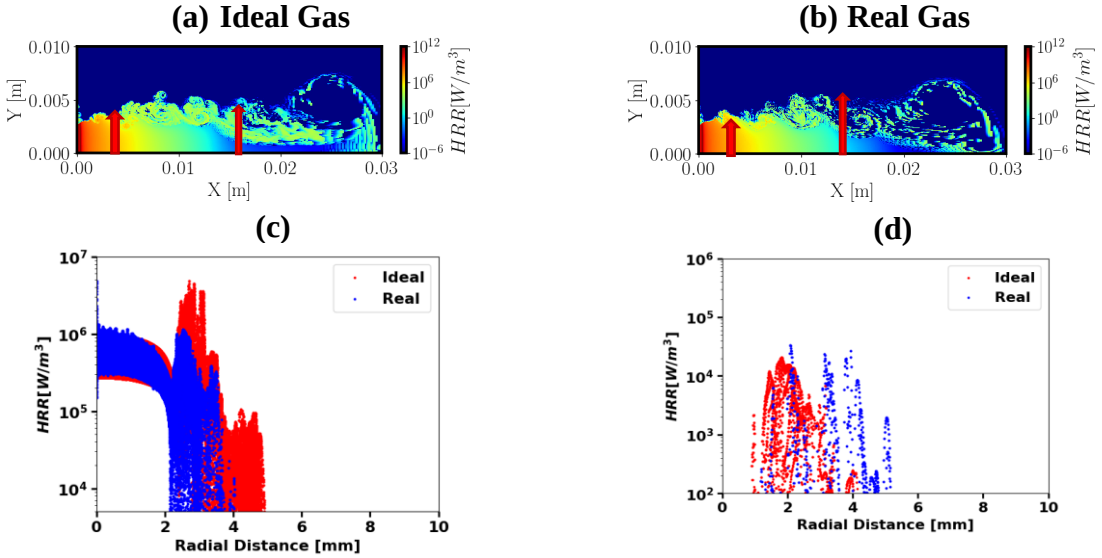

Figure 18. Contour plots for the heat release rate (HRR) for the SWRI case: (a) ideal gas; (b) real gas; radial profiles of HRR at (c) x = 5 mm and (d) x = 20 mm in the axial direction.

The real-gas case shows a wider region with a high-density gradient (spanning to ~3 mm) compared to that of the ideal-gas case (~1.5 mm) confirming the existence of the density gradient barrier predicted by the real-gas EoS which persists further downstream (x = 15 and 20 mm in Figure 19) which results in different mean flame wrinkle wavelengths as shown in Figure 20. The distance between two consecutive peaks in the temperature profile shown in Figure 20a-b is considered as the flame wrinkling wavelength denoted by λ in Figure 20c. A longer wavelength is observed for the real-gas case owing to its higher density gradient barrier since the flame wrinkling occurs when turbulent eddies penetrate the reacting zone.

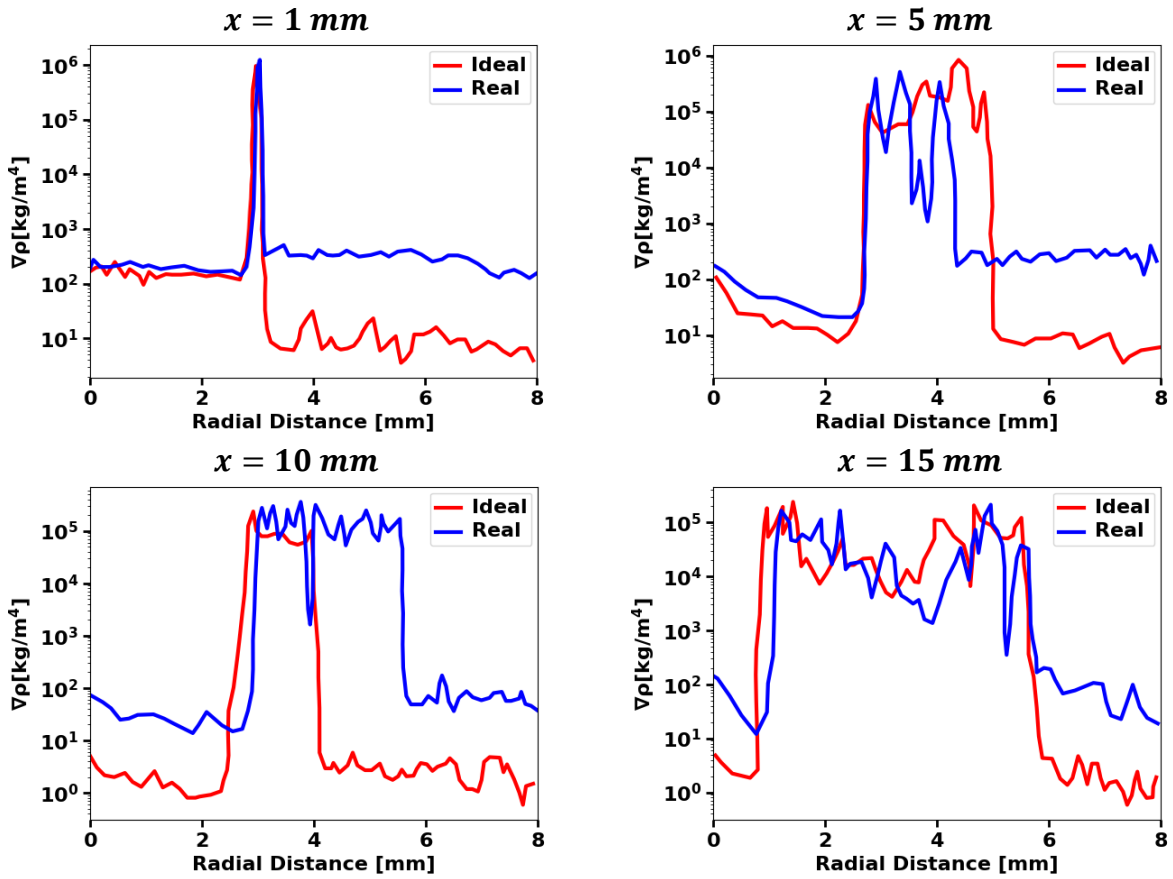

Figure 19. Radial distribution of density gradient at different axial locations for ideal- and real-gas cases.

The scatter plot of vorticity as a function of density gradient for the dataset encompassing the entire computational domain shown in Figure 21 indicates that vorticity is strongly correlated with density gradient. This figure shows that at higher density gradients ($\nabla\rho$ = 1 to 2 kg/m^4) which is correlated with the near-inlet behavior (red box), the ideal-gas case exhibits higher vorticity compared to the real-gas case. This is consistent with Figure 18 that showed more enhanced mixing and a higher HRR is observed for the ideal-gas case near the inlet. As the density gradient decreases downstream of the inlet where the core fuel and oxidizer stream entirely disintegrates corresponding to $\nabla\rho$ = 0 to1 kg/m^4, the difference in vorticity magnitude between the ideal and real-gas diminishes (yellow box) and a peak in vorticity is observed at significantly lower density gradient which is approximately the same for both cases at $\nabla\rho \sim 0.3\times10^6$ kg/m^4 (green box). In general, a lower vorticity magnitude is seen for higher density gradients as mixing/vortex formation is opposed by the density gradient barrier which becomes more significant for the real-gas case.

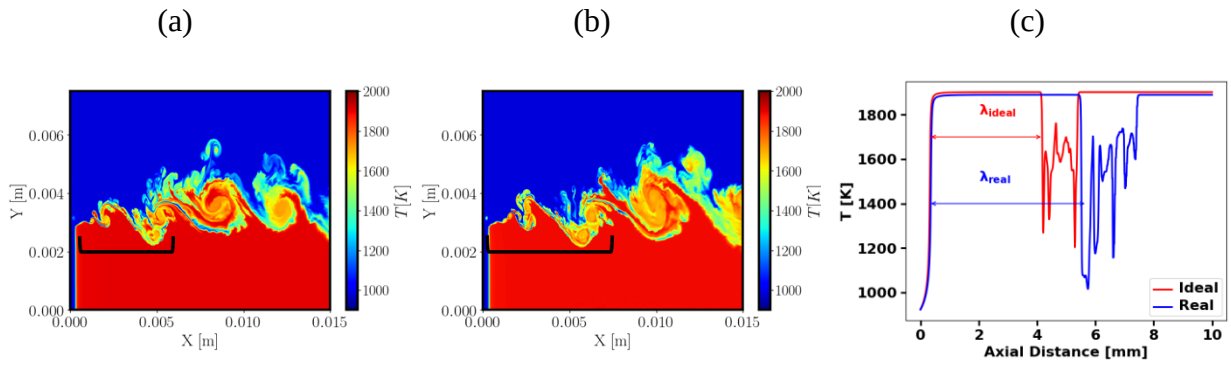

Figure 20. Contour plots of temperature showing the flame wrinkling wavelength: (a) ideal-gas; (b) real-gas case; (c) axial profile of temperature showing the difference between flame wrinkling wavelengths calculated based on the distance between two consecutive peaks in temperature contours.

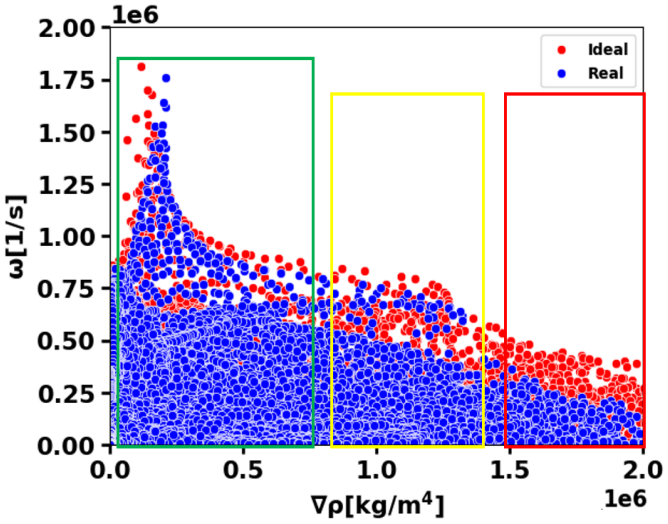

Figure 21. Scatter plots showing the relationship between vorticity magnitude and density gradient calculated for the entire computational domain for ideal- and real-gas cases.

To further probe into the sCO_2 oxy-combustion behavior affected by the choice of EoS, the scalar dissipation rate is defined based on the temperature gradient as $\chi = \alpha \boldsymbol{\nabla T}.\boldsymbol{\nabla T}$. The thermal diffusivity (α) which is predominantly a function of temperature is constant on an isothermal line and therefore can be neglected for simplicity consistent with previous studies. [133] The conditional scalar dissipation rate (CSDR) at an isothermal line $T = T_0$ is defined as the square of the temperature gradient as shown in Eq. 5:

$$\chi_{T=T_0} = \boldsymbol{\nabla T}.\boldsymbol{\nabla T} \tag{5}$$

The Probability Density Function (PDF) of the conditional scalar dissipation rate is shown in Figure 22 and the solid vertical lines denote the mean values for the entire dataset. It has been shown [133] that CSDR is inversely related to the local flame thickness in premixed combustion. Higher dissipation rates are also indicative of a smaller flame edge thickness as the flame edge thickness (δ_L) is defined as:

$$\delta_L = \frac{T_b - T_u}{|\boldsymbol{\nabla T}|_{T=T_0}}, \tag{6}$$

where T_b and T_u are the burnt and unburnt gas temperatures, respectively and the gradient is calculated at an isothermal line of T_0 =1500 K which is the average temperature between burnt and unburnt gases. The flame edge thickness is a key parameter in identifying the premixed combustion regimes and indicates the thickness of the region at which heat release occurs between the burnt and unburnt gases.

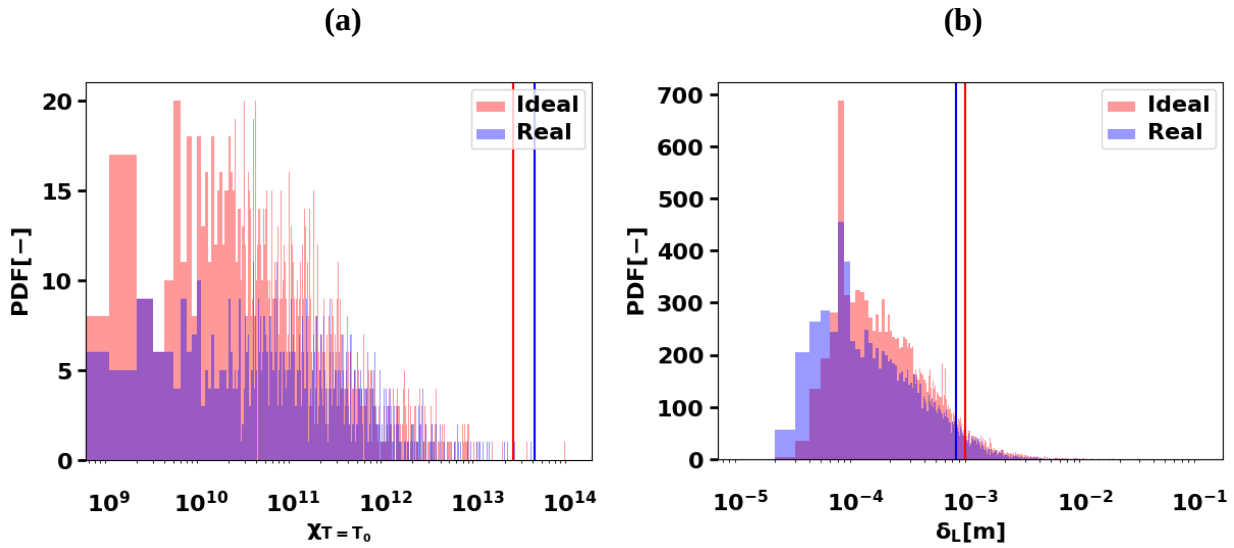

Figure 22. PDF of (a) conditional scalar dissipation rate; (b) flame thickness (vertical solid lines show the average values.)

A smaller flame edge thickness promotes flame wrinkling due to the inability of turbulent eddies to penetrate the flame edge region[91]. This type of combustion regime characterized by *Ka* < 1 (Karlovitz number: the ratio between the chemical timescale to Kolmogorov timescale) occurs when the flame is turbulent but the flame propagation speed is close to the convective speed [91]. Figure 22 indicates higher scalar dissipation rate values and a smaller flame thickness for the real-gas case. The ideal-gas case exhibits a larger flame edge thickness (Figure 22b) which is consistent with the HRR plot in Figure 18 that showed a radially wider region of heat release for the ideal-gas case. The real-gas case, on the other hand, shows a more distributed heat release

along the flame edge which leads to a thicker flame edge. Repeating this analysis at an iso-line temperature of 1400 K showed that the flame edge thickness varied within 1% when the temperature is changed from 1400 to 1500 K which shows that the choice of temperature does not have a strong effect on the calculation of the CSDR and flame edge thickness in this study.

Species Production and Consumption Rates

Figure 23 shows the consumption/production rates for the fuel, i.e., CH_4 $(\rho\dot{\omega})_F$ and carbon dioxide $(\rho\dot{\omega})_{CO_2}$ along the axial direction. Differences are observed for all species with a common trend of lower rates for the real-gas case with peaks further downstream compared to the ideal-gas case. The differences noticed in Figure 23 can be attributed to the differences in density, and specific heat predicted by real- and ideal-gas EoS that can affect the HRR as shown in Figure 24. The differences in density and specific heat lead to a difference in the peak of heat release rate resulting in the discrepancies observed in the consumption and production rates of key species through the one-step combustion model.

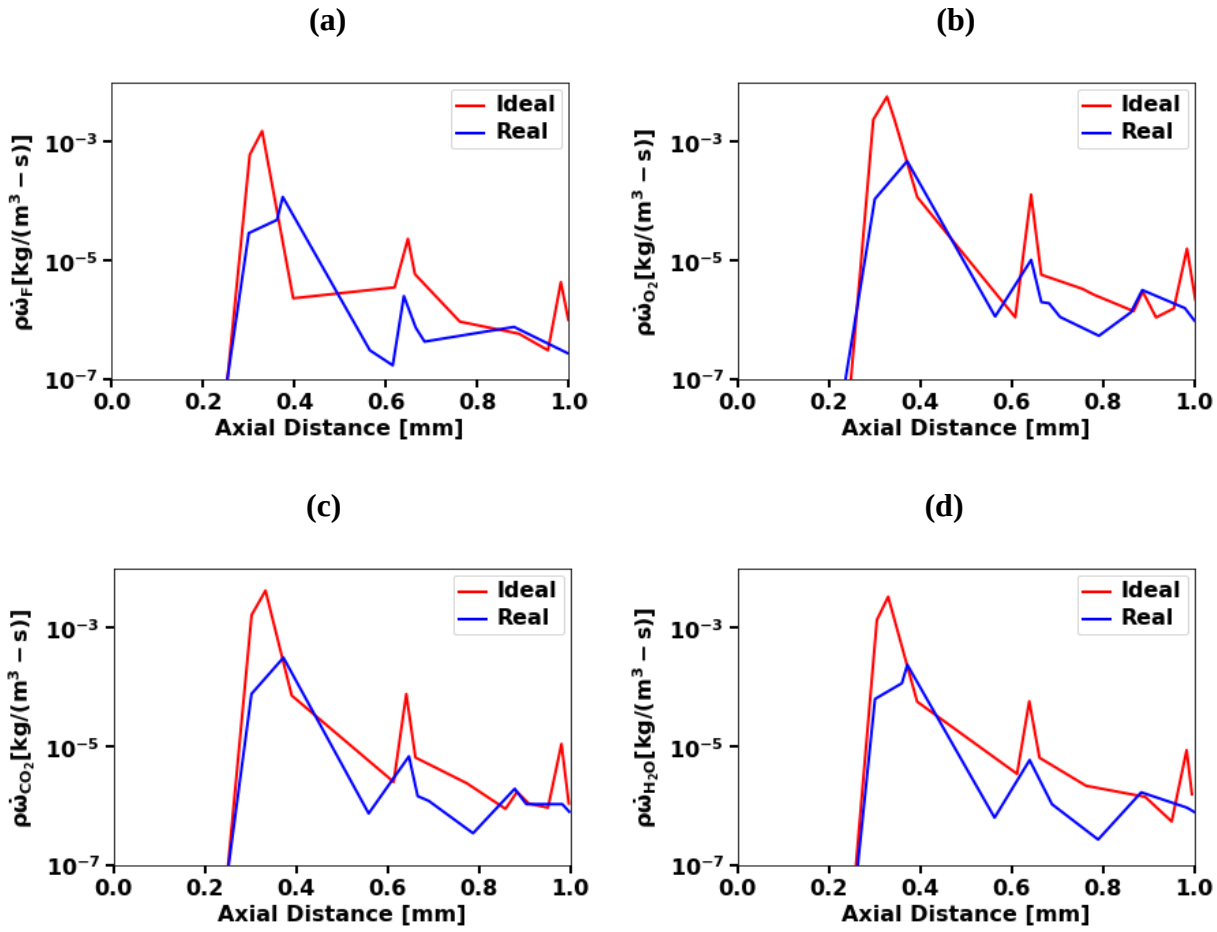

Figure 23. Axial profile of production/consumption rates for ideal- and real-gas cases: (a) consumption rate of methane; (b) consumption rate of oxygen; (c) production rate of carbon dioxide; (d) production rate of water.

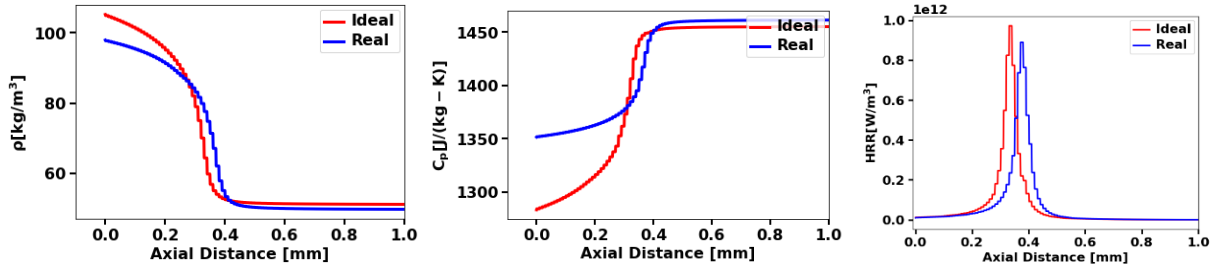

Figure 24. Axial profile of density, specific heat, and HRR for ideal and real-gas cases

In summary, comparing the ideal- and real-gas cases displays key differences mainly in the near-inlet region. For the non-reacting case, the real-gas case exhibits a longer intact flow region

with limited initial mixing compared to the ideal-gas case. This behavior is linked to the higher density gradients predicted by the real-gas EoS which acts as a barrier that tends to shift the complete mixing between fuel and the background CO_2 to further downstream locations. The reacting flow predicted by the real-gas model showed a wider density gradient barrier, a longer wavelength at the flame edge, and a smaller flame edge thickness. The higher flame propagation rate is evidenced by the location of the HRR peak which was further downstream for the real-gas case. Differences are noted between the consumption/production rates of key species between real and ideal cases where the ideal-gas case predicted higher rates due to higher heat release rate caused by its higher specific heat.

% CO_2 Dilution Effect

A qualitative comparison of temperature distribution for 65, 80, and 90% CO_2 dilution is shown in Figure 25 and the radial distribution of temperature for these three cases at different axial locations is depicted in Figure 26. It is shown that there is a significant difference in the maximum flame temperature that varies from 3200 K at 65% to 1700 K at 90% dilution. In addition, the flame propagation length is reduced from 30 mm to 25 mm with an increase in dilution rates as shown in Figure 25. Moreover, the radial expansion of the flame decreases with an increase in CO_2 dilution as can be seen from the qualitative comparison which is consistent with higher flame edge thickness for higher dilution rate that will be discussed in Figure 26.

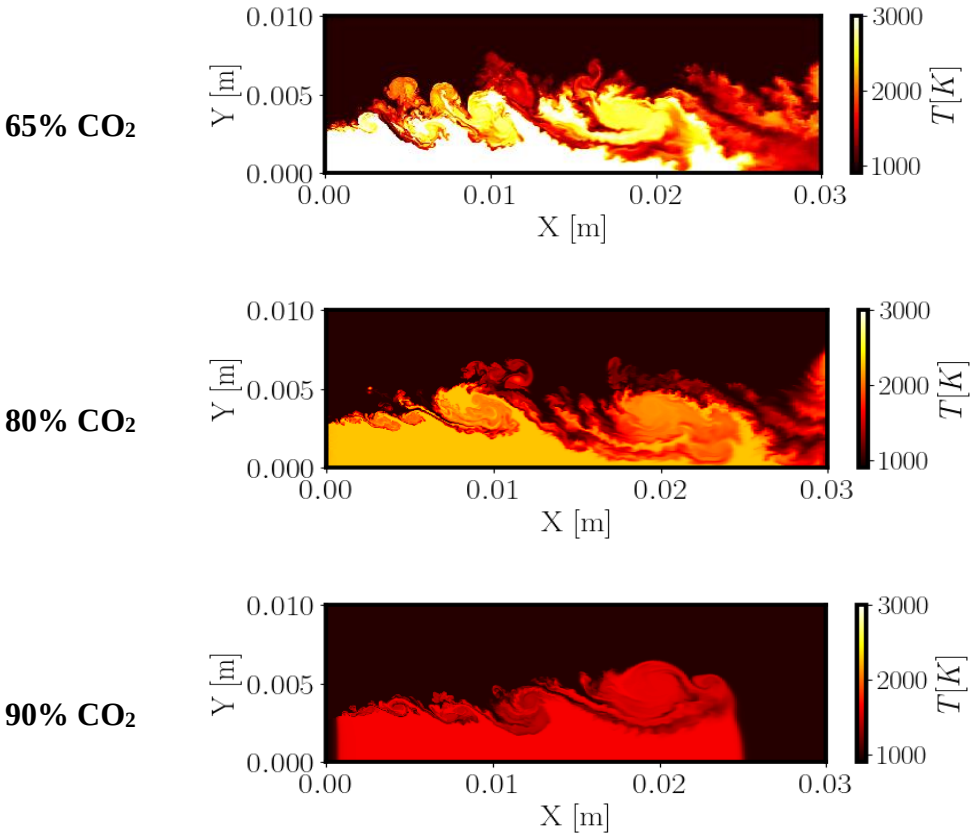

Figure 25. Temperature contours for different CO_2 dilutions for SWRI oxy-combustor configuration.

The axial distribution of density, specific heat, and the maximum HRR as shown in Figure 27 shed light on the discrepancies observed in temperature distribution for different dilutions. The higher dilution case, i.e., 90% exhibits a much higher density in the axial direction due to the higher content of sCO2 in the mixture; however, the specific heat is lower for lower dilution rates (i.e., 65% and 80%). Due to higher specific heat, the 65% case shows a higher HRR and ignites in a region very close to the inlet which leads to a much higher flame temperature as shown in Figure 25 and Figure 26. The peak in HRR is lower and shifted further downstream of the inlet for the 80% and 90% dilution which exhibit a lower specific heat. This behavior is consistent with the 0D simulation that showed a shorter IDT at lower dilution rates. For the highest dilution rate, the peak

in HRR is expanded over a wider axial region which indicates less reactivity in the mixture compared to lower dilution rates. Comparing the radial distribution of the density gradient shown in Figure 28 indicates that the highest percentage dilution displays a lower density gradient in the radial direction at different axial locations and the differences between the cases increase downstream.

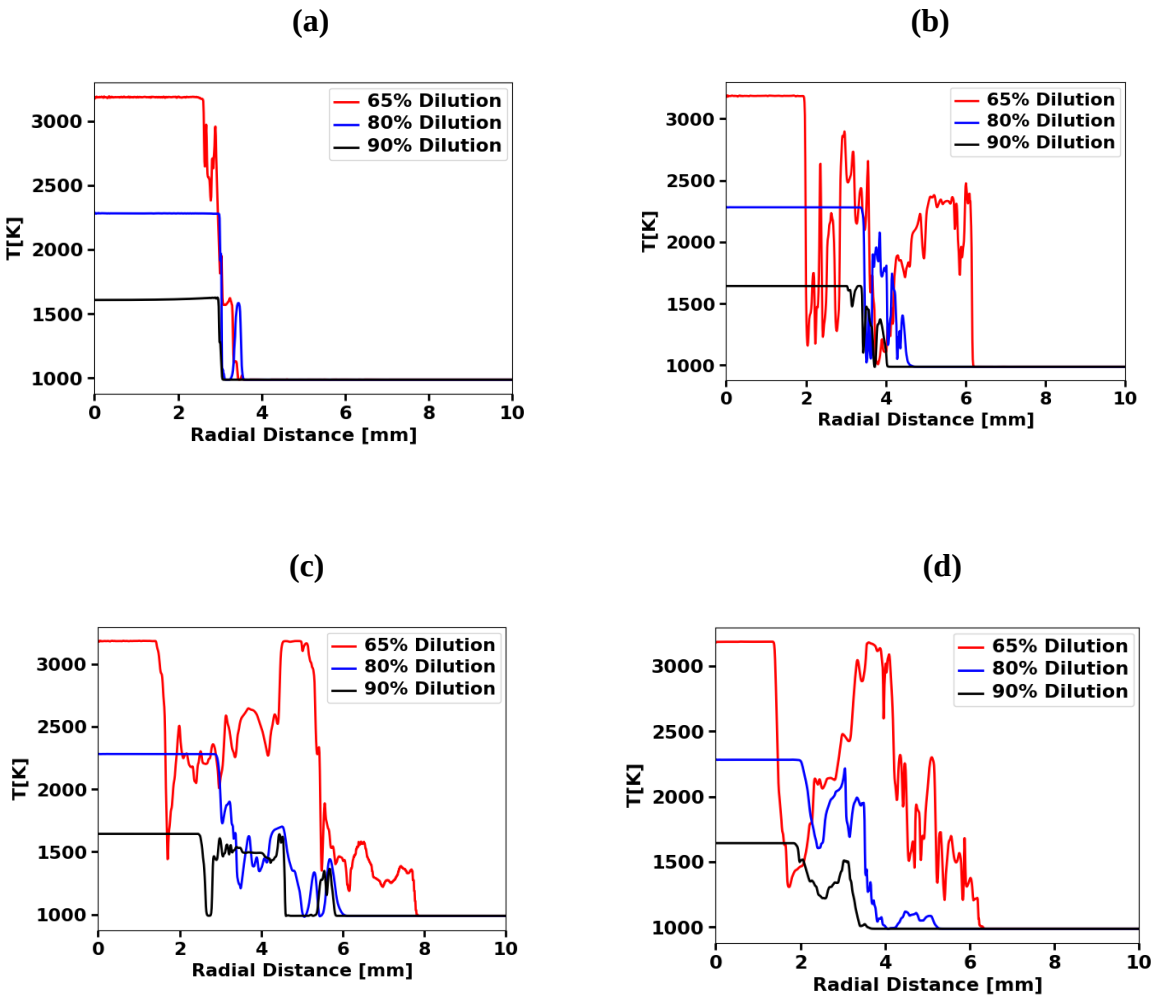

Figure 26. Radial profiles of temperature at different axial locations for different CO_2 dilutions: (a) 1 mm; (b) 5 mm; (c) 10 mm; and (d) 15 mm.

This behavior shows that increasing the dilution rate enhances the mixing with the ambient CO2; however, it ignites further downstream due to its lower specific heat and HRR (see Figure 27) and results in a lower flame temperature as shown in Figure 26.

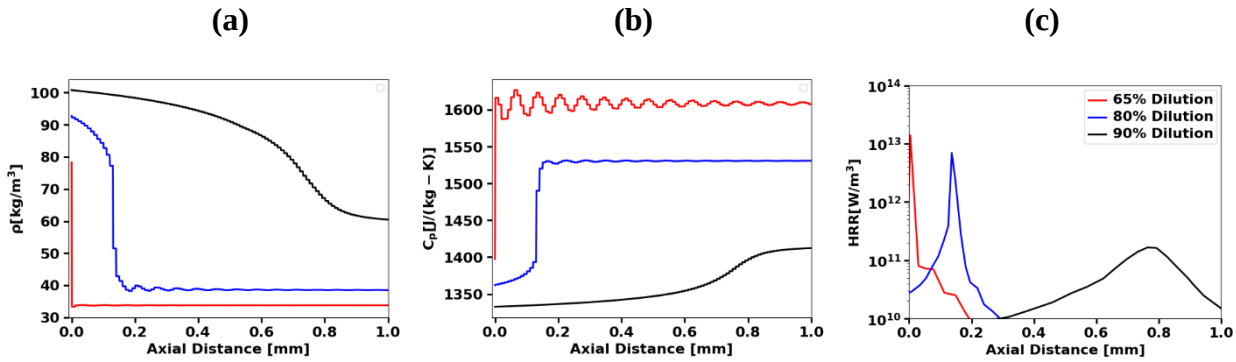

Figure 27. Axial profiles for (a) density, (b) specific heat, and (c) HRR for different % sCO2 dilution.

Figure 29 depicts the axial distribution for production/consumption rates for the fuel, i.e., CH_4, oxidizer, CO_2, and H_2O for different %CO_2 dilution. This figure clearly shows that the ignition occurs further downstream of the inlet (~x = 0.6 mm) for the 90% dilution case which is consistent with the temperature distribution shown in Figure 25 and Figure 26. Interestingly, the production/consumption rate remains the highest for the intermediate CO_2 dilution, i.e., 80% dilution that exhibited an HRR distribution very close to the 65% dilution as shown in Figure 27c. In addition, the ignition occurs very close to the inlet for the 80% dilution. This indicates that there is an optimum CO_2 dilution that leads to the highest HRR at a distance very close to the inlet with minimal fuel/oxidizer consumption and lower adiabatic flame temperature which is highly desirable in designing sCO_2 oxy-combustors.

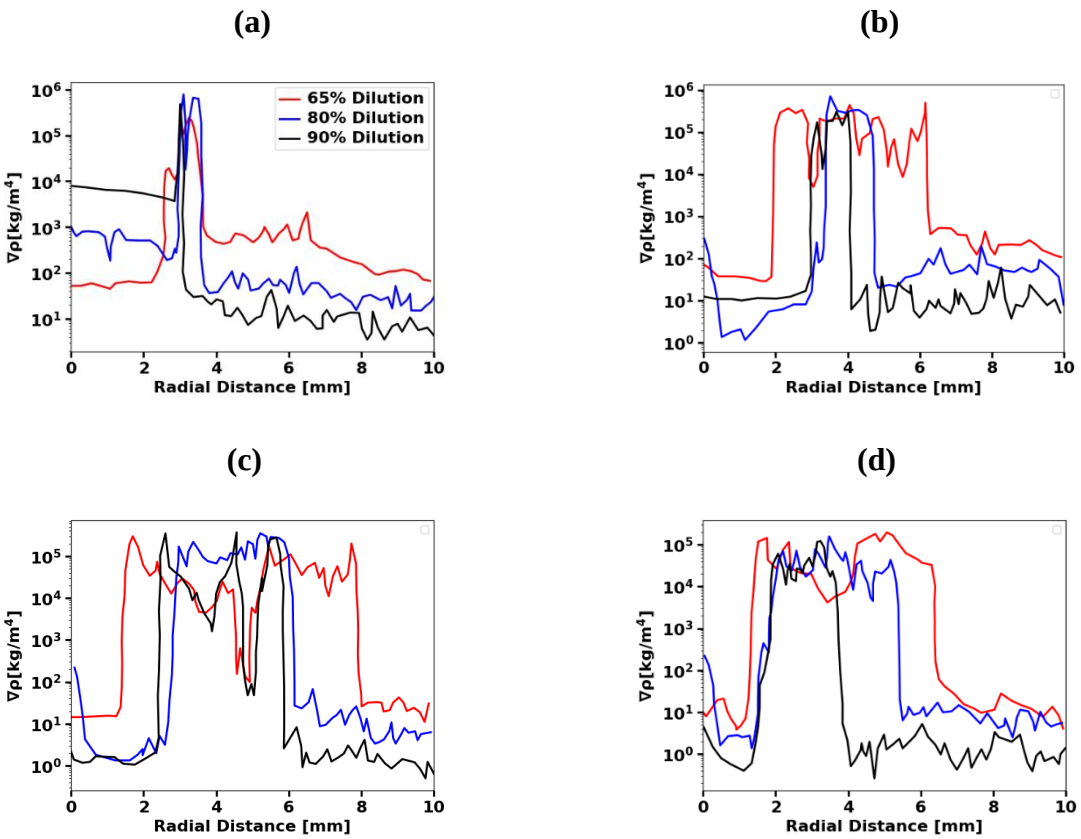

Figure 28. Radial profiles of density gradients at different axial locations: (a) 1 mm; (b) 5 mm; (c) 10 mm, and (d) 15 mm.

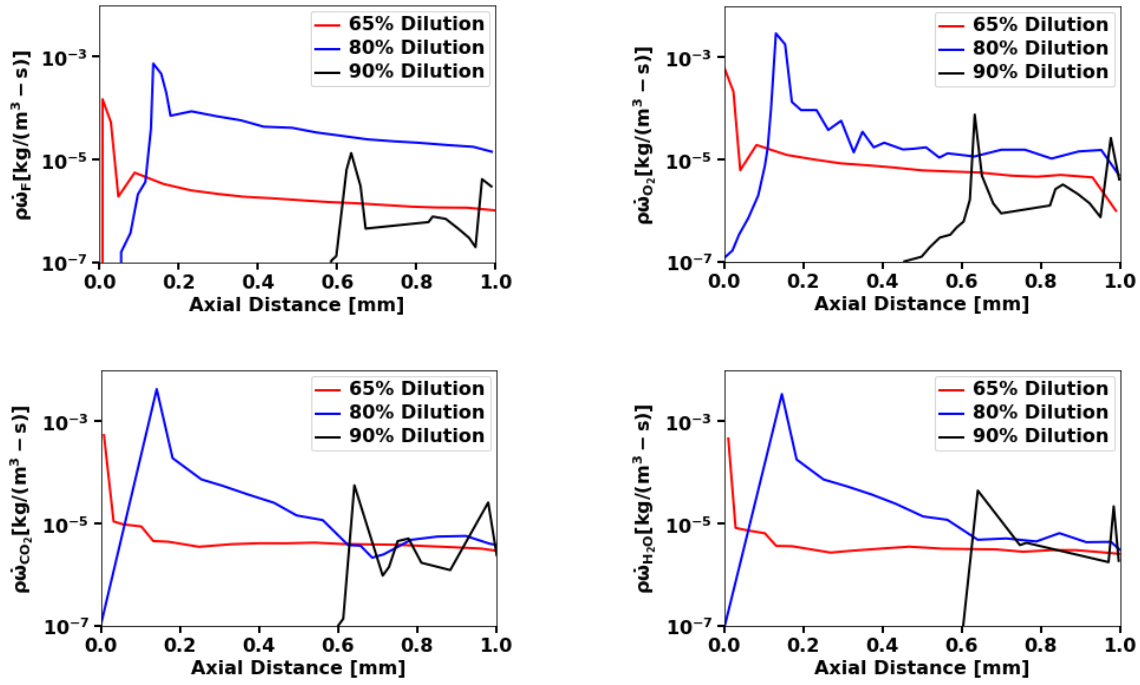

Figure 29. Axial profiles for production/consumption rates of the fuel, i.e., CH_4, oxidizer, CO_2, and H_2O for different %CO_2 dilution.

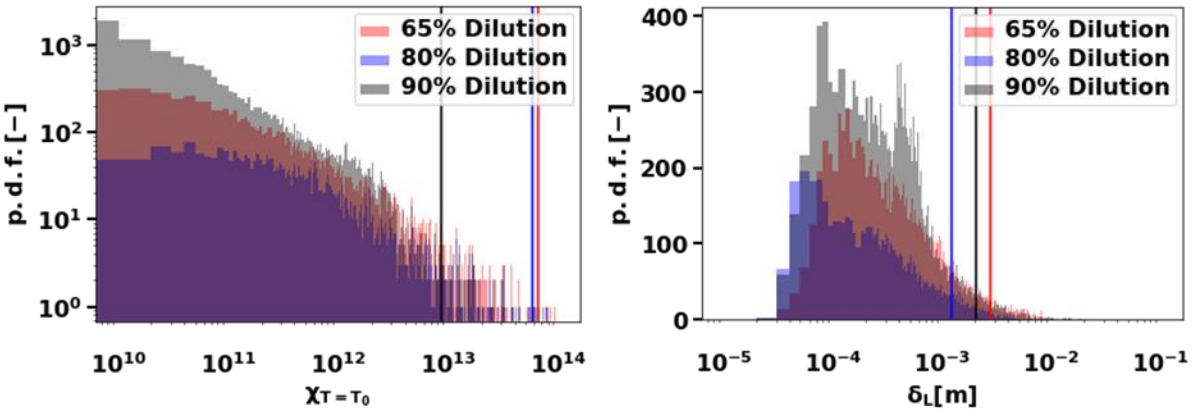

Figure 30. PDF of (a) CSDR; (b) flame edge thickness for different dilution rates. Vertical lines represent the average values.

Figure 30 illustrates the PDF of conditional scalar dissipation rate (CSDR) and the flame edge thickness for different dilution rates following the approach discussed before. The temperature is set to T_0=1500K to be consistent across all the cases. The average values for CSDR

and flame thickness are shown with vertical lines in Figure 30. Figure 30a shows that CSDR decreases with increasing % dilution and the highest dilution case, i.e., 90% displays the lowest CSDR. As shown in Figure 27, this case exhibited the lowest HRR and highest density which indicate less reactivity. Figure 30b shows that the highest value of flame edge thickness is observed for the 65% dilution case. This can be attributed to the competing effects of temperature difference in unburnt and burnt gases and the length over which the temperature gradient is calculated. Even though the gradient of temperature is larger for the 65% case as shown in Figure 25 and Figure 26, the difference in the unburnt and burnt gases is also higher for this case which leads to a larger flame edge thickness for the lowest dilution.

The premixed turbulent combustion regime diagrams defined based on the velocity and length scale ratios have been proposed by Borghi and Peters [91] and Abdel-Gayed and Bradley. [134] Figure 31 shows the combustion regime for different % dilutions on the Borghi-Peters diagram. The non-dimensional numbers are Damkohler number (*Da*) which indicates the liquid residence time to reaction time, and Karlovitz number (*Ka*) which compares the chemical timescale to the Kolmogorov timescale. The horizontal and vertical axes represent the length scales and velocity scales, respectively. The flame speed s_L is calculated using the following equation [135]:

$$\frac{dr_f}{dt} = v_u + s_L, \tag{7}$$

where dr_f is the displacement of the flame front in time and v_u of the unburnt mixture velocity. The turbulent velocity fluctuations, i.e., u' and the integral length scales, i.e., L_x are calculated as detailed in Appendix. In this study, the flame front tracking method is based on the location of the maximum temperature gradient across the entire computational domain. The flame edge thickness is calculated following Eq. 6 based on the definition of CSDR given in Eq. 5. Figure 31 shows that

the sCO_2 oxy-combustion behavior for SWRI configuration resides within the corrugated flame regime for all tested CO_2 dilution. The 90% dilution case is closer to the thickened corrugated flame regime. These results are in contrast to the RANS analysis performed by Strakey et al. [15] where the combustion regime is shown to be prone to the thickened corrugated flame regime. This discrepancy is mainly linked to differences in dilution, oxidizer concentration, and simplifying assumptions involved in the RANS approach.

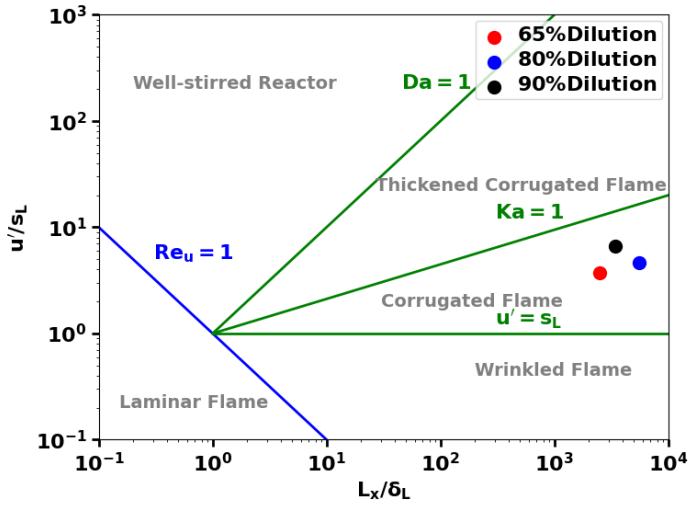

Figure 31. Regime identification for different dilutions on the Borghi-Peters diagram [91].

In summary, the percentage dilution comparison shows an increase in flame temperature and HRR as the % CO_2 dilution is decreased. The flame edge thickness is higher for the lower dilution. An optimum dilution exists which leads to the least consumption rate of fuel/oxidizer that is desired to lower the turbine inlet temperature. The results presented in this section provide the design metrics to achieve favorable operating conditions for sCO_2 oxy-combustors. Moreover, the DNS datasets generated will serve as validation for computationally less expensive and lower fidelity approaches such as RANS and LES which is discussed in Chapter 4.

2.4 Summary and Conclusions

The Allam cycle is a direct-fired supercritical CO_2 (sCO_2) power cycle that operates as a recuperated, high-pressure, and closed-loop Brayton cycle and employs sCO_2 as the working fluid and uses sCO_2 recirculation in the combustion chamber as a diluent. SCO_2 dilution used for moderating the combustor exit temperature, as well as high pressure, and high preheat temperature in sCO_2 oxy-combustors pose a unique combustion behavior compared to the conventional air-breathing propulsion systems. This study provides an in-depth understanding of the mixing and combustion behavior in sCO_2 oxy-methane combustion with high sCO_2 dilution which does not currently exist due to experimental challenges at such high pressure and temperatures. A reacting flow DNS framework using a single-step chemistry model for methane combustion and implementing PR EoS for considering the real-gas effects at supercritical conditions is developed and validated for non-reacting supercritical mixing for single and multiple species. The DNS solver is then used for modeling the sCO_2 oxy-methane combustor by adopting the SWRI combustor for the first time. The effects of using an ideal gas EoS under non-reacting and reacting conditions are thoroughly studied. Finally, three test cases with different CO_2 dilutions are studied using 0D reacting simulations followed by DNS for the same SWRI combustor using the real-gas model. The following conclusions are made from the results:

1. The validation cases show that the solver can accurately capture the flow physics by comparing the mixing metrics with the experimental results for supercritical mixing of single and multiple species.
2. Comparing the ideal- and real-gas model for SWRI combustor configurations shows key differences mainly in the near-inlet region. For the non-reacting case, the real-gas case exhibits a longer intact incoming flow region with limited initial mixing compared to the

ideal-gas case. This behavior is linked to the higher density gradients predicted by the real-gas EoS which acts as a barrier that tends to shift the complete mixing to downstream locations.

3. The reacting flow predicted by the real gas EoS showed a wider density gradient barrier, a longer wavelength at the flame edge, and a smaller flame edge thickness. The higher flame propagation rate is also evidenced by the axial location of the maximum HRR which is further downstream for the real-gas case. The flame edge wavelength is higher for the real-gas case and the flame morphology for the ideal-gas case is more radially expanded which indicates a higher flame edge thickness.
4. Differences are observed between the consumption/production rates of key species between real- and ideal-gas cases where the ideal-gas case predicted higher rates due to higher heat release rate caused by differences in density and specific heat.
5. The 0D simulations indicated a strong dependence of ignition delay time on $\%CO_2$ dilution and weak dependence on equivalence ratio. Based on CO mole fraction and ignition delay time calculations, the optimum combustion condition occurs with an equivalence ratio (0.5-0.65) and intermediate $\%CO_2$ dilution (75-90%).
6. The comparison of different $\%CO_2$ dilutions indicates clear differences in the structure and behavior of the flame. For higher CO_2 dilutions, lower flame edge thickness is seen with lower HRR and lower peak temperature. The density gradient barrier has a wider span for the lower dilutions and therefore the heat release is spreads more across the flame edge.
7. An optimal $\%CO_2$ dilution exists between 65%-80% which exhibits the highest HRR, lower production/consumption rates, and lower maximum adiabatic flame temperature desired to lower the turbine inlet temperature leading to a favorable combustor design.

8. The results predict that the sCO_2 oxy-combustion process using the SWRI configuration is closer to the corrugated flame regime across all dilution cases tested in this study.

3. DETAILED CHEMISTRY REDUCTION *

3.1 Introduction

3.1.1 Chemical Kinetics for sCO_2 Oxy-Combustion

A major aspect where the sCO_2 oxy-combustion technology development is clearly lagging is the development of chemical mechanisms that can capture high-pressure kinetics with significant CO_2 dilution. Figure 32 clearly shows the knowledge gap in the field of oxy-methane combustion with CO_2 dilution while well-developed mechanisms mainly cover up to 20 bar and CO_2 is mainly a product and not a diluent.

Experimental Studies

A series of relevant experimental data for high-pressure and high-dilution methane combustion are presented in studies from Petersen et al. [136-138]. However, the mixture dilution was considered using nitrogen and Argon rather than sCO_2.

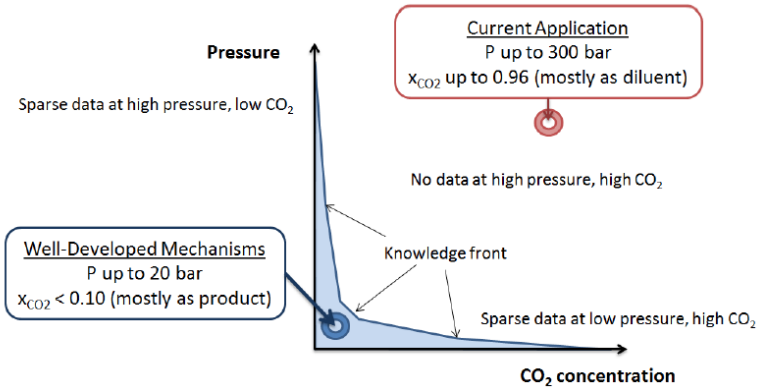

Figure 32: Mechanism space: Pressure vs. CO_2 dilution. Experimental data available for low pressure and low dilution while data becomes sparse as pressure and CO_2 concentration increases. Reprinted from [139].

* Part of this chapter is reprinted with permission from "Adaptive global pathway selection using artificial neural networks: A-priori study" by Mishra., R., Nelson, A., Jarrahbashi, D., 2022. Combustion and Flame, Volume 244, Copyright 2022 by Elsevier.

Pryor et al. [29] conducted shock tube experiments at high pressure and high CO_2 dilution to indicate the ignition delay time for oxy-methane combustion. The temperature and pressure ranges were 1300-2000 K and 6-31 atm, respectively with CO_2 dilution up to 85%. Well-known mechanisms such as Aramco 1.3 and GRI3.0 were able to predict the ignition delay times as reported in the experiments. The key finding is that CO_2 decelerates the overall reaction rate, thereby increasing the ignition delay time. Karimi et al. [140] reported methane auto-ignition delay time for diluted CO_2 environment for 100-200 bar pressure and 1139-1433 K temperature. The Aramco 2.0 mechanism was found to perform the best in predicting autoignition compared to other tested mechanisms. Laich et al. [141] performed a series of shock tube experiments for methane/O_2 mixtures in high-dilution environments of N_2 and CO_2 at 16 bar and the data was compared to Aramco 2.0 and GRI3.0. The results showed that these two mechanisms were not able to capture the ignition delay time especially at lower temperatures. The impurities are reported to significantly change the ignition delay time in sCO_2 methane-oxy-combustion process. Impurities due to NOx are shown to reduce CO formation while the presence of H_2S increases the CO formation. [142] Therefore, the GRI3.0 chemistry mechanism was adjusted to account for C1-C3, H_2S oxidation [143], and NOx formation [144] to capture the ignition delay time accurately. The final mechanism which showed better prediction of ignition delay time compared to Aramco 3.0 includes 106 species and 916 reactions and is applicable to both low pressure (30 bar) and high pressure ranges (275-300 bar). Park et al. [145] conducted a series of experiments relevant to Allam cycle conditions (310-450 K and 0-150 bar) and showed that the density and speed of sound were following the National Institute of Standards and Technology Reference Properties (NIST REFPROP) [146] data even for these extreme regimes. Karimi et al. [147] conducted high-pressure shock tube experiments to measure the ignition delay times of syngas (H_2/CO=95:5) at 95.5% CO_2

dilution at 10 MPa and 20 MPa for a temperature range of 1161-1365 K. These conditions were repeated for a second set of experiments using Argon as the diluent instead of CO_2. Globally, CO_2 does not significantly alter the ignition delay time compared to Argon. This study shows that the following reaction ($H+O_2(+M) \rightarrow HO_2(+M)$) is critical in controlling the ignition for both the cases. This study also showed that Aramco 2.0, FFCM-1, HP-Mech, and USC Mech II better captured the experimental ignition delay times. Due to challenges in high-pressure shock tube experiments with high dilution rates, Gonzalez et al. [148] performed atomistic molecular dynamics simulations of syngas oxy-combustion in sCO_2 and identified that CO2 → CO + O reaction is dominant at high temperatures and high CO_2 dilution and increasing CO_2 dilution and decreasing O_2 concentration delays the ignition.

Computational Studies

Coogan et al. [139] showed that USC-2 mechanism can better capture high-pressure, high-dilution oxy-methane combustion. By showing that ignition delay time changes within 3% for the pressure range up to 85 bar, the authors justified the use of ideal-gas assumption in their analysis. Liu et al. [149] developed a 13-species mechanism from USC Mech II for 150 atm to 300 atm and 900 K to 1800 K and equivalence ratio of 0.7 to 1.3. This new mechanism was tested for predicting autoignition delay and was found to be within 12% error to that of USC Mech II. The above studies operate based on extrapolating the experimental data available for mechanisms at low pressure and low CO_2 dilution to account for combustion at elevated pressures and high CO_2 dilutions. Manikantachari et al. [111] reduced the Aramco 2.0 mechanism which has shown high capabilities in predicting high-pressure, high-CO_2 dilution methane combustion. A 23 species gas-phase mechanism is derived by employing Path Flux Analysis (PFA) analysis and validated for ignition delay time in a range of pressure and equivalence ratios. It was reported that the choice of EoS

does not have a significant impact on the ignition delay time of supercritical $CH_4/O_2/CO_2$ mixtures; however, it influences the supercritical $H_2/O_2/CO_2$ mixtures.

Summary: The above studies introduced several reduced chemistry mechanisms relevant to sCO_2 oxy-combustion conditions. The reduced chemical mechanisms developed for sCO_2 oxy-combustion entail uncertainty as the reduction is made from a detailed mechanism which was not developed for high dilution conditions. Even though the reduced mechanisms introduced in this section can perform well in 0D simulations, their ability to capture 3D turbulent reacting flows has not been examined. The existence of several species and reactions in chemistry mechanisms and the use of real-gas EoS needed for accurate prediction of mixing and combustion at supercritical conditions poses computational costs as major challenges. To overcome these challenges, we adopt different chemistry mechanisms techniques using Machine Learning (ML) techniques to enable high-fidelity yet computationally feasible simulation of oxy-combustion at supercritical conditions using detailed chemistry mechanisms. A brief survey of chemistry reduction techniques is discussed below.

3.1.2 Chemistry Mechanism Reduction

The first group of chemistry mechanisms techniques are considered as sensitivity and rate analyses approach require removing certain species and reactions while examining the effect of their removal on the model predictions to determine the species needed to be included in the reduced mechanism. Although effective, these methods do not provide the timescales of different reaction groups or the Quasi Steady-State (QSS) and partial equilibrium groups automatically. [150] The second group of mechanism reduction techniques includes reaction Jacobian analysis, e.g. Computational Singular Perturbation (CSP) [151] and Intrinsic Low-Dimensional Manifolds (ILDM) [152] methods. In the CSP method, the eigenvalues and eigenvectors of independent

reaction modes are calculated to rank the fast and slow reactions. In the ILDM approach, the Jacobian matrix of the system's governing equations is initially used to obtain a set of eigenvectors. These eigenvectors are then used to find subsets of the composition space to define the slow reactions, which are assumed to dominate the system's behavior after a short time, while the fast reactions have already reached equilibrium. This assumption allows for a significant reduction in the number of reactions that need to be modeled explicitly, making the ILDM approach computationally efficient for simulations of complex combustion systems.

Parameterization techniques are based on the integration of the stiff ODEs *a priori* and storing them in tables. Flamelet tables are classified under this broad category of reduction. In-Situ Adaptive Tabulation (ISAT) [153] is one of the examples of this type of chemistry reduction. ISAT simplifies chemistry integration by tabulating the integration results. The data is used to produce a function called reaction mapping, which relates initial and final compositions for a fixed timestep. During subsequent iterations, if the initial composition resembles a state from the tabulated data, the algorithm uses the mapping function by employing a linear approximation to find the next composition instead of direct integration. Finally, reaction path relation methods are used to analyze chemical reactions and determine the degree of interaction among species. Such methods are based on the concept that chemical reactions follow reaction paths consisting of sequences of elementary steps involving the formation and dissociation of chemical species. These methods can be used to identify the key species and reactions that contribute to the overall reaction process, and to construct reduced reaction mechanisms that capture the essential features of the complex reaction system. Directed Relation Graph (DRG), [154] Directed Relation Graph with Error Propagation (DRGEP), [155] Path Flux Analysis (PFA), [156] and Global Pathway Selection (GPS) [157] are among the reaction path relations methods.

3.1.3 Machine Learning-Based Chemistry Mechanism Reduction

Application of ML tools is gaining traction in aiding expensive computational simulations through reducing the number of species and reactions in chemistry mechanisms. [158] Zhang et. al. [159] trained artificial neural networks (ANNs) to predict the gradient of thermo-chemical scalars at each timestep used for time stepping and the neural network was used to advance the simulation in time instead of classical numerical integration methods. In 0D simulations of dimethyl ether combustion, such ANN integrator achieved similar accuracies with computational times 20 times faster compared with a previously developed numerical integration method, i.e., hybrid multi-timescale (HMTS). [159] A similar method developed by Ranade et. al. [160] used a two-layer ANN combined with the hybrid chemistry (i.e., HyChem) approach which decoupled the pyrolysis and oxidation stages of combustion. Using experimental data from the shock tube, ANNs were used to produce temporal profiles of various species. In that approach, the chemical states were mapped to the derivatives of the temporal profiles using a deeper ANN used to integrate the simulation. [160] Sample-Partitioning Adaptive Reduced Chemistry (SPARC) is a method developed by D'Alessio et. al. [161] that employs unsupervised learning to map local reduced mechanisms to a multi-dimensional flame simulation. It first takes a dataset containing the composition space and temperature and pre-partitions the dataset into a set of kinetically homogenous clusters using an unsupervised learning algorithm. For each cluster, a reduced mechanism is generated using the DRGEP approach. This method was effectively used to model both steady-state and transient 2D laminar flames. [161]

The promise shown by these ML studies motivates the application of ML in reducing the chemistry mechanisms for modeling sCO_2 oxy-combustion. A novel approach that will be pursued in this study is the use "on-the-fly" or dynamic chemistry mechanism reduction using ML tools

where for different range of pressure and temperature, the reactions, and species relevant to those conditions are called during the simulations. This approach significantly reduces the costs of 3D reacting flow simulations. The wide range of conditions relevant for sCO_2 oxy-combustion can only be reliably and more efficiently modeled using an on-the-fly ML-based reduction tool that will be introduced in this study. The key knowledge gaps and unresolved questions are summarized in the next section.

3.2 Computational Methods

Cantera [162] is a powerful open-source software suite for chemical kinetics, thermodynamics, and transport processes. It provides a range of solvers for simulating chemical systems, including a 0D solver. The 0D solver in Cantera is designed to simulate the behavior of a well-stirred, perfectly mixed reactor, also known as a batch reactor. In a 0D simulation, the reactor is assumed to have uniform temperature, pressure, and composition throughout. The solver models the time evolution of the chemical system by solving a system of ordinary differential equations (ODEs) that describe the rates of change of the species concentrations. Here is a general description of the 0D solver workflow in Cantera:

1. Defining the chemical system: This step involves specifying the thermodynamic and kinetic properties of the species involved in the reaction. Cantera provides a flexible interface to define the chemical system using various input formats, such as Chemkin, CTI, and YAML.
2. Setting initial conditions: Specify the initial values of the species concentrations, temperature, and pressure in the reactor.

3. Defining the reactor: Create a reactor object and set its parameters, e.g., volume, temperature, and pressure. Cantera supports different reactor types including ideal gas reactors, constant-pressure reactors, and constant-volume reactors.
4. Specifying the simulation time span: Set the start and end times for the simulation.
5. Integrating the ODE system: Use the 0D solver in Cantera to integrate the system of ODEs over the specified time span. The solver uses numerical integration techniques, such as implicit or explicit methods to approximate the solution.
6. Access the results: After the integration is complete, one can access the time-dependent evolution of species concentrations, temperature, and other relevant quantities. Cantera provides functions to extract and analyze the simulation results.

Mass and energy conservation equations play a crucial role in describing the behavior of chemical systems, including well-stirred reactors. These equations ensure that the total mass and energy within the system remain constant, accounting for reactant consumption, product formation, and any associated heat effects. Here are the details on mass and energy conservation equations:

Mass Conservation Equation:

The mass conservation equation, also known as the continuity equation, states that the rate of change of species mass within a control volume is equal to the net rate of mass transfer into or out of the volume, considering reaction rates and flow rates:

$$\frac{\partial(\rho_i V)}{\partial t} = \sum_i (-v_i' A)$$

where:

ρ_i is the density of species i, V is the volume of the reactor, $\frac{\partial(\rho_i V)}{\partial t}$ is the rate of change of species mass within the volume with respect to time, v_i' is the stoichiometric coefficient of species i in the reaction (negative for reactants, positive for products), A is the surface area through which mass transfer occurs.

The right-hand side of the equation represents the sum of the mass fluxes due to reaction and mass transfer across the control volume boundaries.

Energy Conservation Equation:

The energy conservation equation accounts for the energy balance within the well-stirred reactor, considering heat effects, temperature changes, and the enthalpy of the species involved:

$$\rho C_v V \frac{\partial T}{\partial t} = \sum_i (-v_i' \Delta H_i A) + \sum_i \left(-v_i' \Delta H_{i,f} A\right) + Q$$

where:

C_v is the heat capacity at constant volume of the reactor mixture, T is the temperature, $\frac{\partial T}{\partial t}$ is the rate of change of temperature with respect to time, ΔH_i is the enthalpy change associated with the reaction of species i, $\Delta H_{i,f}$ is the standard enthalpy of formation of species i, Q represents any heat exchange with the surroundings (e.g., heat transfer through the reactor walls).

The first term on the right-hand side represents the heat of reaction, accounting for the heat released or absorbed due to the stoichiometry of the reaction. The second term accounts for the heat of formation of the species. The third term, Q, represents any external heat added or removed from the reactor.

Species Conservation Equation:

$$\frac{\partial(\rho_i Y_i V)}{\partial t} = \sum_k (-v_{ik}' A \rho_{ik})$$

where:

Y_i is the mass fraction of species i, ρ_{ik} is the partial density of species i due to the kth reaction (v'_{ik} is the stoichiometric coefficient for species i in the kth reaction)

The left-hand side of the equation represents the rate of change of the total mass of species i within the reactor volume with respect to time. The right-hand side consists of the sum of the contributions from each reaction, where $v'_{ik}$is the stoichiometric coefficient for species i in the kth reaction, A is the surface area through which mass transfer occurs, and ρ_{ik} is the partial density of species i due to the kth reaction.

In the case of a well-stirred reactor, the species conservation equations are typically coupled with the mass and energy conservation equations, as well as the reaction rate expressions, to form a system of ordinary differential equations (ODEs). The numerical integration of this system of equations allows for the simulation of species concentrations, temperature, and other relevant quantities as a function of time.

By considering mass, energy, and species conservation equations together, a comprehensive representation of the behavior of a well-stirred reactor can be achieved, accounting for the evolution of species concentrations, temperature, and the associated chemical reactions. By simultaneously solving the mass conservation equation and the energy conservation equation, along with the appropriate reaction rate expressions, it is possible to simulate the time-dependent behavior of a well-stirred reactor, including the evolution of species concentrations and temperature.

3.2.1 Chemistry Reduction Tool (Python – Cantera, TensorFlow)

In this section, we first describe the algorithm of the classical Global Pathway Selection (GPS) method [157] and then introduce a new adaptive GPS approach and compare the predictions

of this model with detailed mechanism and classical GPS method. We will then introduce our supervised learning-aided GPS method and validate it for three cases of 0D methane and ethanol auto-ignition using the detailed mechanism and classical and adaptive GPS methods. A sensitivity study is conducted on the SL-GPS method for various architectures and training sizes to see their effect on ignition delay time error. Finally, the SL-GPS method's prediction of ignition delay time will be tested on 120 cases of methane combustion and 120 cases of ethanol combustion and compared to the predictions of the classic GPS and DRGEP methods.

3.2.2 Classical Global Pathway Selection Method

To determine the species and reactions that are most active in the combustion of a particular fuel, data from a "training simulation" using a detailed mechanism is required. The primary information from this simulation that GPS uses as a criterion to determine which species are important is the rate of atoms of a given element passing through that species, a quantity called element flux. The element flux for element *e* from species *i* to species *j* is given by

$$A_{e,i\to j} = \sum_r a_{e,r,i\to j,} \tag{1}$$

where $a_{e,r,i\to j}$ is the element flux from *i* to *j* for reaction *r*. For each reaction, the flux is given by

$$a_{e,r,i\to j} = \max\left(0, C_{e,r,i\to j}\dot{R}_r\right), \tag{2}$$

where $\dot{R}_r$ is the net reaction rate for *r* and $C_{e,r,i\to j}$ is the element flux associated with a single stoichiometric occurrence of the r^{th} reaction represented by

$$C_{e,r,i\to j} = \begin{cases} n_{e,r,j}\frac{n_{e,r,i}}{n_{e,r}}, & \nu_{e,r,j}\nu_{e,r,i} < 0 \\ 0, & \text{otherwise} \end{cases}, \tag{3}$$

where $n_{e,r,i} = \nu_{r,i}N_{e,i}$ is the net number of atoms of element *e* transferred to species *i* in a single occurrence of reaction *r*. $\nu_{r,i}$ is the stoichiometric coefficient (negative if reactant, positive if product) for species *i* in *r*, and $N_{e,i}$ is the number of *e* atoms in a molecule of species *i*. $n_{e,r}$ is the

total number of *e* atoms involved in reaction *r* [157]. By defining this directed edge between any two species, a measure for the total element flux passing through a single species to and from any other species is defined as

$$\alpha_{e,i} = \frac{\max(\sum_k A_{e,i\to k}, \sum_k A_{e,k\to i})}{\max_{\mathrm{M}}(\sum_k A_{e,M\to k}, \sum_k A_{e,k\to M})}. \quad (4)$$

Eqn. 4 is used as a metric for a species' contribution to the overall combustion, and by comparing $\alpha_{e,i}$ to a threshold parameter, i.e., α_{crit}, several critical "hub species" are chosen. For each of these hub species, multiple pathways from source to target passing through the hub species are found and the fastest *K* pathways are considered for each hub (*K* = 1 for all applications in this study). The speeds of the various pathways are ranked using a graph based on the reciprocal of the element flux following the Yen et al. approach [163]. Each of these pathways consists of a series of chemical steps as one species is converted to the next, and each of these steps includes contributions from multiple reactions. $\beta_{e,i\to j}$ is another metric defined for the normalized element flux of the top n_r contributing reactions for a given conversion step from species *i* to *j* as follows

$$\frac{\sum_{r=1}^{n_r} a_{e,r,i\to j}}{A_{e,i\to j}} = \beta_{e,i\to j,r=1\sim n_r} \quad (5)$$

$\beta_{e,i\to j}$ is compared to another threshold parameter β_{crit} (0.5 for all applications in this study) for each value of n_r. For the lowest value of n_r for which β exceeds this threshold, the top n_r reactions (and all associated species) are included in the mechanism. This process is repeated for each step of each pathway for each hub species and all selected species. This entire process is repeated for each relevant element and combination of source and target at several chemical timesteps of the training simulation from which the flux graph is derived. Finally, the reduced mechanism is produced from the union of all included species and all reactions in the detailed mechanism that

include only those selected species [157]. The algorithm for the classic GPS method is schematically illustrated in Figure 33.

3.2.3 Adaptive GPS Method

As the mechanism derived from GPS is based on the detailed results from a training simulation, the element flux and chosen species and reactions are dependent upon the conditions, such as temperature, pressure, and initial mole fractions under which that simulation was performed. For instance, species that are typically produced at 1 atm and 1300 K may not be actively involved in reactions at 40 atm and 1800 K. As GPS takes the union of all species and reactions throughout the training simulations, species relevant to certain conditions (e.g., low pressure and temperature) will be carried throughout the simulation even when those conditions no longer hold, leading to needless computational costs and complexity. The novel approach proposed by the authors is to perform the reduction process adaptively, where at certain time intervals during the main simulation a new detailed simulation is adopted for the next time interval. The initial conditions of this training simulation are based on the current conditions of the main simulation, and GPS is trained using this shorter time interval simulation. The new reduced mechanism produced by GPS will be used for simulating the next several chemical timesteps of the main simulation until the change in conditions warrants adopting a new mechanism.

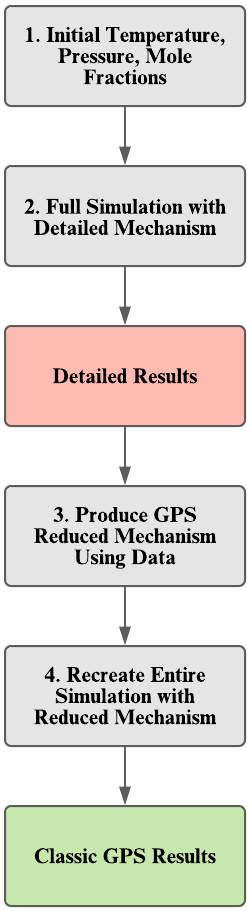

Figure 33. Algorithm for classic GPS adopted from Gao et al. [157]. Reprinted from [164].

The code for the novel concept of adaptively updating the mechanism is developed by the authors using Python 3, with the Cantera 2 module for the chemistry simulation and adopting the GPS repository developed by Gao et al. [157]. By following the adaptive reduction scheme at the start of a certain time interval, a new background simulation using the detailed mechanism is produced under the same initial conditions as the main simulation. The training simulation proceeds until the start of the next time interval. A new GPS-reduced mechanism is trained using the element flux generated by this training simulation and this reduced mechanism is used to simulate that interval in the main simulation. The use of a new training simulation at each time interval ensures that the element fluxes used by GPS to construct the reduced mechanism represent the chemistry associated with the main simulation during that specific time. Once the next time

interval is reached, a new training simulation is performed, a new reduced mechanism is generated, and the main simulation proceeds with that updated reduced mechanism. During conditions where rapid changes occur in species states, the adaptive GPS reduced mechanism must be updated in response to these changes more rapidly. Therefore, the lengths of the time intervals at which the mechanisms are updated (hereafter referred to as the "GPS interval") are reduced when the simulation reaches a period of exceptionally high reactivity, e.g., during autoignition. The heat release rate (HRR), the rate at which energy is generated by the combustion, correlates with chemical reactivity, and consistently peaks during ignition. Thus, HRR is used as an indicator for further refining the GPS intervals. Once the HRR rises above a set threshold, the GPS interval is reduced to a fraction of its original value until HRR falls below the threshold again. The initial GPS interval, reduced interval, and HHR threshold are input by the user at the start of the main simulation. By following this approach, the mechanism adapts itself to the sudden changes in the reaction space. The computational time required for the training simulation and the GPS algorithm would outweigh any gains from simpler mechanisms and limits its applications in 2D and 3D reacting flow simulations. However, the strategy of producing a series of smaller reduced mechanisms rather than a single, large mechanism is necessary for the supervised learning algorithm which addresses these computational concerns, as will be discussed in Section 3.2.5. The adaptive GPS algorithm is represented schematically in Figure 34**.**

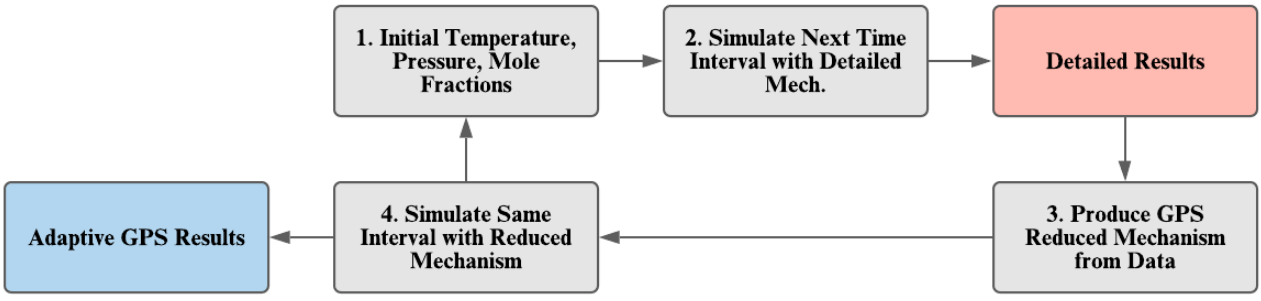

Figure 34. Schematic of the developed algorithm for the adaptive GPS method.

3.2.4 Comparing Adaptive GPS Method with Classical GPS Method and Detailed Mechanism

To demonstrate the benefits of the adaptive GPS algorithm, a simulation of 0D methane autoignition is performed using Cantera at an initial temperature of 1505 K, 1.05 atm pressure, and an equivalence ratio of 1.05. Temperature, HRR, and relevant mole fractions are plotted against time in Figure 35. Each plot shows three sets of results: the first is precited using the GRI 3.0 detailed mechanism [165]; the second is obtained by developing a single GPS mechanism using the GRI 3.0 results as the training simulation, and the third uses the adaptive reduction scheme described in 2.2. Each plot in Figure 35 shows the change in the corresponding state variable during the time just before and after ignition which occurs at around 1.2 ms. Comparing the mole fraction of CH_4, CO_2, CO, OH, O, H, H_2O, CH_3, and CH_2O, as well as temperatures and HRR in Figure 35 shows that the adaptive GPS predictions follow the results of the detailed mechanism far more closely than the classic GPS. This implies that our developed adaptive GPS approach can replicate the predictions of the detailed chemistry more accurately.

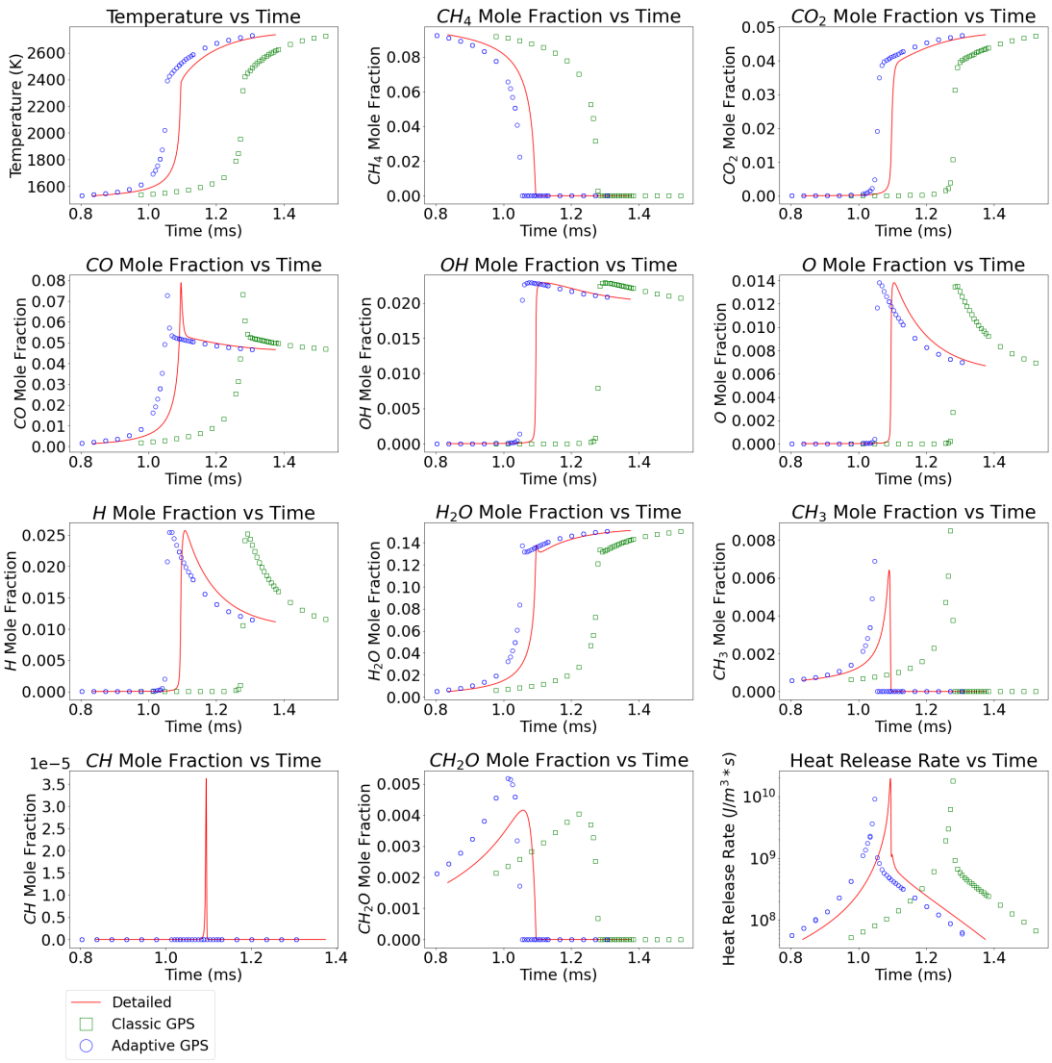

Figure 35. Temperature, mole fraction of various species, and HRR using the detailed mechanism (red), classic GPS (green square symbols), and adaptive GPS methods (blue circle symbols). The initial reactor temperature is 1505 K, pressure is 1.05 atm, and the equivalence ratio is 1.05. Classic GPS skeletal results not available for CH mole fraction as CH was not included in the reduced mechanism.

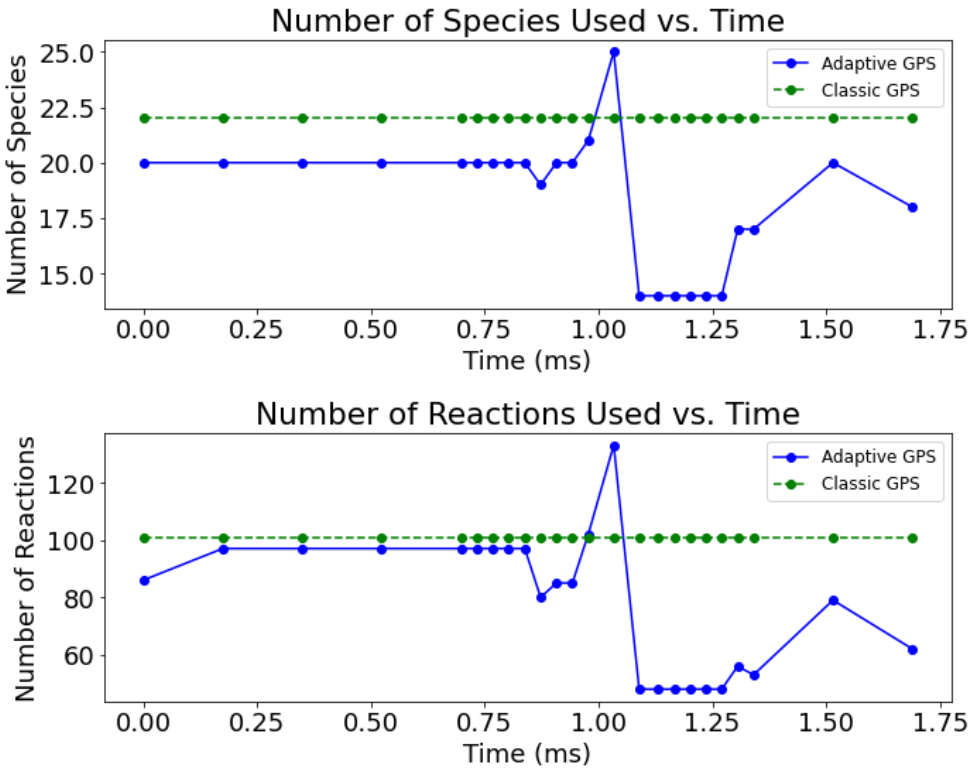

Figure 36. Number of species (top) and reactions (bottom) for T = 1505 K, equivalence ratio = 1.05, and pressure = 1.05 atm obtained using adaptive GPS (blue) and classic GPS (green).

Shown in Figure 36 are the number of species and reactions used in the adaptive GPS, which vary during the simulations, compared to the total number of species used in the classic GPS approach, which remains constant throughout the simulation. Figure 36 shows that the adaptive GPS approach invokes consistently lower numbers of species and reactions compared to the classic GPS mechanism, except for a short duration after ignition at about 1.2 ms. Therefore, in addition to more accurate prediction of mole fractions of various species, temperature, and HHR (as was shown Figure 35), the adaptive GPS method delivers a reduced mechanism with substantially lower numbers of reactions and species throughout the simulations. Such reduced mechanisms are essential for conducting 3D turbulent reacting flow simulations as will be discussed later.

3.2.5 Supervised Learning-Aided GPS Method (SL-GPS)

Although the adaptive GPS method is more accurate compared to the classic GPS method, the additional computational costs of running GPS multiple times as discussed in the previous section needs to be reduced before using this approach in practical 3D simulations. To address this problem, we propose integrating the adaptive GPS method with supervised machine learning (SL) techniques to produce an adaptive reduction scheme that is computationally feasible.

Figure 37 shows a flowchart representing the proposed algorithm that includes a training stage followed by a simulation stage. Training involves a set of 0D autoignition simulations conducted across a space of initial conditions with a selected detailed chemistry mechanism for methane (GRI 3.0 with 53 species and 325 reactions [165]) and ethanol (PCRL-Mech1 with 67 species and 1016 reactions [166]). For training the GPS method based on the results from methane combustion in the GRI 3.0 mechanism, we considered 7 initial temperatures varying between 1300 K to 1900 K, 3 equivalence ratios varying between 0.6 to 1.4, and 7 pressures varying from 1 atm to 100 atm, for a total of 245 cases. For ethanol combustion using the PCRL-Mech1 mechanism, we varied the temperature for 5 values from 1000 to 1400, 3 equivalence ratios from 0.6 to 1.4, and 5 pressures from 1 to 100 atm for total of 75 simulations. These were simulated using Cantera, where each simulation was ended at steady state, as signified by the heat release rate dropping below a specified threshold. After each simulation, the element flux data was taken at the GPS intervals and used to produce the reduced mechanisms using the adaptive GPS algorithm. For each base mechanism, the α_{crit} parameter described in **Eq. 4** was set at a constant value: 0.001 for GRI and 0.1 for PCRL. Similar to the adaptive GPS, these time intervals were reduced during or close to ignition using an HRR threshold. For each simulation, the initial GPS interval was defined as the length of the detailed simulation divided by a constant (10 for GRI 3.0 and 7 for PCRL). The

ignition GPS interval was defined as a third of the normal interval, and an HRR threshold was defined as the maximum HRR of the detailed simulation divided by a constant (700 for GRI and 100 for PCRL).

This approach ensures that a sufficient number of mechanisms are created for each simulation despite the wide variability in ignition delay time across the range of tested initial conditions. Larger GPS intervals and HRR thresholds were used for the PCRL mechanism to reduce the necessary computational time to gather the mechanism data, which was larger compared to GRI due to the PCRL's relative complexity. Each mechanism produced at each GPS interval of each simulation yields a list of species that GPS selected as important. The list of important species is collected with the corresponding temperature, pressure, and mole fraction conditions under which they were selected.

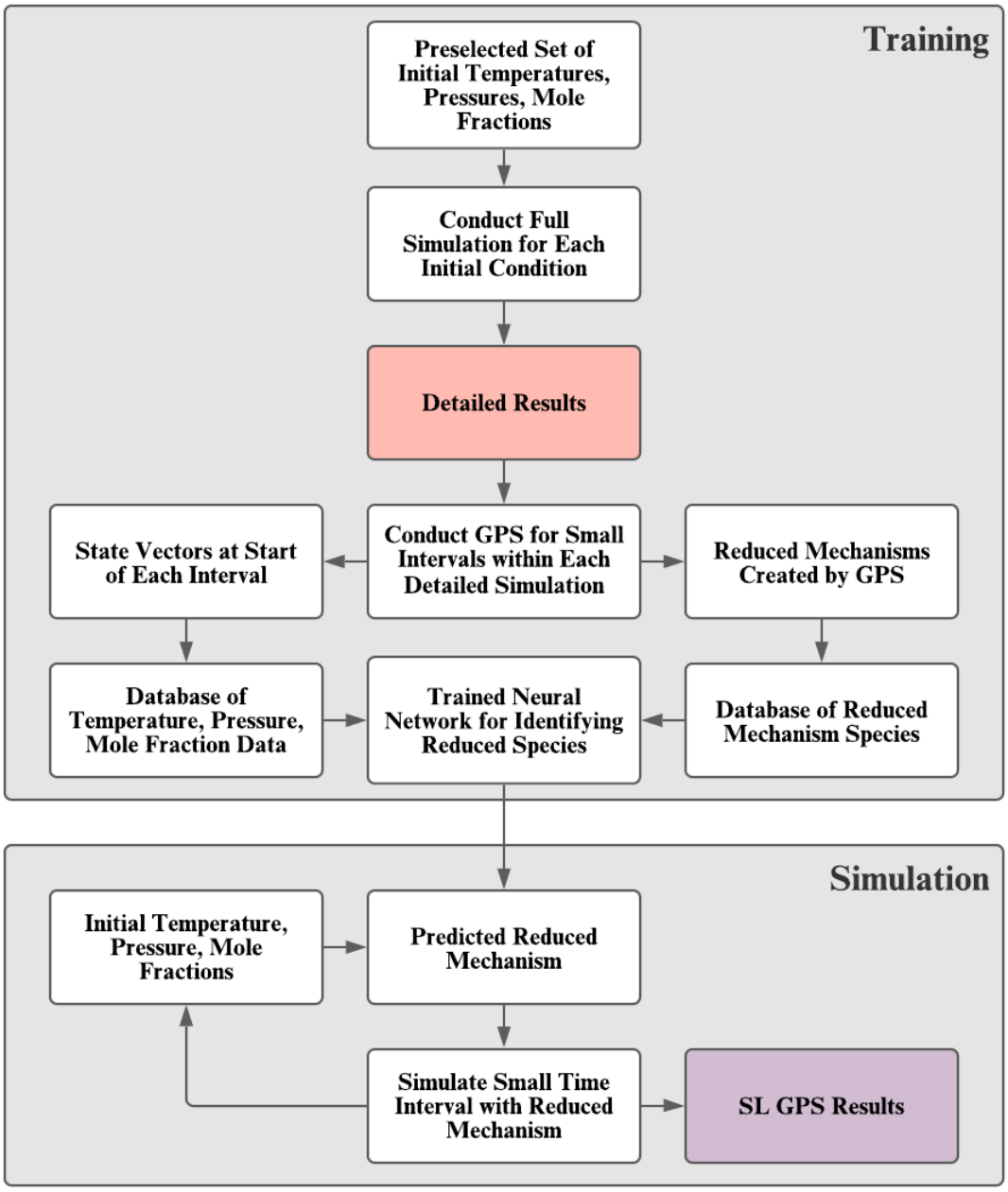

Figure 37. Supervised learning algorithm for adaptive GPS method constructed of a training stage followed by the simulation stage.

These mechanisms are converted to binary lists, where 1 indicates that a species is present and 0 indicates otherwise. The frequency of each species' inclusion is determined, and those

species which are included more than 99% of the time are marked to be always included, and those which are included less than 1% of the time will be excluded. The remaining species and their normalized temperature, pressure, and mole fraction data are included in the binary data set to train an artificial neural network (ANN) as illustrated in Figure 38.

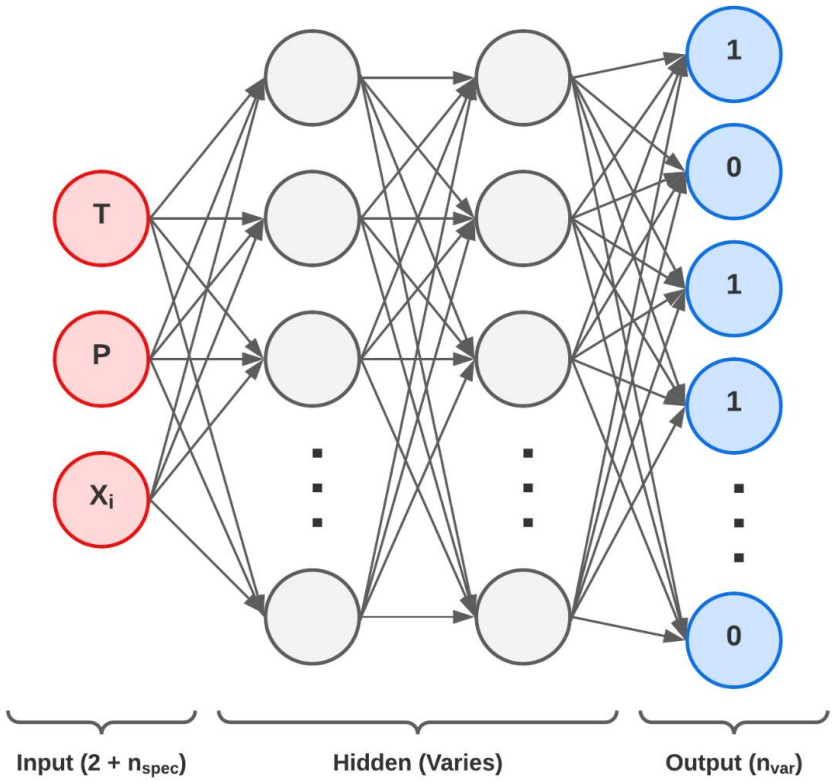

Figure 38. Neural network architecture for species selection in the GRI 3.0 showing the number of neurons in each layer. n_{spec} refers to the number of species chosen for training, and n_{var} refers the number of species which have not been marked as always or never included.

Two hidden layers are used, and the number of neurons in each layer is tailored to each base mechanism to ensure proper training. For GRI 3.0, the first layer has 256 neurons, and the second layer includes 128 neurons. Data training for this case is run through the model for 150

epochs where an epoch is one full run-through of the training data. For the PCRL mechanism, the first layer has 512 neurons, the second has 256, and the training data is run through the model for 500 epochs. Both use mini batching with batch sizes of 32 and use the Adam optimizer [167]. After training, the developed ANN is used as a function that takes temperature, pressure, and mole fraction data as input and outputs binary data that encodes a list of species to include in the reduced mechanism. Using the mole fraction data from the entire list of species in the detailed mechanism as input would introduce needless complexity and training time to the neural network. Therefore, for each base mechanism, only the mole fraction of the set of important species is used as input. For GRI 3.0, CH_4, H_2O, OH, H, CO, O_2, CO_2, O, CH_3, CH were selected and for the PCRL, C_2H_5OH, H_2O, OH, H, CO, O_2, CO_2, O, and CH_3 are chosen as important species. The network's output is a number between 0 and 1 that decides whether a species is included (> 0.5) or excluded (≤ 0.5). The network's loss function used in this study is binary cross entropy (BCE), which is standard for binary classification problems [168]. The network's loss function is a measure of the ANN's inaccuracy that is minimized as the model is trained.

The rationale for the choice of ANN architecture is illustrated in Figure 39**,** Figure 40**,** Figure 41 and Figure 42. In Figure 39 and Figure 40 , bar charts are shown for the binary cross entropy (BCE) of the model's output (as compared to the actual GPS binary species lists) on a test dataset calculated based on a 20-80% test/train split of the GPS data for various numbers and arrangements of hidden neurons. These cases include double and single hidden layer cases, where for simplicity the number of neurons in the second layer is selected as half the number in the first layer. Each case was trained until the loss function failed to decrease for five consecutive epochs or until a maximum of 600 epochs was reached. We adopted a two-layer model as they exhibited a slight decrease in error compared to the single-layer models for all first-layer neuron counts (see

Figure 39). Two-layer models allow greater adaptability and more flexibility in modeling complex nonlinear relationships that can be beneficial in chemistry reduction. In Figure 39, the 256/128 model that implies 256 neurons in layer one and 128 neurons in layer two showed a significant decrease in error compared to 128/64 and 64/32 cases. However, doubling the number of neurons as in the 512/256 case actually increased the BCE. The same trend was detected for the 512/256 model using the PCRL mechanism in Figure 40. Therefore, the optimum architecture is 256/128 for the GRI mechanism and 512/256 for PCRL. The learning curves for the binary accuracy and BCE versus the number of epochs over which the model is trained are shown for the GRI 3.0 and PCRL in Figure 41 and Figure 42, respectively. The binary accuracy is defined as the percentage of the species that the ANN's predictions correctly identify as included or excluded. The learning curves of both metrics are relatively flattened by 150 epochs for GRI or 500 epochs for PCRL. To avoid overtraining and reducing the computational time, the number of epochs of training is truncated to 150 and 500 for GRI and PCRL, respectively.

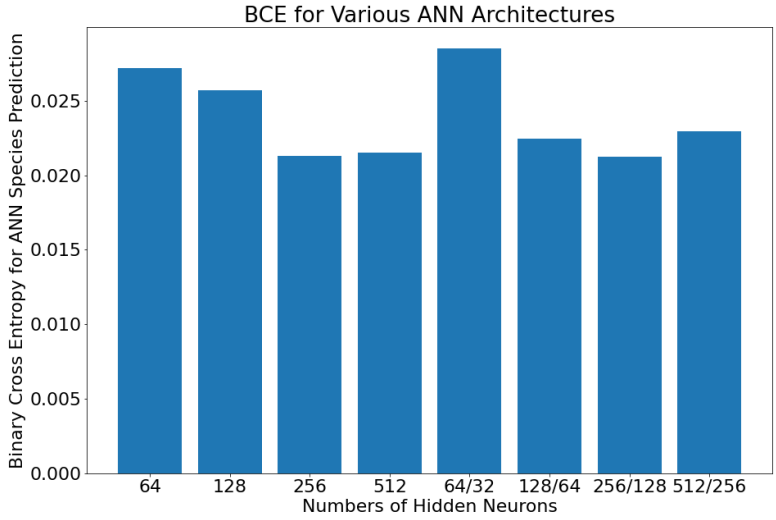

Figure 39. Binary cross entropy (BCE) for predictions of GPS-trained ANN. N_1/N_2 label indicates the number of neurons in the first and second hidden layer, respectively. Training performed using GRI 3.0.

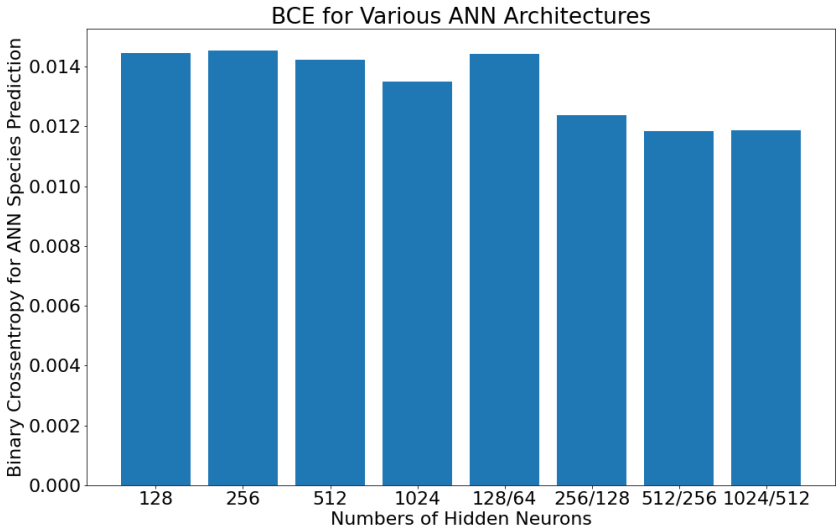

Figure 40. BCE for predictions of GPS-trained ANN. N_1/N_2 label indicates the number of neurons in the first and second hidden layer, respectively. Training performed using PCRL.

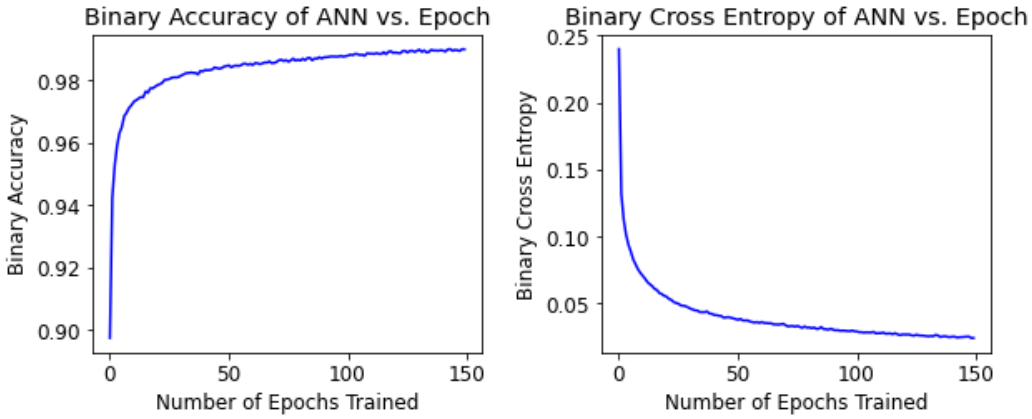

Figure 41. Learning curves for binary accuracy and binary cross entropy for GPS-trained ANN. Training performed using GRI 3.0 with $\alpha_{crit} = 0.001$.

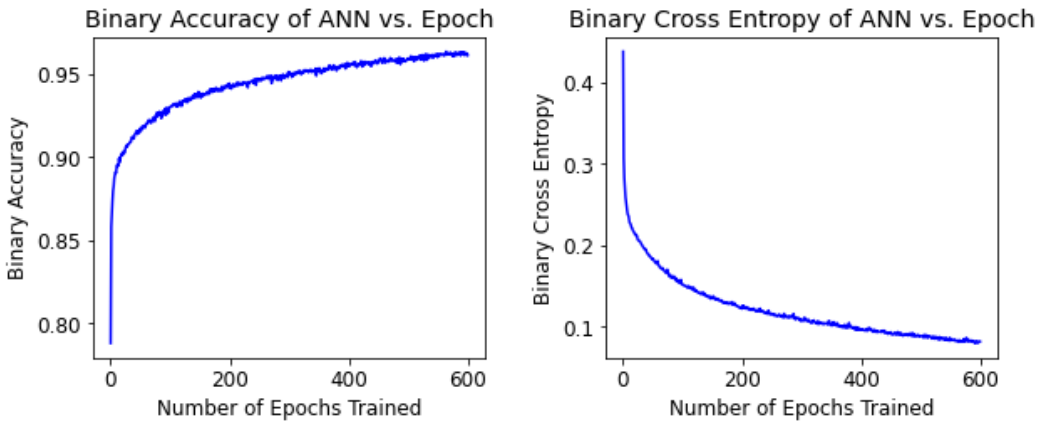

Figure 42. Learning curves for binary accuracy and binary cross entropy for GPS-trained ANN. Training performed using PCRL-Mech1 with $\alpha_{crit} = 0.1$.

In the simulation stage, we will replace the adaptive GPS method with the trained ANN model discussed above. During the simulation stage, the current state of the system is passed to the ANN as input at the GPS intervals. The output of the ANN model is a new list of species. The list of species is used to create a new mechanism, more representative of the current state, which will be used for simulating the GPS interval, similar to the adaptive GPS. Unlike adaptive GPS, updating the mechanism requires only a pre-trained neural network call, rather than a new training simulation. The outcome is a more accurate reduced chemistry mechanism with reasonable computational efficiency. In the next sub-section, we investigate the performance of adaptive GPS and the supervised learning algorithm for 0D simulations of methane and ethanol combustion using GRI 3.0 and PCRL detailed mechanisms. The variation in the species rankings by element flux over the course of simulations and the advantages of the adaptive over classic GPS are discussed.

3.3 Results and Discussion

3.3.1 Comparing the SL-GPS with Classical and Adaptive GPS Methods & Detailed Mechanism

The initial conditions and base mechanisms used for seven 0D simulations of methane and ethanol combustion are outlined in Table 3. The base mechanisms include the GRI 3.0 mechanism for methane combustion (V1) and the PCRL mechanism for ethanol combustion (V2). Results are shown for the detailed mechanisms and the three reduction algorithms discussed in this study i.e., a single mechanism produced by a single pass of GPS (Classic GPS) (2.1), adaptive GPS algorithm (2.2), and the GPS-trained ANN method, referred to as SL-GPS in the following sub-sections. The initial conditions are chosen to represent the conditions at which the neural network is trained including long ignition delay time (low temperature and pressure) at fuel-lean conditions (C1), long ignition delay time at fuel-rich conditions (C2), short ignition delay time (high temperature and pressure) with near-stoichiometric equivalence ratio (C3), and a fourth case for the GRI 3.0 mechanism similar to the conditions of the simulation shown in Figure 35 (C4). If the neural network is overfit on the training data, it “memorizes” the output species for the training inputs without learning their meaningful relationship to the state vector. To avoid this issue and properly train the model, we selected test conditions such that they do not quite lie at the boundaries of the training space, or any exact point of the training space.

Table 3. Initial conditions for validation cases.

Test Case	Detailed Mechanism	Temperature (K)	Pressure (atm)	Equivalence Ratio
V1-C1	GRI 3.0 (Methane)	1310	1.1	0.65
V1-C2		1310	1.1	1.35
V1-C3		1890	99	1.05
V1-C4		1505	1.05	1.05
V2-C1	PCRL-Mech1(Ethanol)	1110	1.1	0.65
V2-C2		1110	1.1	1.35
V2-C3		1390	99	1.05

3.3.2 Methane Combustion

We first present Figure 43, which shows the results for each methane validation case, including temperature, heat release rate, and mole fractions for OH. For brevity, the comparison for other species e.g. (CH_4, CH_2O CO_2, CO, O, H, H_2O, and CH_3) are shown in Appendix. Comparing the results obtained using the classic GPS, adaptive GPS, and SL-GPS reduction schemes shows that the adaptive and SL results follow the detailed results more closely than the classic GPS predictions for temperature, OH mole fraction, and HRR for all cases.

This is particularly noticeable in case V1-C4, where the classic GPS mechanism results for all three metrics are far from the detailed results as compared to the adaptive GPS and SL-GPS predictions that closely follow the temperature, OH, and HRR variations obtained using the detailed mechanism. This suggests that the mechanisms produced by the adaptive GPS and SL-GPS are capable of replicating the results of the detailed GRI 3.0 mechanism with greater accuracy than the classic GPS method.

Figure 44 shows the number of species and reactions in the reduced mechanism for each method at each GPS interval during the simulations. Note that the species and reaction count for classic GPS are constant across the GPS intervals, as it uses a single mechanism created before the start of the simulation. For most of the simulation duration, the number of species and reactions in both the SL-GPS and adaptive GPS mechanisms remains below that of the classic GPS mechanism, except for a spike in the number of species and reactions close to ignition time which can rise above those of the classic GPS mechanism.

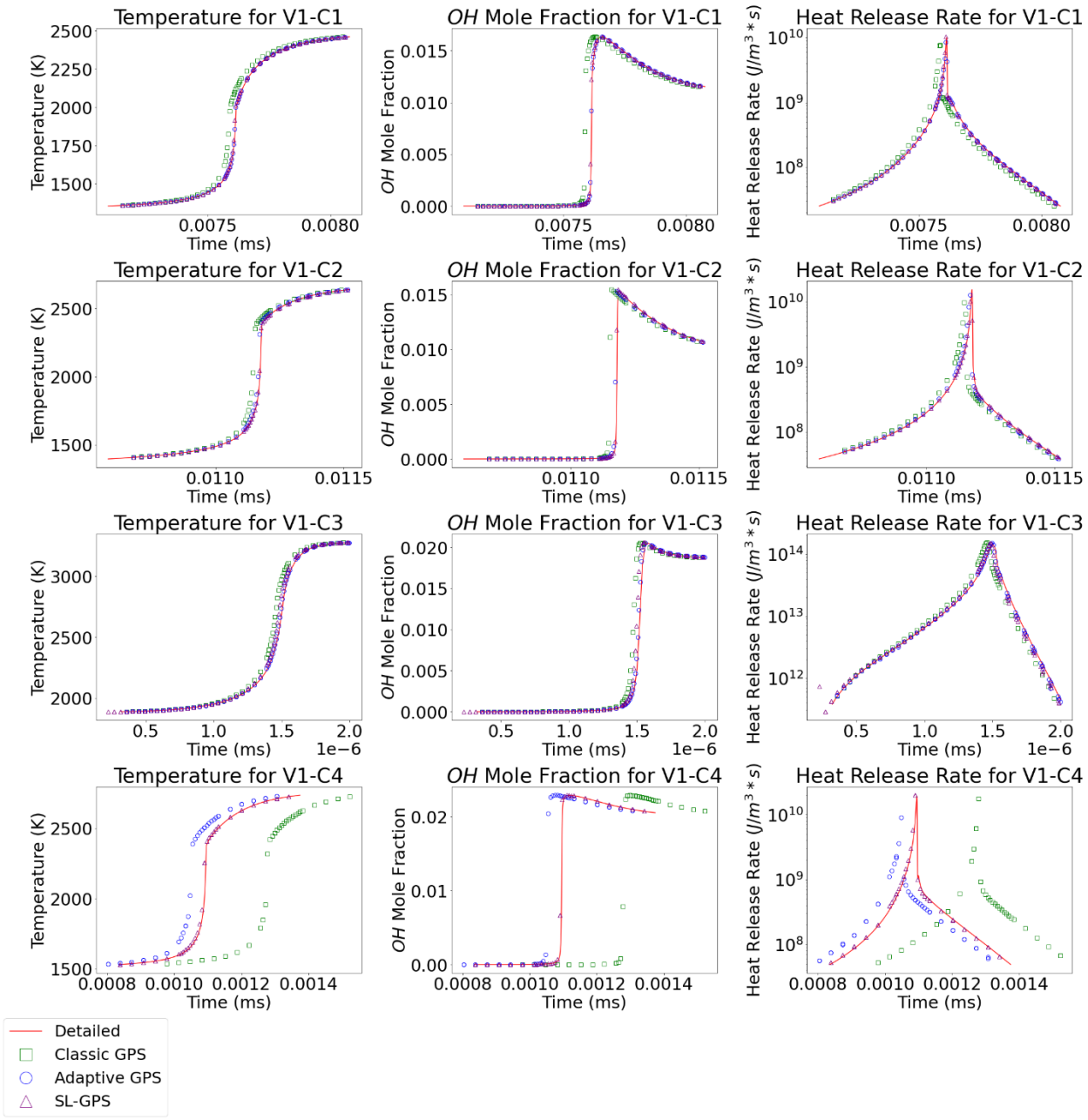

Figure 43. Temperature, OH mole fraction, and HRR for methane combustion cases using detailed (solid red line), classic GPS (open green square symbol), adaptive GPS (open blue circle symbol), and SL-GPS (open purple triangle) mechanisms.

However, as the spike generally comprises a small fraction of the total time of the simulation, it does not negate the advantages of the adaptive GPS mechanism over the classic GPS

method. In fact, it suggests that the proposed adaptive algorithm can distinguish between periods of high reactivity that require consideration of a larger number of pathways (e.g., during ignition) and accurately identifies periods of low reactivity. As the adaptive algorithm encounters a shift in reactivity, it automatically adds new pathways which are important for that time period and removes the excessive pathways and species at other times to conserve computational costs. The reduction in species and reactions is especially dramatic in case V1-C3, where the SL-GPS reaction count drops to as low as 56 after ignition compared to the classic GPS count of 196, and even during the ignition spike, the adaptive and SL species and reaction count only barely reach the classic GPS count. Combined with the improved accuracy seen in Figure 43, the reduction in species and reactions indicates that using the proposed adaptive GPS mechanism enhances the predictions of species, temperature, and HRR compared to the detailed mechanism and can potentially lower the computational time of higher order reacting flow simulations by reducing the number of species and reactions as will be discussed later.

Figure 43 and Figure 44 indicate that the SL-GPS method performs at a similar accuracy, species count and reaction count to the adaptive GPS and significantly better than the classic GPS. This is important to the practicality of the previously observed benefits of the adaptive GPS method, as the SL-GPS method employs the same principles as the adaptive GPS, i.e., updating the mechanisms in response to changes in chemical reactivity, without the prohibitive cost of running GPS at each GPS interval. Instead, it only requires a call of the trained ANN to select species from a state vector, which incurs very little computational cost. Although the SL-GPS appears to perform at a greater accuracy than adaptive GPS in Figure 43 for case C1-V4, this is not indicative of increased performance since in Figure 44 we can see that SL-GPS often uses a larger number of species and reactions than adaptive GPS for that test case.

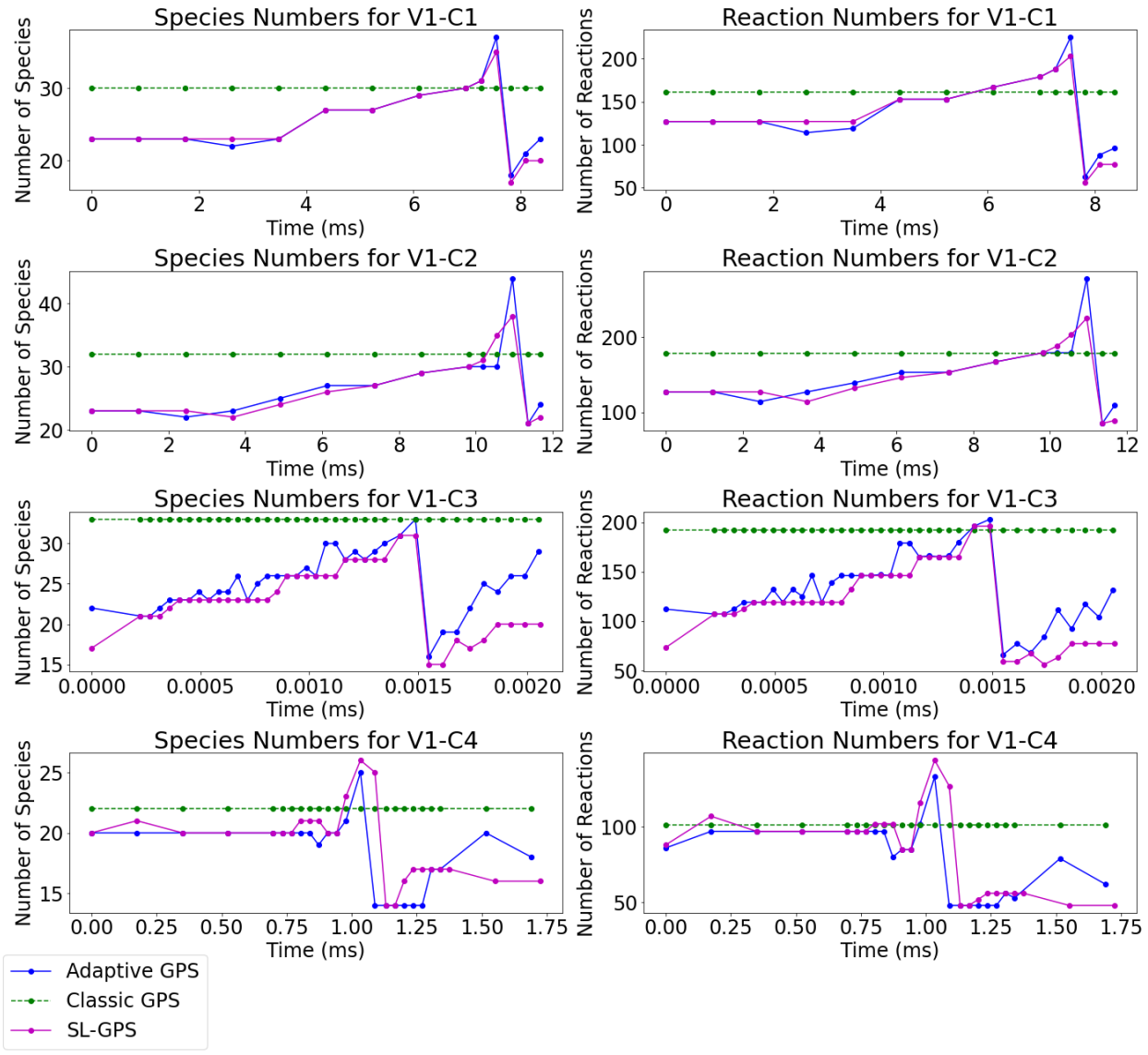

Figure 44. The number of species and reactions in the reduced mechanisms obtained using the classic GPS (blue), adaptive GPS (green) and SL-GPS (purple) methods for methane combustion.

As the ANN in SL-GPS is trained based on the GPS data, we would not expect any improvement in mechanism prediction from the adaptive to SL-GPS, however, the accompanying increase in computational efficiency makes the latter far more practical. As mentioned previously, the most significant accuracy increases from classic to adaptive and SL-GPS are seen in case V1-

C4 in Figure 43, while the most significant reductions in species and reaction count were seen in case V1-C3. The adaptive and SL methods for the other two cases, performed at lower temperatures and pressures, showed less dramatic improvements in accuracy and reaction reductions, but still displayed improvements over the classic GPS. This indicates that adaptive and SL-GPS Equation 4) selected by GPS at each GPS interval are shown. The top four species are shown for the GRI 3.0 validation cases.

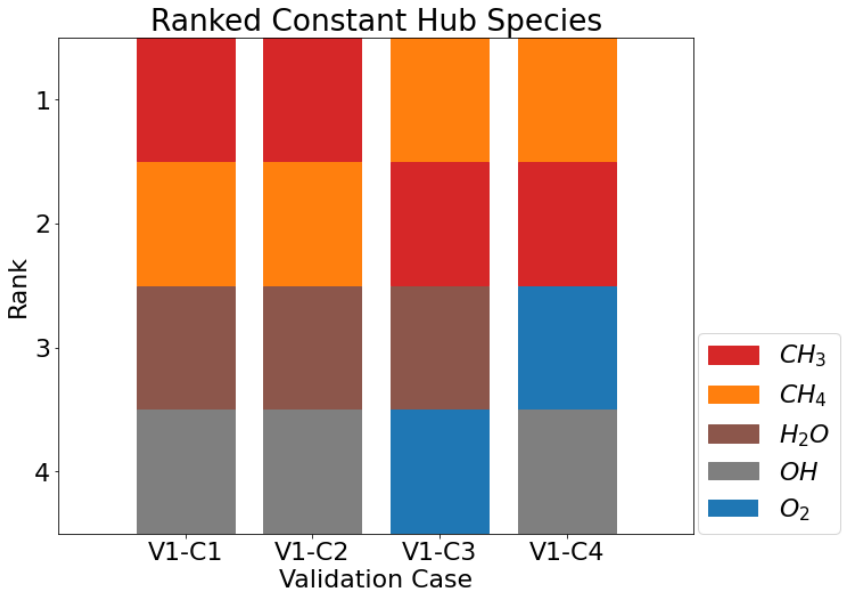

Figure 45. Hub species rankings using Classic GPS for methane combustion.

To demonstrate how the adaptive GPS mechanism outperforms the classic GPS, we examined the evolution of hub species for case V1-C3 in Figure 45. At the first GPS interval, CH_4 is ranked first, followed by CH_3, O_2, and HO_2, respectively. This corresponds to the brief dominance of the chain initiating reactions that convert CH_4 to the more reactive methyl radical (CH_3) following R.1-3 reactions.

$$OH + CH_4 \rightarrow CH_3 + H_2O \quad \text{(R.1)}$$

$$H + CH_4 \rightarrow CH_3 + H_2 \quad \text{(R.2)}$$

$$O + CH_4 \rightarrow CH_3 + OH \quad \text{(R.3)}$$

The CH_3 produced here is then converted via several parallel pathways to CO, which is, in turn, oxidized to the target species CO_2 primarily via:

$$OH + CO \rightarrow H + CO_2. \quad \text{(R.4)}$$

As CH_3 accumulates from the initiation reactions, the pathways from CH_3 quickly become the dominant reactions, as indicated by the long period from the initial GPS interval to about 0.014 ms where CH_3 switches places with CH_4 and becomes the highest-ranked hub species. These reaction pathways strongly depend on the presence of free radicals like O, H, OH, and HO_2 to proceed, as indicated by the presence of HO_2 and OH at rank 4 throughout the initiation and CH_3-dominant periods.

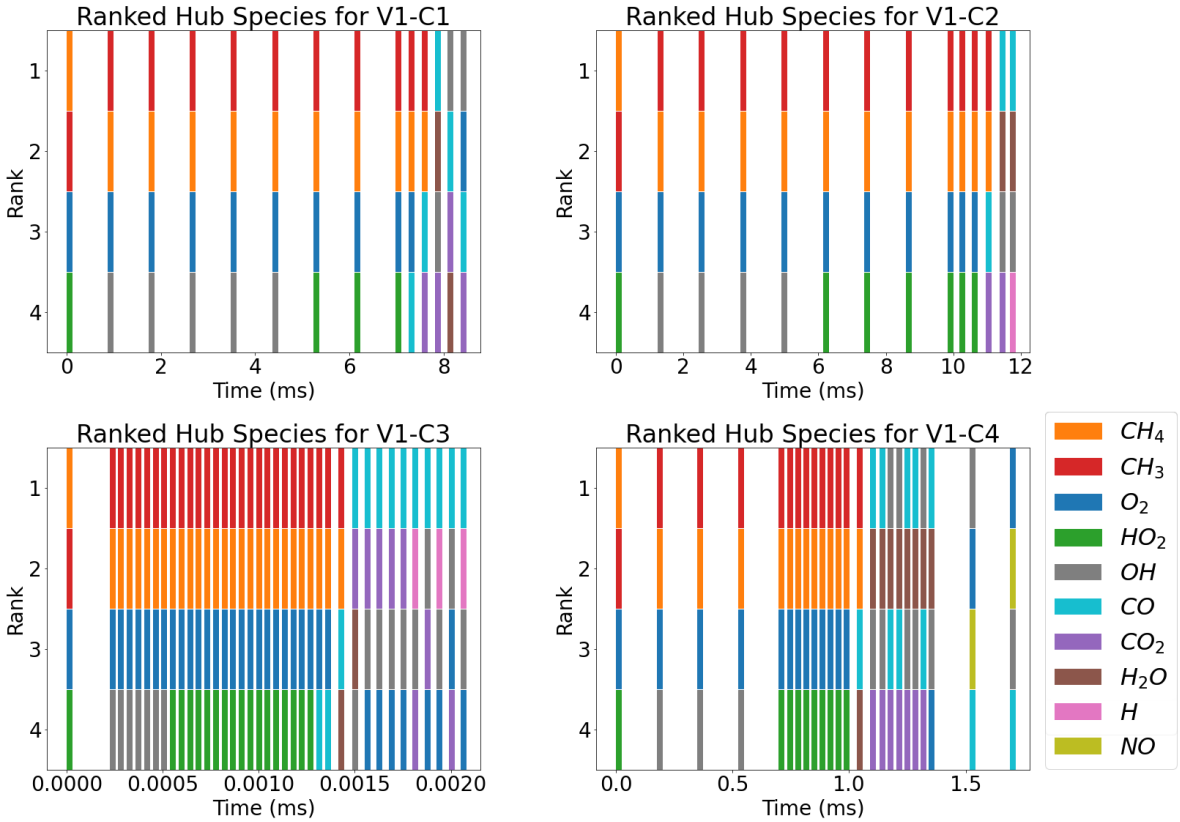

Figure 46. Top four hub species ranked by $\boldsymbol{\alpha}$ vs. time for adaptive mechanisms in methane combustion for cases outline in Table 3.

As the reactions continue, more of these radicals are produced through chain-branching reactions, where one radical combined with a stable species yields two or more radicals. Examples of such reactions are:

$$H + O_2 \rightarrow OH + O \quad \text{(R.5)}$$

$$O + H_2 \rightarrow OH + H. \quad \text{(R.6)}$$

This causes the net production of radicals to be positive, which increases the concentration of radicals and that in turn increases the rate of chain-branching reactions. This gradual buildup of radicals explains the gradual rise in species and reaction count before ignition as seen in Figure 44 for V1-C3. As the number of radicals increase, reaction rates increase and more chemical pathways that depend on those radicals become important, necessitating more reactions in the reduced mechanisms. Eventually, at around 0.014 ms, these branching reactions begin to produce radicals much faster than chain-terminating reactions that convert radicals to stable species. This leads to an exponential explosion of radicals, as observed in the sudden spike of OH mole fraction in the V1-C3 plot in Figure 43. The sudden abundance of radicals, in turn, causes a sudden increase in speed of the $CH_3 \rightarrow CO$ reaction pathways and an increase in reactivity, temperature, and heat release rate during ignition. The expedited pathways rapidly deplete the system of CH_3 and CH_4, at which point the dominant reactions become the conversion of CO to CO_2, as in R.4. This behavior explains that rank 1 is taken by CO after ignition for case V1-C3, generally occupied by CO_2, OH, and H. Once the focus shifts to the oxidation of CO, the complex network of reactions involved in the CH_3-CO conversion becomes largely irrelevant. Therefore, the adaptive GPS is able to detect this behavior. This is evident from Figure 44 and case V1-C3 where the number of species and reactions used in the mechanism suddenly drops at around 0.015 ms right after the ignition. The proceeding mechanisms are then able to model the CO oxidation without being

burdened by the needless complexity of the CH_3-CO pathways. However, the classic GPS method cannot adapt to such shifts in the dominating pathways. As seen in Figure 45 for case V1-C3, the significance of species measured by classic GPS, based on the entire detailed simulation, ranks CH_4 and CH_3 first. As the classic GPS uses this mechanism throughout the simulation, it must consider the reaction pathways relevant to CH_4 and CH_3 throughout the simulation. Considering these pathways imposes an additional computational effort for the post-ignition CO oxidation phase. Although this discussion was based on the results for V1-C3, a similar argument holds for the other three methane combustion cases. That is, the transition from CH_3-dominated chemistry to CO oxidation is seen for cases V1-C1, V1-C2, and V1-C4. It is also notable in Figure 46 that the average frequency of mechanism updates, relative to the total simulation time, increases with increasing the initial temperature and pressure. This is apparently due to the larger HRR expected in high temperature and pressure combustion, which causes the threshold for GPS interval to be met earlier in the combustion process. This can be seen in V1-C1 where the smaller GPS intervals are only used just before and after the ignition, whereas in case V1-C3 the smaller GPS intervals are always used except for the very first reduced mechanism.

The post-ignition phase is better captured using the adaptive GPS method. Based on the hub species identification this phase can be further divided into two phases namely: initial post ignition (hub species ordered by rank: CO-CO_2-OH-O_2) and final post ignition (hub species ordered by rank: CO-H-OH-O_2). The initial post-ignition phase is dominated by the oxidation of CO to CO_2 using OH and O_2 as oxidizers. This leads to the second heat release event that needs to be accurately predicted in hydrocarbon combustion. Noticeably, this secondary heat release is not sustained for the entire post-ignition phase as the hub species in the later half (defined as final post-ignition phase) focuses on H radical instead of the CO_2 stable species. This characterizes the

formation of water molecules when the hydrogen and hydroxyl radicals react and contribute to the chain termination reaction (i.e., $H + OH \rightarrow H_2O$). The above discussion proves that the adaptive GPS method captures both pre-ignition and post-ignition events more accurately than the classic GPS method for methane combustion.

3.3.3 Ethanol Combustion

In this sub-section, we investigate the performance of the adaptive GPS and SL-GPS in predicting the temperature and combustion products for ethanol that entails a more complex detailed chemistry mechanism compared to methane. Figure 47 shows the prediction of temperature, OH mole fraction, and HRR for the three ethanol combustion cases Table 3.For brevity, the comparison for other species is shown in Appendix. The adaptive and SL-GPS mechanisms yield results far more accurate to the detailed mechanism predictions than classic GPS, to an even greater extent than seen in the methane cases (see Figure 43). Figure 48 shows the species and reaction counts for each mechanism. Similar to methane combustion, far fewer species and reactions are invoked by the SL-GPS and adaptive GPS to produce the superior accuracy seen in Figure 47, although the spike in species and reactions is observed right before ignition similar to methane combustion (see Figure 44). The use of a more complex detailed mechanism as in PCRL-Mech1 forces the adaptive GPS and SL-GPS methods to more frequently update the reduced mechanism during simulation. Therefore, these two methods outperform the classic GPS more noticeably for the more complex chemistry mechanisms in ethanol combustion.

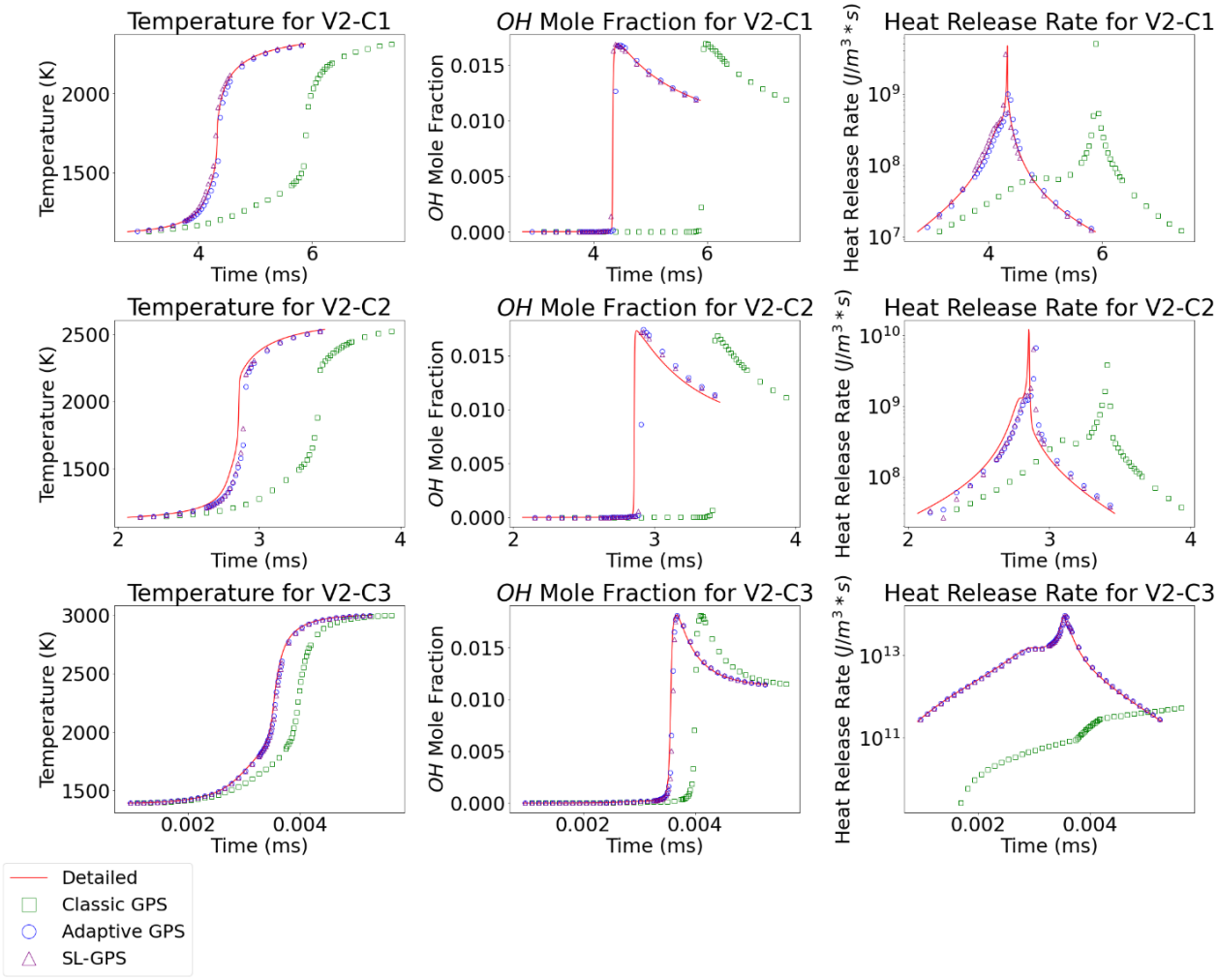

Figure 47. Temperature, OH mole fraction, and HRR for ethanol combustion using detailed (solid red line), classic GPS (open green square symbol), adaptive GPS (open blue circle symbol), and SL-GPS (open purple triangle) mechanisms.

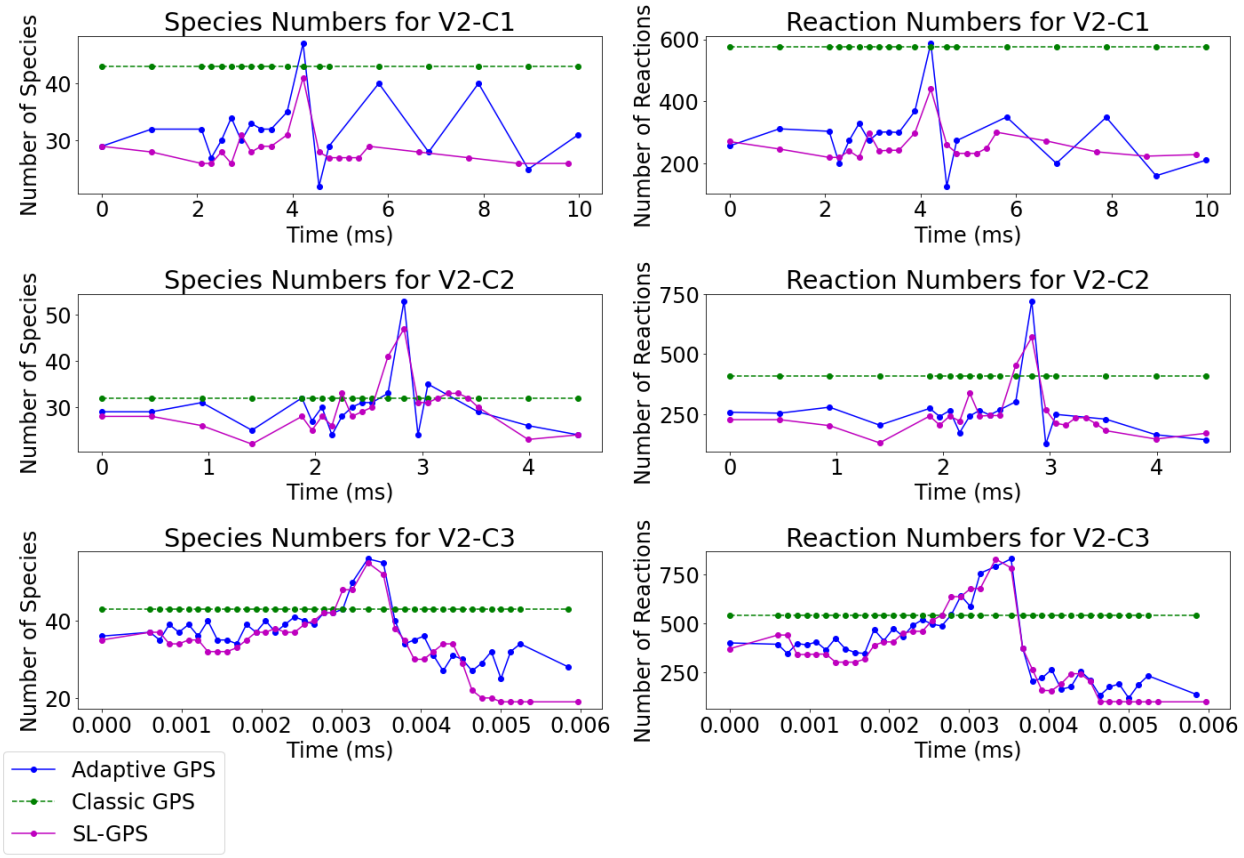

Figure 48. The number of species and reactions in the reduced mechanisms obtained using the classic GPS (blue), adaptive GPS (green), and SL-GPS (purple) methods for ethanol combustion across different cases.

Figure 49 shows the top two ranked hub species for the ethanol cases, again using the normalized element flux α as a metric. Although the kinetics for ethanol combustion involves far more species and reactions than for methane, we can still identify a transition in species importance around the time of autoignition analogous to the CH_3-CO shift for methane as seen in case V2-C3 at 0.003 ms. At that instant of time, the mechanism goes from being dominated by C_2H_5OH (ethanol), O_2, and $C_3H_5O_2$ to a larger variety of species like OH, H, CH_2CO, CO_3 (1046) and (3061), CO_2, and C_2O_3 (1043). Although CH_3 and CO do not appear to play as large a role in this

transition as in the methane combustion, the shift in species importance is due to the explosion of free radicals caused by chain branching reactions represented by R.5 and R.6 which rapidly reduce the mole fraction of initial reactants, e.g., C_2H_5OH and the significance of the chain initiating and propagating reactions that they tend to facilitate. Therefore, similar to the methane combustion, the adaptive GPS method eliminates these reactions in post-ignition reduced mechanisms. This yields faster computing times compared to classic GPS which considers all these reactions throughout the simulation. Our future work will focus on *a posteriori* study of the proposed adaptive and SL-GPS method in 3D reacting flow simulations to illustrate the effectiveness of these methods in practice.

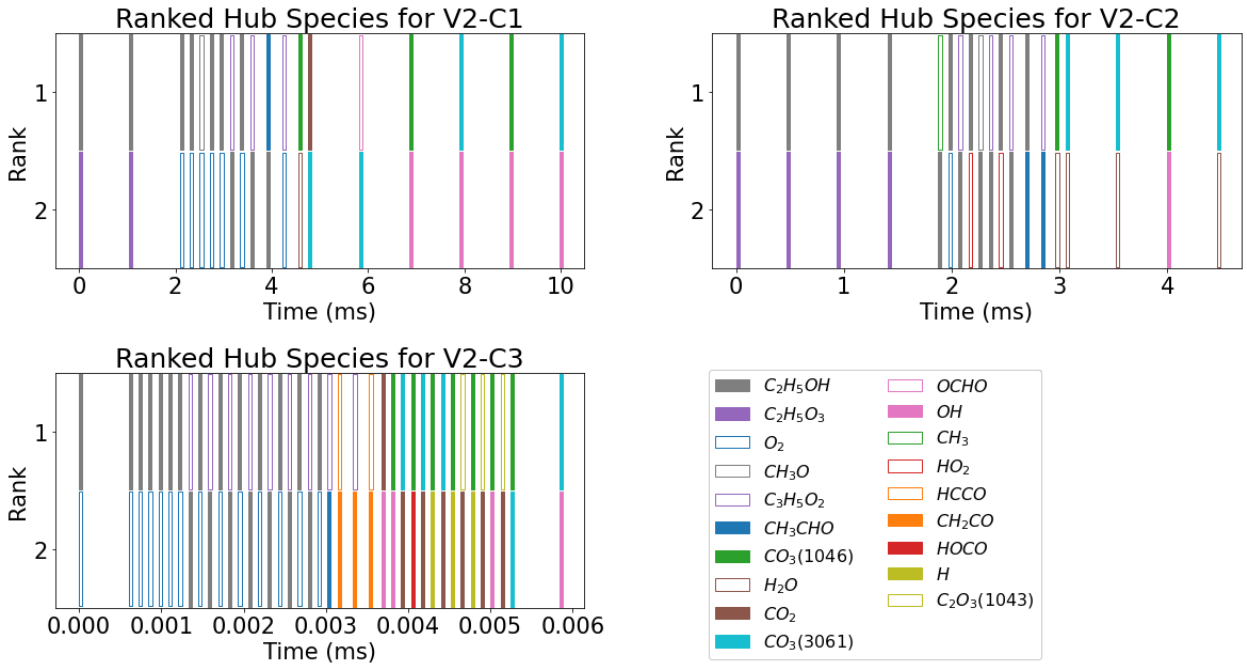

Figure 49. Top two hub species ranked by $\boldsymbol{\alpha}$ vs. time for adaptive mechanisms in ethanol combustion cases.

So far, we discussed the benefits of the new SL-GPS method for two mechanisms. This targeted study helped in understanding the capabilities of the SL-GPS method to identify combustion phase-specific hub species and its superior prediction while using fewer species. The architecture of neural network can still be improved for the entire range of conditions. In sub-section, a sensitivity study is conducted to identify the ideal architecture for a given mechanism with respect to both ANN architecture and the data size used for training. In sub-section, the optimum trained neural network identified in previous sub-section is implemented to validate the SL-GPS method with a range of conditions on the ignition delay time.

3.3.4 Sensitivity Study with respect to the Ignition Delay Time

To further optimize the implementation of our SL-GPS strategy, a sensitivity study was conducted to determine the effect of various network architectures and training data sizes on the performance of the proposed reduction method. Figure 50 and Figure 51 present the relative errors in ignition delay time using SL-GPS for methane combustion with the GRI 3.0 mechanism. These were averaged over 20 sets of initial pressure, equivalence ratio, and temperature chosen randomly from ranges of 0.1 atm to 100 atm, 0.6 to 1.4, and 1300 K to 1900 K, respectively. Figure 50 displays the error's variation for 100, 300, and 500 detailed simulations conducted for training and testing the SL-GPS, each randomly chosen from the same range of initial conditions as above. This is shown for network architectures of 1, 2, and 3 layers of neuron counts. The ANNs were trained for as many epochs before no improvement in binary cross entropy over a specified tolerance was found for 20 consecutive epochs. The 20 sets of conditions are the conditions used for the GPS-SL simulations using the trained and tested ANN, which are averaged to derive the results shown in Figs. 19-22 for the sensitivity study. It is apparent from the trend that the relative error is minimized for most architectures at 500 cases, except for the 256, 128, 64 and 128, 64 neuron

structures, the latter of which spikes at 500 cases. This spike in error is likely due to the network being overfit that typically occurs when the network memorizes the species selected for each training data point without learning the physical principles underlying their selection. The network applied to 20 sets of conditions different from the training cases might result in significant error. By increasing the number of training cases from 300 to 500 cases compared to the 16, 128 and 16, 8 neuron architectures the predictions do not exhibit significant improvements. This shows that large architectures (256, 128 and 256, 128, 64 neurons) are more prone to overfit. The architectures with 256, 128 and 256, 128, 64 neurons do not show error spike at 500 cases and often produce smaller errors than the simpler architectures. This behavior might be due to the random way training cases are selected. The randomly selected conditions under which overfitting occurs is within the range of 20 sets training dataset. If this network is applied to a general condition randomized further or averaged over more random dataset (50 sets of conditions in comparison to 20 sets used) we expect a spike in error similar to 128, 64 neuron networks. Regardless, for the simpler architectures at least, the largest possible number of training simulations is desirable for more accurate prediction.

Figure 51 shows the variation of relative error with the GPS interval during ignition. This interval was determined from the time the detailed simulation takes to reach steady state (defined as the heat release rate dropping below a certain threshold, 200,000 J/m^3-s for this study). A specified fraction (either 0.005, 0.01, or 0.02) of this time was taken and used as the GPS interval during ignition (defined as the heat release rate being above a certain threshold, determined by dividing the maximum heat release rate of the detailed simulation by 400 for methane combustion and 100 for ethanol combustion). Prior to ignition, a GPS interval five times the size of the ignition interval was used. From Figure 20, it appears that most of the architectures have minimum error

at a GPS interval of 0.01 of the simulation time except for the smaller architectures of 16 and 16, 8.

Figure 52 and Figure 53 show the maximum number of species in any reduced mechanism predicted by the SL-GPS over the twenty random cases as they vary over the number of train/test cases and the GPS interval. It is seen that the simple architectures of 16 neurons and 16, 8 neurons yield smaller number of species, which suggests simulations with mechanisms predicted by these architectures will further reduce the computational cost. Reducing the size of the GPS interval also appears to reduce the maximum number of species for the simpler architectures. This is likely because each GPS mechanism used to train the network is based on a smaller time range of simulation data (the time range from one update to the next). If this interval is smaller, the chemistry will have less time to evolve and there will be less time for more species to become relevant. This will cause GPS to include fewer species in the generated reduced mechanism. In turn, the neural network trained on this mechanism predicts fewer species. In summary, the 16-node architecture demonstrated the lowest number of maximum species at the 0.005 GPS interval, and the relative error correlated negatively with the number of training/testing cases for the simple architectures (indicating that they are not overfit). Therefore, the 16-node architecture trained/tested with 500 cases at a GPS interval that is 0.005 of the detailed simulation time is selected as the ideal configuration of SL-GPS for the values studied for the GRI 3.0 mechanism in this study.

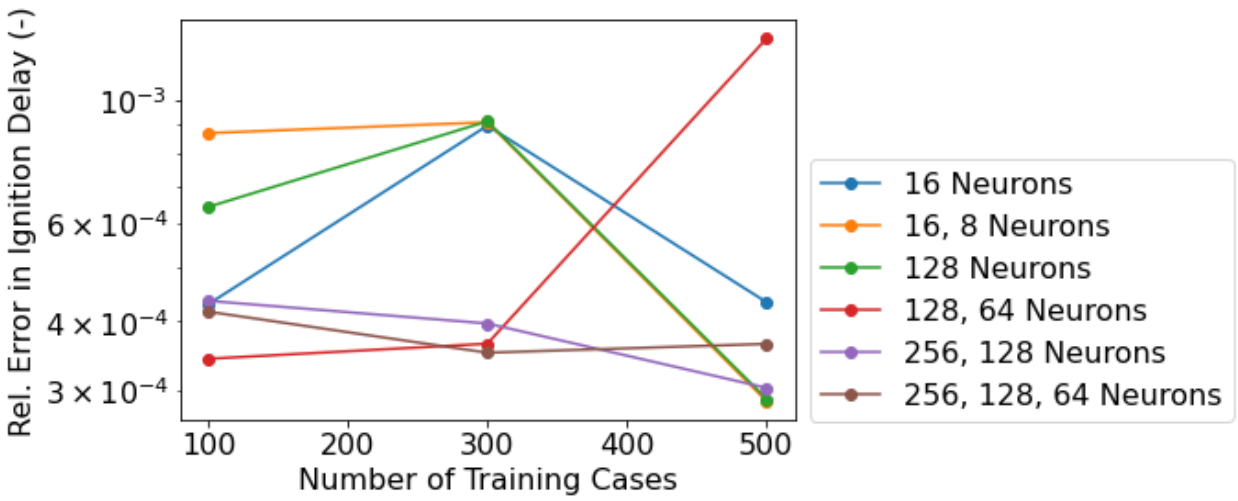

Figure 50. Ignition delay errors for different training set sizes.

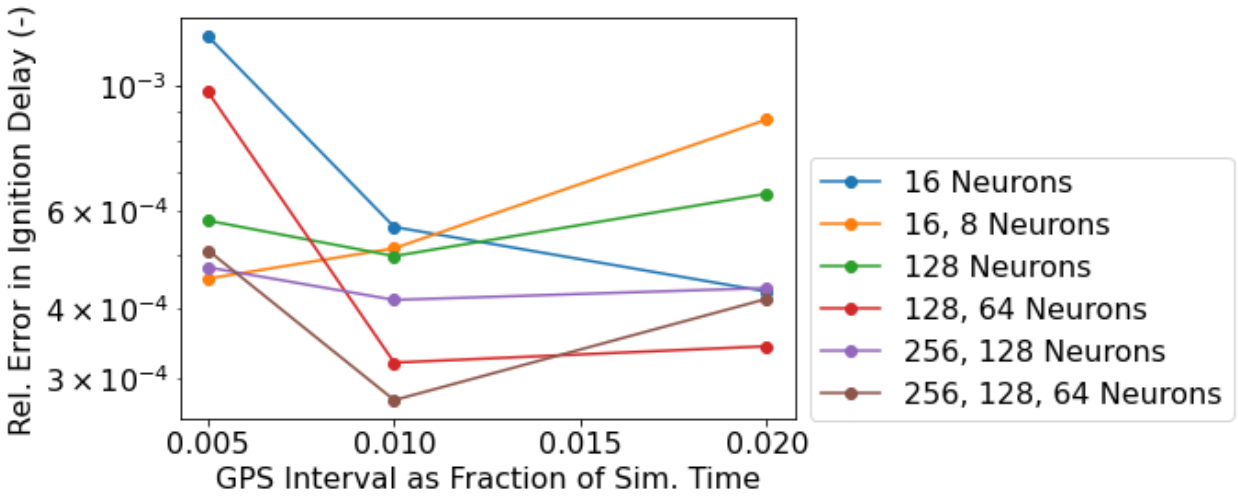

Figure 51. Ignition delay errors for different sizes of GPS interval.

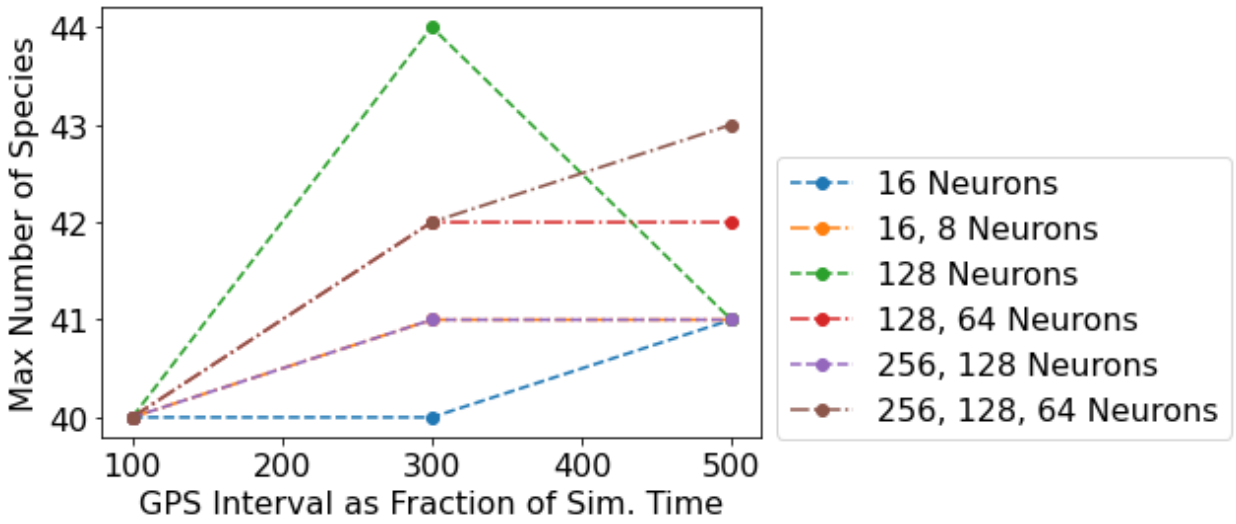

Figure 52. Maximum species counts for different training set sizes

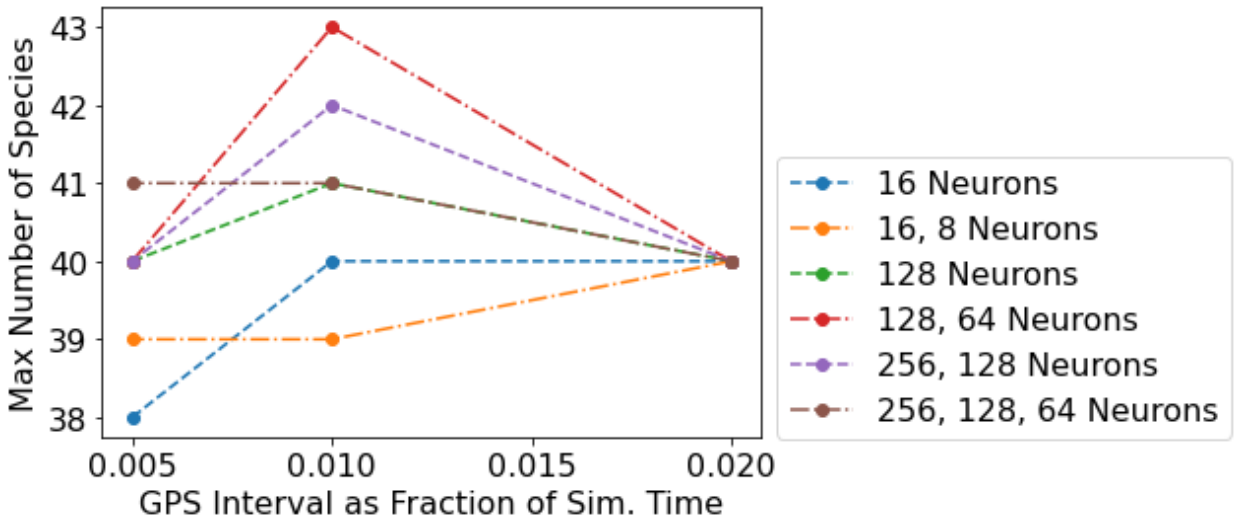

Figure 53. Maximum species counts for different sizes of GPS interval

3.3.5 Ignition Delay Time Validation for Methane and Ethanol Combustion

A validation study was conducted to compare SL-GPS's efficiency in predicting ignition delay time to other reduction methods, i.e., classic GPS and DRGEP, across a wide range of conditions for both methane (using GRI 3.0) and ethanol (using PCRL) combustion. The ideal

network and training set identified in section 2.6 was used here, but an additional hidden layer of 8 neurons was added to the network architecture for the ethanol cases to account for the increased complexity of the PCRL mechanism for a total of two hidden layers with 16 and 8 neurons. The 16, 8 architectures showed no change in maximum species count as the GPS interval was changed from 0.010 to 0.005 in Figure 53. Therefore, a 0.010 GPS interval was used for the ethanol cases. The range of parameters considered for this study are described in Table 4 and Table 5, where temperature, pressure, and equivalence ratio are varied at uniform increments from a lower to an upper limit (except for pressure, which is varied at log-uniform increments). All permutations are tested for a total of 120 cases. These ranges are identical to those used to train the reduction ANN. However, the cases used for training are chosen randomly rather than at increments. Two values for each parameter outside the training range were also used with one case for each permutation for a total of 8 outlier cases. This is to test the prediction capabilities of the ANN model on data ranges it was not previously trained on.

Figure 54 and Figure 55 shows the distribution of relative errors in ignition delay time across the 120 training range cases for the methane and ethanol results, respectively. In both figures, SL-GPS possesses a high narrow peak near zero, while DRGEP exhibits a wider peak and is shifted to either side of the 0-error mark. The error of the SL-GPS exceeded the maximum error of DRGEP for ethanol combustion in a few cases for ethanol combustion, but the majority of DRGEP cases clearly had a larger error than the bulk of the SL-GPS cases. Classic GPS shows a wide peak at zero for methane combustion, and two small peaks (one around 0 and another around 0.10) for ethanol combustion. Compared to the other methods, SL-GPS demonstrated a significantly tighter distribution of errors that suggests a greater reliability in accurately predicting ignition delay time for both mechanisms.

This is confirmed by the average absolute-value relative errors reported in Figure 56 and Figure 57. SL-GPS's average error over the 120 cases is nearly a full order of magnitude lower than both the Classic GPS and DRGEP mechanisms for methane combustion and it is significantly lower than the Classic GPS error and slightly lower than DRGEP's error for ethanol combustion. Figure 56 and Figure 57 also report the average computational time for a single chemical timestep, which constitutes the Jacobian evaluation and advancing the simulation by a single integration step. In addition to demonstrating significant improvements in accuracy, SL-GPS's mechanisms took less time on average to solve the necessary chemistry at each chemical timestep for both methane and ethanol combustion. This suggests that SL-GPS is made more efficient than current reduction methods by adaptively changing the mechanism at intervals to fit the detailed chemistry. Figure 58 and Figure 59 show the variation of ignition delay time predicted by SL-GPS as temperature and pressure are changed, overlaid with the detailed results for an equivalence ratio of 0.6. The results for 1.0 and 1.4 are given in Appendix. SL-GPS clearly succeeds in predicting the expected positive log relationship of ignition delay time with the inverse of temperature (scaled by a factor of 1000), and its decrease with greater pressure at lean, stoichiometric, and rich equivalence ratios for both fuels.

To assess whether the ANN of SL-GPS is capable of extrapolation outside of its training range, the average errors and chemical timestep computational times are reported for 16 outlier cases (8 for each fuel) in Figure 60 and Figure 61. For methane combustion (Figure 58), the error for SL-GPS is still significantly lower than that of classic GPS while exhibiting slight improvement over DRGEP. However, while SL-GPS's computational time is still lower than Classic GPS, DRGEP appears to perform better at these conditions. This suggests that SL-GPS's efficiency is reduced when predicting mechanisms for methane combustion under conditions outside its training

range due to the limitations of its neural network in extrapolating data. SL-GPS demonstrates accuracy and computational times comparable to DRGEP and better than classic GPS under such conditions. This behavior indicates that the neural network has not been overfit and has internalized the physical principles that underpin GPS. As those principles apply just as well in conditions outside the training range as within, GPS-SL is still able to select reasonable species for reduction under the outlier conditions. For ethanol combustion (Figure 59), a significant reduction in both error and computational time for SL-GPS as compared to DRGEP and Classic GPS is seen. SL-GPS (used with ethanol combustion) is therefore capable of extrapolating beyond its training range to maintain its superior efficiency at extreme temperatures, pressures, and equivalence ratios, unlike for the methane cases. This may support the previous conclusion that the improvements in efficiency that SL-GPS offers are more pronounced for more complex mechanisms like PCRL-Mech1, where the more complex and varied chemistry has greater need for adaptive reduction.

Table 4. Initial conditions used for SL-GPS ignition delay time validation for GRI 3.0.

Parameters	**Temperature (K)**	**Pressure (atm)**	**Equivalence Ratio (-)**
Lower Limit	1300	0.1	0.6
Upper Limit	1900	100	1.4
Number of Increments	10	4 (logarithmic)	3
Lower Outlier	1200	0.05	0.4
Upper Outlier	2000	200	2.0

Table 5. Initial conditions used for SL-GPS ignition delay time validation for PCRL-Mech1.

Parameter	**Temperature (K)**	**Pressure (atm)**	**Equivalence Ratio (-)**
Lower Limit	1000	1	0.6

Upper Limit	1400	100	1.4
Number of Increments	10	4 (1, 10, 50, 100)	3
Lower Outlier	900	0.1	0.4
Upper Outlier	1500	200	2.0

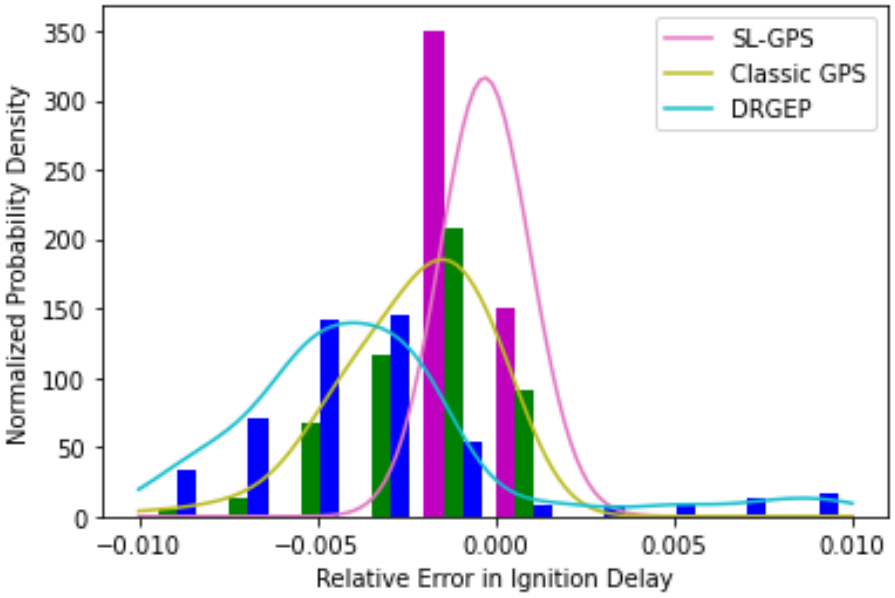

Figure 54. Histogram of relative error in ignition delay time for methane combustion. Kernel density estimated probability functions are shown for each method.

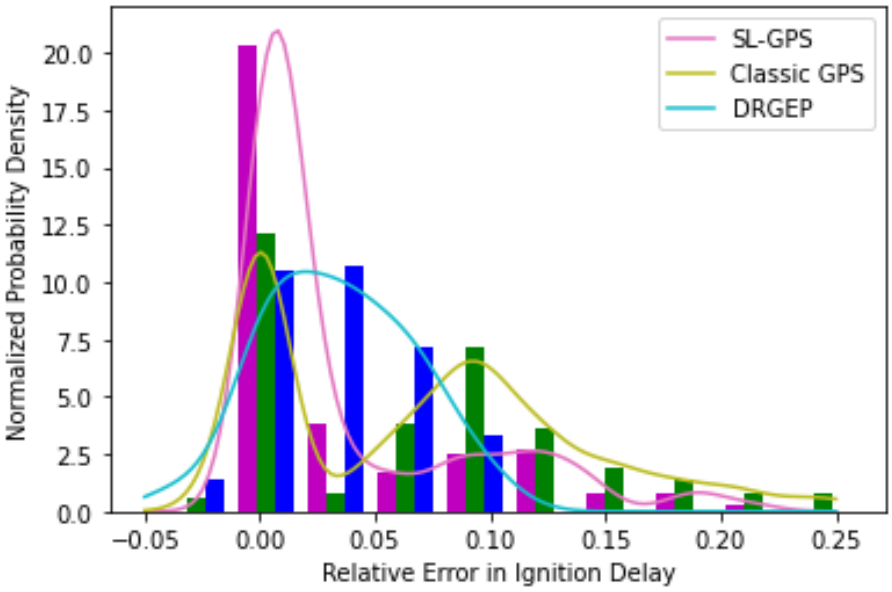

Figure 55. Histogram of relative error in ignition delay time for ethanol combustion. Kernel density estimated probability functions are shown for each method.

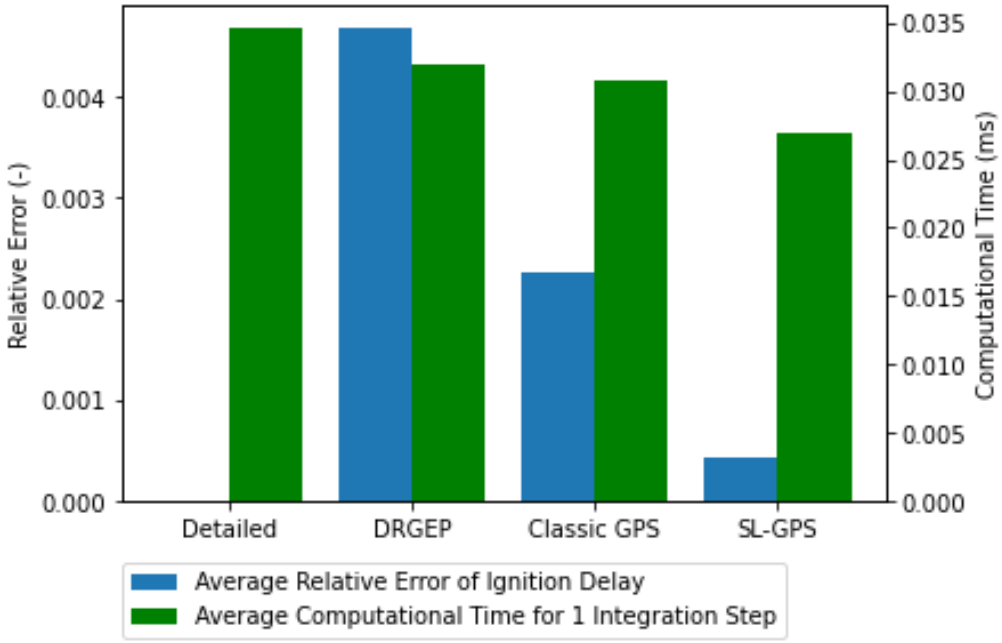

Figure 56. Computational times and relative errors for training range cases for GRI 3.0.

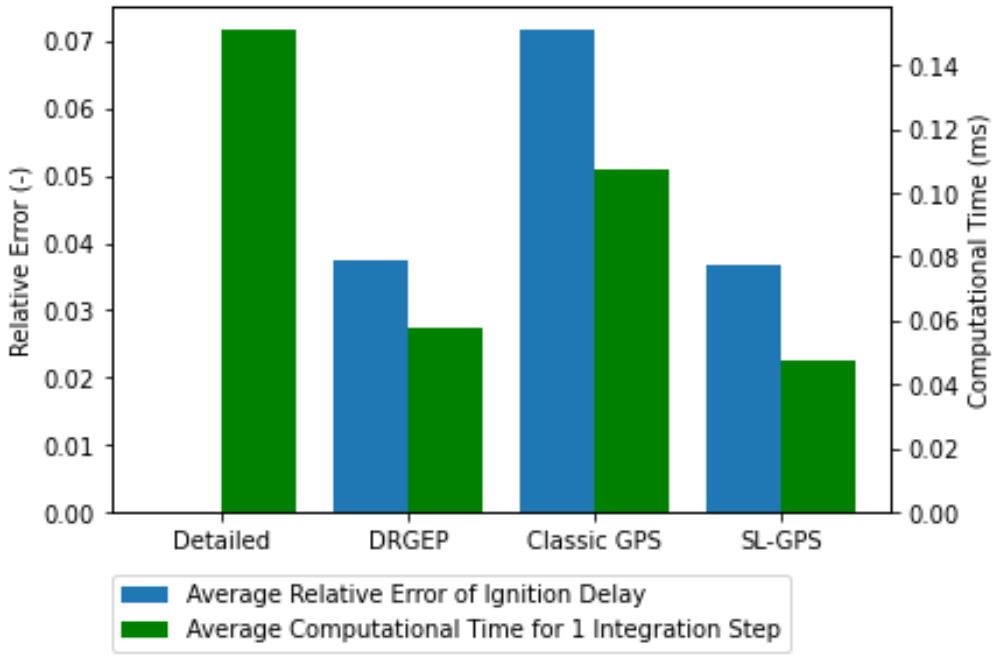

Figure 57. Computational time and relative error for training range cases (Table 5) for PCRL-Mech1.

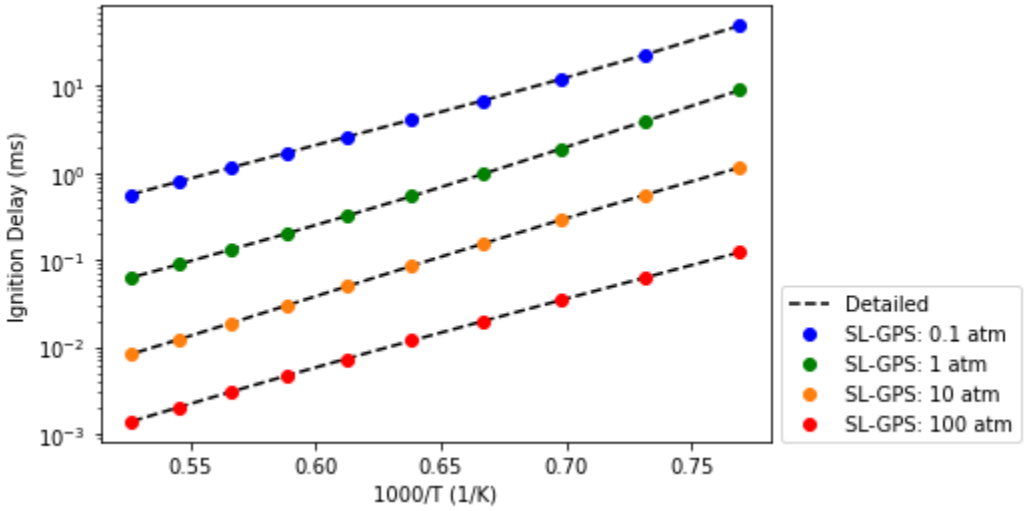

Figure 58. Ignition delay time for training range cases at an equivalence ratio of 0.6 (Table 4) for GRI 3.0.

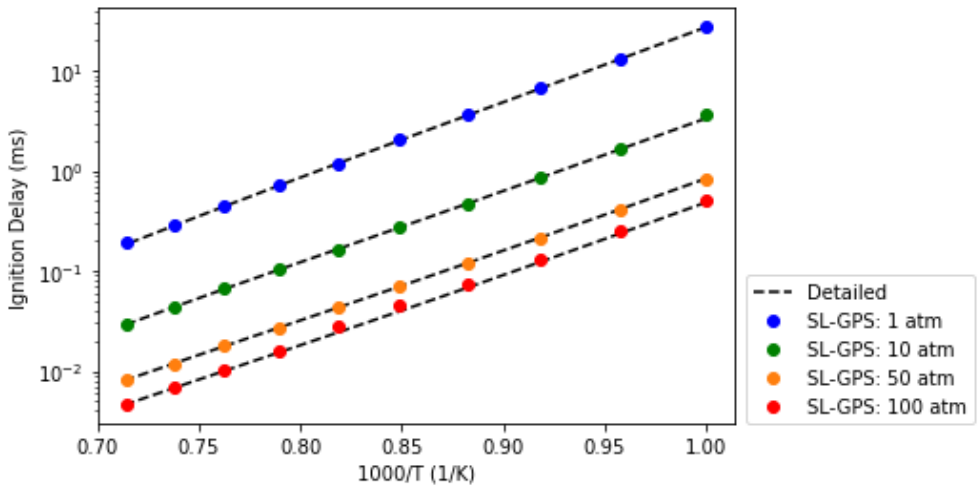

Figure 59. Ignition delays for training range cases at an equivalence ratio of 0.6 (Table 5) for PCRL-Mech1.

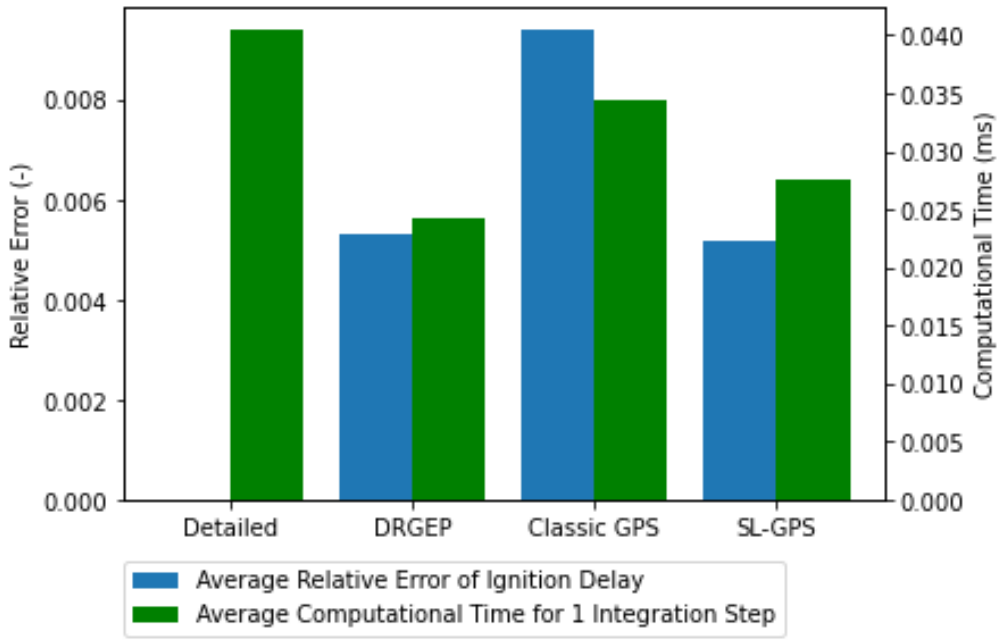

Figure 60. Computational times and relative errors for outlier cases for the GRI 3.0 mechanism for methane combustion.

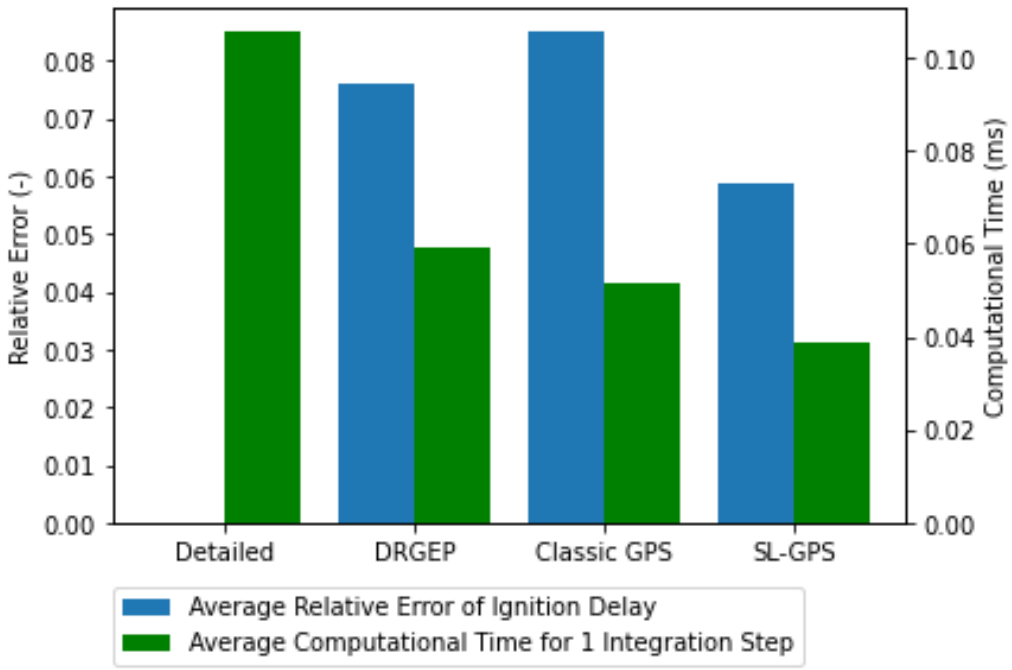

Figure 61. Computational times and relative errors for outlier cases for PCRL-Mech1.

3.3.6 0D – Chemical Analysis of sCO_2 oxy-combustion

Large amounts of sCO_2 dilution used for moderating the combustor exit temperature, high pressure and high preheat temperature in sCO_2 oxy-combustors make this environment very different from conventional air-breathing propulsion systems [6]. Different percentage dilutions of CO_2, i.e., 65%, 80%, and 90% defined by mole fraction are considered in this study for the same SWRI configuration while maintaining the same oxidizer and fuel ratio of 0.25 for all cases outlined in Table 6. The results include the auto-ignition behavior in 0D configuration at the conditions outlined in Table 6.

Table 6. Different $\%CO_2$ dilution keeping the fuel-air ratio constant $\left(\frac{n_{fuel}}{n_{air}} = \mathbf{0.25}\right)$.

Case #	$\%CO_2$	$\%O_2$	$\%CH_4$
1	90	8	2

2	80	16	4
3	65	28	7

Preliminary 0D auto-ignition simulations are conducted using GRI 3.0 mechanism and Redlich-Kwong EoS to capture the real-gas effects embedded in Cantera. [162] Simulations are initiated with the mass fractions given in Table 6 at 200 bar pressure and 1200 K in a real-gas reactor. Investigating the role of chemistry mechanisms on ignition behavior is of high importance yet beyond the scope of the current study and will be pursued in our future paper. Although several new chemistry mechanisms relevant to sCO_2 oxy-combustion have been proposed recently, e.g., UCF with 23 species reduced from the Aramaco 2.0 mechanism, this preliminary study adopts GRI 3.0 to understand the effects of sCO_2 dilution on the ignition delay time (IDT) consistent with previous studies due to the uncertainties that might exist in the newly developed mechanisms. [140] Figure 62 shows the temporal profiles of major and important intermediate species, e.g., CH_4, O_2, CH_3, H_2O, CO_2, CO, OH, and CH. CO_2 mole fraction does not change significantly over the duration of combustion indicating the limited chemical role of CO_2 dilution in line with the experimental observations [140] which highlighted the key pathways that govern sCO_2 combustion. The concentration of three key intermediate species, i.e., CH_3, C_2H_6, and CH_3O are plotted for different equivalence ratios, i.e., ϕ= 0.5, 1.0, 1.5 and % dilutions, i.e., 65, 80, and 90% in Figure 63. We consider the following chemical pathways highlighted in a previous study [140]:

$$CH_3 \rightarrow CH_3O \text{ (Promotes)}$$

$$CH_3 \rightarrow C_2H_6 \text{ (Hinders).}$$

At 90% CO_2 dilution and equivalence ratio equal to 1 and 1.5, the hindering effect of C_2H_6 formation is shown as the C_2H_6 mole fraction is diminished shortly after the ignition. The criteria

considered for ignition delay time in this study is based on the time it takes from the start of simulations to reach a peak in CH concentration which is about ~0.02 s at 90% dilution. C_2H_6 formation prevents the further transformation of CH_3 and limits the chain propagating reactions and follows a different pathway. The two reaction pathways highlighted by Karimi et al. [140] are:

$$CH_4 \rightarrow CH_3 \rightarrow CH_4O \rightarrow CH_2O \rightarrow HCO \rightarrow CO$$

$$CH_4 \rightarrow CH_3 \rightarrow C_2H_6 \rightarrow C_2H_5 \rightarrow C_2H_4 \rightarrow C_2H_3 \rightarrow CH_2CHO \rightarrow CH_2CO \rightarrow HCCO \rightarrow CO.$$

The second pathway is preferred and is reflected in Figure 64a where higher CO_2 dilution and higher equivalence ratio values lead to higher CO generation. Although the hindering effect is most pronounced for higher percentage dilution, the intermediate dilution (i.e., 80%) with an

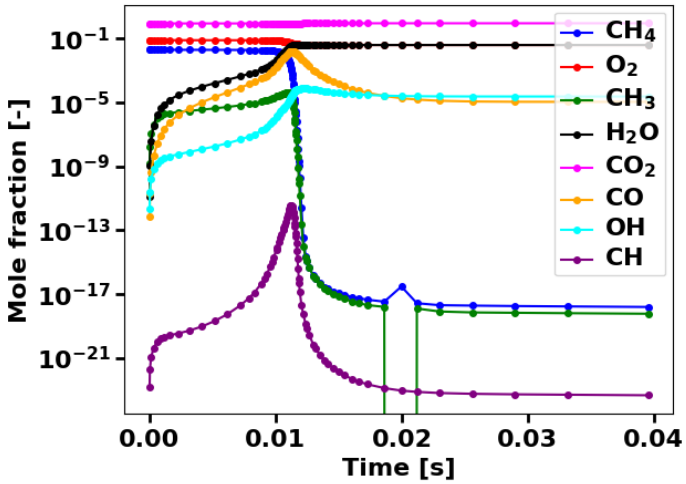

Figure 62. Temporal profile of different species for 90% sCO_2 dilution and equivalence ratio equal to one.

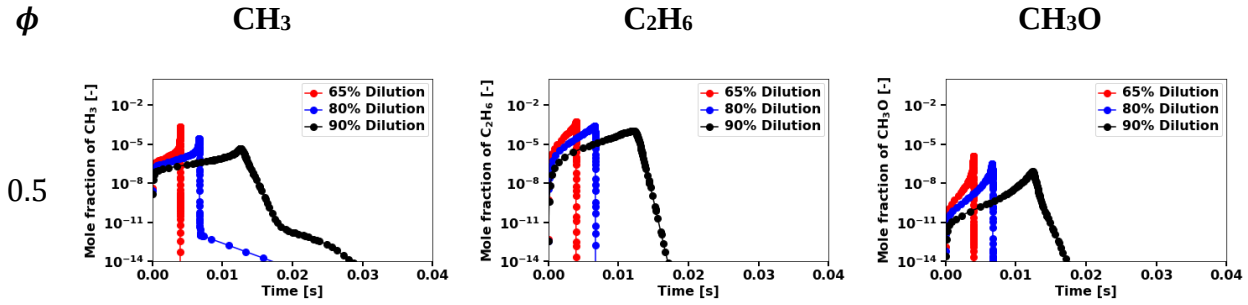

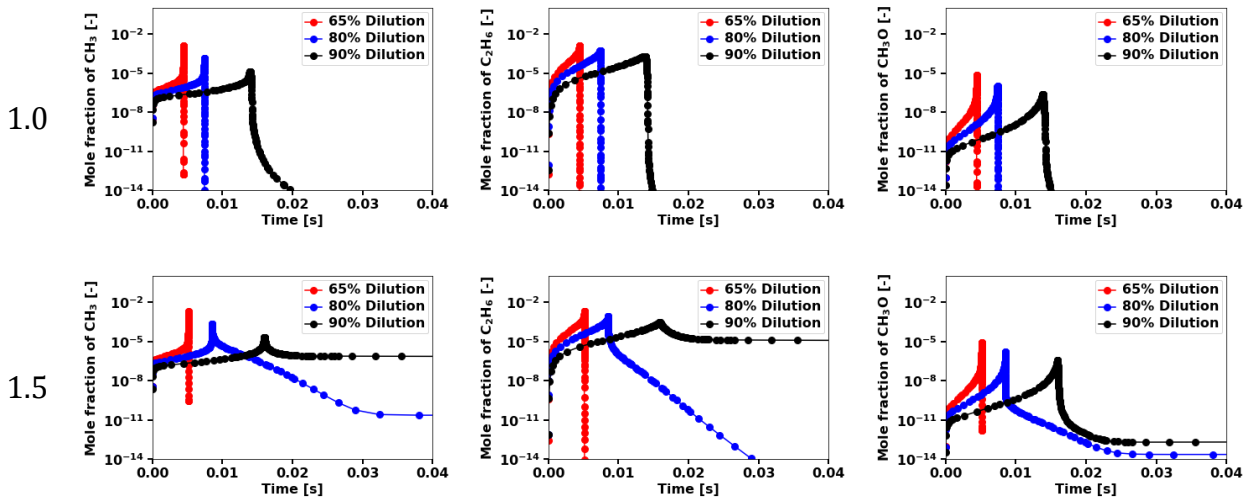

Figure 63. Important intermediate species for different sCO_2 dilution and equivalence ratios.

equivalence ratio equal to 1.5 also exhibits the hindering effect. Formation of C_2H_6 decays after ignition which in turn delays CH_3 oxidation. However, at lower equivalence ratios, only the higher % dilution shows the slow propagation as evidenced by slow oxidation of CH_3 post ignition.

In summary, higher equivalence ratios and higher dilution rates result in slower oxidation of CH_3 due to the hindering pathways discussed above that can cause incomplete combustion and higher CO formation. Figure 64a shows that there is a region between 75% and 90% and an equivalence ratio between 0.5-1 that exhibits the lowest CO production. Figure 20b shows that IDT calculated based on the same criteria discussed above is very sensitive to the percentage dilution while it does not vary significantly with the equivalence ratio. IDT is an order of magnitude higher with 90% dilution compared to 65%. Figure 64c shows the IDT contours for the entire vector space of % dilutions and equivalence ratios. It can be noted that IDT increases beyond the 80% CO_2 dilution and is lower at smaller equivalence ratios. Therefore, the 0D analysis presented here shows that an optimum combustion condition with low CO production and low IDT can be achieved at lower equivalence ratios (0.5-0.65) with intermediate dilution (75-90%) based on IDT and CO mole fraction results.

3.4 Summary and Conclusions

In this study, we introduced a new adaptive GPS approach and a new supervised learning aided GPS (SL-GPS) method trained on the developed adaptive GPS approach and validated both methods against 0D simulation of methane and ethanol combustion using detailed mechanism and classical GPS methods. Validations are performed for methane combustion with the GRI 3.0 mechanism at temperatures from 1310 to 1890 K, pressures from 1.1 to 99 atm, and equivalence ratios from 0.6 to 1.4, and ethanol combustion with the PCRL-Mech1 mechanism at temperatures

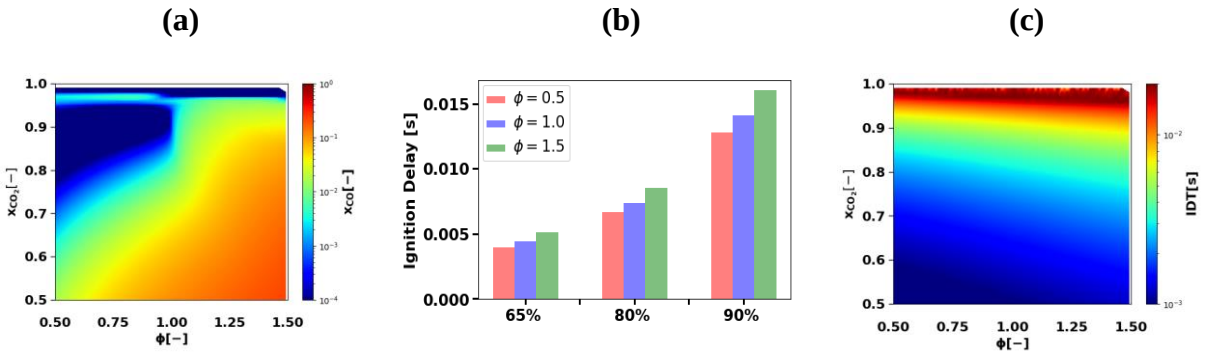

Figure 64 (a) CO mole fraction across dilution rates and equivalence ratios for different CO_2 mole fraction; (b) IDT vs. different dilution rates and equivalence ratios; (c) IDT across dilution rates and equivalence ratios and CO_2 mole fraction.

from 1110 to 1390 K, pressures from 1.1 to 99 atm, and equivalence ratios from 0.6 to 1.4. The main conclusions from this work are summarized below:

- Adaptive GPS method predicted the results of detailed mechanism (temperature, HHR, and species mole fractions) with greater accuracy and generally fewer species and reactions than the classic GPS mechanisms. This is true of all temperature, pressure, and equivalence ratios tested, and for both methane and ethanol combustion. The enhanced performance was particularly noticeable in the high temperature/pressure cases for

methane combustion.

- The only major exception to the adaptive GPS algorithm using fewer species and reactions was limited spikes in adaptive species and reaction counts, which may be indicative of the adaptive algorithm's ability to distinguish between periods of high reactivity that warrant a greater number of reactions in the reduced mechanism and periods of low reactivity that do not require all those reactions.
- The enhanced performance of the adaptive GPS algorithm over the classic GPS mechanism is attributable to the former's ability to exclude reactions once they become irrelevant, such as the CH_3 to CO conversion pathways in methane combustion after ignition occurs, whereas the classic GPS considers such reactions throughout the entire simulation period.
- Since adaptive GPS requires a new detailed simulation and a call of a full reduction algorithm at each GPS interval it is not computationally feasible in reacting flow simulations. To overcome this limitation, a supervised learning ANN trained using the adaptive GPS is proposed in this study. This SL-GPS method gives the benefits of the reduced mechanisms of adaptive GPS with much lower computational costs.
- SL-GPS mechanisms performed with similar accuracy and similar species and reaction counts to the adaptive GPS mechanisms and likewise outperformed the classic GPS, despite involving far less computational cost compared to both classic and adaptive GPS.
- An ideal architecture was identified for the SL-GPS method for both the mechanisms. In general, relatively simpler architecture tend to perform better due to the nature of the problem. However, an increase in complexity is required as the mechanisms involve more species and reactions.

- Validation of ignition delay time demonstrates the improved accuracy of the SL-GPS method over the classic-GPS and DRGEP. The main highlight of SL-GPS method was the improved computational time and accuracy in comparison to the existing methods. For ethanol combustion, this extended to cases outside the training conditions.
- Successful validation in 0D simulations proves the high potentials of the proposed SL-GPS to improve simulation capabilities for 2D and 3D turbulent reactive flow simulations. It is noted that the number of GPS execution can increase to enhance the accuracy and lower the number of species included in the reduced mechanism. As we are only limited by the chemical timescale, we can execute GPS at finer timescales than the current order of refinement which is 10 times the chemical timescale. Therefore, the scope of improvement of the SL-GPS method is improved in both accuracy and computational times in higher order simulations.

4. SCO_2 OXY-COMBUSTION USING FINITE RATE CHEMISTRY

4.1 Introduction

4.1.1 Application of the SL-GPS Method to Higher-Order Simulations

As shown in Figure 44, the SL-GPS method is capable of predicting a larger number of species just before ignition, compared to the classic GPS method. However, it generally uses a smaller number of species. Although larger numbers of species do not pose a problem in 0D simulations, it becomes computationally expensive to simulate reactions with a large number of species in 1D/2D/3D simulations. This is because the governing equations of the combustion process need to be solved for each species, and the computational cost increases exponentially with the number of species. Therefore, methods such as SL-GPS that can predict combustion with fewer species without compromising accuracy are desirable for large-scale simulations.

We propose two approaches for reducing the maximum number of species predicted by the SL-GPS algorithm near ignition time: (1) set a strict upper bound to the number of maximum species through the GPS accuracy parameter (i.e., α.) By increasing α, fewer species will be included in the reduced mechanism while the accuracy of the SL-GPS is reduced just for a very short duration. This approach will limit the maximum number of species to that predicted by the classic GPS algorithm; (2) increase the number of GPS executions during certain time intervals where the number of species in the reduced mechanism surpasses that predicted by the classic GPS algorithm. It is noted that the number of GPS executions can increase to enhance the accuracy and lower the number of species included in the reduced mechanism. Since we are only limited by the chemical timescale, we can execute GPS at finer timescales than the current order of refinement which is 10 times the chemical timescale. Therefore, the scope of improvement of the SL-GPS method is improved in both accuracy and computational times.

In summary, from the start of simulation until the SL-GPS reaches the maximum species limit (i.e., close to the ignition time), only the species predicted by the SL-GPS at a particular time during combustion, which is smaller than those predicted by classic GPS method, will be transported. This approach will reduce the computational time required for solving additional diffusive and convective terms. In addition, the time required to setup and evaluate the Jacobian matrix of reacting species is based on the number of source terms that need to be solved. This step is dependent on the total number of species participating in the entire combustion while all non-participating species are considered as 3rd body. Since SL-GPS mainly predicts smaller number of species in the reduced mechanism, we expect a much lower computational cost using SL-GPS. The use of SL-GPS in 2D and 3D reacting flow simulations is investigated in the following sections.

4.1.2 Extending the code for real gas effects

For running full-scale 3D CFD ILES of SWRI combustor, apart from the necessary reduction mentioned above the OpenFOAM solver needs to be expanded for the real-gas effects. As discussed in the case of DNS, the OpenFOAM code has also been augmented with Peng-Robinson EOS, mixing and transport rules. The same set of models are used for ILES as were used for the DNS to maintain consistency. These models initially implemented in OpenFOAM by Nguyen et al.[169] has been used in this study and fortified with the chemistry reduction tools to simulate oxy-combustion by leveraging the SWRI combustor.

4.2 Computational Methods

4.2.1 Tabulation of Dynamic Adaptive Chemistry (TDAC)

The state-of-the-art algorithm for reduction of computational expense in solving the reactive simulation is called the Tabulation of Dynamic Adaptive Chemistry [170]. This method integrates two commonly used approaches to reduce computational time namely: tabulation and reduction. The tabulation technique used in this method is In-Situ Adaptive Tabulation (ISAT) [153] while the reduction technique used is the Dynamic Adaptive Chemistry (DAC) [171]. The ISAT tabulates an existing chemical mapping with new ODE solutions corresponding to new compositions dynamically as the CFD simulation proceeds. The DAC is an on-the-fly chemistry reduction tool that is an extension to the DRGEP method. Another feature of DAC is considering the active species only and passing them to the ODE solver, thereby creating a compact Jacobian matrix without the inactive (third body) species. The TDAC method as the name suggests is an integration of ISAT as the tabulation technique and DAC as the reduction technique. This integration further enhances the computational speed while maintaining the required accuracy.

4.2.2 Tabulated Supervised Learning – Global Pathway Selection (TSL-GPS)

A new reduction library is developed as the Tabulated Supervised Learning – Global Pathway Selection (TSL-GPS). The schematic for TSL-GPS is shown in Figure 65. The dashed arrow going from ISAT to CFD block in the figure represents the retrieval of existing mapping from the ISAT table. If the solver identifies a new composition of mass fraction, the addition/growth pathway is triggered as highlighted by the blue arrows. The SL-GPS then identifies the active species to be solved for and only the active species and their relevant reactions are passed to the ODE solver. The new mapping is computed and passed back to the ISAT where the existing table is extended by adding the new mapping. By implementing this approach, the

algorithm can efficiently retrieve tabulated values for similar compositions without the need for time-consuming iterations. This optimization significantly improves computational speed and reduces processing time.

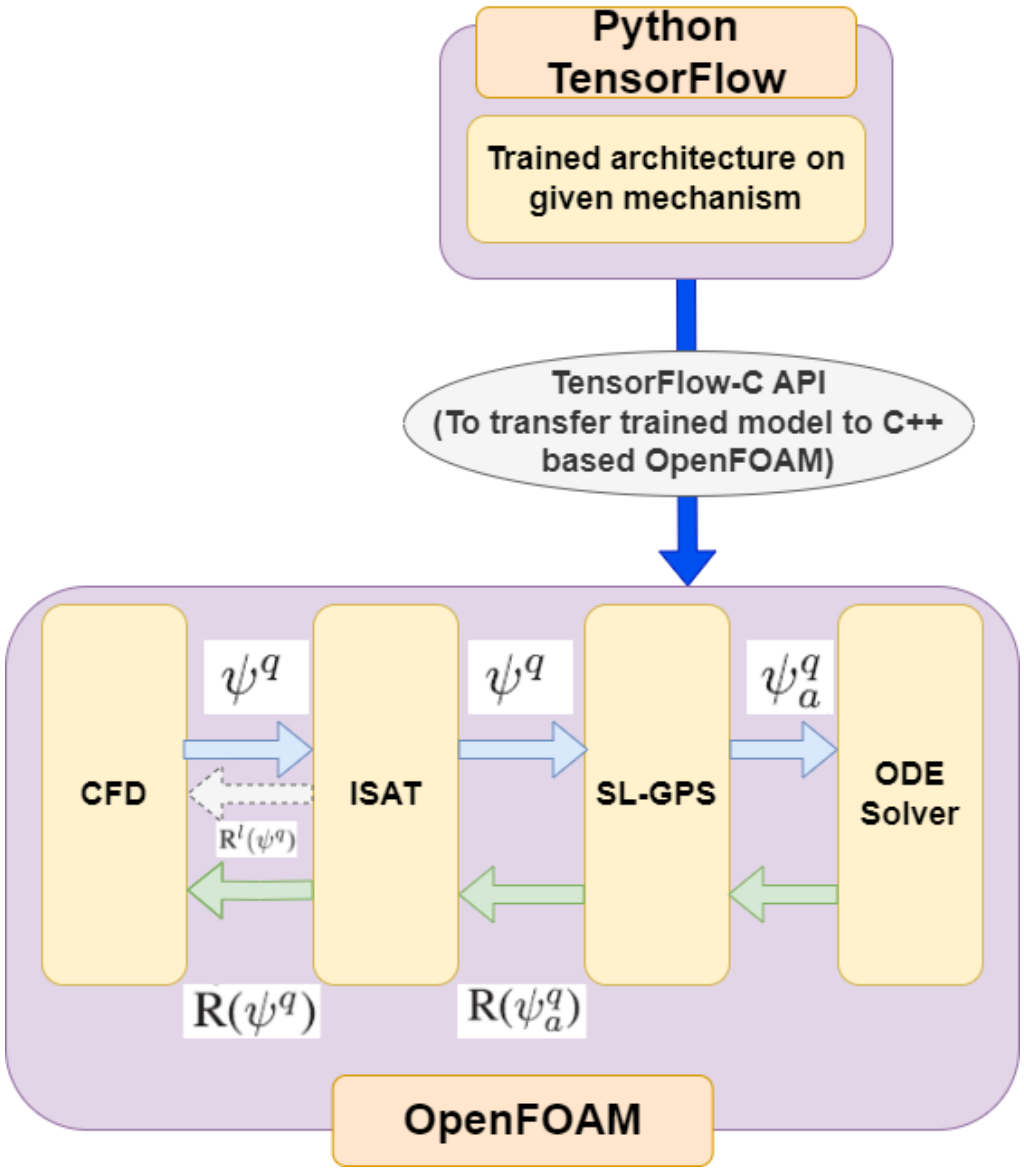

Figure 65. Schematic of the TSL-GPS method and its implementation in OpenFOAM.

4.2.3 Real gas Implicit Large Eddy Simulation (ILES)

Implicit Large Eddy Simulation (ILES) is a simulation approach employed in computational fluid dynamics (CFD) to model turbulent flows. It integrates elements from both Large Eddy Simulation (LES) and implicit numerical methods. In LES, turbulent structures at large scales are explicitly resolved, while smaller scales are represented using subgrid-scale models. This method captures the prominent turbulent features while reducing computational costs compared to simulating all scales explicitly. In ILES, the numerical scheme utilized to solve the governing equations of fluid flow incorporates implicit time integration. This allows for larger time steps, resulting in more efficient computations. By using an implicit approach, ILES focuses on capturing the larger, more dominant turbulent structures while implicitly representing the effects of smaller scales. While the smaller scales are not directly resolved, their influence is indirectly incorporated through the implicit numerical scheme, providing stability and accuracy to the simulation. The ILES code used for simulation of sCO_2 oxy-combustion is originally developed by Nguyen et al. [169] to enable modeling real-gas behavior in OpenFOAM v6. The base code is further expanded in this study to enable chemistry reduction techniques such as TDAC and the TSL-GPS.

4.2.4 Governing Equations

The ILES solver in OpenFOAM solves the unsteady Navier-Stokes equations coupled with additional equations for modeling combustion. These equations describe the conservation of mass, momentum, energy, and species transport. For incompressible, reacting flows, the governing equations are as follows:

Conservation of Mass

The continuity equation is as follows:

$$\frac{\partial \rho}{\partial t} + \nabla \cdot (\rho \mathbf{v}) = 0$$

Conservation of Momentum

The momentum equation is expressed as:

$$\frac{\partial (\rho \mathbf{v})}{\partial t} + \nabla \cdot (\rho \mathbf{v}\mathbf{v}) - \nabla \cdot \boldsymbol{\tau} = -\nabla p$$

where $\boldsymbol{\tau}$ represents the viscous stress tensor defined by $\boldsymbol{\tau} = -\frac{2}{3}\mu(\nabla . \boldsymbol{v})\boldsymbol{I} + \mu[\nabla \boldsymbol{v} + (\nabla \boldsymbol{v})^{\boldsymbol{T}}]$.

Conservation of Energy:

The energy equation is modified to include the effects of combustion:

$$\frac{\partial \left(\rho h_s\right)}{\partial t} + \nabla \cdot \left(\rho h_s \mathbf{v}\right) + \frac{\partial (\rho K)}{\partial t} + \nabla \cdot (\rho K \mathbf{v}) - \frac{\partial p}{\partial t} - \nabla \cdot \left(\frac{\lambda}{c_p} \nabla h_s\right)$$
$$= -\nabla \cdot \left(\sum_{k=1}^{N} \frac{\lambda}{\boldsymbol{C}_p} h_{s,k} \nabla Y_k\right) - \nabla \cdot \left(\rho \sum_{k=1}^{N} h_{s,k} Y_k \mathbf{V}_{\boldsymbol{k}}\right) + \dot{Q}_r$$

Where h_s is sensible enthalpy, K is kinematic energy and $\dot{Q}_r$ represents the heat release due to combustion.

Species Transport

Additional transport equations are solved for each species involved in the combustion process. These equations account for the transport and reaction of species coupled with the other governing equations.

$$\frac{\partial \left(\rho Y_i\right)}{\partial t} + \nabla \cdot \left(\rho \mathbf{v} Y_i\right) + \nabla \cdot \left(\rho Y_i \mathbf{V}_{\boldsymbol{i}}\right) = \dot{w}_i$$

where Y_i, $\mathbf{V}_{\boldsymbol{i}}$, $h_{s,i}$, $\dot{w}_i$ are mass fraction, diffusion velocity vector, the individual sensible enthalpy and the net reaction rate of the i[th] species. λ is the thermal conductivity, c_p is the specific heat

capacity, h_s is the sensible enthalpy, K is the kinematic energy, and $\dot{Q}_r$ is the net heat of combustion.

4.2.5 Numerical Discretization

The ILES solver in OpenFOAM employs a finite-volume discretization scheme to numerically solve the governing equations. The computational domain is divided into a mesh consisting of cells, and the equations are integrated over these control volumes.

a. Spatial Discretization

The spatial derivatives in the governing equations, including those for species transport, are approximated using a cell-centered approach. The variables are defined at the center of each cell, and the discretized form of the equations results in a system of algebraic equations for each cell.

b. Temporal Discretization

The ILES solver utilizes an implicit time integration scheme to discretize the unsteady terms in the governing equations including the reactions. The time derivatives are approximated implicitly, resulting in a system of algebraic equations solved iteratively.

4.2.6 Sub-models

Subgrid-Scale Modeling

Similarly, the subgrid-scale turbulence modeling is achieved through the inherent numerical dissipation of the discretization scheme, without requiring explicit turbulence models. The unresolved turbulent fluctuations are damped by the implicit treatment of the equations, effectively filtering out small-scale turbulence. Overall, ILES strikes a balance between accuracy and computational efficiency by capturing the dominant turbulent features explicitly while indirectly incorporating the effects of smaller scales through the implicit numerical scheme.

Combustion Modeling

The ILES solver enables the modeling of combustion through additional terms and equations including the calculation of heat release due to combustion ($\dot{Q}_r$) in the energy equation and the transport equations for species involved in the combustion process. Different combustion models, such as finite-rate chemistry or flamelet models, may have different formulations for these terms. By solving the species transport equations along with the other governing equations, the ILES solver in OpenFOAM allows for a comprehensive simulation of combustion processes, taking into account the transport and reaction of multiple species involved in the reaction mechanism.

In summary, the ILES solver in OpenFOAM solves the unsteady Navier-Stokes equations coupled with additional equations for combustion modeling. It utilizes a finite volume discretization scheme, implicit time integration, and inherent numerical dissipation to capture large-scale turbulent structures while effectively filtering out unresolved turbulence. The solver also accounts for the transport and reaction of species involved in the combustion process.

Reduction method

The base code referred to as r*ealFluidReactingFoam* solver has been augmented with reduction models to enable full-scale ILES simulation of the realistic SWRI combustor. The TDAC method was integrated from existing OpenFOAM libraries. For the TSL-GPS, the tabulation follows the TDAC method, i.e., In-Situ Adaptive Tabulation (ISAT) while the reduction method is the SL-GPS where the trained models from TensorFlow is transferred to OpenFOAM by using the TensorFlow C API as discussed before. The two methods, namely the TDAC and TSL-GPS are compared for accuracy and computational effectiveness in the *a-posteriori* validation of the TSL-GPS method.

4.3 Results and Discussion

4.3.1 TSL-GPS for Sandia Flame D

The SL-GPS method is validated *a-posteriori* after implementing the TensorFlow-C API in OpenFOAM v6 to transfer the trained neural network. A new reduction library called TSL-GPS has been created as discussed earlier. The Sandia Flame D configuration is shown in Figure 66. The mesh and geometry used for simulating the Sandia Flame D adopted from Morev et al. [172] is shown in Figure 67. The chemical mechanism used in Sandia Flame D and subsequent SWRI case is GRI3.0[173] which consists of 53 species and 353 reactions.

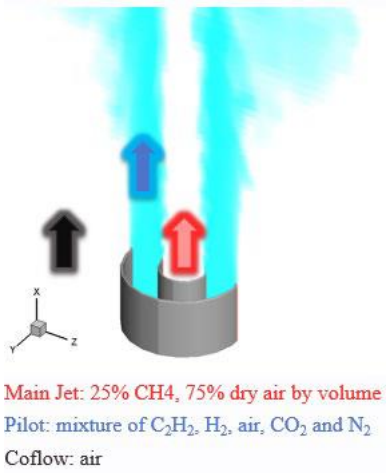

Figure 66. Sandia Flame D configuration. Reprinted from [174]

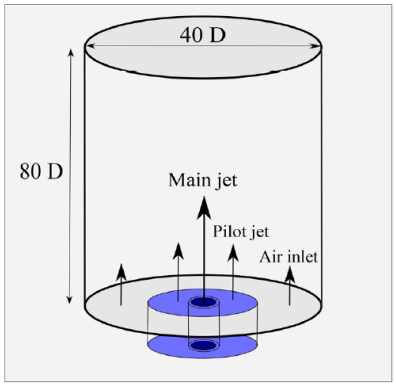

Figure 67. Sandia Flame D geometry. Reprinted from [172]

Details of the mesh can be found in [172]. Qualitative results in the form of instantaneous temperature contour, as shown in Figure 68, indicate that the TDAC method predicts the flame to be located further downstream in comparison to the SL-GPS method. Similar observations can be seen from the instantaneous mass fraction contour plots for CO_2 and H_2O shown in Figure 69.

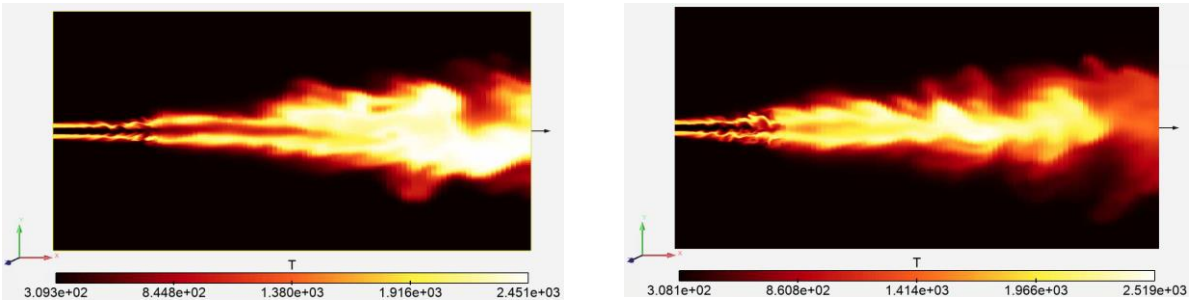

(a) (b)

Figure 68. Qualitative comparison of temperature contours using (a) TDAC and (b) SL-GPS.

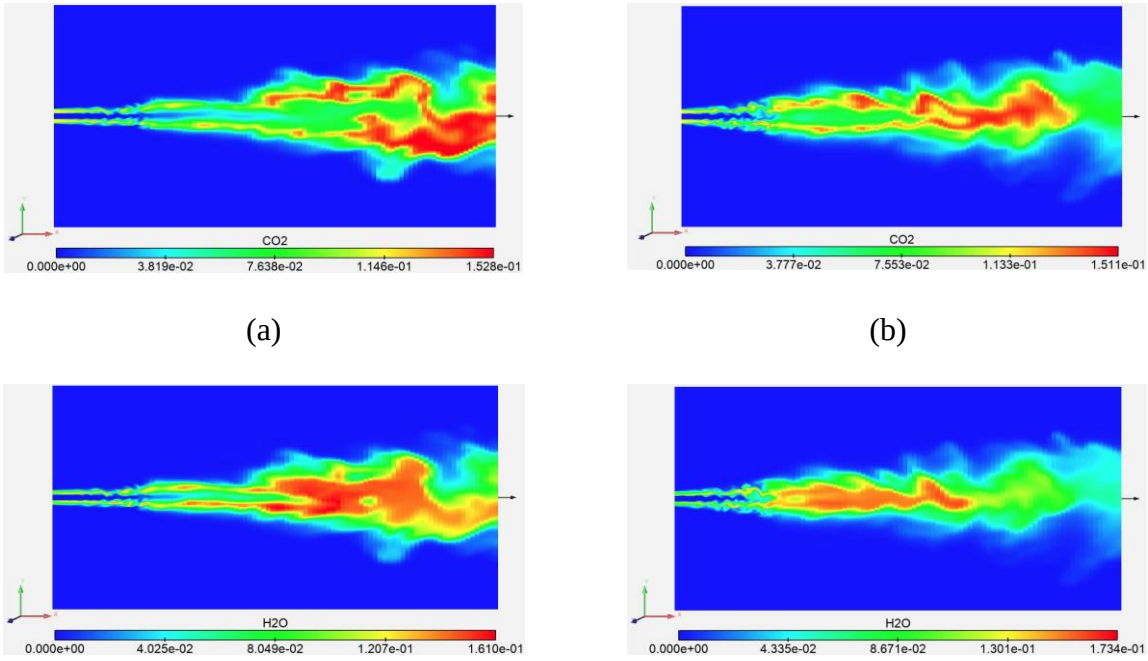

(a) (b)

(c) (d)

Figure 69. Qualitative comparison of CO_2 mass fraction contours using (a) TDAC; (b) SL-GPS and H_2O mass fraction contours (c) TDAC (d) SL-GPS

Quantitavive comparison of the centerline temperature profile among TDAC, SL-GPS, and experiments shown in Figure 70 indicates the higher acuracy of the TSL-GPS method in capturing the flame location. The peak temperature is more accurately captured around *x/d* = 40 location using the TSL-GPS method. Towards the end of the domain, the temperature prediction is improved by approximately 30% using the TSL-GPS method over the TDAC method. However, for the near-inlet region, TDAC is able to better capture the temperature profile. The overall trend is clearly better captured using the TSL-GPS. The main reason of the overall high accuracy of TSL-GPS is the due to the higher accuracy of the chemistry reduction algorithm of SL-GPS to pick species based on progress of combustion. While the DAC scheme works on top of DRGEP to remove third body species from calculation, the SL-GPS method dynamically finds only the important species for a particular composition and this unique indentification renders the scheme more effective.

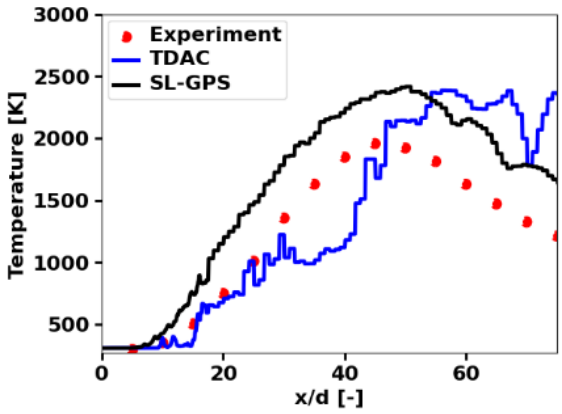

Figure 70. Centerline temperature comparison for Sandia Flame D; data averaged for 150ms after a simulation time of 100 ms as the flame reaches a steady state.

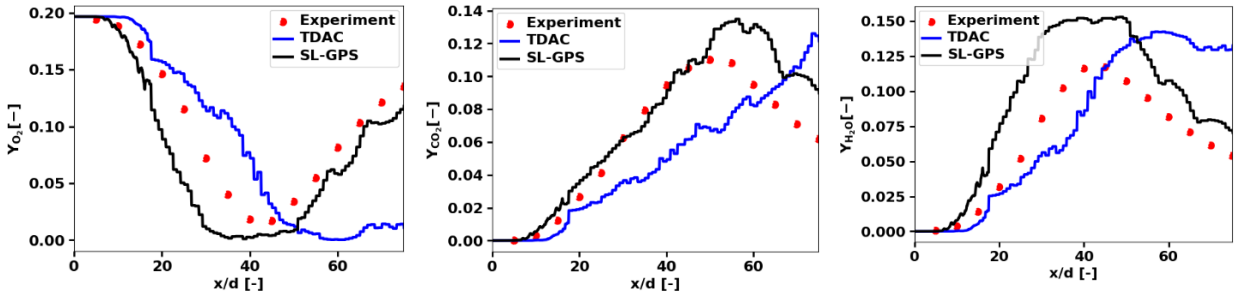

(a) (b) (c)

Figure 71. Centerline mass fraction comparison for Sandia Flame D (a) O_2 mass fraction (b) CO_2 mass fraction (c) H_2O mass fraction; data averaged for 150 ms after a simulation time of 100 ms when the flame reaches steady state.

Major combustion products such as CO_2 and H_2O are better predicted by the TSL-GPS method as shown in Figure 71b and c. The improvement in predicting the mass fraction of combustion species using TSL-GPS over the TDAC method varies from 20%-300%. The improvement in predictions further increases at further locations with respect to the inlet region where TDAC method deviates drastically from the experimental results. The TSL-GPS method offers not only high accuracy, but also computational efficiency compared to the TDAC method. It provides a balance between accuracy and computational cost, making it a favorable choice for various applications. As shown in Table 7, the TSL-GPS method requires 6% less average computational time for 1 ms of simulation compared to the TDAC method.

Table 7. Comparison of average computational time (in seconds) per millisecond of simulation. 6% improvement in computational time for TSL-GPS method over TDAC.

Method	Average Computation Time (in seconds) per ms
TDAC	1133
SL-GPS	1068

4.3.2 TSL-GPS for SWRI

The SWRI geometry used for the 3D ILES is shown in Figure 72. The mesh details are listed in Table 8.

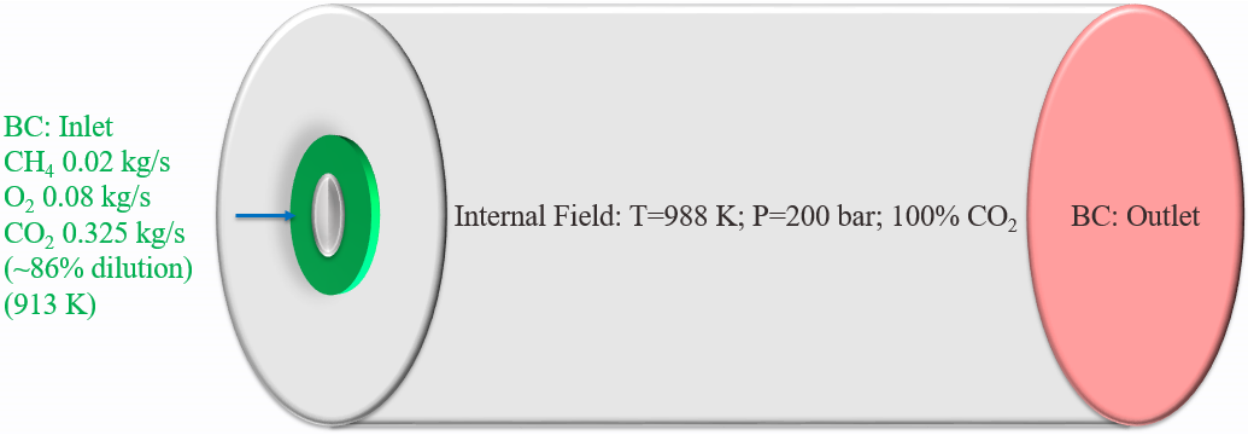

Figure 72. Schematic of the 3D geometry of SWRI combustor for ILES. Green region is the inlet with the entire grey region showing combustor walls. The red region has the outlet BC.

Table 8. Mesh parameters for 3D CFD of SWRI combustor

Parameter	Value
Maximum skewness	0.73
Mesh count	2,115,052
Minimum cell size	0.8mm

The TSL-GPS method is integrated with the real-gas effects and ILES is carried out for the SWRI combustor described above. A comparison is made for the prediction of temperature between two cases namely: detailed chemistry and TSL-GPS reduced chemistry. Figure 73 demonstrates a remarkable agreement between the TSL-GPS method and the detailed chemistry prediction of the radial temperature profile, with an error percentage of only 20%. This finding is particularly noteworthy considering that the TSL-GPS simulation required nearly three times less

computational time compared to the detailed case, which took approximately 336 hours to run on 140 processors.

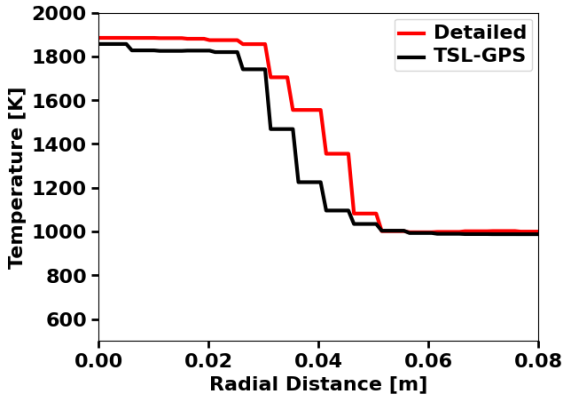

Figure 73. Radial temperature profile comparison for ILES simulations at 100 mm axial distance from injection

Temperature contour plots for a refined mesh TSL-GPS ILES is shown in Figure 74 (left column) highlighting the ignition behavior. Figure 74 clearly illustrates the ignition process initiates at t = 0.005 s near the periphery of the incoming stream, where a vortex is formed. This observation aligns with the understanding that ignition typically takes place in regions characterized by high turbulence dissipation. Subsequently, the flame expands inward toward the central axis while simultaneously spreading radially outward from the injection point. As the flame develops, the flame edge vortex is large enough to interact with the side walls making it evident that heat transfer for wall modeling is important for such an application. For simplicity wall heat transfer model is not included in this study. Figure 74 (right column)**Error! Reference source not found.** captures the subsequent stage of complete flame development. As the flame interacts with the wall, the vortex undergoes a collapse, giving rise to a highly turbulent region depicted in Figure 74 (right column) at t=0.025s and t=0.03s. Within this turbulent environment, the flame propagates predominantly in the axial direction, accompanied by a concentrated release of heat. This is evident

from the presence of elevated temperatures. Notably, the high heat release region remains confined to the core of the flame.

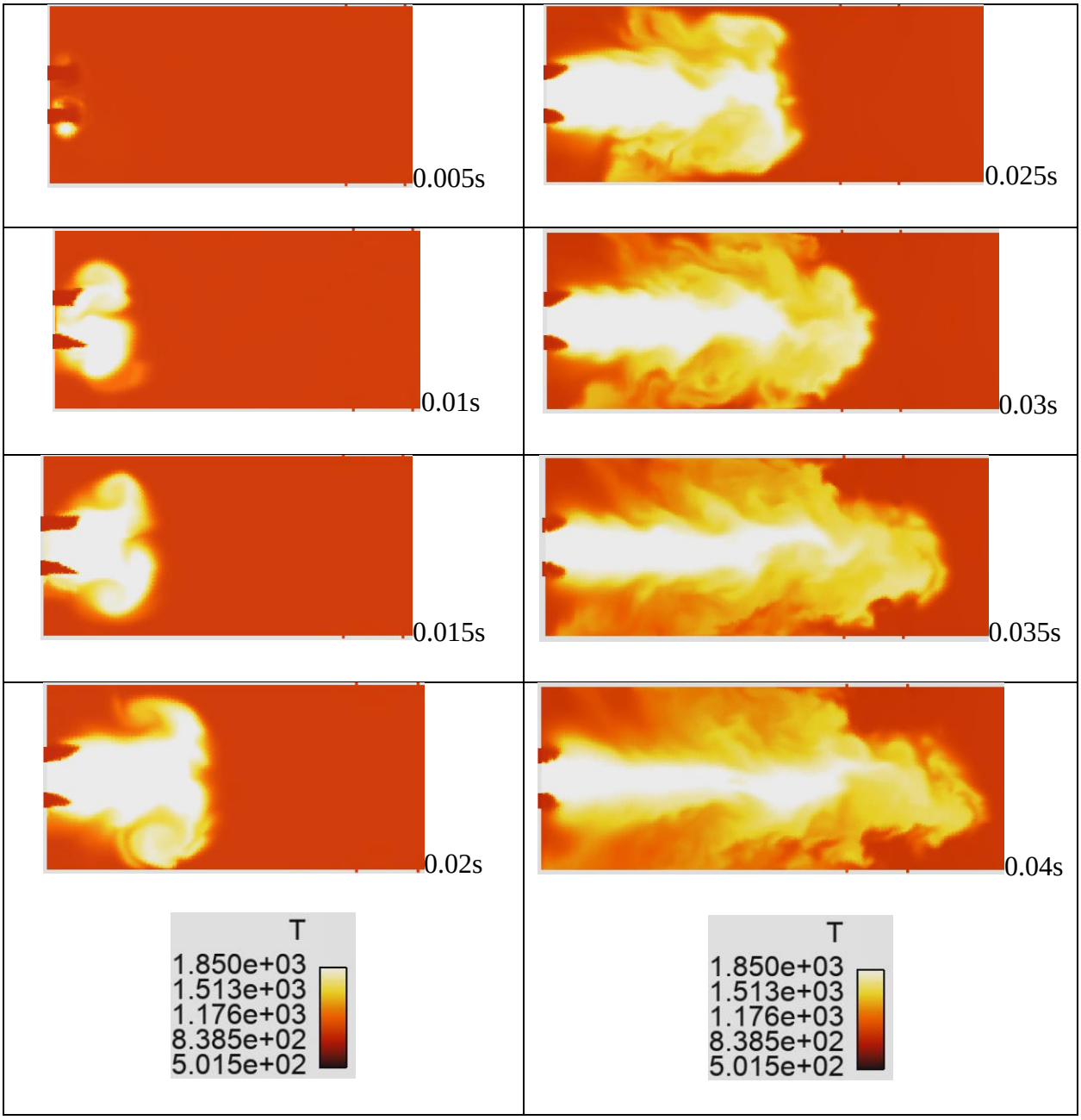

Figure 74. Evolution of flame: Ignition behavior (left column) and full flame development (right column). The entire combustor is shown which is 0.7 m long and 0.2 m diameter.

To further understand the ignition behavior and flame anchoring, the temporal radial profiles of important combustion species near the injection point (i.e., 20 mm from the injection

point) are plotted for different species in Figure 75, Figure 76 and Figure 77. OH and CO mass fraction profiles are plotted in Figure 75. The OH mass fraction exhibits a distinct peak, reaching its maximum value at an intermediate time of 0.02 s. This behavior shows a significant increase in combustion intensity, followed by a stabilization phase at a lower level. This trend is also reflected in the radial profiles of CO mass fraction depicted in Figure 75 (right). Notably, the CO mass fraction demonstrates the presence of a secondary ignition region, indicated by a second peak located radially outward. This observation suggests that the flame is anchored throughout the radial extent of the co-axial injection region.

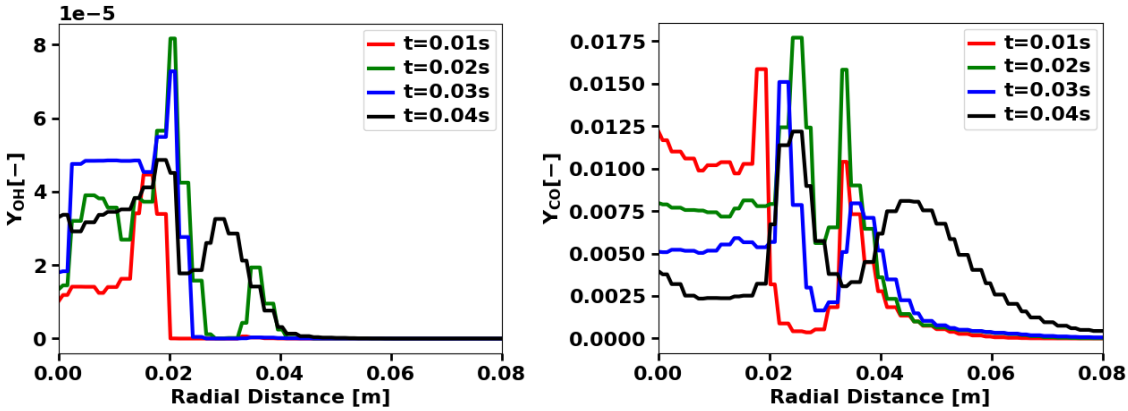

Figure 75. Temporal evolution of radial profiles of mass fractions of intermediate species OH (left) and CO (right). Axial distance: 20 mm from the injection point.

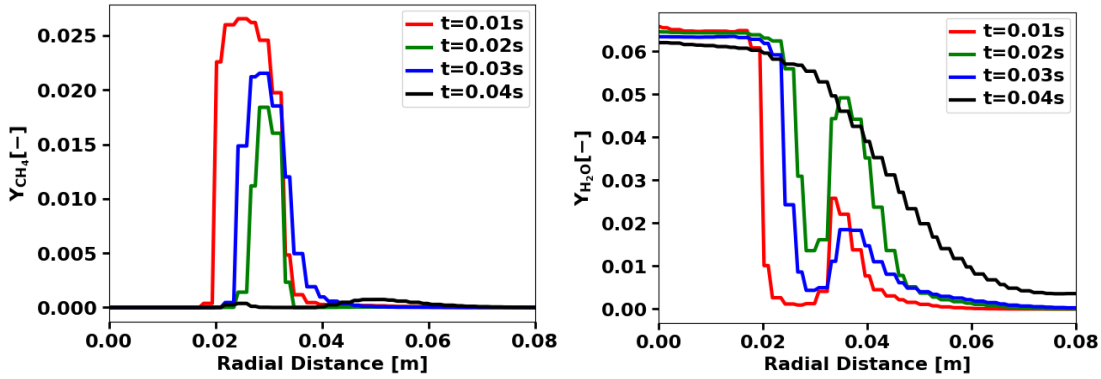

Figure 76. Temporal evolution of radial profiles of mass fractions of major species CH_4 (left) and H_2O (right). Axial distance: 20 mm from the injection point.

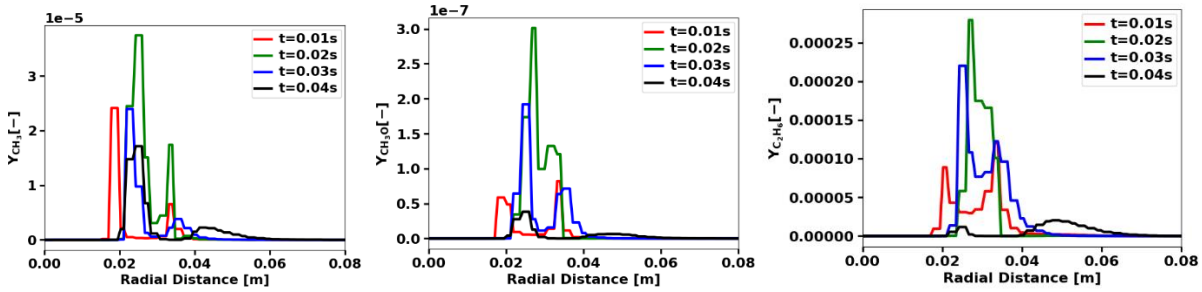

Figure 77. Temporal evolution of radial profiles of mass fractions of intermediate species CH_3 (left), CH_3O (middle) and C_2H_6 (right). Axial distance: 20 mm from the injection point.

A noticeable shift in the ignition location is apparent from the major species profile presented in Figure 76. Initially, the flame was anchored across the entire radial width of the injection region. However, at t= 0.04s, the flame position has shifted, becoming more centered and closer to the injection point. This shift is evident in the mass fraction profiles of CH_4 and H_2O. Additionally, the behavior of intermediate species such as CH_3, C_2H_6, and CH_3O, as depicted in Figure 77, further emphasizes this observed flame displacement.

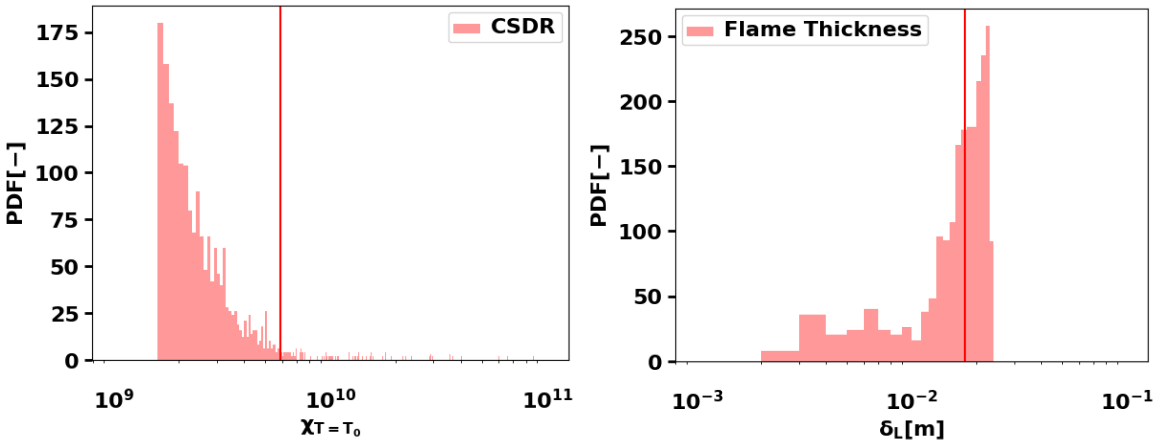

Figure 78. PDF of conditional scalar dissipation rate (CSDR) (left) and flame edge thickness (right) for ILES real gas simulation of the SWRI combustor.

From the CSDR and flame thickness PDF plots in Figure 78, at a time when the flame stabilizes the mean thickness of the flame is around 0.02 m. Figure 79 and Figure 80 shows the iso-surface of temperature (1800 K) colored by CO mass fraction and OH mass fraction, respectively. The formation of the ignition kernel is prominently observed near the injection region, specifically localized at the outer edge of the injection domain. This region is characterized by high turbulence levels and a notable concentration of CO mass fraction. As the flame propagates, it undergoes expansion in both the radial and axial directions. Upon reaching full development, the flame becomes anchored closer to the injector, with the incoming mixture playing a significant role in stabilizing its position. In addition to the significant production of CO and OH near the injection region, there is also noticeable CO and OH production downstream of the flame. However, the same trend is not observed for other intermediate species of interest. As shown in Figure 81 and Figure 82, the production of CH_3 and C_2H_6 is limited to a small region in close proximity to the injection point and around the initial ignition location.

t=0.005s

t=0.015s

t=0.035s

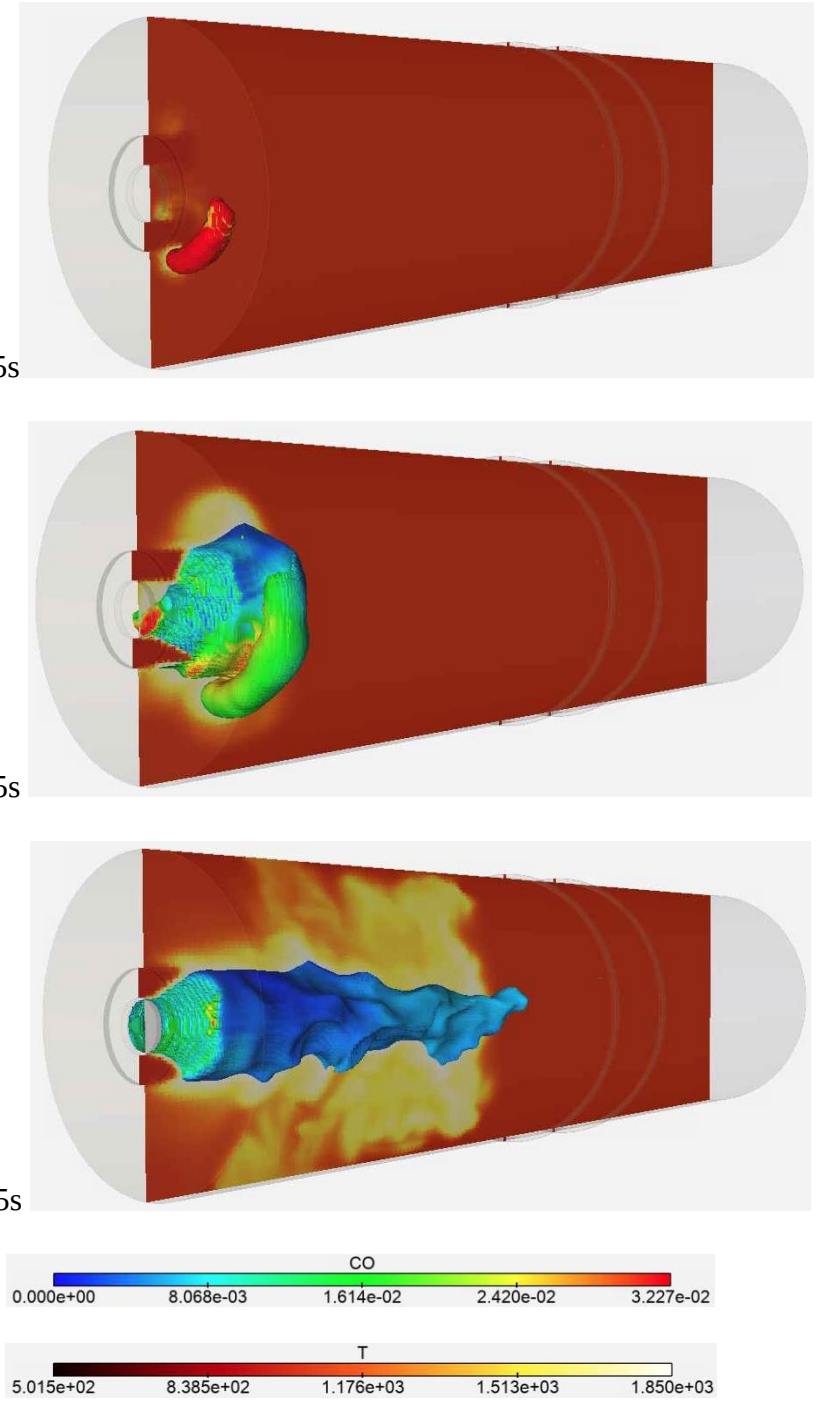

Figure 79. Temporal evolution of iso-surface of temperature (1800K) colored by CO mass fraction.

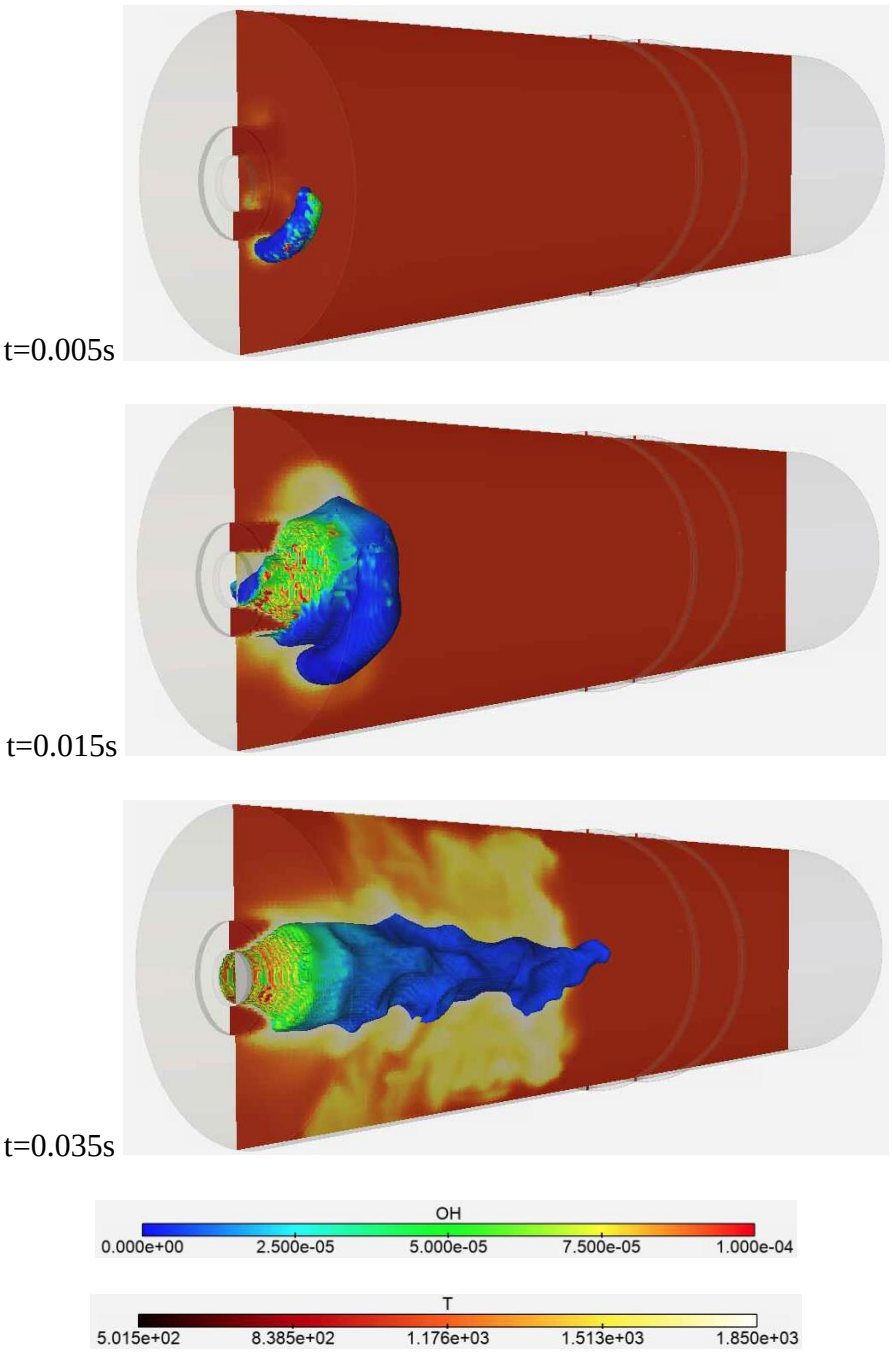

Figure 80. Temporal evolution of iso-surface of temperature (1800 K) colored by OH mass fraction.

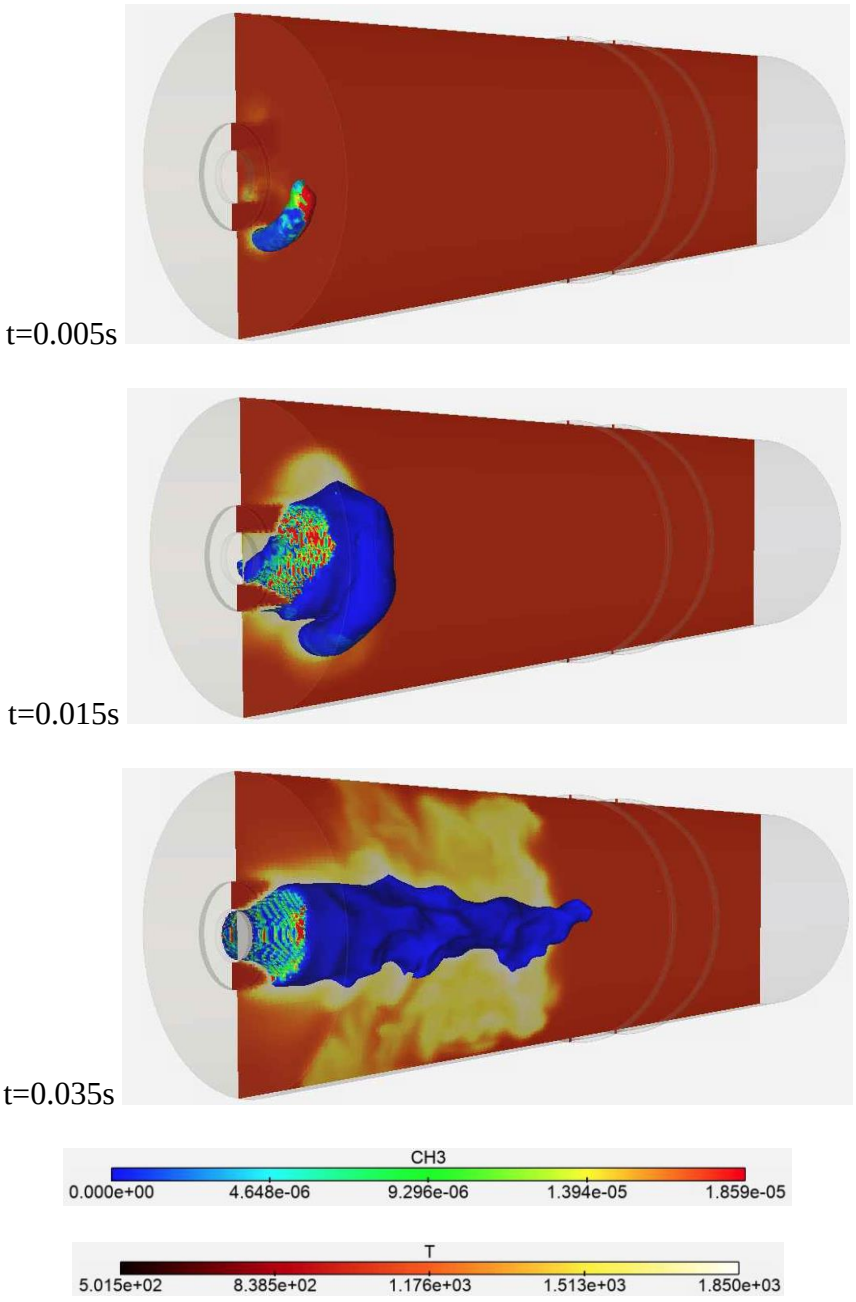

Figure 81. Temporal evolution of iso-surface of temperature (1800 K) colored by CH_3 mass fraction.

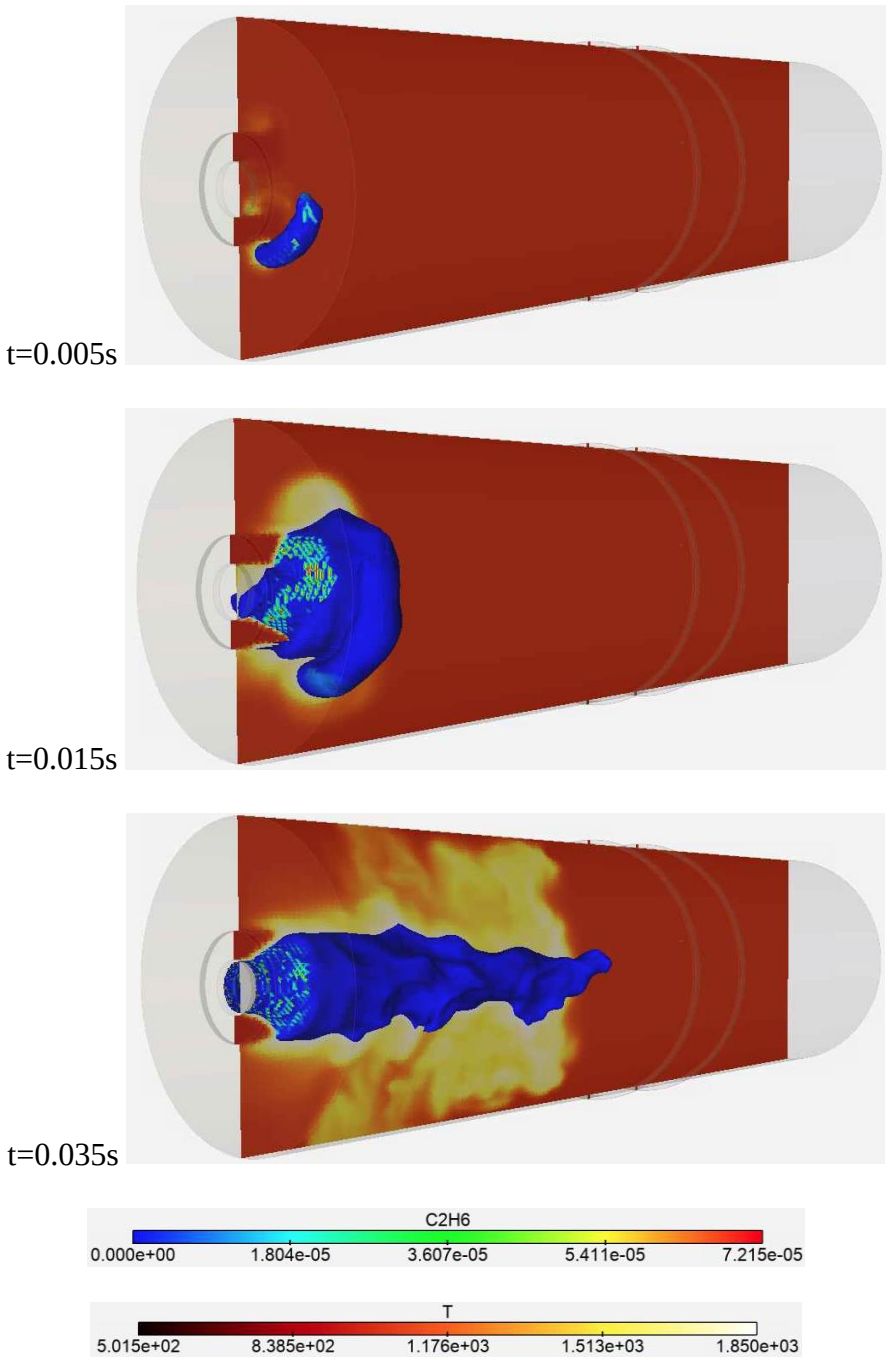

Figure 82. Temporal evolution of iso-surface of temperature (1800K) colored by C_2H_6 mass fraction.

This highlights the importance of these species in the overall flame structure and formation, as they play a crucial role in flame stability. The formation of C_2H_6 introduces a quenching effect, which is counterbalanced by the formation of species involved in branching reactions. This can be

observed by the localized formation of CH_3 and C_2H_6 species near the injector. Excessive formation of C_2H_6 has the potential to induce a shift in flame location or even result in complete flame quenching within the combustor. Further analysis is necessary to comprehensively understand the effects of dilution on C_2H_6 formation and the quenching-re-ignition phenomenon in sCO2 oxy-combustion flames.

4.4 Summary and Conclusions

A-posteriori validation of the SL-GPS method integrated with the ISAT method (named TSL-GPS) on the Sandia Flame D shows better performance of the TSL-GPS method over the existing state of the art method – TDAC. The TSL-GPS method is able to accurately capture the flame location as indicated by the peak temperature location metric. Overall, the centerline temperature profile along with the mass fraction profiles shows an improvement of accuracy in the range of 20-30%, with higher improvement downstream of the flow. Apart from having higher accuracy the TSL-GPS method tool 6% less average computational time for 1 ms of simulation as compared to the TDAC method.

The TSL-GPS method is successfully integrated with the real gas effects to run ILES of SWRI combustor. The TSL-GPS predicts the temperature within 20% error margin as compared to the detailed chemistry case. Qualitative analysis of the flame reveals unique behavior at the time of ignition. The flame ignites at some distance from the injector and at the periphery of the vortex generated by the incoming stream. The flame evolves radially outward until it reaches the combustor wall at which point it collapses resulting in rapid axial expansion. This expansion is accompanied by shrinking of maximum heat release region to the flame core.

A detailed analysis of intermediate and major species near the injector highlights important ignition and flame evolution behavior. The flame ignites in a region of high turbulence near the

edge of the outer wall of the injector. The flame then moves both radially and axially and is anchored around the entire width of the injector. The flame stabilizes closer to the injector and with smaller radial span. The intermediate species such as OH, CO although produced mainly near the injector region can be seen throughout the flame, however, the species such as C_2H_6 and CH_3 is seen only close to the injection location. The balance of C_2H_6 and CH_3 (as seen from the spotty ignition behavior near the inlet) is important for understanding quenching-re-ignition behavior.

Future work involves studying the flame behavior at different conditions such as varying combustion chamber pressure, dilution rate and equivalence ratios. Furthermore understanding the effect of swirl angle, diffusion and effusion inlets hold significance from a practical design perspective.

5. OVERALL SUMMARY AND CONCLUSIONS

Following is the overall summary from the study:

1. 1st real gas Direct Numerical Simulation (DNS) combustion solver for high pressure and high dilution condition is developed to model practical combustion flame. It is shown that % dilution plays a crucial role in flame formation and flame edge development. The peak temperature achieved for different dilutions ranging from 65% to 90% varied between 1800K-3000K. The main combustion regime identified from the DNS was corrugated flame regime, with highest dilution closer to thickened corrugated flame.

2. A novel chemistry reduction tool is developed and validated called the Supervised Learning – Global Pathway Selection (SL-GPS). The new tool is able to predict the ignition delay with higher accuracy as compared to the existing reduction techniques like DRGEP at lower computational times.

3. The SL-GPS method is integrated with the In-situ Adaptive Tabulation (ISAT) method in OpenFOAM and tested against the state of the art technique called the Tabulation of Dynamic Adaptive Chemistry (TDAC) for Sandia Flame D. The TSL-GPS shows higher accuracy in predicting the temperature and mass fraction of major species as compared to the TDAC method while being computationally less expensive. The Implicit Large Eddy Simulation (ILES) of South-West Research Institute (SWRI) combustor shows unique ignition and flame kernel expansion behavior. The ignition occurs in the radially outward region of the injection at a high turbulence zone. The ignition kernel is composed mainly of the CO mass fraction among the minor species which indicates incomplete combustion. This CO mass fraction reduces as the flame propagates and secondary oxidation takes over converting CO to CO_2. The flame expands radially and axially and interacts with the wall where major swirl motion takes over and the

flame collapses onto itself leading to formation of a thin stable flame centered on the axis. This stable flame is closer to the injection point as compared to the original ignition location.

The new DNS and LES solvers developed help in gaining a fundamental understanding of the high dilution and high pressure sCO_2 oxy-combustion of methane. Future work will involve running multiple test simulations to identify optimum combustion regime using ILES for SWRI combustor. Key parameters such as the dilution rate, pressure and incoming gas temperature along with the swirl angle and diffusion and effusion rates have to be identified to develop an ideal high pressure combustor. Moreover, through multi-step chemistry, quenching and re-ignition zones can be identified and flame stability can be investigated.

REFERENCES

1. Breidenich, C., et al., *The Kyoto protocol to the United Nations framework convention on climate change.* American Journal of International Law, 1998. **92**(2): p. 315-331.
2. Metz, B., et al., *Carbon dioxide capture and storage: Intergovernmental Panel on Climate Change special report*. 2005, Cambridge, Cambridge University Press.
3. Hoffert, M.I., et al., *Advanced technology paths to global climate stability: energy for a greenhouse planet.* Science, 2002. **298**(5595): p. 981-987.
4. Brown, A., S. Müller, and Z. Dobrotkova, *Renewable energy: Markets and prospects by technology.* IEA information paper, 2011.
5. Finkenrath, M., *Cost and performance of carbon dioxide capture from power generation.* OECD/IEA, 2011.
6. Allam, R.J., et al., *High efficiency and low cost of electricity generation from fossil fuels while eliminating atmospheric emissions, including carbon dioxide.* Energy Procedia, 2013. **37**: p. 1135-1149.
7. Ertesvåg, I.S., H.M. Kvamsdal, and O. Bolland, *Exergy analysis of a gas-turbine combined-cycle power plant with precombustion CO2 capture.* Energy, 2005. **30**(1): p. 5-39.
8. Fu, C. and T. Gundersen, *Heat integration of an oxy-combustion process for coal-fired power plants with CO2 capture by pinch analysis.* Chem. Eng. Trans., 2010. **21**: p. 181-186.

9. Fu, C. and T. Gundersen, *Power reduction in air separation units for oxy-combustion processes based on exergy analysis*, in *Comput. Aided Chem. Eng.* 2011, Elsevier. p. 1794-1798.

10. Jericha, H., W. Sanz, and E. Go¨ ttlich. *Design concept for large output graz cycle gas turbines*. in *Turbo Expo: Power for Land, Sea, and Air*. 2006.

11. Kvamsdal, H.M., K. Jordal, and O. Bolland, *A quantitative comparison of gas turbine cycles with CO2 capture.* Energy, 2007. **32**(1): p. 10-24.

12. Bolland, O. and P. Mathieu, *Comparison of two CO2 removal options in combined cycle power plants.* Energy Convers. Manag., 1998. **39**(16-18): p. 1653-1663.

13. Mathieu, P. and R. Nihart, *Sensitivity analysis of the MATIANT cycle.* Energy Convers. Manag., 1999. **40**(15-16): p. 1687-1700.

14. Allam, R., et al. *The oxy-fuel, supercritical CO2 Allam Cycle: New cycle developments to produce even lower-cost electricity from fossil fuels without atmospheric emissions*. in *Turbo Expo: Power for Land, Sea, and Air*. 2014. American Society of Mechanical Engineers.

15. Strakey, P.A., *Oxy-combustion modeling for direct-fired supercritical CO2 power cycles.* J. Energy Resour. Technol., 2019. **141**(7).

16. Iwai, Y., et al. *Development approach to the combustor of gas turbine for oxy-fuel, supercritical CO2 cycle*. in *Turbo Expo: Power for Land, Sea, and Air*. 2015. American Society of Mechanical Engineers.

17. Unger, D.P. and H.J. Herzog, *Comparative study on energy R & D performance: Gas turbine case study*. 1998: Energy Laboratory, Massachusetts Institute of Technology.

18. Metz, B., et al., *IPCC special report on carbon dioxide capture and storage*. 2005: Cambridge: Cambridge University Press.

19. Rubin, E.S., et al., *The outlook for improved carbon capture technology.* 2012. **38**(5): p. 630-671.

20. Mathieu, P., et al. *New concept of CO2 removal technologies in power generation, combined with fossil fuel recovery and long term CO2 sequestration*. in *Turbo Expo: Power for Land, Sea, and Air*. 2000. American Society of Mechanical Engineers.

21. Parsons Brinkerhoff, E.G.C., *Model-2013 Update of Non-renewable Technologies*.

22. Lu, X., et al. *Integration and optimization of coal gasification systems with a near-zero emissions supercritical carbon dioxide power cycle*. in *Turbo Expo: Power for Land, Sea, and Air*. 2016. American Society of Mechanical Engineers.

23. Weiland, N.T. and C.W. White, *Performance and cost assessment of a natural gas-fueled direct sCO2 power plant*. 2019, National Energy Technology Laboratory (NETL), Pittsburgh, PA, Morgantown, WV ….

24. Ferrari, N., et al., *Oxy-turbine for Power Plant with CO2 capture.* 2017. **114**: p. 471-480.

25. Zhao, Y., et al., *Thermodynamic study of an improved MATIANT cycle with stream split and recompression.* 2017. **125**: p. 452-469.

26. Chan, W., et al., *Thermodynamic analysis and optimization of Allam cycle with a reheating configuration.* 2020. **224**: p. 113382.

27. Allam, R., et al., *Demonstration of the Allam Cycle: an update on the development status of a high efficiency supercritical carbon dioxide power process employing full carbon capture.* 2017. **114**: p. 5948-5966.

28. Zambon, A.C., et al., *A High-Fidelity Modeling Tool to Support the Design of Oxy-Combustors for Direct-Fired Supercritical CO2 Cycles.* 2021. **143**(1).

29. Pryor, O., et al., *High pressure shock tube ignition delay time measurements during oxy-methane combustion with high levels of CO2 dilution.* 2017. **139**(4).

30. Nishikawa, K. and I.J.C.p.l. Tanaka, *Correlation lengths and density fluctuations in supercritical states of carbon dioxide.* 1995. **244**(1-2): p. 149-152.

31. Nishikawa, K., et al., *Density fluctuation of a van der Waals fluid in supercritical state.* 2003. **118**(3): p. 1341-1346.

32. Simeoni, G., et al., *The Widom line as the crossover between liquid-like and gas-like behaviour in supercritical fluids.* 2010. **6**(7): p. 503-507.

33. Santoro, M. and F.A.J.P.R.B. Gorelli, *Structural changes in supercritical fluids at high pressures.* 2008. **77**(21): p. 212103.

34. Sato, T., et al., *Structural difference between liquidlike and gaslike phases in supercritical fluid.* 2008. **78**(5): p. 051503.

35. Morita, T., et al., *Structure study of supercritical CO2 near higher-order phase transition line by X-ray diffraction.* 1997. **101**(36): p. 7158-7162.

36. Maxim, F., et al., *Visualization of supercritical water pseudo-boiling at Widom line crossover.* 2019. **10**(1): p. 1-11.

37. Fisher, M.E. and B.J.T.J.o.C.P. Wiodm, *Decay of correlations in linear systems.* 1969. **50**(9): p. 3756-3772.

38. Brazhkin, V., et al., *Two liquid states of matter: A dynamic line on a phase diagram.* 2012. **85**(3): p. 031203.

39. Xu, L., et al., *Relation between the Widom line and the dynamic crossover in systems with a liquid–liquid phase transition.* 2005. **102**(46): p. 16558-16562.

40. Banuti, D., M. Raju, and M.J.T.J.o.S.F. Ihme, *Between supercritical liquids and gases–Reconciling dynamic and thermodynamic state transitions.* 2020. **165**: p. 104895.

41. Boyd, B. and D. Jarrahbashi, *A diffuse-interface method for reducing spurious pressure oscillations in multicomponent transcritical flow simulations.* Computers & Fluids, 2021: p. 104924.

42. Ma, P.C., et al., *Large-eddy simulations of transcritical injection and auto-ignition using diffuse-interface method and finite-rate chemistry.* 2019. **37**(3): p. 3303-3310.

43. Ma, P.C., et al., *On the numerical behavior of diffuse-interface methods for transcritical real-fluids simulations.* 2019. **113**: p. 231-249.

44. Mayer, W.O., et al., *Atomization and breakup of cryogenic propellants under high-pressure subcritical and supercritical conditions.* 1998. **14**(5): p. 835-842.

45. Oefelein, J., et al., *Effects of Pressure on the Fundamental Physics of Fuel Injection in Diesel Engines*. 2012, Sandia National Laboratories (SNL), Albuquerque, NM, and Livermore, CA ….

46. Oschwald*, M., et al., *Injection of fluids into supercritical environments.* 2006. **178**(1-3): p. 49-100.

47. Crua, C., J. Manin, and L.M.J.F. Pickett, *On the transcritical mixing of fuels at diesel engine conditions.* 2017. **208**: p. 535-548.

48. Dahms, R.N. and J.C.J.P.o.F. Oefelein, *On the transition between two-phase and single-phase interface dynamics in multicomponent fluids at supercritical pressures.* 2013. **25**(9): p. 092103.

49. Dahms, R.N. and J.C.J.P.o.t.C.I. Oefelein, *Non-equilibrium gas–liquid interface dynamics in high-pressure liquid injection systems.* 2015. **35**(2): p. 1587-1594.

50. Dahms, R.N., J.C.J.J.o.P. Oefelein, and Power, *Atomization and dense-fluid breakup regimes in liquid rocket engines.* 2015. **31**(5): p. 1221-1231.

51. Oefelein, J.C. *Advances in modeling supercritical fluid behavior and combustion in high-pressure propulsion systems*. in *AIAA Scitech 2019 Forum*. 2019.

52. CANDEL*, S., et al., *Structure and dynamics of cryogenic flames at supercritical pressure.* 2006. **178**(1-3): p. 161-192.

53. Chehroudi, B., et al., *Cryogenic shear layers: experiments and phenomenological modeling of the initial growth rate under subcritical and supercritical conditions.* 2002. **23**(5): p. 554-563.

54. Locke, J., et al. *High speed visualization of LOX/GH2 rocket injector flowfield: hot-fire and cold-flow experiments*. in *46th AIAA/ASME/SAE/ASEE Joint Propulsion Conference & Exhibit*. 2010.

55. Roy, A., C. Segal, and C.J.A.j. Joly, *Spreading angle and core length analysis of supercritical jets.* 2013. **51**(8): p. 2009-2014.

56. Mayer, W., et al., *Raman measurements of cryogenic injection at supercritical pressure.* Heat Mass Transf., 2003. **39**(8): p. 709-719.

57. Oschwald, M., et al. *Investigation of coaxial LN2/GH2-injection at supercritical pressure by spontaneous Raman scattering*. in *35th Joint propulsion conference and exhibit*. 1999.

58. Ruiz, A.M., et al., *Numerical benchmark for high-Reynolds-number supercritical flows with large density gradients.* 2016. **54**(5): p. 1445-1460.

59. Gerber, V., et al., *Fluid injection with supercritical reservoir conditions: Overview on morphology and mixing.* 2021. **169**: p. 105097.

60. Ries, F., et al., *Effect chain analysis of supercritical fuel disintegration processes using an Les-based entropy generation analysis.* 2020. **192**(11): p. 2171-2188.

61. Sengupta, U., et al., *Fully compressible low-Mach number simulations of carbon-dioxide at supercritical pressures and trans-critical temperatures.* Flow Turbul. Combust., 2017. **99**(3): p. 909-931.

62. Ovais, S.M., K.A. Kemenov, and R.S. Miller, *Direct numerical simulation of supercritical oxy-methane mixing layers with CO2 substituted counterparts.* Phys. Fluids, 2021. **33**(3): p. 035115.

63. Purushotham, D., K.A. Schau, and J.C. Oefelein. *Analysis of Compressibility Effects and Nonlinear Property Variations in a Supercritical CO2 Mixing Layer*. in *AIAA SCITECH 2022 Forum*. 2022.

64. Lacaze, G., et al., *Large eddy simulation of laser ignition and compressible reacting flow in a rocket-like configuration.* 2009. **156**(6): p. 1166-1180.

65. Schmitt, T., et al., *Large-eddy simulation of oxygen/methane flames under transcritical conditions.* 2011. **33**(1): p. 1383-1390.

66. Maestro, D., et al., *Large Eddy Simulation of combustion and heat transfer in a single element GCH4/GOx rocket combustor.* 2019. **103**(3): p. 699-730.

67. Blanchard, S., Q. Cazères, and B.J.A.A. Cuenot, *Chemical modeling for methane oxy-combustion in liquid rocket engines.* 2022. **190**: p. 98-111.

68. Mardani, A. and S.J.I.J.o.H.E. Tabejamaat, *Effect of hydrogen on hydrogen–methane turbulent non-premixed flame under MILD condition.* 2010. **35**(20): p. 11324-11331.

69. Salavati-Zadeh, A., et al., *Kinetic simulation of flameless burners with methane/hydrogen blended fuel: Effects of molecular diffusion and Schmidt number.* 2018. **43**(11): p. 5972-5983.

70. Sabia, P., et al., *Hydrogen-enriched methane mild combustion in a well stirred reactor.* 2007. **31**(5): p. 469-475.

71. Liu, C., et al., *Characteristics of oxy-fuel combustion in gas turbines.* 2012. **89**(1): p. 387-394.

72. Saanum, I., M.J.E. Ditaranto, and Fuels, *Experimental study of oxy-fuel combustion under gas turbine conditions.* 2017. **31**(4): p. 4445-4451.

73. Shakeel, M.R., Y.S. Sanusi, and E.M.J.A.e. Mokheimer, *Numerical modeling of oxy-methane combustion in a model gas turbine combustor.* 2018. **228**: p. 68-81.

74. Rutland, C., *Large-eddy simulations for internal combustion engines–a review.* International Journal of Engine Research, 2011. **12**: p. 421-451.

75. Brown, P.N., et al., *VODE: A variable-coefficient ODE solver.* 1989. **10**(5): p. 1038-1051.

76. Cohen, S.D., A.C. Hindmarsh, and P.F.J.C.i.p. Dubois, *CVODE, a stiff/nonstiff ODE solver in C.* 1996. **10**(2): p. 138-143.

77. Wanner, G. and E. Hairer, *Solving ordinary differential equations II*. Vol. 375. 1996: Springer Berlin Heidelberg New York.

78. Shampine, L.F.J.A.T.o.M.S., *Implementation of Rosenbrock methods.* 1982. **8**(2): p. 93-113.

79. Magnussen, B.F. *The eddy dissipation concept: A bridge between science and technology*. in *ECCOMAS thematic conference on computational combustion*. 2005. Libson, Portugal.

80. Ertesvåg, I.S., B.F.J.C.s. Magnussen, and technology, *The eddy dissipation turbulence energy cascade model.* 2000. **159**(1): p. 213-235.

81. Matheis, J. and S.J.I.J.o.M.F. Hickel, *Multi-component vapor-liquid equilibrium model for LES of high-pressure fuel injection and application to ECN Spray A.* 2018. **99**: p. 294-311.

82. Lacaze, G., et al., *Comparison of energy-, pressure-and enthalpy-based approaches for modeling supercritical flows.* 2019. **181**: p. 35-56.

83. Ma, P.C., Y. Lv, and M.J.J.o.C.P. Ihme, *An entropy-stable hybrid scheme for simulations of transcritical real-fluid flows.* 2017. **340**: p. 330-357.

84. Banuti, D.T., et al., *Thermodynamic structure of supercritical LOX–GH2 diffusion flames.* 2018. **196**: p. 364-376.

85. Wang, X., H. Huo, and V. Yang. *Supercritical combustion of general fluids in laminar counterflows*. in *51st AIAA Aerospace Sciences Meeting including the New Horizons Forum and Aerospace Exposition*. 2013.

86. Oefelein, J.C.J.C.S. and Technology, *Mixing and combustion of cryogenic oxygen-hydrogen shear-coaxial jet flames at supercritical pressure.* 2006. **178**(1-3): p. 229-252.

87. Mardani, A., E.J.E. Barani, and Fuels, *Numerical Investigation of Supercritical Combustion of H2–O2.* 2018. **32**(3): p. 3851-3868.

88. Juniper, M., et al., *Structure of cryogenic flames at elevated pressures.* 2000. **28**(1): p. 1103-1109.

89. Poschner, M. and M. Pfitzner. *Real gas CFD simulation of supercritical H2-LOX in the MASCOTTE single injector combustor using a commercial CFD code*. in *46th AIAA aerospace sciences meeting and exhibit*. 2008.

90. Benarous, A. and A.J.T.S. Liazid, *H2-O2 Supercritical combustion modeling using a CFD code.* 2009. **13**(3): p. 139-152.

91. Peters, N., *Turbulent combustion*. 2001, IOP Publishing.

92. Peters, N., *Laminar diffusion flamelet models in non-premixed turbulent combustion.* Progress in energy & combustion science, 1984. **10**: p. 319-339.

93. Chung, T.H., et al., *Generalized multiparameter correlation for nonpolar and polar fluid transport properties.* Ind. Eng. Chem. Fundam., 1988. **27**(4): p. 671-679.

94. Singla, G., et al., *Flame stabilization in high pressure LOx/GH2 and GCH4 combustion.* 2007. **31**(2): p. 2215-2222.

95. Lux, J., O.J.J.o.P. Haidn, and Power, *Flame stabilization in high-pressure liquid oxygen/methane rocket engine combustion.* 2009. **25**(1): p. 15-23.

96. Joo, H.I., Ö.L.J.C. Gülder, and Flame, *Soot formation and temperature structure in small methane–oxygen diffusion flames at subcritical and supercritical pressures.* 2010. **157**(6): p. 1194-1201.

97. Lux, J., O.J.J.o.P. Haidn, and Power, *Effect of recess in high-pressure liquid oxygen/methane coaxial injection and combustion.* 2009. **25**(1): p. 24-32.

98. Singla, G., et al., *Transcritical oxygen/transcritical or supercritical methane combustion.* 2005. **30**(2): p. 2921-2928.

99. Majda, A. and J. Sethian, *The derivation and numerical solution of the equations for zero Mach number combustion.* Combust. Sci. Technol., 1985. **42**(3-4): p. 185-205.

100. Bell, J.B., et al. *Numerical simulation of low Mach number reacting flows*. in *Journal of Physics: Conference Series*. 2007. IOP Publishing.

101. Bell, J., et al., *Adaptive low Mach number simulations of nuclear flame microphysics.* J. Comput. Phys., 2004. **195**(2): p. 677-694.

102. Oefelein, J.C., *Large eddy simulation of turbulent combustion processes in propulsion and power systems.* Prog. Aerosp. Sci., 2006. **42**(1): p. 2-37.

103. Oefelein, J. and G. Lacaze, *Low-Temperature Injection Dynamics and Turbulent Flame Structure in High-Pressure Supercritical Flows*. 2011, Sandia National Lab.(SNL-CA), Livermore, CA (United States).

104. Ruiz, A., et al., *Stabilization of a supercritical hydrogen/oxygen flame behind a splitter plate.* 25th - 26th May, 2011, Co-organised by CNRS, Rouen University and INSA of Rouen, 2011.

105. Lacaze, G. and J.C. Oefelein, *A non-premixed combustion model based on flame structure analysis at supercritical pressures.* Combust. Flame, 2012. **159**(6): p. 2087-2103.

106. Paolucci, S., *On the filtering of sound from the Navier-stokes equations* Sandia National Labs, Livermore, 1982.

107. Müller, B., *Low-Mach-number asymptotics of the Navier-Stokes equations*, in *Floating, flowing, flying*. 1998, Springer. p. 97-109.

108. Munz, C.-D., et al., *The extension of incompressible flow solvers to the weakly compressible regime.* Comput. Fluids, 2003. **32**(2): p. 173-196.

109. Ouazzani, J. and Y. Garrabos. *A new numerical algorithm for Low Mach number supercritical fluids*. in *Proceedings of CHT-08 ICHMT International Symposium on Advances in Computational Heat Transfer*. 2008. Begel House Inc.

110. Ovais, S.M. and R.S. Miller, *A numerical investigation of methane ignition in supercritical CO2.* Phys. Fluids, 2022. **34**(4): p. 047115.

111. Manikantachari, K., et al., *Reduced chemical kinetic mechanisms for oxy/methane supercritical CO2 combustor simulations.* J. Energy Resour. Technol., 2018. **140**(9).

112. Liu, Z., et al. *Sensitivity of Reduced Kinetic Models: The CFD Simulation of SCO2 Oxy-Combustion*. in *Turbo Expo: Power for Land, Sea, and Air*. 2018. American Society of Mechanical Engineers.

113. Morley, C.J.V., *Gaseq: a chemical equilibrium program for Windows.* 2005.

114. Kasuya, H., et al., *LES/flamelet/ANN of oxy-fuel combustion for a supercritical CO2 power cycle.* 2022: p. 100083.

115. Doran, E.M., H. Pitsch, and D.J.J.P.o.t.C.I. Cook, *A priori testing of a two-dimensional unsteady flamelet model for three-feed combustion systems.* 2013. **34**(1): p. 1317-1324.

116. Yu, P., et al., *Analysis of a Quasi-Two-Dimensional Flamelet Model on a Three-Feed Non-premixed Oxy-Combustion Burner.* Flow, Turbulence and Combustion, 2022. **108**: p. 303–327.

117. Keum, K., et al., *Large eddy simulation of turbulent partially premixed flames in oxy-fuel combustor under subcritical and supercritical conditions.* 2022. **36**(4): p. 1825-1834.

118. Kumar, G., et al., *Study of the effect of*

119. Ramachandran, S., et al., *Numerical study of turbulent non-premixed cool flames at high and supercritical pressures: Real gas effects and dual peak structure.* Combust. Flame, 2023. **249**: p. 112626.

120. Desjardins, O., V. Moureau, and H. Pitsch, *An accurate conservative level set/ghost fluid method for simulating turbulent atomization.* J. Comput. Phys., 2008. **227**(18): p. 8395-8416.

121. Desjardins, O., et al., *High order conservative finite difference scheme for variable density low Mach number turbulent flows.* J. Comput. Phys., 2008. **227**: p. 7125-7159.

122. Capecelatro, J. and O. Desjardins, *An Euler–Lagrange strategy for simulating particle-laden flows.* J. Comput. Phys., 2013. **238**: p. 1-31.

123. Capecelatro, J., P. Pepiot, and O. Desjardins, *Numerical investigation and modeling of reacting gas-solid flows in the presence of clusters.* Chem. Eng. Sci., 2015. **122**: p. 403-415.

124. Chong, S.T., et al. *Turbulent mixing and combustion of supercritical jets*. in *55th AIAA Aerospace Sciences Meeting*. 2017.

125. Fernández-Tarrazo, E., et al., *A simple one-step chemistry model for partially premixed hydrocarbon combustion.* Combust. Flame, 2006. **147**(1-2): p. 32-38.

126. Peng, D.-Y. and D.B. Robinson, *A new two-constant equation of state.* Ind. Eng. Chem. Fundam., 1976. **15**(1): p. 59-64.

127. Kee, R.J., et al., *CHEMKIN-III: A FORTRAN chemical kinetics package for the analysis of gas-phase chemical and plasma kinetics*. 1996, Sandia National Lab.(SNL-CA), Livermore, CA (United States).

128. Fuller, E.N., P.D. Schettler, and J.C. Giddings, *New method for prediction of binary gas-phase diffusion coefficients.* Ind. Eng. Chem., 1966. **58**(5): p. 18-27.

129. Takahashi, S., *Preparation of a generalized chart for the diffusion coefficients of gases at high pressures.* J. Chem. Eng. Japan, 1975. **7**(6): p. 417-420.

130. Jafari, S., et al., *Towards Understanding the Structure of Subcritical and Transcritical Liquid–Gas Interfaces Using a Tabulated Real Fluid Modeling Approach.* Energies, 2021. **14**(18): p. 5621.

131. Müller, H., et al., *Large-eddy simulation of coaxial LN2/GH2 injection at trans-and supercritical conditions.* J. Propuls. Power, 2016. **32**(1): p. 46-56.

132. Delimont, J., N. Andrews, and L. Chordia. *Computational modeling of a 1mw scale combustor for a direct fired sco2 power cycle*. in *Turbo Expo: Power for Land, Sea, and Air*. 2018. American Society of Mechanical Engineers.

133. Chaudhuri, S., et al., *Flame thickness and conditional scalar dissipation rate in a premixed temporal turbulent reacting jet.* Combust. Flame, 2017. **184**: p. 273-285.

134. Abdel-Gayed, R., D. Bradley, and M. Lawes, *Turbulent burning velocities: a general correlation in terms of straining rates.* Proc. Math. Phys. Eng. Sci. , 1987. **414**(1847): p. 389-413.

135. Pitsch, H., *Laminar premixed flames: kinematics and burning velocity.* CEFRC Combustion Summer School, 2014.

136. Petersen, E.L., et al., *Methane/propane oxidation at high pressures: Experimental and detailed chemical kinetic modeling.* 2007. **31**(1): p. 447-454.

137. Petersen, E., et al., *Kinetics modeling of shock-induced ignition in low-dilution CH4/O2 mixtures at high pressures and intermediate temperatures.* 1999. **117**(1-2): p. 272-290.

138. Petersen, E.L., et al., *Ignition delay times of Ram accelerator CH/O/diluent mixtures.* 1999. **15**(1): p. 82-91.

139. Coogan, S., et al. *Evaluation of kinetic mechanisms for direct fired supercritical oxy-combustion of natural gas*. in *Turbo Expo: Power for Land, Sea, and Air*. 2016. American Society of Mechanical Engineers.

140. Karimi, M., et al., *Measurement of methane autoignition delays in carbon dioxide and argon diluents at high pressure conditions.* Combust. Flame, 2019. **204**: p. 304-319.

141. Laich, A.R., et al., *Effects of high fuel loading and CO2 dilution on oxy-methane ignition inside a shock tube at high pressure.* 2020. **142**(10): p. 102103.

142. Rahman, R.K., et al., *Probing the effects of NOx and SOx impurities on oxy-fuel combustion in supercritical CO2: Shock tube experiments and chemical kinetic modeling.* 2020. **142**(12).

143. Bongartz, D., A.F.J.C. Ghoniem, and flame, *Chemical kinetics mechanism for oxy-fuel combustion of mixtures of hydrogen sulfide and methane.* 2015. **162**(3): p. 544-553.

144. Konnov, A.J.C. and Flame, *Implementation of the NCN pathway of prompt-NO formation in the detailed reaction mechanism.* 2009. **156**(11): p. 2093-2105.

145. Park, S., et al., *Measurements of density and sound speed in mixtures relevant to supercritical CO2 cycles.* 2020. **142**(10): p. 102105.

146. Lemmon, E., M.L. Huber, and M.O. Mclinden, *NIST standard reference database 23: reference fluid thermodynamic and transport properties-REFPROP, version 8.0.* 2007.

147. Karimi, M., et al., *High pressure ignition delay times of H2/CO mixture in carbon dioxide and argon diluent.* 2021. **38**(1): p. 251-260.

148. Grajales-González, E., M. Monge-Palacios, and S.M.J.J.o.C.U. Sarathy, *Atomistic simulations of syngas oxy-combustion in supercritical CO2.* 2021. **49**: p. 101554.

149. Liu, Z., et al. *Simulation of sCO 2 oxy-combustion using reduced chemical kinetic mechanism: effects of reduced mechanism and sensitivity to mechanism parameters*. in *The 6th international supercritical CO 2 power cycles symposium, Pittsburgh, Pennsylvania*. 2018.

150. Peters, N. and B. Rogg, *Reduced kinetic mechanisms for applications in combustion systems*. Vol. 15. 2008: Springer Science & Business Media.

151. Lu, T., Y. Ju, and C.K. Law, *Complex CSP for chemistry reduction and analysis.* Combustion & Flame, 2001. **126**: p. 1445-1455.

152. Maas, U. and S.B. Pope, *Simplifying chemical kinetics: intrinsic low-dimensional manifolds in composition space.* Combustion & flame, 1992. **88**: p. 239-264.

153. Pope, S.B., *Computationally efficient implementation of combustion chemistry using in situ adaptive tabulation.* Combust. Theory Model., 1997. **1**: p. 41-63.

154. Lu, T. and C.K. Law, *Linear time reduction of large kinetic mechanisms with directed relation graph: n-Heptane and iso-octane.* Combustion & flame, 2006. **144**: p. 24-36.

155. Pepiot-Desjardins, P. and H. Pitsch, *An efficient error-propagation-based reduction method for large chemical kinetic mechanisms.* Combustion & Flame, 2008. **154**: p. 67-81.

156. Sun, W., et al., *A path flux analysis method for the reduction of detailed chemical kinetic mechanisms.* Combustion & Flame, 2010. **157**: p. 1298-1307.

157. Gao, X., S. Yang, and W. Sun, *A global pathway selection algorithm for the reduction of detailed chemical kinetic mechanisms.* Combustion & Flame, 2016. **167**: p. 238-247.

158. Ihme, M., et al., *Combustion machine learning: Principles, progress and prospects.* 2022. **91**: p. 101010.

159. Zhang, T., et al. *DLODE: a deep learning-based ODE solver for chemistry kinetics*. in *AIAA Scitech 2021 Forum*. 2021.

160. Ranade, R., et al., *An ANN based hybrid chemistry framework for complex fuels.* Fuel, 2019. **241**: p. 625-636.

161. D'Alessio, G., et al., *Adaptive chemistry via pre-partitioning of composition space and mechanism reduction.* Combustion & Flame, 2020. **211**: p. 68-82.

162. Goodwin, D.G., H.K. Moffat, and R.L. Speth, *Cantera: An object-oriented software toolkit for chemical kinetics, thermodynamics, and transport processes.* Caltech, Pasadena, CA, 2009. **124**.

163. Yen, J.Y., *Finding the k shortest loopless paths in a network.* Manage. Sc., 1971. **17**: p. 712-716.

164. Mishra, R., A. Nelson, and D. Jarrahbashi, *Adaptive global pathway selection using artificial neural networks: A-priori study.* Combust. Flame, 2022. **244**: p. 112279.

165. Gregory P. Smith, D.M.G., Michael Frenklach, Nigel W. Moriarty, Boris Eiteneer, Mikhail Goldenberg, C. Thomas Bowman, Ronald K. Hanson, Soonho Song, William C. Gardiner, Jr., Vitali V. Lissianski, and Zhiwei Qin, *GRI-MECH 3.0*.

166. Roy, S. and O. Askari, *A New Detailed Ethanol Kinetic Mechanism at Engine-Relevant Conditions.* Energy Fuels, 2020. **34**: p. 3691-3708.

167. Da, K., *A method for stochastic optimization.* J arXiv preprint arXiv:. 2014.

168. Rusiecki, A., *Trimmed categorical cross-entropy for deep learning with label noise.* Electron. Lett. Comput. Vis. Image Anal., 2019. **55**: p. 319-320.

169. Nguyen, D.N., et al., *Real-fluid thermophysicalModels: An OpenFOAM-based library for reacting flow simulations at high pressure.* 2022. **273**: p. 108264.

170. Contino, F., et al., *Coupling of in situ adaptive tabulation and dynamic adaptive chemistry: An effective method for solving combustion in engine simulations.* Proceedings of the Combustion Institute, 2011. **33**: p. 3057-3064.

171. Liang, L., J.G. Stevens, and J.T. Farrell, *A dynamic adaptive chemistry scheme for reactive flow computations.* Proceedings of the Combustion Institute, 2009. **32**: p. 527-534.

172. Morev, I., et al., *Fast reactive flow simulations using analytical Jacobian and dynamic load balancing in OpenFOAM.* 2022. **34**(2): p. 021801.

173. Smith, G.P., et al., *GRI 3.0 Mechanism*. 1999.

174. Mishra, R., et al., *Hybrid Unsupervised Cluster-wise Regression Approach for Representing the Flamelet Tables.* 2023. **37**(4): p. 3056-3070.

175. Petzold, L.R., *Description of DASSL: a differential/algebraic system solver*. 1982, Sandia National Labs., Livermore, CA (USA).

176. Pope, S.B. and S.B. Pope, *Turbulent flows*. 2000: Cambridge university press.

APPENDIX

Real-gas and mixture property calculation

1. Thermal properties:

The thermal properties are calculated based on the Peng-Robinson[126] equation of state. The departure function for enthalpy is shown as follows:

$$p(\underline{v},T,\mathbf{z}) = \frac{\mathcal{R}T}{\underline{v}-b} - \frac{a\alpha}{\underline{v}^2 + 2b\underline{v} - wb^2} \tag{1}$$

$$\alpha = \left[1 + c_0\left(1-\sqrt{T_r}\right)\right]^2 \tag{2}$$

$$c_0 = 0.37464 + 1.54226\omega - 0.2699\omega^2 \tag{3}$$

$$a\alpha = \sum_i^{N_c}\sum_j^{N_c} z_i z_j a_{ij}\alpha_{ij} \quad \text{and} \quad b = \sum_i^{N_c} z_i b_i . \tag{4}$$

$$T_{c,ij} = \sqrt{T_{c,i}T_{c,j}}\left(1-k_{ij}^{'}\right), \quad p_{c,ij} = Z_{c,ij}\left(\mathcal{R}T_{c,ij}/v_{c,ij}\right) \tag{5}$$

$$v_{c,ij} = \frac{1}{8}\left[v_{c,i}^{1/3} + v_{c,j}^{1/3}\right]^3,$$

$$\omega_{ij} = 0.5\left(\omega_i + \omega_j\right) \quad \text{and} \quad Z_{c,ij} = 0.5\left(Z_i + Z_j\right)$$

$$h = G - T\left(\frac{dG}{dT}\right)_{p,X} = h^0 + pv - RT + K_1\left(A_m - T\frac{dA_m}{dT}\right) \tag{6}$$

$$K_1 = \frac{1}{2\sqrt{2}B_m}\ln\left(\frac{V_m + (1-\sqrt{2})B_m}{V_m + (1+\sqrt{2})B_m}\right) \tag{7}$$

$$\frac{dA_m}{dT} = \frac{0.457236R^2T_c^2}{P_c}\left(\frac{k^2}{T_c} - \frac{k(1+k)}{\sqrt{TT_c}}\right)$$

Here Eq. 2 accounts for polarity of a fluid. ω is the acentric factor which is a fluid property associated with non-sphericity of the molecule. T_r, p_r is the reduced temperature and pressure which is given by T/T_c and p/p_c. Here $T_c, p_c, v_c\, Z_c$ are critical temperature, pressure, molar volume and compressibility.

2. Transport properties:

The transport properties are found based on the Chung transport rules [93]. The averaged mass diffusion coefficients D_i are based on Fickian law [127]. The binary diffusion coefficients $D_{i,j}$ are found using Fuller's model [128] and Takahashi's correction [129].

$$\eta_0 = 4.0785\times10^{-5}\frac{\sqrt{MT}}{V_c^{2/3}\Omega^*}F_c \tag{8}$$

(9)

$$\eta = \eta_0\left(\frac{1}{G_2}+A_6Y\right)+\left(36.344\times10^{-6}\frac{\sqrt{MT_c}}{V_c^{2/3}}\right)A_7Y^2 \times G_2\exp\left(A_8+\frac{A_9}{T^*}+\frac{A_{10}}{T^{*2}}\right).$$

$$\lambda_0 = 7.452\frac{\eta_0}{M}\Psi \tag{10}$$

$$\lambda = \lambda_0\left(\frac{1}{H_2}+B_6Y\right)+3.039\times10^{-4}\left(\frac{\sqrt{T_c/M}}{V_c^{2/3}}B_7Y^2H_2\sqrt{T_r}\right) \tag{11}$$

$$D_i = \frac{1-Y_i}{\sum_{j\neq i}^{N}X_j/D_{j,i}} \tag{12}$$

$$D_{i,j} = \phi\frac{1.00\times10^{-3}T^{1.75}\sqrt{1/M_i+1/M_j}}{p\left(v_i^{1/3}+v_j^{1/3}\right)^2} \tag{13}$$

Here the η_0 is the viscosity of pure dilute gas while η is the viscosity of the dense fluid. Similarly λ_0 and λ are dilute and dense gas thermal conductivity.

3. Mixing rules:

Since the simulation have multiple mixing species in different regimes (super/sub critical) a criterion is required to identify the regime of the resulting mixture. This is done by finding the critical properties of the mixture based on the following set of rules [93].

$$\sigma_m^3 = \sum_i^N \sum_j^N X_i X_j \sigma_{ij}^3 \tag{14}$$

$$\frac{\epsilon_m}{k} = \frac{\sum_i^N \sum_j^N X_i X_j \left(\epsilon_{ij}/k\right)\sigma_{ij}^3}{\sigma_m^3} \tag{15}$$

$$V_{cm} = \left(\frac{\sigma_m}{0.809}\right)^3$$

$$T_{cm} = 1.2593\epsilon_m / k$$

$$\omega_m = \frac{\sum_i^N \sum_j^N X_i X_j \omega_{ij} \sigma_{ij}^3}{\sigma_m^3} \tag{16}$$

(17)

(18)

$$M_m = \left(\frac{\sum_i^N \sum_j^N X_i X_j \left(\epsilon_{ij}/k\right) \sigma_{ij}^2 M_{ij}^{1/2}}{\left(\epsilon_m/k\right)\sigma_m^2} \right)^2 \tag{19}$$

$$\mu_m^4 = \left(\sum_i^N \sum_j^N \frac{X_i X_j \left(\mu_i^2 \mu_j^2\right)}{\left(\epsilon_{ij}/k\right)\sigma_{ij}^3} \right) \sigma_m^3 \left(\frac{\epsilon_m}{k} \right) \tag{20}$$

$$\kappa_m = \sum_i^N \sum_j^N X_i X_j \kappa_{ij}$$

(21)

4. Combustion Model:

The combustion model used is based on the one-step model proposed by Fernández-Tarrazo et al. [125]. Here ω is the global rate B is the pre-exponential factor, T_a is the activation temperature, q heat released per mole of fuel consumed.

$$\mathrm{C}_n\mathrm{H}_m + \left(n + \frac{m}{4}\right)\mathrm{O}_2 \rightarrow n\mathrm{CO}_2 + \frac{m}{2}\mathrm{H}_2\mathrm{O} + q \tag{22}$$

$$\omega = Be^{-T_a/T} C_{\mathrm{C}_n\mathrm{H}_m} C_{\mathrm{O}_2} \tag{23}$$

$$q = -(2n + m/2)h_{\mathrm{H}_2\mathrm{O}} + \phi\left[h_{\mathrm{C}_n\mathrm{H}_m} - n\left(h_{\mathrm{CO}_2} - 2h_{\mathrm{H}_2\mathrm{O}}\right) + N_{\mathrm{CO}}\left(h_{\mathrm{CO}_2} - h_{\mathrm{CO}} - h_{\mathrm{H}_2\mathrm{O}}\right)\right] \tag{24}$$

$$\begin{cases} \phi \leqslant 1 : q/q_o = 1 \\ \phi \geqslant 1 : q/q_o = 1 - \alpha(\phi - 1) \end{cases} \tag{25}$$

$$\alpha = -\left[h_{\mathrm{C}_n\mathrm{H}_m} - n\left(h_{\mathrm{CO}_2} - 2h_{\mathrm{H}_2\mathrm{O}}\right)\right] / q_o \tag{26}$$

$$T_a = \frac{\alpha T_b^2 \left(T^0 - T_u\right)}{\left(T_b - T^0\right)\left(T_b - T_u\right)} \tag{27}$$

$$\begin{cases} \phi \leqslant 0.64 : T_a / T_{ao} = 1 + 8.250(\phi - 0.64)^2 \\ 0.64 \leqslant \phi \leqslant 1.07 : T_a / T_{ao} = 1 \\ \phi \geqslant 1.07 : T_a / T_{ao} = 1 + 1.443(\phi - 1.07)^2 \end{cases} \tag{28}$$

$$\phi = \frac{32(n + m/4)}{12n + m} \frac{Y_{C_nH_m,F}}{Y_{O_2,A}} \frac{Z}{1 - Z} \tag{29}$$

5. Real-gas chemistry for one-step combustion:

Real-gas chemistry source term is accounted for by calculating real-gas C_p and thermal properties of participating species.

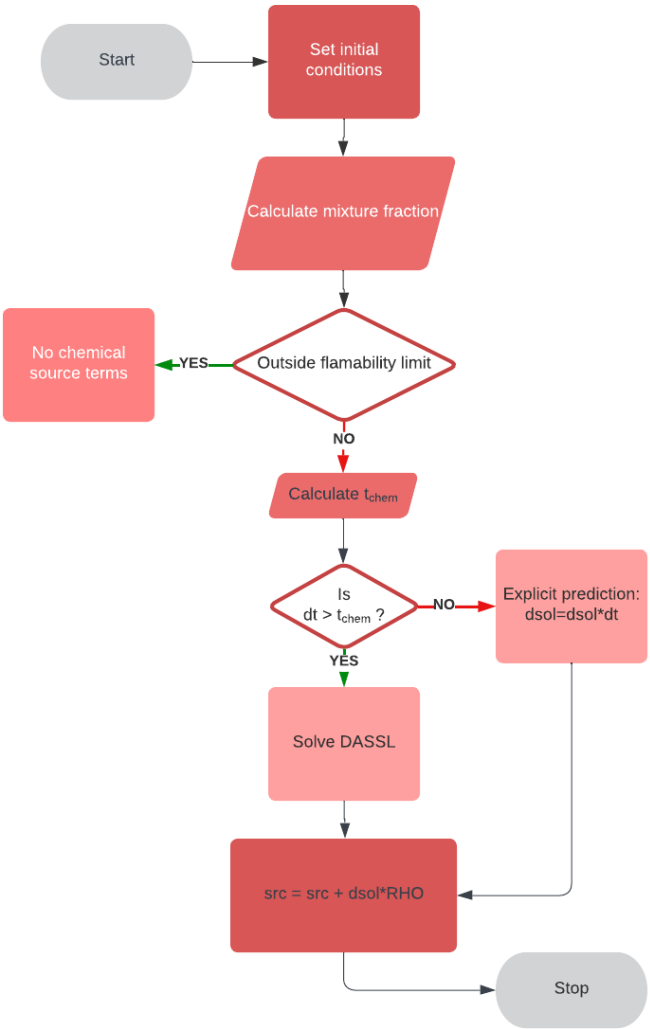

Figure A1. Flowchart for one-step chemical source term calculation in NGA.

Since the participating species are species in the global reaction, a system of ODE exists. This has to be solved iteratively to avoid any divergence due to sudden heat release and formation of products. To mitigate the stiffness problem many ODE solvers exist in the literature. DASSL solver [175] Figure is used for chemical time integration. Since one-step combustion model is used the contribution from the reaction to the source terms can be found without an elaborate Jacobian.

Real-gas and mixture property validation

Figure A2 and Figure A3 show the thermal and transport property validation of N_2 and H_2 at varying pressure conditions against the NIST database. Figure A4 shows the thermal property validation of CH_4, O_2, CO_2 against the NIST database and Figure A5 shows the transport property validation.

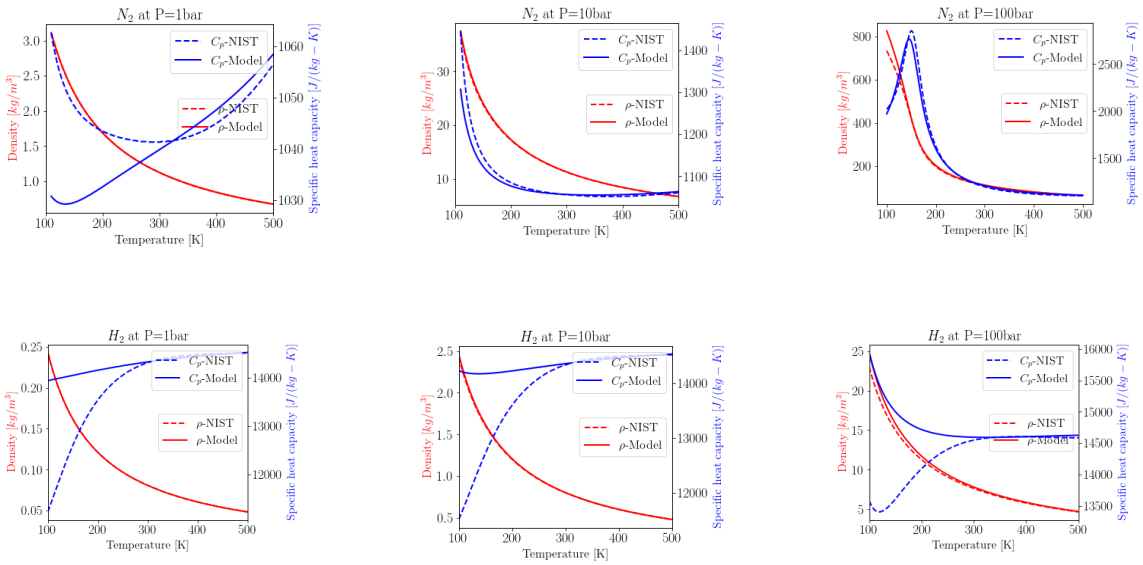

Figure A2. N_2 and H_2 thermal property validation.

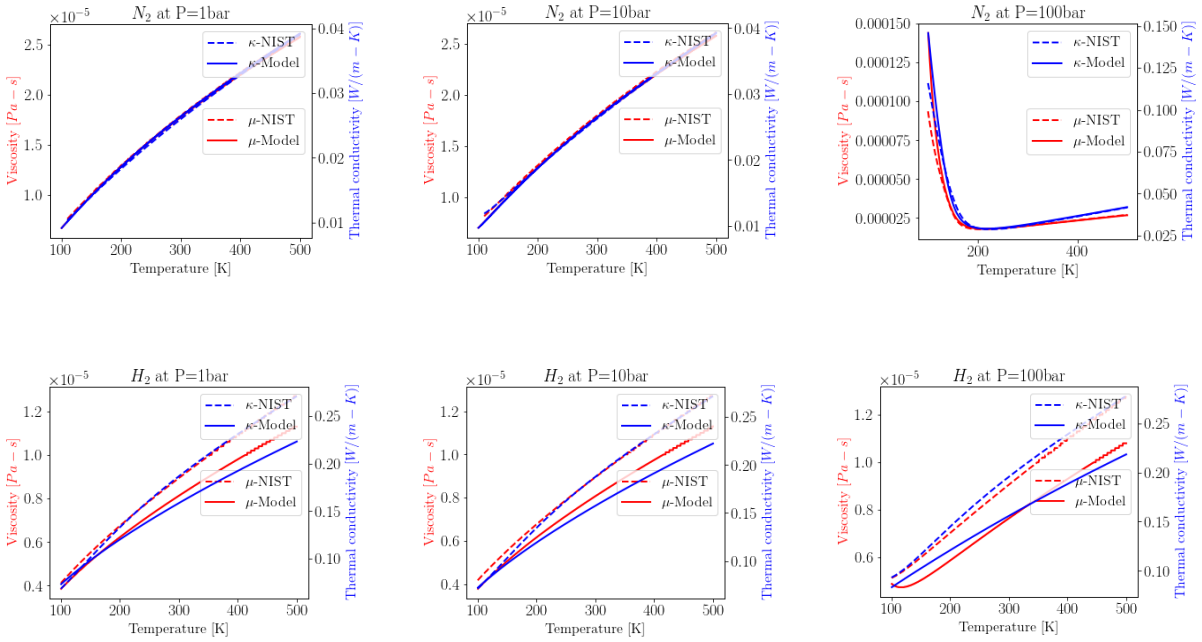

Figure A3. N_2 and H_2 transport property validation.

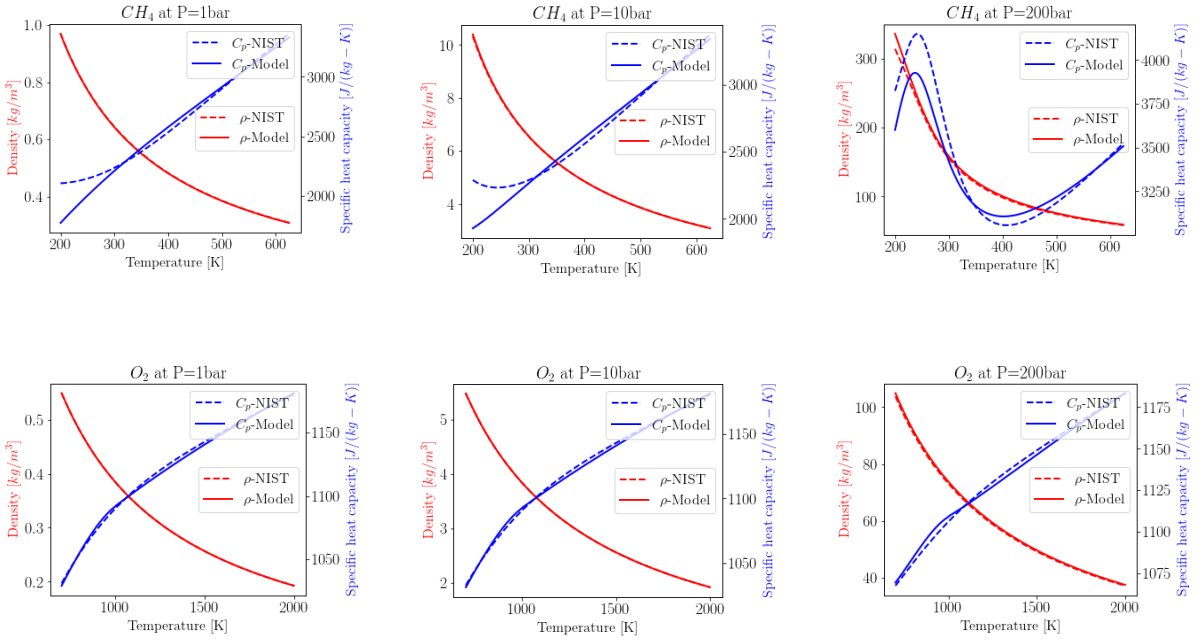

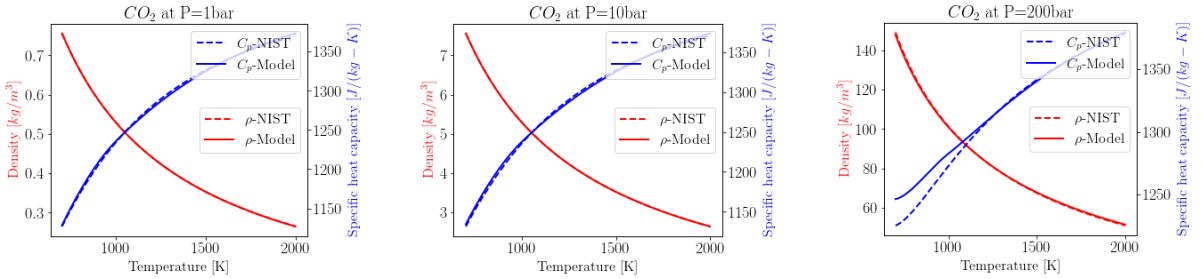

Figure A4. CH_4, O_2, CO_2 thermal property validation

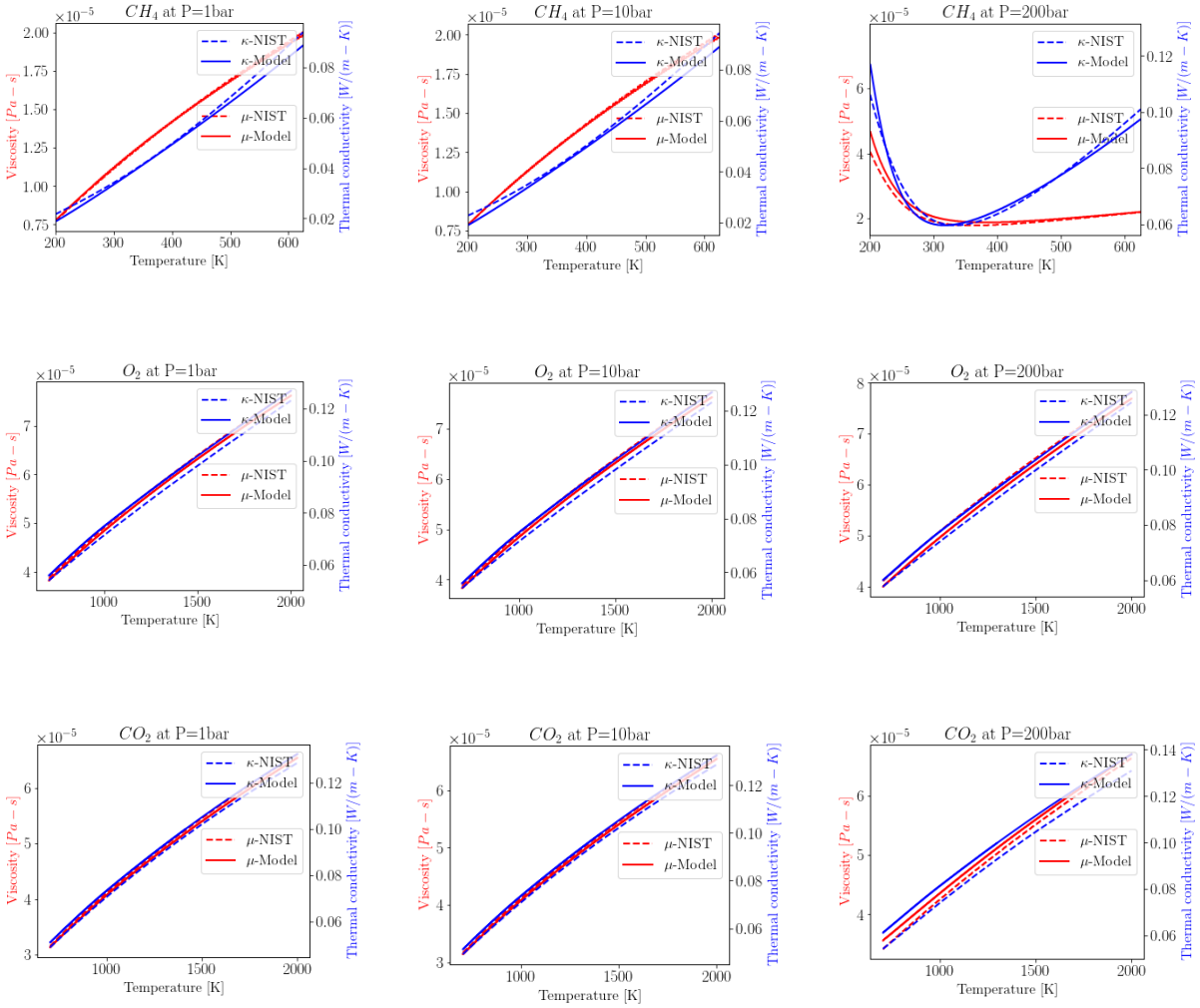

Figure A5. CH_4, O_2, CO_2 transport property validation

7.3 Supercritical Single-Species Validation:[56]

The description of the DNS simulation for single supercritical specie modeling is shown in Table 4. The mesh used is shown in Figure A6. The total number of cells was: 238,000 and minimum cell size was: 10 microns

$P\ [MPa]$	$U_{jet,bulk}\ [\frac{m}{s}]$	$T_{jet}[K]$	$T_{coflow}[K]$	$D[mm]$
4.0	5.0	130	298	2.2

Table 8. Description of Case 4 from Mayer et al.[56]

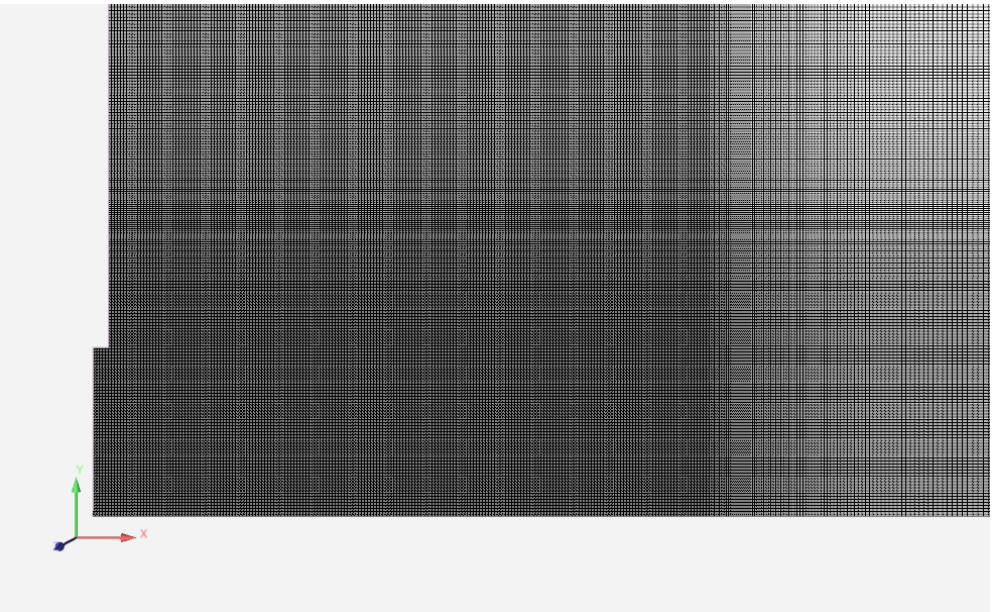

Figure A6: 2D mesh for modeling Mayer et al. experiment.

Two-Species Supercritical Mixing Validation:[57]

The description for two species supercritical mixing DNS simulation is shown in Table 5. The 2D mesh used for the modeling is shown inFigure A7. The total number of cells was 169,920 and minimum cell size was 15microns.

$v_{N2,jet[\frac{m}{s}]}$	$T_{N2,jet}[K]$	$v_{H2}[\frac{m}{s}]$	$T_{H2}[K]$	$\frac{\rho_{N2,jet}}{\rho_{H2}}[-]$	$\frac{v_{N2,jet}}{v_{H2}}$[-]
5	140	60	270	43.1	0.083

Table 9. Description of Case-D4 from Oschwald et al.[57]

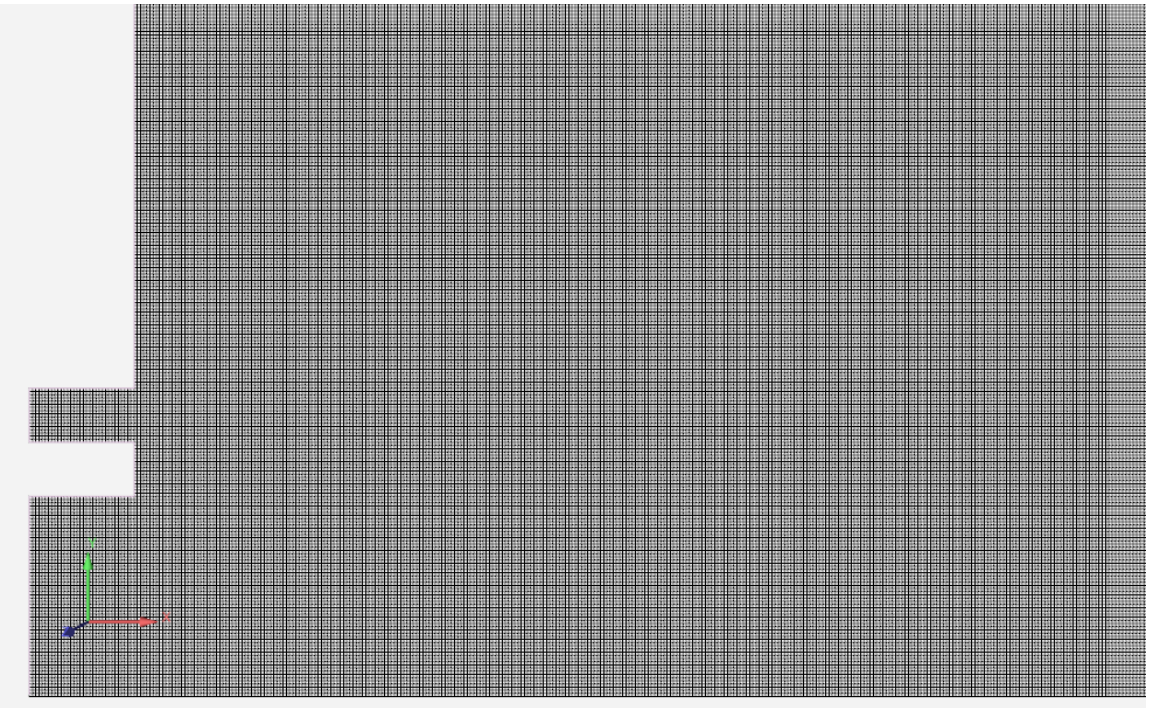

Figure A7. 2D mesh for modeling Oschwald et al. experiment.

SWRI Combustor Configuration:[132]

The original combustion geometry has been simplified as shown in Figure A8. Some simplifying assumptions are made such as: No swirl, no effusion/diffusion inlet, completely premixed mixture. Table 6 and Table 7 shows the description for DNS simulation for 2D SWRI combustor. Figure A9 shows the 2D mesh generated for the simulation. The total number of cells was 800,000 and minimum cell size was 10microns.

Species	Mass Flow Rate [kg/s]	T [K]
CH4	0.02	300
O2	0.08	923
CO2	0.325	923

Table 10. Description of inlet composition of SWRI sCO_2 oxy-methane combustor.[132]

Co-flow radius	5.5mm
Length and radius of domain	30mm/10mm
Pressure	200bar
Temperature	988K

Table 11. Description of SWRI sCO_2 oxy-methane combustor

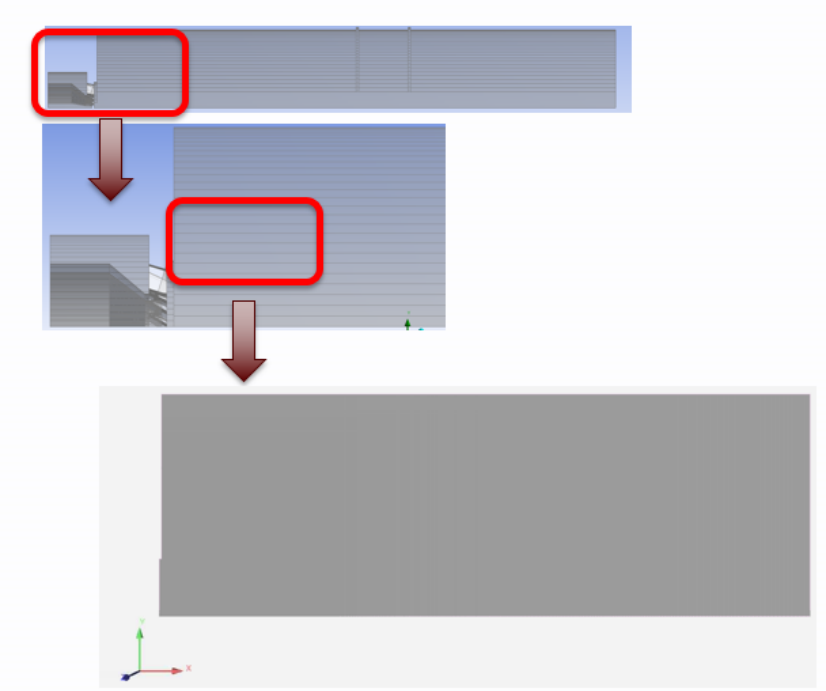

Figure A8. Simplifying original SWRI combustor geometry for 2D axis-symmetric DNS simulation; Full 3D SWRI combustor geometry highlighting the region of interest (Top); Zoomed-in region of interest (Middle); Actual DNS computational domain reduced from the region of interest (Bottom)

Figure A9. 2D mesh for modeling SWRI combustor.

Assumptions:

1. No swirl angle
2. No diffusion or effusion inlets
3. Fuel, oxidizer and CO_2 streams are completely mixed at the inlet

Calculation of u' and L_x[176]:

One commonly used equation for characterizing the turbulent fluctuations in velocity is the root-mean-square (RMS) velocity:

$$u' = \sqrt{\frac{\sum(u-U)^2}{N}}$$

where u' is the RMS velocity, N is the number of samples, u is the instantaneous velocity, and U is the mean velocity. This equation calculates the standard deviation of the velocity fluctuations

around the mean velocity over a given sample size. The RMS velocity provides a measure of the intensity of the turbulent fluctuations in velocity.

The integral length scale is a characteristic length scale of the turbulent flow, which represents the distance over which the turbulent fluctuations in velocity become uncorrelated. The integral length scale can be estimated from the velocity data using the autocorrelation function of the velocity fluctuations.

To estimate the integral length scale, the velocity fluctuations (u') are first extracted from the velocity data by subtracting the mean velocity. Then, the autocorrelation function $R(u', x')$ is calculated as a function of distance x'. Finally, the integral length scale is obtained by integrating the autocorrelation function over all distances, weighted by $1/R$.

DNS length scales

The Kolmogorov length scale based on the following equations [176] for the simulations in this paper varied from 3 microns for the validation cases to 5 microns for the SWRI case.

$$R_l = ul/\nu$$

$$\eta_K = R_l^{-3/4} l$$

Here, R_l is the turbulence Reynolds number, u is the injection velocity, l is the characteristic length (respective injector diameter) and ν is the kinematic viscosity of the injected fluid. η_K is the Kolmogorov length scale.

To limit the simulation cost, the smallest cell size in the domain were resolved to 10 microns which made the simulations “DNS-like”.

SL-GPS Results

Appendix A: Results for other species mole fractions obtained using different reduction methods for methane combustion for four different cases outlined in Table 1.

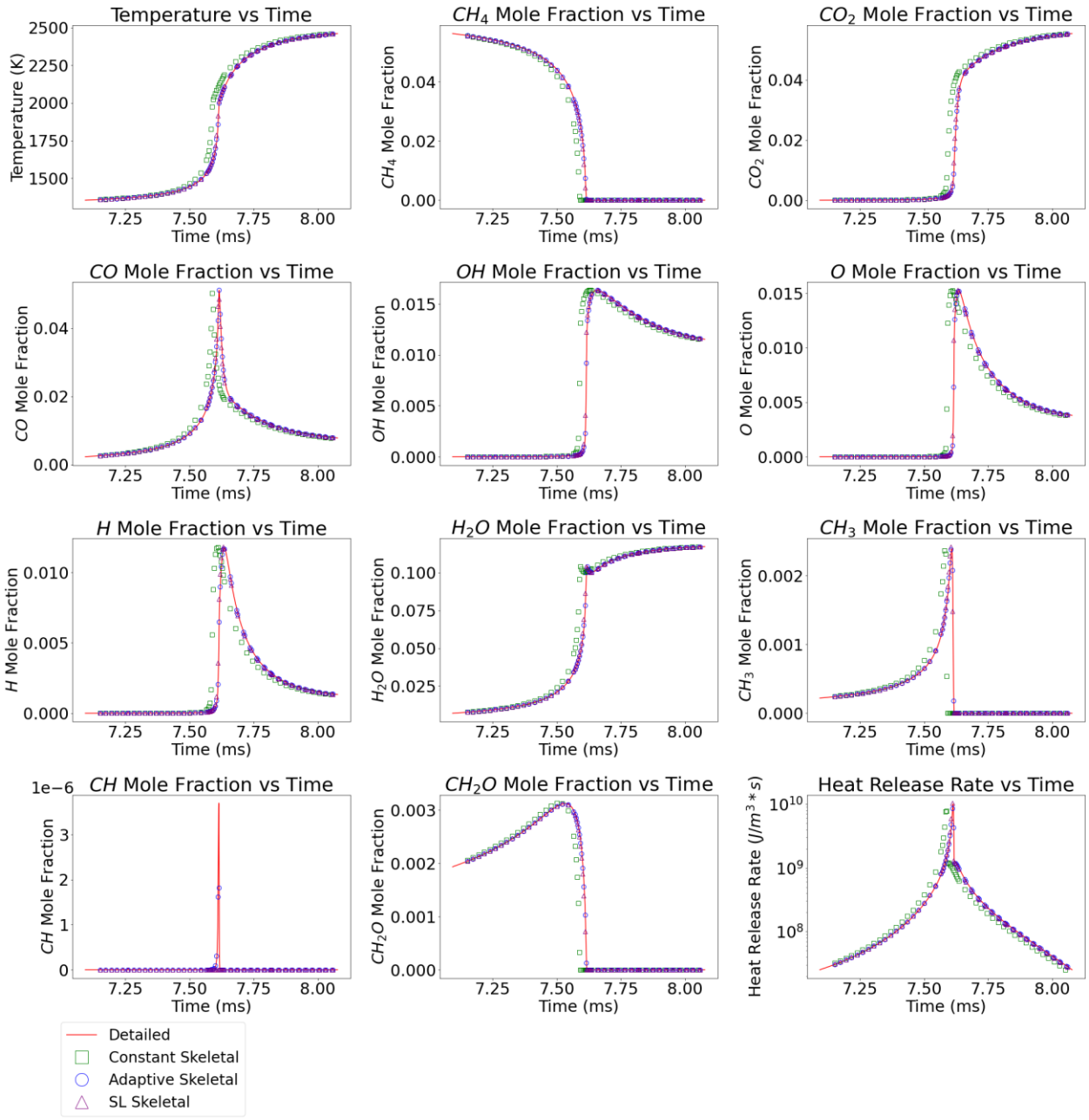

Figure A1: Temperature, CH_4, CH_2O CO_2, CO, O, H, H_2O, and CH_3 mole fraction, and HRR for methane combustion cases using detailed (solid red line), classic GPS (open green square symbol), adaptive GPS (open blue circle symbol), and SL-GPS (open purple triangle) mechanisms for case V1-C1. Classic GPS results not available for CH mole fraction as CH was not included in the reduced mechanism.

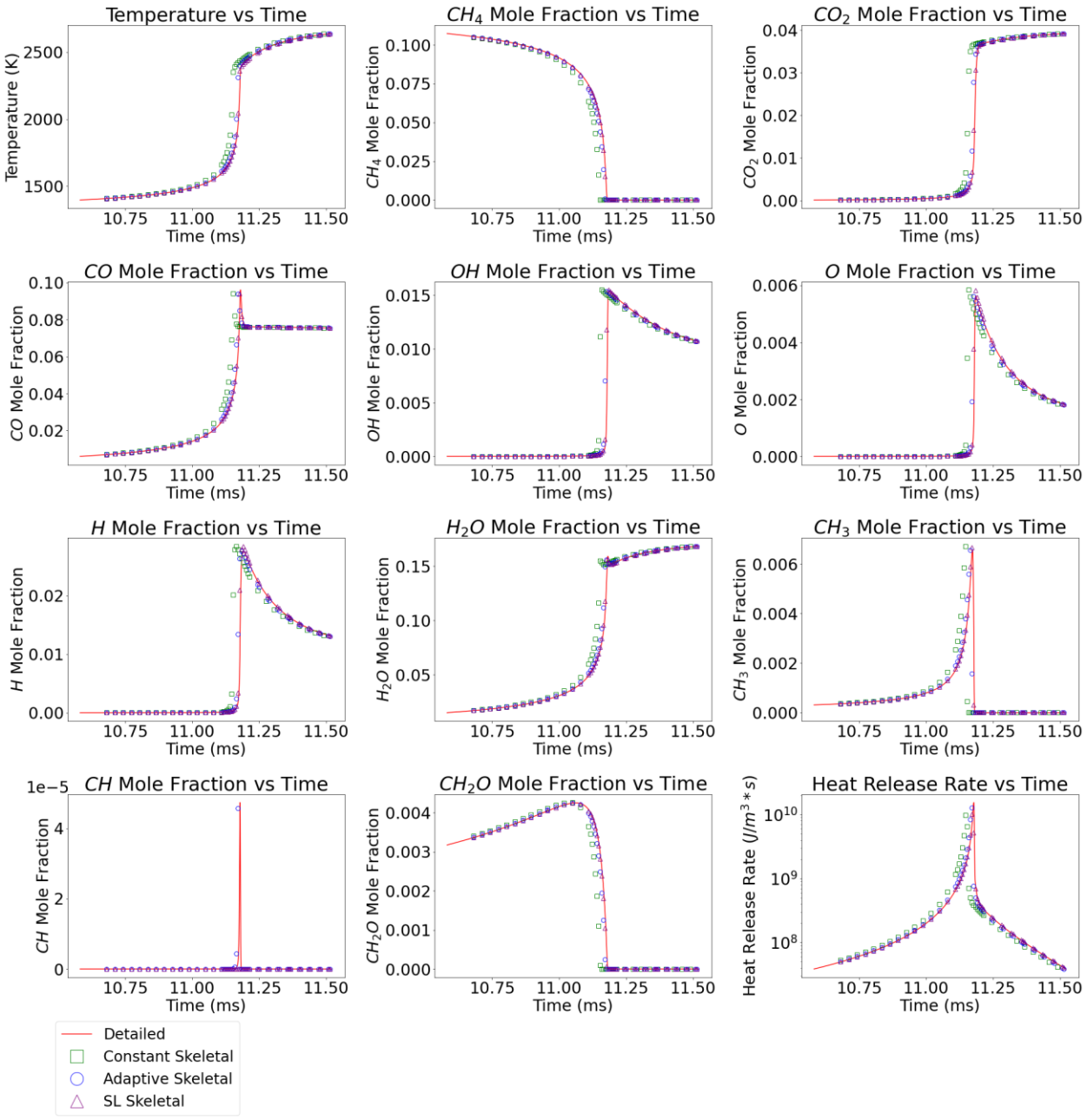

Figure A2: Temperature, CH_4, CH_2O CO_2, CO, O, H, H_2O, and CH_3 mole fraction, and HRR for methane combustion cases using detailed (solid red line), classic GPS (open green square symbol), adaptive GPS (open blue circle symbol), and SL-GPS (open purple triangle) mechanisms for case V1-C2. Classic GPS results not available for CH mole fraction as CH was not included in the reduced mechanism.

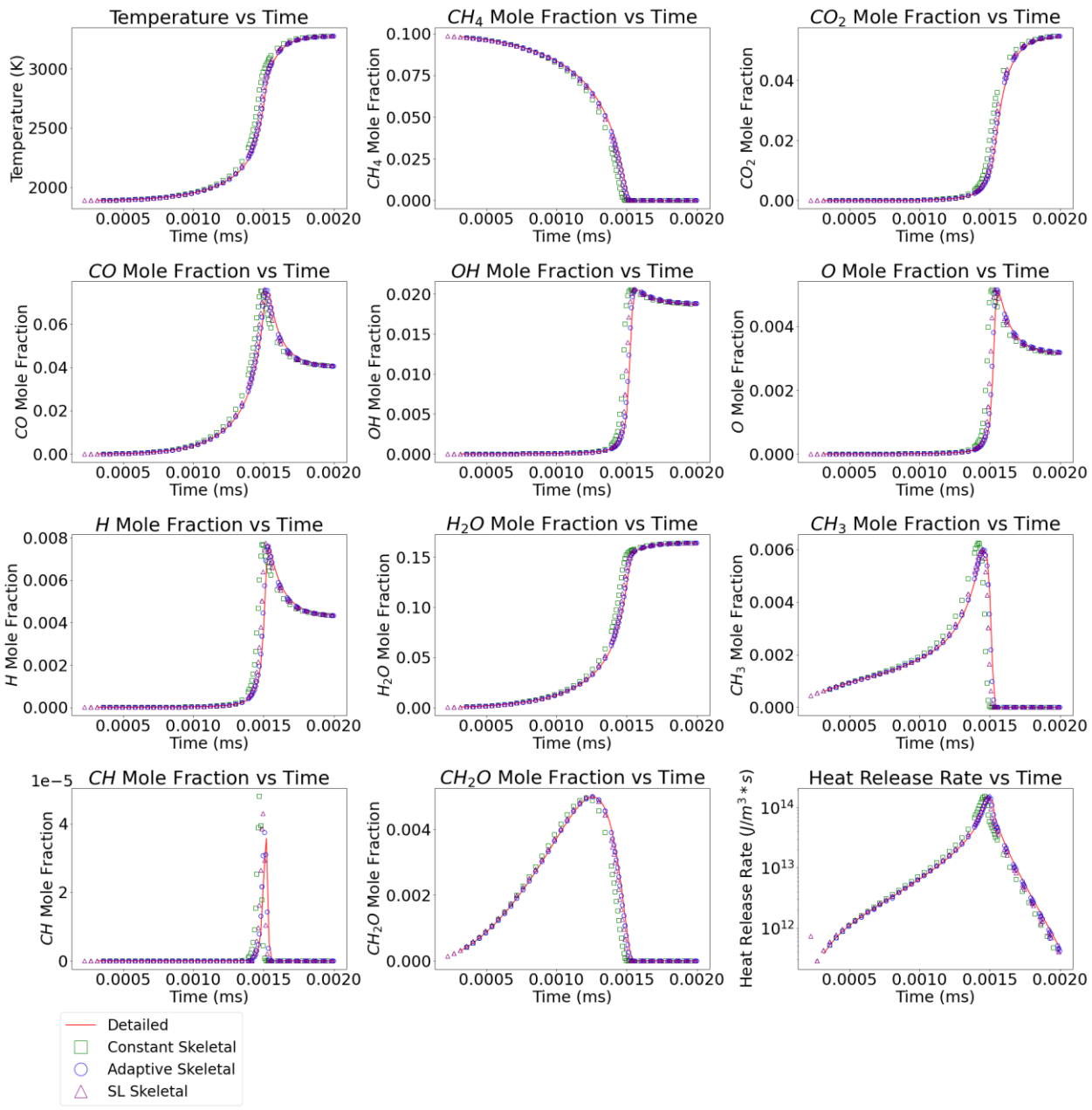

Figure A3: Temperature, CH_4, CH_2O CO_2, CO, O, H, H_2O, and CH_3 mole fraction, and HRR for methane combustion cases using detailed (solid red line), classic GPS (open green square symbol), adaptive GPS (open blue circle symbol), and SL-GPS (open purple triangle) mechanisms for case V1-C3. Classic GPS results not available for CH mole fraction as CH was not included in the reduced mechanism.

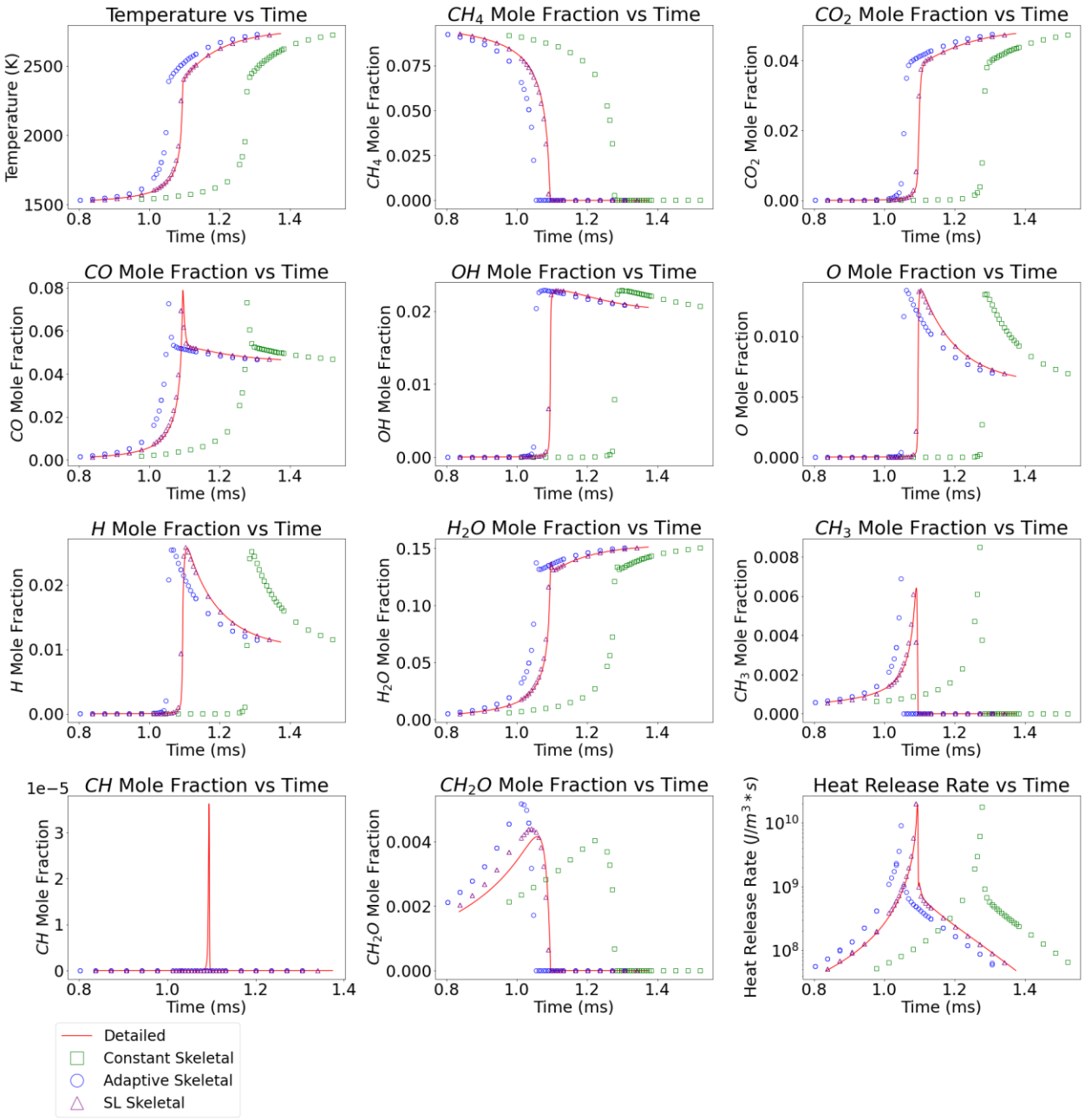

Figure A4: Temperature, CH_4, CH_2O CO_2, CO, O, H, H_2O, and CH_3 mole fraction, and HRR for methane combustion cases using detailed (solid red line), classic GPS (open green square symbol),

adaptive GPS (open blue circle symbol), and SL-GPS (open purple triangle) mechanisms for case V1-C4. Classic GPS results not available for CH mole fraction as CH was not included in the reduced mechanism.

Appendix B: Results for other species mole fractions obtained using different reduction methods for ethanol combustion for three different cases outlined in Table 1.

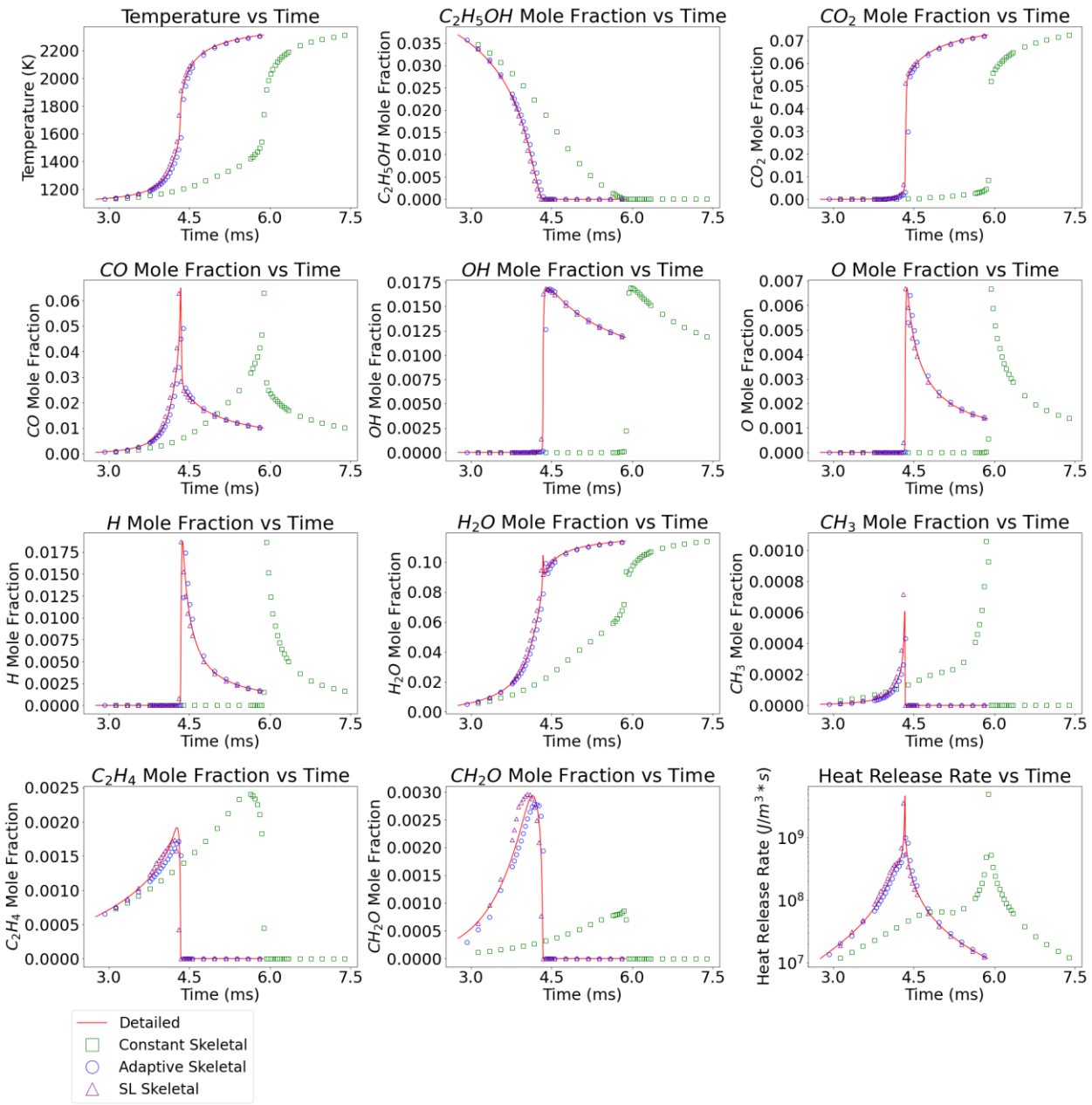

Figure B1: Temperature, C_2H_5OH, C_2H_4, CH_2O CO_2, CO, O, H, H_2O, and CH_3 mole fraction, and HRR for methane combustion cases using detailed (solid red line), classic GPS (open green square symbol), adaptive GPS (open blue circle symbol), and SL-GPS (open purple triangle) mechanisms for case V2-C1. Classic GPS results not available for CH mole fraction as CH was not included in the reduced mechanism.

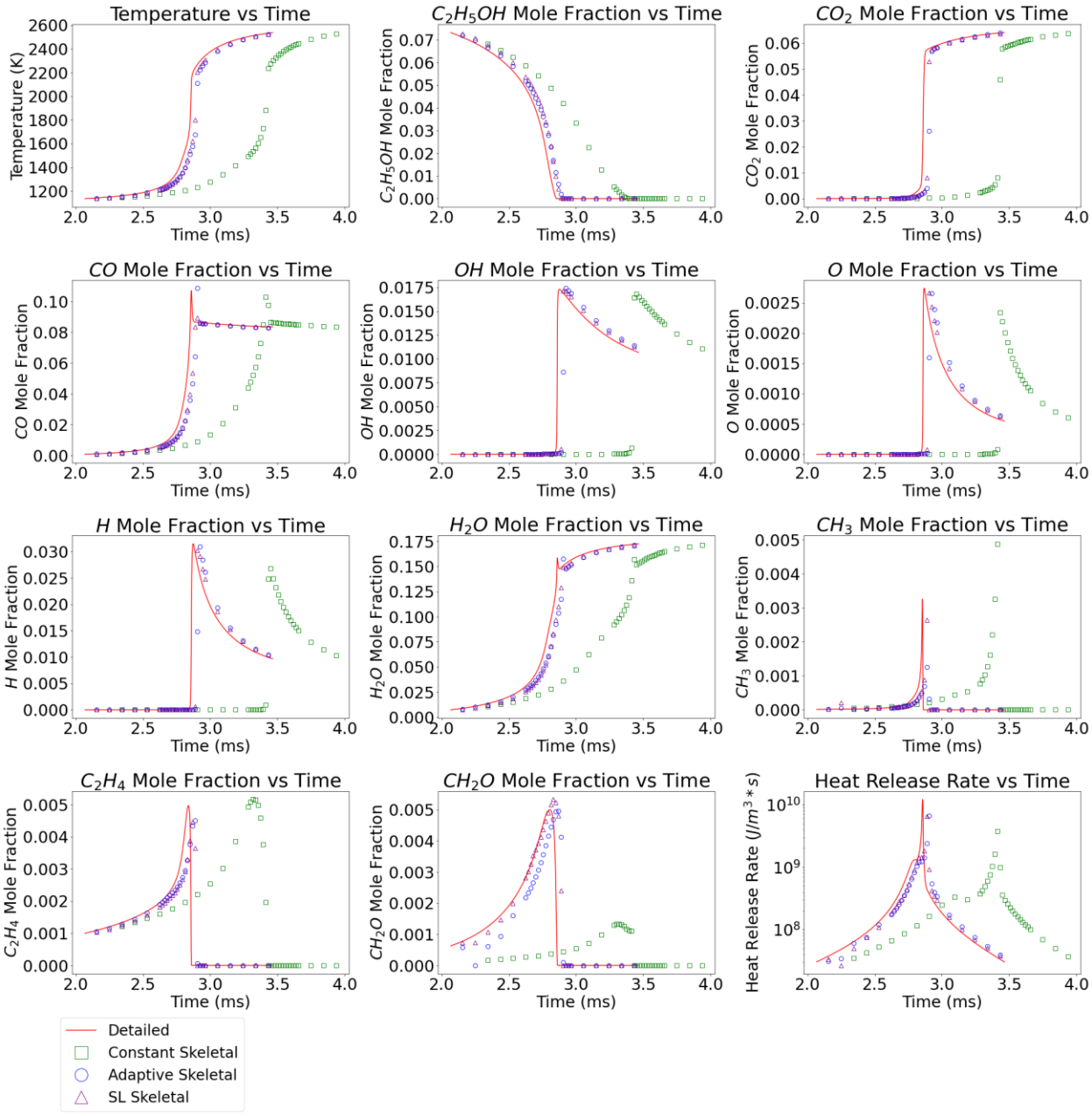
Temperature vs Time
Temperature (K)
Time (ms)
C_2H_5OH Mole Fraction vs Time
C_2H_5OH Mole Fraction
Time (ms)
CO_2 Mole Fraction vs Time
CO_2 Mole Fraction
Time (ms)
CO Mole Fraction vs Time
CO Mole Fraction
Time (ms)
OH Mole Fraction vs Time
OH Mole Fraction
Time (ms)
O Mole Fraction vs Time
O Mole Fraction
Time (ms)
H Mole Fraction vs Time
H Mole Fraction
Time (ms)
H_2O Mole Fraction vs Time
H_2O Mole Fraction
Time (ms)
CH_3 Mole Fraction vs Time
CH_3 Mole Fraction
Time (ms)
C_2H_4 Mole Fraction vs Time
C_2H_4 Mole Fraction
Time (ms)
CH_2O Mole Fraction vs Time
CH_2O Mole Fraction
Time (ms)
Heat Release Rate vs Time
Heat Release Rate (J/m^3*s)
Time (ms)
Detailed
Constant Skeletal
Adaptive Skeletal
SL Skeletal

Figure B2: Temperature, C_2H_5OH, C_2H_4, CH_2O CO_2, CO, O, H, H_2O, and CH_3 mole fraction, and HRR for methane combustion cases using detailed (solid red line), classic GPS (open green square symbol), adaptive GPS (open blue circle symbol), and SL-GPS (open purple triangle) mechanisms for case V2-C2. Classic GPS results not available for CH mole fraction as CH was not included in the reduced mechanism.

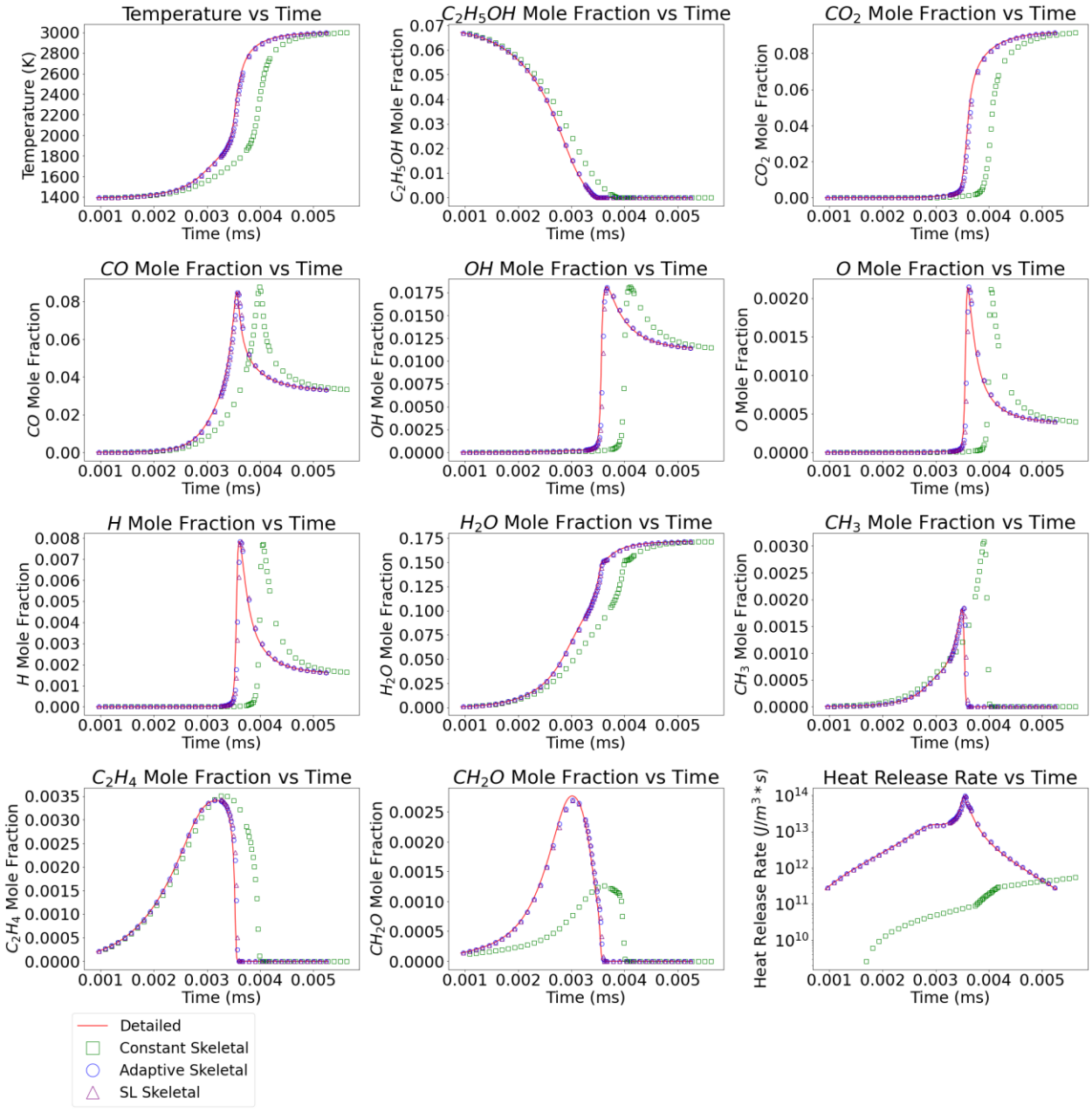

Figure B3: Temperature, C_2H_5OH, C_2H_4, CH_2O CO_2, CO, O, H, H_2O, and CH_3 mole fraction, and HRR for methane combustion cases using detailed (solid red line), classic GPS (open green square symbol), adaptive GPS (open blue circle symbol), and SL-GPS (open purple triangle) mechanisms

for case V2-C3. Classic GPS results not available for CH mole fraction as CH was not included in the reduced mechanism.

Appendix C: Ignition delay results for equivalence ratio values not included in the figures in sections 2.7.

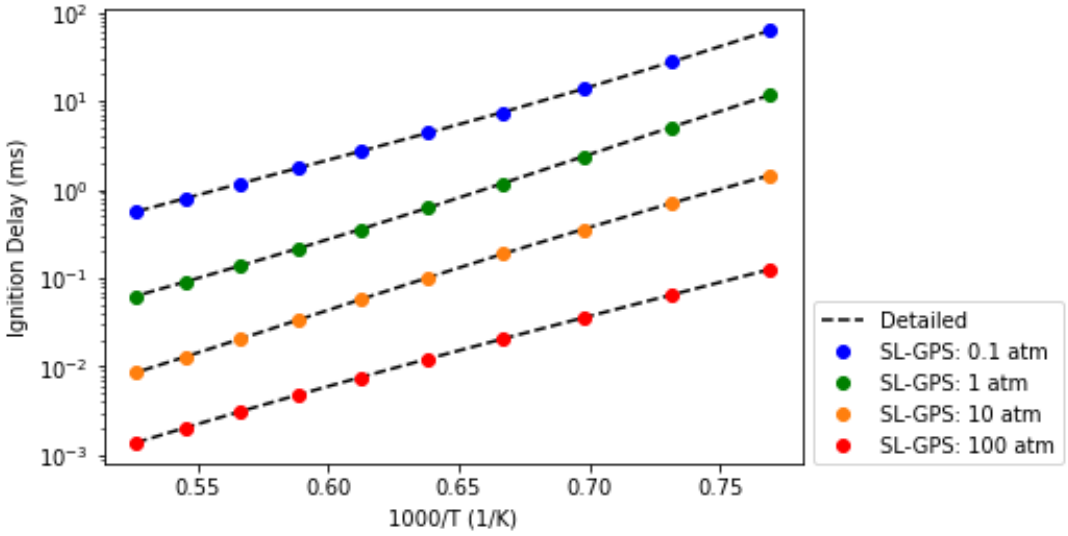

Figure C1: Ignition delays for training range cases at an equivalence ratio of 1.0 (Table 2) for GRI 3.0.

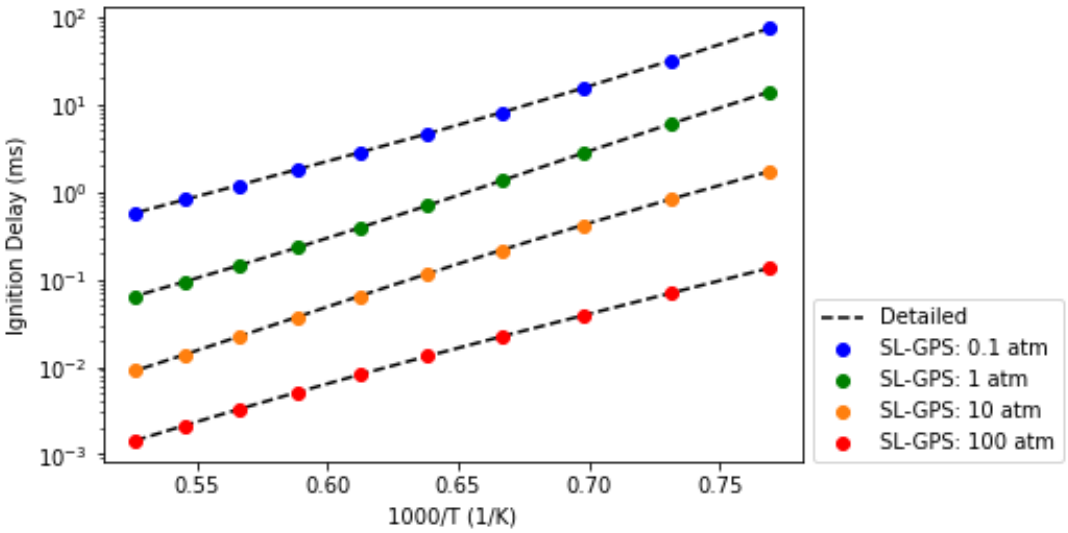

Figure C2: Ignition delays for training range cases at an equivalence ratio of 1.4 (Table 2) for GRI 3.0.

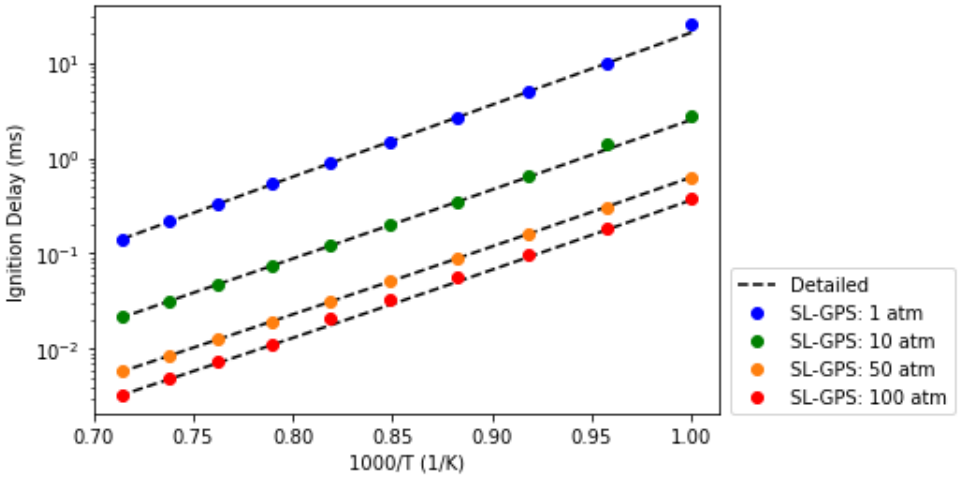

Figure C3: Ignition delays for training range cases at an equivalence ratio of 1.0 (Table 3) for PCRL-Mech1.

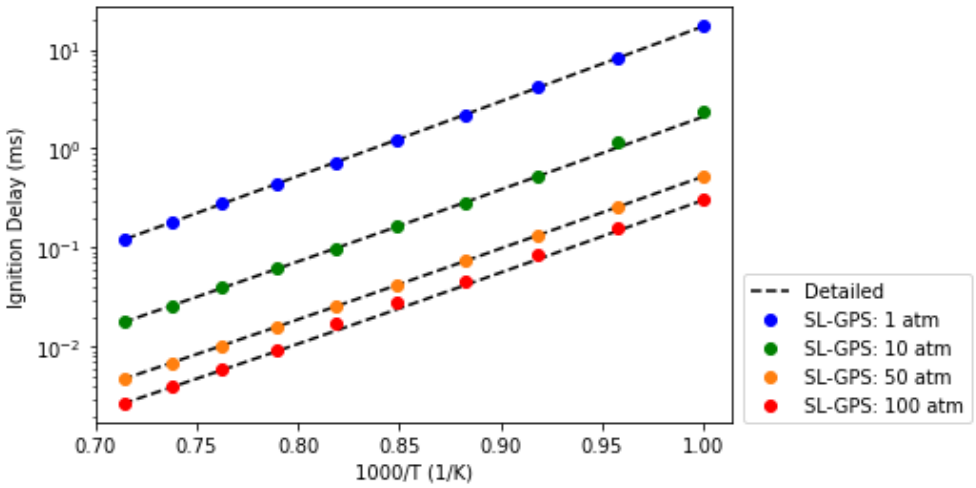

Figure C4: Ignition delays for training range cases at an equivalence ratio of 1.4 (Table 3) for PCRL-Mech1.